Investigating the generation and properties of model network systems

Oliver Peter Whitaker

Brasenose College
University of Oxford

A thesis submitted for the degree of
Doctor of Philosophy

Michaelmas 2024

Abstract

Understanding the structure and properties of thin film materials is an area of continued research, due to the experimental synthesis and characterisation of carbon, boron nitride, silica and aluminosilicate thin films. The structures of these films can be atomically resolved, providing a high level of structural detail for small sample areas. These experimental images show atoms arranged in network structures, interpreted as a percolating net of rings. This atomistic structure has a direct impact on mechanical and permeation properties, meaning the ability to characterise and control the structure has the potential to unlock a wide range of technologically useful properties.

The overall aim of this thesis is to improve the simulation and characterisation of experimentally realisable two dimensional disordered materials. With accurate means to simulate a range of two-dimensional structures, we can begin to understand the feasibility of using these materials effectively for a range of applications. Characterising known and potential structures is crucial to understanding how well our simulations fit with experimentally observed structures. This is accomplished in this work by examining a range of metrics, both empirical laws (namely Lemaître's law and the Aboav-Weaire law) and graph theory metrics, evaluated by interpreting the atomic systems as mathematical networks.

In this thesis, low level potential models are developed for thin films of graphene, boron nitride and bilayer silica systems. Example structures are generated across a range of disorder using a bond switching algorithm, and evaluated against experimental samples where present, with the goal of evaluating the effectiveness of our potential models. These potential models are then applied to systems with 'pores', to generate structures predicted to have technologically useful permeation properties. Both periodic and aperiodic approaches are used to predict the structure and stability of graphene and silica bilayer pore structures with pore density. Continuing work on silica bilayers, this thesis then establishes an escalating potential model to generate and evaluate a broad range of bilayer configurations efficiently. Moving from computationally 'cheap' to 'expensive' potentials allows us to sequentially narrow the phase space of interest, providing an efficient high-throughput method. The data set generated allows for an understanding of energetic and structural trends with disorder. In addition to disordered structures, novel crystalline bilayer structures derived from zeolite structures are proposed and evaluated. These structures are predicted to approximate zeolite pore sizes, and have similar permeability characteristics. Novel techniques for using procrystal methods are developed and introduced, allowing for the generations of sample three-dimensional silica structures.

Investigating the generation and properties of model network systems

Oliver Peter Whitaker

Brasenose College

University of Oxford

A thesis submitted for the degree of

Doctor of Philosophy

Michaelmas 2024

This work is dedicated to Peter Gray Bell (4.5.1940 - 25.3.2023)

Figure 1: Grandma, Me and Grandad, on the day of my graduation, Jesus College 2019

Peter was my Grandad, teacher, confidant, and fountain of all knowledge. Although his own education was complicated by family movements, he was always the first to advocate for mine. He stood alongside my mum to educate me when my school failed to, and was always in my corner, visibly and behind the scenes. He and grandma drove me to exams, and to interviews, and offered support beyond what could be asked for. He taught me an excitement for knowlegde, from teaching me car models as a small child, to maths and sciences when I was home educated, and to European geography and politics on a map at the top of his stairs whenever I would visit. I would certainly not be in a position to have attended Oxford, let alone to attend post graduate study, without his tireless help and proud support. I hope that Grandad would be proud of this work, in particular its attempts to stay on a 'real world' track. Although the impact Grandad had on my life could not fit in the length of this thesis, I am incredibly grateful to have this opportunity to lay out his contributions to my academic life here. I am particularly proud to have the opportunity to preserve his memory in the Oxford archives.

He is sorely missed.

Acknowledgements

Institutional

I am very grateful for the institutional support that made my DPhil possible, and extend my thanks to the EPSRC Centre for Doctoral Training in Theory and Modelling in Chemical Sciences (grant EP/L015722/1).

Personal

This thesis represents the culmination of 9 years at Oxford, over which time I have accrued quite a few debts of gratitude.

First, I must thank Mark Wilson. Mark provided both the freedom to explore such a rich field of chemistry, whilst also informally keeping regular tabs on where progress was taking me. However random the endeavour, he was happy to listen to crazy ideas ("Maybe Aztec dry stone walls could be modelled as a network?"), providing the most comprehensive post-rationalisations of my more wayward projects. With the tagline 'now this might seem trivial, but it actually isn't...' reassured me in my more apparent results, and gave me the confidence to try new things. I am incredible grateful for the opportunities afforded by Mark's supervision, and the years in his group have been my best in Oxford.

Particular thanks must also go to friends made in the department, from TMCS cohorts past and present to more recent additions. Pre-COVID, the relaxed atmosphere of collaboration and discussion at daily 11am and 4pm coffee breaks provided the basis of both an enjoyable working environment and lasting friendships. The Wilson/Barford group office always offered a supportive atmosphere, with help readily available. In particular, thanks go to David and Laszlo for early and consistent help and high jinks (there are still at least two Laszlo portraits displayed about the office at time of writing). Post-COVID, heartfelt thanks go to those who put the atmosphere back into the department. In particular, thanks go to Matt Bailey, for the pub-finder algorithm (with its Royal Oak factor) and direction for get-togethers more generally, and to Tim, whose company, honesty and all-round friendliness have made the department a much happier and enjoyable place. Within the group, thanks go to the Part II students of all years, who always provided a source of energy and enthusiasm. In particular, thanks go to Jenny,

George and Joe for bringing great ideas and fun to the department (and leaving behind beer). Zuzanna has only been a member of the group for 6 months, but her unparalleled organisational skills have revolutionalised the group, and I am incredibly grateful for all of her efforts.

Beyond the department, I owe a debt of gratitude to the family and friends that have helped me. Firstly, thanks must go to my parents, Kate and Paul. They have always been the strongest proponents of my education, and their continued support and advocacy through my time at Oxford and beyond has made this amazing period of my life possible. Even though I've never managed to properly explain what I've done in the last four years, I know that you have always had my back, and I am eternally grateful for your love, kindness, and dedication to helping me succeed. My grandparents have always provided staunch support, and from driving me back from my Oxford interviews 10 years ago continued to show a deep interest in my life here.

From lockdowns to when I was bed bound post operation, huge thanks must go to George, Jonny and Jack. You have provided a constant point of contact and support however hard things have got, and our evenings online are always the highlight of my week. Thanks go to Jack for always being able to make me smile, chat about tech, and find the fun in life. Over covid and beyond, thanks go to George for the open invite to visit in London and Vancouver, and for sport and sun in the good times and the space for frank and honest discussions in the difficult times. Over the last two years especially, thanks go to Jonny, for providing an honest ear for the difficulties of DPhil life, for accommodating Teresa and I so graciously, for late night visits to Oxford, and for encouraging me back into sport post-op. I couldn't have done it without you. Thanks also must go to Sophie, for always providing a such friendly face in Oxford, and giving me problems I could solve when my code didn't. I remain incredibly grateful for the influence of Matt Clough, who first introduced me to computational chemistry and provided such excellent guidance, and Dr Lawrence, who first introduced me to the concept of post-graduate work (as when science got fun, and when you could leave a reaction on to go and play football).

Finally, thanks go to Teresa. Thank you for your patience during a year of 'I feel like I'm getting close to submitting my thesis!', for putting up with a house full of servers, and for support in drawing a line under this work, not to mention all of your time, love and support over the last years. I am incredibly grateful for all your support, both small and large, that has helped me see beyond the difficulties of the last two years.

Abstract

Understanding the structure and properties of thin film materials is an area of continued research, due to the experimental synthesis and characterisation of carbon, boron nitride, silica and aluminosilicate thin films. The structures of these films can be atomically resolved, providing a high level of structural detail for small sample areas. These experimental images show atoms arranged in network structures, interpreted as a percolating net of rings. This atomistic structure has a direct impact on mechanical and permeation properties, meaning the ability to characterise and control the structure has the potential to unlock a wide range of technologically useful properties.

The overall aim of this thesis is to improve the simulation and characterisation of experimentally realisable two dimensional disordered materials. With accurate means to simulate a range of two-dimensional structures, we can begin to understand the feasibility of using these materials effectively for a range of applications. Characterising known and potential structures is crucial to understanding how well our simulations fit with experimentally observed structures. This is accomplished in this work by examining a range of metrics, both empirical laws (namely Lemaître's law and the Aboav-Weaire law) and graph theory metrics, evaluated by interpreting the atomic systems as mathematical networks.

In this thesis, low level potential models are developed for thin films of graphene, boron nitride and bilayer silica systems. Example structures are generated across a range of disorder using a bond switching algorithm, and evaluated against experimental samples where present, with the goal of evaluating the effectiveness of our potential models. These potential models are then applied to systems with 'pores', to generate structures predicted to have technologically useful permeation properties. Both periodic and aperiodic approaches are used to predict the structure and stability of graphene and silica bilayer pore structures with pore density. Continuing work on silica bilayers, this thesis then establishes an escalating potential model to generate and evaluate a broad range of bilayer configurations efficiently. Moving from computationally 'cheap' to 'expensive' potentials allows us to sequentially narrow the phase space of interest, providing an efficient high-throughput method. The data set generated allows for an understanding of energetic and structural trends with disorder. In addition to disordered structures, novel

crystalline bilayer structures derived from zeolite structures are proposed and evaluated. These structures are predicted to approximate zeolite pore sizes, and have similar permeability characteristics. Novel techniques for using procrystal methods are developed and introduced, allowing for the generations of sample three-dimensional silica structures.

Contents

List of Figures

List of Abbreviations

1D, 2D, 3D . . One- or two-dimensional, referring in this thesis to spatial dimensions in an image.

BN . . . . . Boron Nitride

h-BN . . . . . hexagonal Boron Nitride

a-BN . . . . . amorphous Boron Nitride

Si . . . . . Silicon

O . . . . . Oxygen

STM . . . . . Scanning Tunneling Microscope

ML . . . . . Machine Learning

DFT . . . . . Density Functional Theory

NSV . . . . . Null Space Void

IZA . . . . . International Zeolite Association

FTC . . . . . Framework Type Code

CBU . . . . . Composite Building Unit

SRC . . . . . Shape Regularity Coefficient

MC . . . . . Monte Carlo

MD . . . . . Molecular Dynamics

MCMC . . . . Monte Carlo Markov Chain

LAMMPS . . Large Atomic/Molecular Massibe Parallel Simulations

GUI . . . . . Graphical User Interface

1 Introduction

Since Zachariasen's groundbreaking work on the amorphous structure of glass[1], chemists have sought to understand these irregular, aperiodic systems as collections of percolating rings. At the time, glasses had proved a hindrance to prevailing models of solid state structures. While increasingly accurate theories were being developed to explain crystal structures, glasses remained elusive, neither fully conforming to, nor completely deviating from, the characteristics that described crystalline systems.

Glasses share the same mechanical properties as crystals over a wide range in temperatures, indicating that the same fundamental interactions hold them both together. However, glasses show no periodicity or symmetry in their extended 3D network, as evidenced by X-ray diffraction measurements; as such, models predicated on repeated unit cells were unreliable. Unlike crystals, which undergo a sharp phase transition between solid and liquid states, glasses experience a continuous structural breakdown near the melting point, a consequence of no two atoms being structurally equivalent. This is reflected in their structure factors, which reveal similar local arrangements but no long-range order.

These factors led to Zachariasen's proposition for the archetypal silica glass, presented in a simple two-dimensional diagram, reproduced in Figure 1.1. This image shows a network of three-coordinate silicon atoms, bridged by two-coordinate oxygen atoms, resulting in a system of percolating rings without long range order,

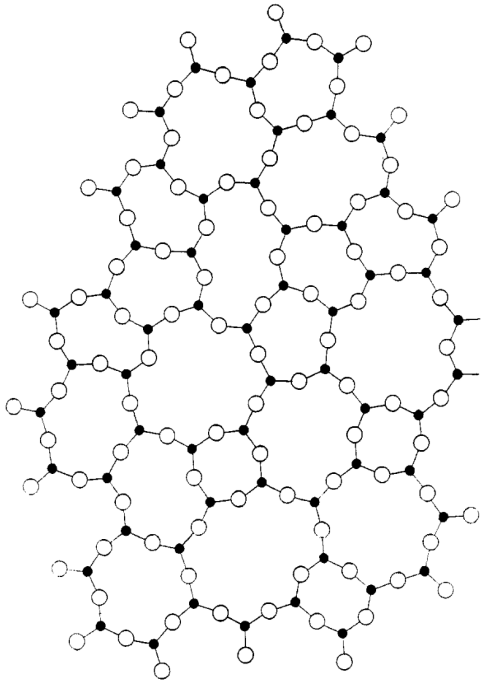

Figure 1.1: Zachariasen's illustration of an A_2O_3 glass network[1]

offering a conceptual foundation for the study of glasses and amorphous materials in three dimensions. Over time, advances in experimental techniques, especially in the realm of two-dimensional materials, have realized many of the concepts Zachariasen proposed. Modern methods have synthesised various two-dimensional amorphous materials which can be considered realisations of Zachariasen's glass, such as carbon[2–5], silica[6, 7], and germania[8].

The emergence of these materials has been a pivotal moment in modern chemistry, enabling the development of technological applications including catalysis and gas separation[9–12]. In particular, as global deaths from both air and water pollution rise[13–15], efficient and cost-effective means to separate gases are becoming ever more important.

By recognising these two-dimensional atomic systems as mathematical graphs, we gain an additional level of understanding of the constraints imposed on these seemingly unconstrained systems. The first of these controls is the mean ring size (*i.e.* the average number of sides formed by the polygons in a network), which can be defined for a system based on the average coordination number using Euler's

formula. This is readily understandable for chemical systems. Taking the example of three coordinate carbon atoms, we know that in two-dimensions they form hexagonal graphene sheets, and defects introduced into these systems introduce ring sizes which average out to six; for instance, Stone-Wales defects introduce five- and seven-membered rings in equal number[16]. Euler's law gives us an understanding of the physical limits on the range of rings that can be formed. However, within each distribution of rings, there are many ways to arrange them, of which only a subset are experimentally observed. Local ordering was first investigated in polycrystals in 1970, leading to the empirical Aboav-Weaire law[17, 18], proposing that the mean ring size surrounding a central ring may be captured by a single fitting parameter and the size of the central ring. This relationship provides a global factor for quantifying the likelihood of small rings to be adjacent to large rings, detailing the first order ring correlations. With an understanding of local ordering, we can turn our attention to the distribution of rings present in the system. While our systems are now constrained to a given mean ring size and local environment, the distribution beyond this is not constrained. Empirically, Lemaître's law shows that that the distribution of natural ring sizes approximates an entropic solution[19], offering a predictor for the global ring statistics of a system at a given level of disorder.

The uniqueness and potential applications of novel two-dimensional materials make them ideal candidates for computational study, complementing and enhancing experimental efforts. For instance, thin silica bilayer films have been the subject of numerous computational studies, utilising methods such as *ab initio* calculations[20] and molecular dynamics simulations with classical force fields[21]. To conduct these simulations, an initial atomistic configuration is required, which can be acquired through various methods.

The simplest approach is to use existing experimental images. The first detailed images of silica bilayers were captured in 2012, when the bilayers were synthesised and imaged on metallic substrates like ruthenium[22]. Since then, additional studies have produced more images, but the overall number remains limited because of the difficulty in obtaining bilayers with reliable coverage which can be fully resolved.

There are also significant challenges posed by imaging two-dimensional amorphous materials at atomic resolution, and accurately determining atom positions from these images, which limit the areas we can image. Furthermore, certain experimental systems (*e.g.* germania bilayers, monolayers of boron nitride) have been difficult to synthesis[8, 23], providing limited starting configurations for computational modelling of these systems.

An alternative approach is to generate starting configurations using computational methods, allowing for the fast generation of a large number of fully resolved configurations. However, where experimental evidence exists, these systems must be representative of this evidence, and so must behave similarly, as evaluated using key metrics (*e.g.* bond length and angle distributions, ring distributions). The simulations which use these networks as their starting configurations can only be as accurate as their seed, and so it is vitally important to understand the systems themselves, and match the seed accordingly. To this effect, this thesis presents four two-dimensional systems; graphene, boron nitride, silica bilayers and biological cell networks. Low level potential models for each are developed and presented, with a degree of parameter testing. The key metrics of these systems are evaluated, with novel metrics discussed. Where data is available, our systems are compared to experimental systems.

Of particular interest to silica bilayers are their permeation properties, hypothesised to be correlated with their ring size distribution[12]. As such, we have applied our models for silica bilayers to create aperiodic systems with ring sizes beyond those currently experimentally observed, such as might be formed using templating methods, and evaluated the key metrics of these systems. In particular, we examine the effect on the global structure of the introduction of rings of these size. To understand the effect of the density of these pores on the structures, a novel method of network generation is introduced, termed 'pore evaporation'. This method mirrors experimental work on graphene systems to introduce pores by particle irradiation[24], providing a graphical user interface to allow directed system generation. The pore evaporation method is applied to systems using low level

graphene and silica bilayer potentials, with the aim of understanding the structural effects of generating ring sizes outside of those experimentally observed but which are predicted to have desirable permeation properties.

Continuing work on silica bilayers, this thesis establishes an escalating potential model to generate and evaluate a broad range of bilayer configurations efficiently. The model uses computationally 'cheap' calculations using the lower level potentials developed earlier in this work to scan across a broad range of configurations, with the aim of predicting the phase-space behaviour of computationally 'expensive' potential models. This allows us to narrow the phase space evaluated using high level empirical potentials to energetically realistic areas, improving the efficiency of the process. This method generates a very large data set of structures, minimised using both low level harmonic and more accurate empirical potentials, providing the most comprehensive analysis of theoretical silica bilayer structures to date. Simulations are conducted over a range of densities, to gain a detailed understanding of the effect of the degree of amorphisation on energetics and structure with simulation cell area. Structural analyses show the trends in key metrics with disorder, and energetic calculations show the effect of the degree of amorphisation. In addition, the possibility of two-dimensional analogues of zeolite structures is proposed, and a number of novel zeolite analogues are created and analysed.

Finally, attention will be turned to another system of relatively recent interest, that of "procrystalline" lattices[25]. These procrystals can be considered to have behaviour between crystalline and amorphous systems, displaying crystalline node positions with a disordered ring structure. Of interest to our work modelling disordered systems, procrystals provide an ideal basis for decomposing three-dimensional structures into layers of two-dimensional sheets, for which we have far greater understanding.

2

Experimental Background

In order to model network systems, we need to have an understanding of the properties and the limitations in their synthesis. In this chapter, the key systems we are interesting in modelling are presented, alongside our motivations for studying them, and their are properties summarised.

Contents

2.1 Graphitic Systems

Crystalline graphene, a monolayer of carbon atoms arranged in a two-dimensional honeycomb lattice, was first isolated and identified in 2004[26]. The extensive investigations of this novel low-cost material revealed very high electrical conductivity, mechanical strength and flexibility[27–29].

Atomic-level defects in graphene play a crucial role in determining the material's mechanical, electrical, and chemical properties. These defects occur when the ideal

hexagonal structure of graphene is disturbed, introducing imperfections that can significantly influence its behaviour[3, 30–32]. For instance, introducing larger ring sizes to the network affects the transport properties of the network, with the presence of seven-membered rings allowing for H^+/D^+ permeability[32]. As such, understanding the controlled introduction of defects into graphene is fundamentally important to rationalising and tuning its properties. Where defects form naturally on the surface, they tend to be composed of five-, six- and seven-membered rings[2, 33]. Alongside natural formation, defects can also be introduced directly to the surface using a wide variety of methods, including focused energy beam ablation, focused ion beam ablation and ultraviolet-induced oxidative etching[34]. Depending on the degree of irradiation, the defects can range in size from 5-7 ring defects[3], up to very large defects such as those shown in Figure 2.1, reproduced from literature[34]. Resolved images of graphene surfaces about these defects show the potential for carbon atom under-coordination, depending on the size and nature of the defect formed. Generally, the ring size range for defects introduced in this manner is between four- and eight-membered rings[3]. Recent work using *ab initio* potentials has shown that 5-7 defects are well accommodated within a small local radius[35]

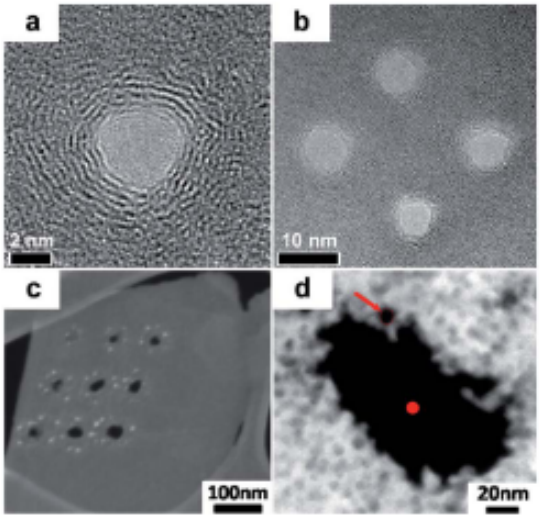

Figure 2.1: (a) Nanopores generated by focused electron beam (FEB) ablation in monolayer graphene. (b) Multiple nanopores made in close proximity to each other by FEB ablation. (c) Nine holes etched in a graphene flake. (d) Etched hole in graphene surface. Images reproduced from literature[34]

Simulations of the potential energy range from *ab initio* methods[35] to lower level Keating potentials[5], with the relative bond and angle force constants derived from experimental data[36].

2.2 Thin film Boron Nitride

Boron Nitride (BN) is a binary material, forming structures isoelectronic with carbon. Thin films ($\simeq 2 - 17$ nanometers) have been created using plasma-chemical vapour decomposition, in both hexagonal (h-BN)[37] and amorphous (a-BN)[38] configurations. The driving force behind this research has been producing dielectrics for nanoscale computing; BN films act as insulators, but exhibit a range of dielectric constants depending on configuration, showing potential for use as 'gate dielectrics' for nano-scale transistors[39, 40]. Hexagonal monolayers analogous to graphene have been synthesised[41], as shown in Figure 2.2. However, there

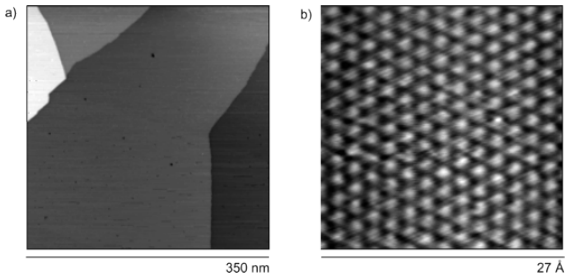

Figure 2.2: STM images for hexagonal boron nitride on a Ni metal surface, showing a large scale image (a) and atomically resolved image (b). Images reproduced from literature[42]

are no amorphous examples. A range of kinetic Monte Carlo simulations, using empirical potentials[43–46] and machine learning density functional theory (ML-DFT)[23] have been applied to propose the structures and dynamics of amorphous monolayer BN structures. These simulations propose a degree of B-B and N-N bonding, termed non-canonical; however, in the absence of experimental data these structures have not been confirmed.

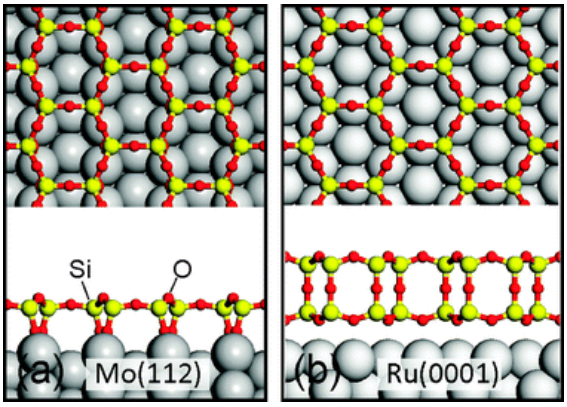

Figure 2.3: Graphic to show the interaction of mololayer (a) and bilayer (b) systems with the metal support. Reproduced from literature[54]

2.3 Bilayer Silica Systems

Over the last decade, novel synthetic pathways have allowed for electrodeposition of thin films ($\leq$ 5 atom thickness) of SiO_2 onto a range of substrates, from metal surfaces[11, 22, 47–53] to graphene[4]. The structures of these films have been analysed using direct imaging techniques and interpreted as monolayers and bilayers of vertex-sharing SiO_4 tetrahedra, in which silicon (Si) and oxygen (O) atoms show classical valence coordinations of 4 and 2 respectively. Figure 2.3 shows representations of these systems. Monolayers form on metal surfaces with a high O affinity, and as such one O atom is directly coordinated to the metal; this strong interaction results in instability when removed from the metal support. In bilayers, the arrangement of these tetrahedra forms two distinct layers, characterised by the presence of a mirror plane, along which the O atoms bridging the layers sit[21, 55], as seen in Figure 2.3 (b). As a result of this plane of symmetry, the top face of the structure is a sufficient descriptor of the bottom face, and so microscopy imaging of the surface allows insight into the connectivity of both layers. Like graphene, these structures adopt a broad range of conformations, from crystalline hexagonal networks[49, 56] to amorphised[22] structures, albeit with a broader ring size distribution (4- to 10-membered rings commonly observed[57, 58]). The generation temperature and choice of support has been identified as a driving factor for amorphicity[11, 59–61], but direct approaches have also shown success,

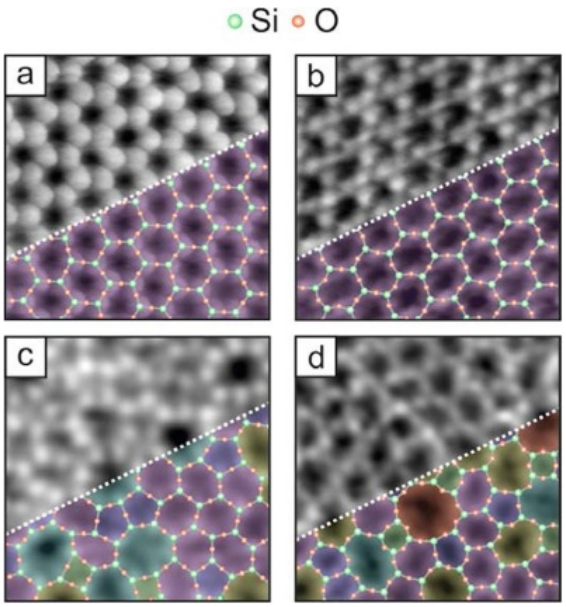

Figure 2.4: Atomic resolution STM images of silica bilayers, with cell size 3.5 nm × 3.5 nm. Structures across a range of disorder are shown, from crystalline with only silicon atom positions resolved (a), and with oxygen atom resolution (b), to two amorphous structures (c) and (d). For the amorphous systems, rings are coloured for clarity. Reproduced from literature[11]

with Stone-Wales defects (5577 ring defects) introduced using electron beams[62, 63]. Recent work has shown that bilayers can be transplanted between surfaces, and are permeable to a range of gasses, with gas selectivity hypothesised to be a function of ring size distribution[12]. As such, with an understanding of the ring size distributions of these systems and why they form, we can understand and predict the gas permeability of silica structures, enabling us to design structures with given permeability characteristics.

Models of silica bilayers have two historical starting points; from experimental images[21] and from computer generated starting configurations[49, 64, 65]. The models used vary in form, from density functional models[66] to empirical potentials[21, 67]. Examples of experimental images for silica bilayers are produced in Figure 2.4, with silicon and oxygen atom positions resolved, which can then be used as a starting configuration for synthesis.

2.4 Zeolitic Behaviour

Zeolites, in particular synthetic zeolites, are a field of intensive research, with their breadth of use as catalysts, absorbants and ion exchangers, and their predominance in the petrochemical industry, drawing significant interest and investment[68–83].

At present, there are 256 zeolite structures[84], but millions more have been proposed based on proposed desired structures, backed up by energetic calculations[85, 86]. These energetic calculations are based on 'ideal' zeolite frameworks. An ideal framework is not a chemical system but a mathematical geometric one, where chemical MX_4 units are replaced with perfect, rigid tetrahedra. These tetrahedra are vertex-sharing, with the vertices acting as force-free spherical joints.

There are distinctions within these models, in particular surrounding the rigidity of the tetrahedral sides. In some models[87–91], 'bars' are used; bars are inflexible, but have stress and strain characteristics. Such models refer to the network of tetrahedra as a 'truss'. In other models[92], springs are used, allowing some distortion of the tetrahedra. In these models, the distortion to these bonds can be used as a metric. For each of these models, the vertices of the tetrahedra are treated as hard spheres, with a contact radius related to measurements of the O atom radius.

Utilizing this sort of modelling, all known zeolites have been shown to exhibit a 'flexibility window'[87, 90, 92]. This is a range of densities over which there is no energetic change (close oxygen atom approaches or intra-tetrahedral strain), bounded by low area and high area 'takeoff' points where the energy rises rapidly. For these frameworks, the high area takeoff point is taken as tension on the bars, whereas the low area takeoff point is compression of the bars. This 'window' is a result of the open nature of zeolite structures; large pores in the structure result in open space for the system to relax into. The mathematical term for the space within the structure is 'Null Space Void' (NSV).

An example of this is provided in Figure 2.5, where we can see that there is a range of cell areas densities over which there is no energetic change (marked here by distortion of the SiO bond length), bounded by low area and high area takeoff points. The mechanism by which the structure relaxes into this space

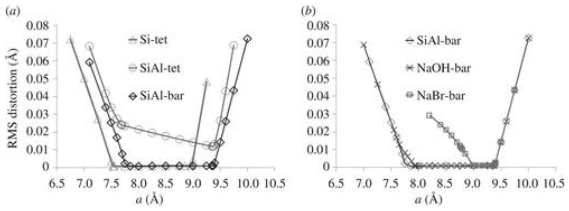

Figure 2.5: Degree of polyhedral distortion as a function of cell area, forming a 'flexibility window'. Different systems are analysed for the same sodalite (SOD) framework; (a) shows 'tet' (flexible tetrahedra) and 'bar' (rigid tetrahedra) models for aluminosilicate mixes, (b) shows the effect of counter ions. Reproduced from literature[92].

leads to a distribution of possible structures; with spherical, force free joints all ideal tetrahedral orientations have the same energy, so long as oxygen atoms are suitably separated. The large internal surface area, and pores which run through the structure, are at the heart of zeolite's performance in catalytic ability and permeation characteristics[93]. The ability to reproduce these structures in thin film environments could produce a host of new applications in this field.

Zeolite structures are incredibly varied, both in their composition and structure. The same arrangement of tetrahedral MX_4 units can be recreated with a range of M and X ion identities (*e.g.* M=Al, Si, P, X=O, S) and ratios, with counter ions (*e.g.* Li, Na) providing even more range in the structures produced. The structures defined are three dimensional, and so there is no all-encompassing, consistent characterisation method based on the structure.

Instead, structures which have been synthesised experimentally are categorised in full by the International Zeolite Association (IZA), which gives each structure a three letter framework type code (FTC)[84]. These codes are derived from names of the Type Materials, rather than any structural traits or characteristics; for instance **AEL** is derived from the structure **A**lPO_4-11 (**EL**even).

Each structure can be described as containing 'building blocks'. The two most relevant for our work are Composite Building Units (CBUs) and Tiles, which are overlapping but distinct ways of understanding the form of zeolite structures, as explained below. These descriptions are not exclusive for a given FTC, for instance **AEL** and **AFO** have identical CBU's and Tiles.

2.4.1 Composite Building Units (CBUs)

CBU are an exhaustive selection of units which are present in all three-dimensional, four-connected nets, of which zeolites are a subset[94]. A limited subsection of 63 of these CBUs are present in discovered zeolites, with those relevant to this work discussed below.

2.4.2 Natural Tiling

The natural tiling approach leans less on the theoretical nature of zeolite networks, instead focusing on crystallographic and topological information. The tiles are labeled using three integers to describe the Euler's law properties of the tiling unit, **V**, **E** and **F**. In addition, the number of kinds of vertices (p), kinds of edges (q) , kinds of faces (r) and kinds of tiles (s) in the tiling. Symmetry and Wyckoff records are provided, with additional entries where tile combinations are combinatorially equal but crystallographically different[95]. There is considerable overlap between a Natural Tilings approach and the CBU approaches. Many of the tiles are equivalent, for instance CBU **d4r** is equivalent to Natural Tiling unit **t-cub** (shown in Figure 2.6). However, this is only true for a small subsection of the building units, and so utilising both allows a better understanding of the structures involved.

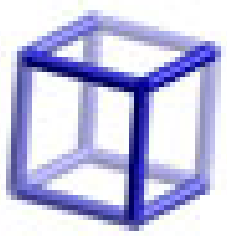

Figure 2.6: Building unit, labeled as **d4r** as a CBU, and **t-cub** as a Tiling unit

2.4.3 Zeolite structure selection

With an understanding of the composition of general zeolite structures, we can begin to make decisions about suitable structures for thin film modelling. Preliminary categorisation of the CBUs and Tiles that posses symmetry elements we believe make

them suitable for silica bilayer analogues are shown in Table 2.1. These are split into 'Strictly Allowed' (building units which can be split into two distinct layers, shows a plane of symmetry between these two layers, and has no nodes lying on this plane of symmetry) and 'Favoured' (those which stack in a layered manner AA', where A' is a mirror image of A, and node coordination is split evenly between two and three).

Unit Type	Strictly Allowed	Favoured
CBU	d3r, d4r, sti, bea, bre, afs, ats, d6r, abw, aww, d8r, imf, gis, phi, pau.	afi, bog, lau.
Tiles	irr-1, cub, kah, mel, ohc, hpr, oth, wwf, bcp, aww, opr, oto, umx, ftt, gsm, osi, red, apf, fry, etn, bph, irr-3.	lov, afi, kaa, lau, oop, odp, uwy-2, sty.

Table 2.1: Table to show CBUs and Tiles evaluated for bilayer structures. These are split into 'Strictly Allowed' (building units which can be split into two distinct layers, shows a plane of symmetry between these two layers, and has no nodes lying on this plane of symmetry) and 'Favoured' (those which stack in a layered manner AA', where A' is a mirror image of A, and node coordination is split evenly between two and three).

The zeolites we have selected for analysis are then shown in Table 2.2, with their key ring statistic and building units. The CBUs present in Table 2.2 are visualised in Figure 2.7.

Zeolite	Rings	μ_2	r	CBUs	Tiles
ATV	4,6,8	2.67	-0.26	afi, bog	afi, kah, lov, oop
AHT	4,10	8.0	-0.35	bog	kah, lov, odp
AEL	4,6,10	4.8	-0.48	afi, bog	afi, kah, lov, odp
AFI	4,6,12	8.0	-0.5	afi ,bog	afi, apf, kah, lov
AET	4,6,14	8.9	-0.36	afi, bog	afi, etn, kah, lov
GIS	4,8	4.0	-0.5	gis	gsm
MOR	4,5,8	6.5	-0.36	mor	dah, kaj, mor, tes

Table 2.2: Near-two-dimensional bilayer zeolitic structures considered in the present work. Each zeolite is labelled using the nomenclature from the International Zeolite Association (IZA). Column two lists the ring sizes for the given network whilst columns three and four give the resultant second moment of the ring size distribution and assortativity respectively. Columns four and five give the CBUs and Tiles present.

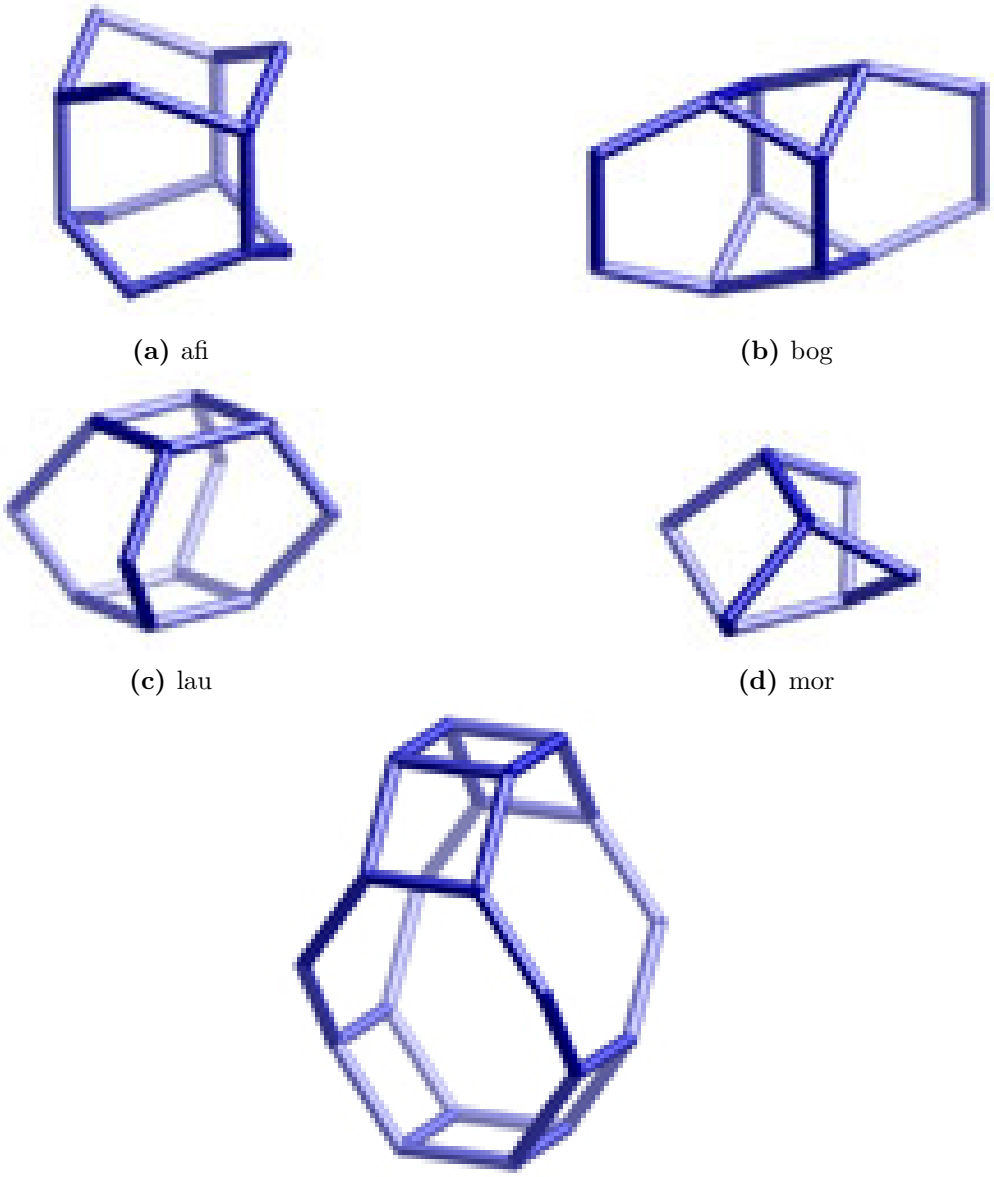

(a) afi **(b)** bog **(c)** lau **(d)** mor **(e)** gis

Figure 2.7: CBUs for zeolites used in this work, reproduced from IZA resources[96]

2.5 Cell Structures

Cell structures are defined in a very different manner to our atomic systems. The structures we are interested in are those which make up a two-dimensional surfaces, and have similar modelling approaches as colloids[97, 98], foams[99, 100] and even geological rock formations[101]. In particular, we have focused on corneal endothelium cells. The corneal endothelium is a monolayer of endothelial cells

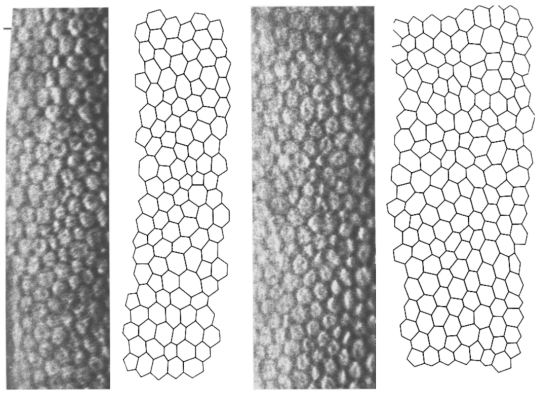

Figure 2.8: Photographs of corneal endothelium taken by specular microscopy, alongside a representation of cell boundaries. Reproduced from literature[103].

forming on the inner surface of the cornea. The cells can be readily imaged using specular and confocal microscopy, with the cells adopting a disordered structure. The distribution is centred around cells approximating to hexagonal shape as the most efficient packing[102], with amorphous sections, as visualised in Figure 2.8. There is extensive body of work on quantifying these systems across a range of different metrics[104–106]. From a modelling perspective, these systems require a different approach to atomic systems, as we do not have such stringent definitions for the length scales of the edges of the polyhedra formed; they are no longer controlled by defined atomic distances. As such, area metrics become an important distinguishing factor, having a more grounded definition at a cellular level. With an increased understanding of the effects of factors such as diabetes[107–111] and contact lens use[112–115] on the structure of the corneal endothelium, we can better characterise and work against their negative impacts.

3
Network Theory

Contents

3.1 Motivation

Network theory can provide an alternative way to understand and quantify a disparate range of systems. The laws which govern these networks, and how we have applied them as a metric for understanding our physical systems, are laid out below.

3.2 Network Theory

Network theory is in essence a branch of graph theory, a mathematical approach to a specific set of problems. It has found a wide range of uses, from its beginnings in

the logic puzzle of the "Seven Bridges of Konigsberg"[116] to big data approaches to analysing social networks and the connections therein[117–121]. The ability to map such disparate systems onto a mathematical model has proved a very useful unifying tool across chemistry, allowing for a common language in understanding systems of connections. Network theory is a useful approach when the system can be defined in terms of interconnected points, termed *nodes*. Connections between nodes are termed *edges*, and can be either directed (*i.e.* one can traverse the edge in one direction only), or undirected (*i.e* one can traverse the edge in either direction). The *nodes* and their *edges*, alongside properties assigned to each, collectively make a graph. For our purposes in atomic networks and their underlying structures, there is no analogy for directed edges, and as such all nodes described in this thesis are undirected.

To understand the networks we are modelling, we must understand the physical and topological constraints that apply. These laws detailed below help us understand the allowed and entropically favourable distributions for our physical systems. These, coupled with the enthalpic considerations discussed in Section 4.4, are used with the aim of generating configurations for further analysis.

3.2.1 Node Degree

The most fundamental description of a network is the node degree, which links the number of edges to the number of nodes. Specifically, the degree of a given node is the number of edges connected to it.

Each edge is shared by exactly two nodes, and as such we can calculate the number of edges from the number of nodes and the mean node degree, $\langle c \rangle$:

$$E = \frac{\langle c \rangle}{2} V, \tag{3.2.1.1}$$

where E is the number of edges, and V is the number of nodes.

3.2.2 Euler's Law

Euler's law for planar graphs (two-dimensional graphs without overlapping edges) goes further than Equation 3.2.1.1, linking the number of nodes, edges and faces

in a graph to a universal constant. The formula is as follows:

$$V - E + F = \chi, \tag{3.2.2.1}$$

with V the number of nodes, E the number of edges and F the number of faces, and the Euler characteristic χ, which is dependent on the global topology. The number of faces to which a node is connected to is its degree. As such, the mean number of nodes per face (*i.e.* the number of edges per ring, n) is the number of nodes divided by the number of faces, accounting double counting due to multiple coordination:

$$\langle n \rangle = \frac{V \times \langle c \rangle}{F}. \tag{3.2.2.2}$$

Substituting Equation 3.2.1.1 and Equation 3.2.2.2 into 3.2.2.1 gives :

$$\langle n \rangle = \frac{2\langle c \rangle(1 - \chi/N)}{\langle c \rangle - 2}. \tag{3.2.2.3}$$

This is a powerful predictive tool, allowing an *ab initio* understanding of the mean ring size based on the physical topology and coordination number.

For our work on amorphous systems, we use periodic boundary conditions (Section 4.3.2) as a simplification of modelling large systems. In two dimensions, the wrapping of our four-sided periodic cell results in a χ value of 0. We can explain this by examining the unique edges, vertices and faces of our unit cell, as shown in Figure 3.1. We can see that taking our unit cell (coloured grey), and replicating it along all edges gives 9 identical cells. If we examine the number of unique faces, edges and vertices, we can see that we have one unique face (coloured grey), two unique edges (coloured red and green, with their periodic images shown as faint lines), and one unique vertex (marked with a filled point). All other faces, edges and vertices are non-unique images of these. As such, using Equation 3.2.2.1, $\chi = 1 - 2 + 1 = 0$.

Realistic chemical structures resembling bulk materials are not periodic, and as such have $\chi = 1$ (constrained planar, aperiodic systems have an equal number of edges and vertices, with one unique face). This poses an issue with our assumption that using a periodic cell well approximates bulk amorphous systems, but referring back to Equation 3.2.2.3, the relevant term for $\langle n \rangle$ is χ/N, which tends to zero as N

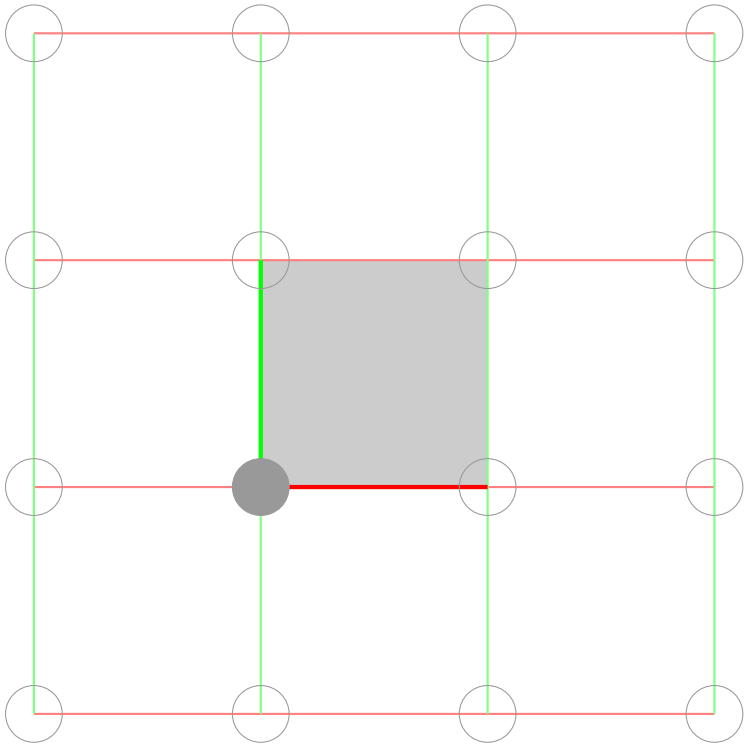

Figure 3.1: Graphic to show V,F,E values for our periodic unit cell

tends large, justifying our assumption in the limit of understanding molecular ($N \geq N_A$) systems.

We can express the mean ring size $\langle n \rangle$ as a sum of the rings present,

$$\langle n \rangle = \sum_n n p_n, \tag{3.2.2.4}$$

where p_n if the proportion of rings in a network of size n. For a given system, we can calculate the value of $\langle n \rangle$, and at fixed coordination number, we can say that $\sum_n n p_n$ is constant.

3.2.3 Aboav-Weaire law

With an understanding of the global average ring size, we have a strong constraint on the system as a whole. We now understand the physical limits on the range of rings that can be formed. However, within each distribution of rings, there are many ways to arrange them, of which only a subset are experimentally observed.

This feature was first investigated by Aboav in 1970[17], and was further developed into a law that estimates the local environment about a ring size n,

denoted as m_k or the mean ring size surrounding a ring of size n.

In Aboav's original paper on the arrangement of grains in a polycrystal in two dimensions, he proposed that the mean ring size followed

$$m_n = 5 + \frac{8}{n}, \tag{3.2.3.1}$$

indicating a $1/n$ empirical relationship. By this logic, the larger the ring size, the smaller the size of the rings surrounding it, as might be expected by considering internal angles of the respective polygons. Further work by Weaire[18] sought to explain this correlation, resulting in Weaire's sum rule

$$\sum_n m_n n p_n = \mu_2 + \langle n \rangle^2, \tag{3.2.3.2}$$

where p_n is the proportion of the rings in the system size n, and μ_2 is the variance in ring size across the system, $\mu_2 = \langle n^2 \rangle - \langle n \rangle^2$.

This formulation led to a reframing of Aboav's original equation for m_n to the more general form $m_n = A + B/n$, which when made to satisfy Equation 3.2.3.2, gives:

$$m_k = A + \frac{\mu_2 + \langle k \rangle^2 - A\langle k \rangle}{k}, \tag{3.2.3.3}$$

which is more commonly presented as:

$$k m_k = Ak - A\langle k \rangle + \mu_2 + \langle k \rangle^2. \tag{3.2.3.4}$$

In which $A = \langle k \rangle(1 - \alpha)$, with α as the Aboav-Weaire parameter, which controls the strength of ring correlations with a single value. A more positive value for α indicates a greater preference for large rings to surround small rings, whilst a more negative value implies greater clustering of similar ring sizes. The value of α can be evaluated for a given system by plotting $\langle n \rangle(n - \langle n \rangle)$ against km_n for each value of n, from which linear regression gives the gradient α.

Despite the fact that the formulation of $m_n = A + B/n$ is empirical, the law holds well for a wide range of diverse natural materials, from colloids[97, 98] to foams[99, 100] and epithelial cells[122, 123], and forms the basis of further laws to determine the structure of natural systems, namely Lemaître's law.

3.2.4 Lemaitre's Law

While our systems are now constrained to a given mean ring size and local environment, the distribution beyond this is not constrained. There is no *ab initio* constraints on the limits of sizes of rings formed, beyond the limit that mean ring size must be a function of $\langle n \rangle$ and node coordination number. However, we would expect physically that the distribution of natural ring sizes would approximate to an entropic solution.

Evaluating the entropy of a given ring size distribution is defined by the Rivier-Lissowski approach as:

$$S = -\sum_n p_n \ln\, p_n. \tag{3.2.4.1}$$

Alongside this we have the normalisation constraint ($\sum_n p_n = 1$) and mean ring size constraint ($\sum_n n p_n = \langle n \rangle$) we have discussed in Section 3.2.2. These constraints in themselves are not sufficient to maximise entropy numerically, and as such Lemaître *et al.* introduced further constraints. Introducing the limit that the area of the system must be constrained gives:

$$\sum_n \langle A_n \rangle p_n = A_0. \tag{3.2.4.2}$$

With an accurate prediction of $\langle A_n \rangle$, we can add a further constraint to p_n. There are two common predictors of A_n, Lewis' law (Equation 3.2.4.3) and a hard disk approximation (Equation 3.2.4.4).

$$A_n = A_0(n - n_0) \qquad n \geq 3. \tag{3.2.4.3}$$

$$A_n = an + b + \frac{c}{n}. \tag{3.2.4.4}$$

Relying on Lewis law does not simplify the expression sufficiently, and relies on determination of further factors detailing short range correlations. Instead, the hard shell simulation basis of the empirical investigation by Lemaître *et al.* resulting in the hard disk approximation being used, such that:

$$\sum_n \langle A_n \rangle p_n = a\langle n \rangle + b + c\langle \frac{1}{n} \rangle. \tag{3.2.4.5}$$

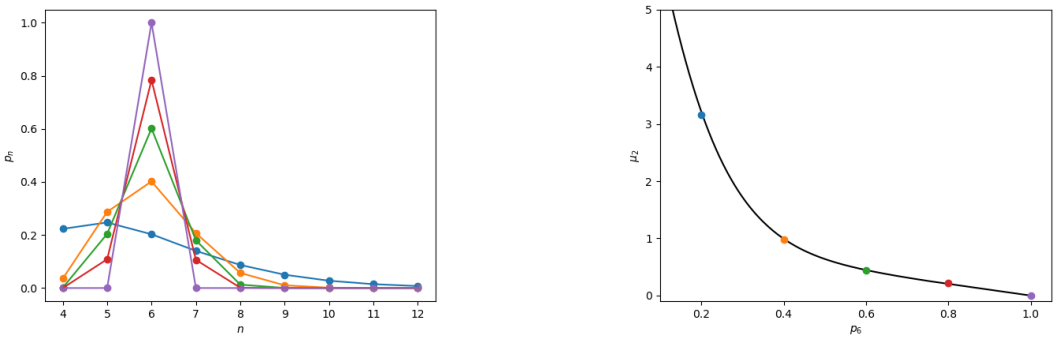

(a) **(b)**

Figure 3.2: Illustration of Lemaître's maximum entropy distribution method. Examples of maximum entropy distributions with different values of p_6 are given in (a) as ring distributions, and in (b) reduced to values of p_6 and μ_2 (Lemaître's law).

This expression, coupled with the observation that the local correlation laid out by Aboav (Equation 3.2.3.1) also follows a linear function of $1/n$, allows us to simplify the equation by combining the terms for local ordering and ring area, leaving only terms in n and $\frac{1}{n}$. With this constraint, the entropy can be maximised using Lagrange's method of undetermined multipliers, giving:

$$p_n = \frac{e^{-\lambda_1 n - \lambda_2/n}}{\sum_k e^{-\lambda_1 n - \lambda_2/k}}. \tag{3.2.4.6}$$

Neglecting Lewis law is a surprising assumption, and there is no strong physical basis for this approach. However, it has empirically been shown to fit a range of natural systems, from geopolitical regions to colloids[124], and as such has been adopted as a means of understanding the underlying distributions of natural systems. As these distributions are difficult to compare in the format of p_n distributions (Figure 3.2 (a)), presentations of Lemaître law plots are usually summarised using the variance $\mu_2 = \langle n^2 \rangle - \langle n \rangle^2$, as a function of the proportion of rings of the mean ring size, $p_{\langle n \rangle}$ (Figure 3.2 (b)).

3.2.5 Assortativity

Alongside the fit to the laws detailed above, network theory provides additional key metrics to understand the systems we create. Assortativity is a similar metric

to the Aboav-Weaire parameter, α, in that it gives an indication of the local environment about a value. However, while α is empirically formulated for a specific situation (short range ring size correlations), assortativity is a far more wide reaching metric, which describes the proclivity of a network's nodes to share edges with nodes of similar or dissimilar properties.

Assortativity is most commonly used to evaluate the preference of nodes to share edges with other nodes of similar degree, with a global value of 'degree assortativity' calculated to reflect this property. It is defined by normalizing the covariance between the attributes of nodes sharing an edge, as in Equation 3.2.5.1,

$$r = \frac{\sum_{i,j}(k_i - \langle k \rangle)(k_j - \langle k \rangle)e(k_i, k_j)}{\langle k^2 \rangle - \langle k \rangle^2}, \tag{3.2.5.1}$$

where k_i, k_j are the populations of discrete attributes i, j, and $e(i, j)$ is the proportion of the total number of edges which make up connections between i and j. However, assortativity measurements are not limited to these values, and can quantify the nearest-neighbour behaviour of any discrete characteristic that can be assigned to a node, referred to as 'attribute assortativity'.

Assortativity values range from -1 to 1, with more positive values reflecting a higher level of assortativity (homophily), where nodes with similar properties are more likely to be connected. For a measurement of degree assortativity, a high homophily corresponds to a higher likelihood of clustering of nodes with similar degrees. A value of zero means that there is no discernible preference in node ordering.

As we can definite attributes as we wish, measurements of assortativity can help us understand the clustering of nodes of given attributes, or a preference for unlike nodes to cluster together, resulting in a powerful analysis tool for understanding an additional level of information from a system beyond averages and variance.

3.2.6 Understanding ring shape

It is important for our understanding of the rings we form to evaluate their 'regularity'. The shape regularity coefficient (SRC) is a geometric measure used

to quantify the 'regularity' of shapes, particularly polygons and polyhedra in computational geometry and finite element analysis (FEA). It reflects how close a given element is to being an ideal, well-proportioned shape. It is defined as the ratio of the inradius (the radius of the largest inscribed circle that fits entirely within the shape, r_{in}) to the circumradius (the radius of the smallest circle that can enclose the entire shape, r_{out}):

$$SRC = \frac{r_{in}}{r_{out}}. \tag{3.2.6.1}$$

A shape regularity coefficient of 1 implies that the shape is perfectly regular, meaning it has equal angles and sides (*e.g.* regular hexagon). The closer the coefficient is to 0, the more distorted or irregular the shape is. This metric is useful for understanding how distorted the rings in the network we create are.

3.3 Network Theory as applied to atomic systems

In order to understand our atomic systems from a network theory perspective, we need to understand equivalent features in network theory to our physical systems. The simplest of these is understanding nodes and edges at an atomistic level, which are trivially comparable to atoms and their bonds. The node degree, or number of edges per node, can be understood as the coordination number of the atom. As such, mapping the atoms and their connections onto a network describes the connectivity of all atoms, allowing for an understanding of nearest neighbours and the dispersion in connectivity.

However, with only this information, we have a very limited understanding of the system. The graphs for systems with the same coordination number are similar, and the statistics we can glean from them are limited. With a fixed coordination number, systems that we understand as chemically crystalline and amorphous are difficult to distinguish.

Instead, we can look to add an additional layer of information. For this work, the next logical step is an understanding of the ring network. We do this by placing

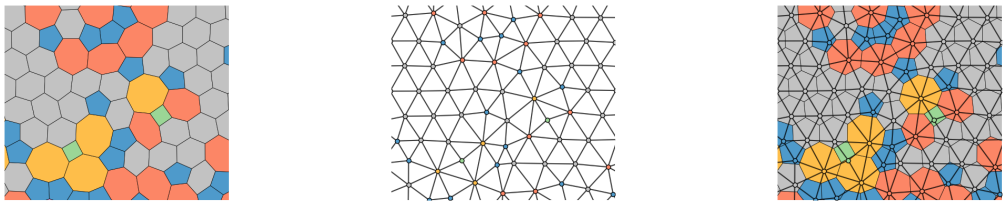

(a) Atomic network **(b)** Ring network **(c)** Dual relationship

Figure 3.3: Panel (a) gives an example of a 3-coordinate periodic network with disordered ring structure. Nodes and edges are shown, and the rings formed by their connections are coloured by size. Panel (b) gives the corresponding ring network, with nodes representing the center of each ring and coloured by degree, and edges linking edge-sharing rings. Panel (c) shows the dual relationship between the networks and its underlying ring connectivities.

nodes at the centre of each primitive ring; whilst in its strictest sense, a ring is defined in network theory as any closed loop of connections, only indivisible rings, known as primitive rings, will be referenced in this thesis.

Edges connect primitive rings that share an atomic edge, and the network created by this process is termed a 'dual' lattice. With this construction, the node degree relates to the ring size, allowing calculations of disorder centred around this characteristic.

Further information can be extracted using tiling units, a meaningful collection of primitive rings that form a useful building block for larger systems. This is referenced in sections discussing zeolites (Section 2.4), where central building units (CBUs) and tiling units are used.

Beyond our atomic systems, network theory is of practical use understanding the ordering of key system metrics. For example, assortativity calculations can extend beyond node degree. We can assign a value, termed an 'attribute', to a node to reflect a physical property, and calculate the 'attribute assortativity' for each property. This allows us to quantify local trends in observable quantities, which is important for high throughput methods.

4
Computational Methods

Contents

4.1 Motivations

Throughout this work, two methods are used to simulate molecular systems numerically. These are Monte Carlo methods (MC), and Molecular Dynamics (MD).

Both techniques have extensive histories in modelling the structures and behaviours of chemical systems, providing additional detail to complement experimental work[125–130]. A central aim in this work is to utilise these methods to provide data complementary to experimental work on silica related systems, and to explore the phase space beyond the available experimental data, with the aim of producing target configurations for future experimental work.

4.2 Monte Carlo Methods

Monte Carlo (MC) methods are a class of calculations that rely on stochastic approaches to produce statistical solutions to many dimensional problems. Outside of chemistry, they have found use in applications ranging from evaluating high-dimensional integrals, through modelling risk in financial markets[131]. For the purposes of this work, MC methods are useful in their ability to traverse complex energy surfaces, allowing exploration of a large phase space of possible configurations.

In this work, MC methods have been used under both equilibrium and non-equilibrium conditions, to allow for structure generation following kinetic or thermodynamic control. However, the underlying process is the same for each, only differing in the reversibility of each step.

4.2.1 Statistical Mechanics

Our goal in using Monte Carlo methods is to traverse between different configurations of the same base number of atoms, with the same fundamental properties. Our work relies on modifying the connectivities and positions of atoms in the system, to create a system with the same number of atoms (N) and volume (V). The available configurations have a range of energies, but identical compositions.

At a fixed temperature (T), we can use a classical canonical partition function to describe the thermodynamic properties of the system.

$$Z = \sum_{k} e^{-\frac{E_k}{k_B T}}. \tag{4.2.1.1}$$

Equation 4.2.1.1 details the canonical partition function (Z), as a function of the sum of states k, each with energy E_k, with k_B as the Boltzmann constant, and T as the temperature in kelvin.

The probability of the system being in a given state, k, at temperature T, is given by Equation 4.2.1.2

$$P(k) = \frac{e^{-\frac{E_k}{k_b T}}}{Z}. \tag{4.2.1.2}$$

Changing the temperature, T, will change the populations of each state according to a Boltzmann distribution.

However, in order to evaluate these probabilities exactly, or the difference in probabilities between two known states j, k, we must be able to evaluate Z, and hence must know the energies of each possible state. This is intractable for systems of meaningful magnitude and so we must find an alternative.

4.2.2 Importance Sampling

Rather than sample all of the phase space, it is possible to approximate Z from a subset of the partition function, composed of the states readily accessible at a given temperature. This approximation is laid out in Equation 4.2.2.1, where S is a subset of states, composed of members k where E_k is less than some threshold. This is based on the fact that as $E_k \ll k_b T$, $e^{\frac{-E_k}{k_b T}} \to 0$.

$$Z = \sum_{k \subseteq S} e^{-\frac{E_k}{k_B T}} + \sum_{k \subset S} e^{-\frac{E_k}{k_B T}}. \tag{4.2.2.1}$$

$$Z_S \simeq \sum_{k \subseteq S} e^{-\frac{E_k}{k_B T}}. \tag{4.2.2.2}$$

The process of sampling from S is referred to as 'importance sampling', and is significantly more efficient when a large number of states that make up Z are inaccessible energetically.

When evaluating systems we expect to find experimentally, we want to explore the configuration space around the energy of the experimentally confirmed structures.

Whilst using a subset of Z results in significant computational cost savings, it is not clear *ab initio* which states this subset should be composed of. In fact, were we to know the states withing the limits of the energies we are interested in, we would have no need for a simulation of this kind.

Finding the subset S would thus mean evaluating the energy of all states in Z, which is infeasible.

4.2.3 Markov Chain Monte Carlo

Rather than evaluate every state of the system at once, we can instead turn to incremental approaches. One such approach is Markov Chain Monte Carlo (MCMC). MCMC allows us to build up a set of states by taking incremental steps, and evaluating whether each state should be included in the importance sampling. The probability of a move between state i and state j is dependent on the nature of each state only, and is unaffected by any other state. As such, we can theorise a matrix of probabilities π, composed of terms π_{ij}. This matrix is referred to as a transition matrix. This matrix is impractical to generate, as its dimensions are the total number of states available to the system, with each value relying on calculable details of these states. However, it provides a reliable language for describing the sequential steps on the Markov chain.

Using this definition, we define the following two relationships.

$$0 \leq \pi_{ij} \leq 1. \tag{4.2.3.1}$$

$$\sum_{j} \pi_{ij} = 1. \tag{4.2.3.2}$$

Equation 4.2.3.1 states that each probability must be between 0 and 1, and Equation 4.2.3.2 states that the sum of probabilities for each transition from state i to any other state must add to 1. This allows for a generalised approach to the Markov chain. Starting from a state i, we can map the probability that after one step, it is in any other state j. We can define the initial state as $\mathbf{P_k}$, with dimensions [N_{states},1].

$$\mathbf{P_k} = [0, 0, \ldots, 0, \underbrace{1}_{\text{at position } k}, 0, \ldots, 0]. \tag{4.2.3.3}$$

As such, each step s on the Markov chain is an interaction between this vector and the transition matrix.

$$\mathbf{P_k}\pi_{\mathbf{i,j}} = \pi_{\mathbf{i=k,j}} = \mathbf{P_s}. \tag{4.2.3.4}$$

Over a sufficient number of steps, we expect to have explored a significant subset of the important states, and moved significantly far from the initial state. At this point, we can treat the system as at equilibrium, and evaluate the thermodynamic properties.

4.2.4 Metropolis Algorithm

Our definitions within the Monte Carlo Markov Chain method (MCMC) rely on a complete definition of π.

Rearranging Equation 4.2.3.4 and Equation 4.2.3.1 to formulate an equation for the global balance, which is effectively a global equilibrium condition. It states that the flow out if state i, given as the sum of all transitions out of state i, is equal to the flow into state i from all other states, as laid out in Equation 4.2.4.1.

$$\sum_i P(k=i)\pi_{i,j} = \sum_i P(k=j)\pi_{i,j}. \tag{4.2.4.1}$$

This definition still relies on a sum over all states, and so it is practically simpler to satisfy the global balance using the stronger condition of detailed balance.

Under these conditions, the total flow from from state i to j is zero, and so the probability of transition $i \to j = j \to i$, expressed in Equation 4.2.4.2.

$$P(k=i)\pi_{i,j} = P(k=j)\pi_{j,i}. \tag{4.2.4.2}$$

The Metropolis condition ensures this balance by setting the probability of a transition of $i \to j$ as in Equation 4.2.4.3.

$$P_{i\to j} = \min\left(1, \frac{P(k=i)}{P(k=j)}\right). \tag{4.2.4.3}$$

Returning to our definition of 4.2.1.2, we can reframe this equation to Equation 4.2.4.4.

$$P_{i\to j} = \min\left(1, \frac{e^{\frac{E_i}{k_b T}}}{\frac{E_j}{k_b T}}\right). \tag{4.2.4.4}$$

This reduces to a transition probability based on energy, $P_{i\to j} = \min[1, e^{\frac{-\Delta U}{k_b T}}]$.

4.3 Molecular Dynamics

Molecular dynamics (MD) is the process of applying classical mechanics to a selection of particles. The starting point for a molecular dynamics simulation is

- The mass of the particles
- A function to define the forces present as a function of particle positions
- The starting positions of the particles
- The initial velocity of the particles

From this information, we can use MD to evolve the system in time, in an effort to mimic the underlying processes at play in real-world analogues of our systems.

In this work, I have utilised MD to relax the structures generated by Monte Carlo methods, giving an understanding of the effect of different potentials on the minimum energy structures formed, and their energies.

4.3.1 Velocity Verlet integration

In order to derive the position of atoms at time t, we utilise Newton's equations of motion.

$$F = m\mathbf{a}. \tag{4.3.1.1}$$

Newton's second law of motion Equation (4.3.1.1) relates the effect of a force, F, on an atom mass m, to the resultant acceleration $\mathbf{a}$ of the particle.

In order to understand the impact of the force on the position of the particle, we need to integrate the acceleration a (4.3.1.2).

$$\mathbf{a} = \dot{\mathbf{v}} = \ddot{\mathbf{r}}. \tag{4.3.1.2}$$

In theory, it is possible to solve this exactly over all time, however practically analytical solutions for many atom systems span many dimensions, meaning the calculations involved are not tractable. As such, integration schemes are used to approximate over incremental time steps. The scheme used in this work is velocity Verlet. This is a symplectic approach, second order in time and time reversible.

We start with a Taylor series expansion of the position, $\mathbf{r}$, at time $t + \Delta t$.

$$\mathbf{r}(t + \Delta t) = \mathbf{r}(t) + \mathbf{v}(t)\Delta t + \frac{F(\mathbf{r}(t))}{2m}\Delta t^2 + \frac{1}{6}b(\mathbf{r}(t))\Delta t^3 + \mathcal{O}(\Delta t^4). \quad (4.3.1.3)$$

We can eliminate the jerk term in Equation 4.3.1.3 by evaluating the previous timestep 4.3.1.4, and subbing this into 4.3.1.3 to give 4.3.1.5, the position at time $t + \Delta t$, as a function of the positions at time t and $t - \delta T$, alongside the force field at time t.

$$\mathbf{r}(t - \Delta t) = \mathbf{r}(t) - \mathbf{v}(t)\Delta t + \frac{F(\mathbf{r}(t))}{2m}\Delta t^2 - \frac{1}{6}b(\mathbf{r}(t))\Delta t^3 + \mathcal{O}(\Delta t^4). \quad (4.3.1.4)$$

$$\mathbf{r}(t + \Delta t) = 2\mathbf{r}(t) - \mathbf{r}(t - \Delta t) + \frac{F(\mathbf{r}(t))}{2m}\Delta t^2 + \mathcal{O}(\Delta t^4). \quad (4.3.1.5)$$

As such, we can define position without needing velocity up to $\mathcal{O}(\Delta t^4)$, if we know the position of all atoms at the previous timestep.

However, for kinetic terms we need to have a definition for $\mathbf{v}(t)$. We can reuse our definitions in Equation (4.3.1.3) and Equation (4.3.1.4) to define the velocity.

$$\mathbf{r}(t + \Delta t) - \mathbf{r}(t + \Delta t) = 2\mathbf{v}(t)\Delta t + \frac{1}{3}b(\mathbf{r}(t))\Delta t^3. \quad (4.3.1.6)$$

$$\mathbf{v}(t) = \frac{\mathbf{r}(t + \Delta t) - \mathbf{r}(t - \Delta t)}{2\Delta t} + b(t)\frac{b(t)\Delta t^3}{3\Delta t}. \quad (4.3.1.7)$$

This gives velocity with error $\mathcal{O}(\Delta t^2)$. This is termed the Stormer Verlet approach. However, further reframing can give better error values.

We can also formulate a Taylor expansion about t for $\mathbf{v}$, in the same manner as Equation 4.3.1.3.

$$\mathbf{v}(t+\Delta t) = \mathbf{v}(t) + \frac{F(\mathbf{r}(t))}{m}\Delta t + \frac{\dot{F}(\mathbf{r}(t))}{2m}\Delta t^2 + \mathcal{O}(\Delta t^3). \tag{4.3.1.8}$$

As $\dot{F}(\mathbf{r}(t))$ is impractical to define explicitly, we can use a Taylor expansion to express it in terms within our reach.

$$F(\mathbf{r}(t+\Delta t)) = F(\mathbf{r}(t)) + \dot{F}(\mathbf{r}(t))\Delta t + \mathcal{O}(\Delta t^2). \tag{4.3.1.9}$$

$$\frac{\Delta t}{2}(F(\mathbf{r}(t+\Delta t)) - F(\mathbf{r}(t)) - \mathcal{O}(\Delta t^2)) = \dot{F}(\mathbf{r}(t))\frac{\Delta t^2}{2m}. \tag{4.3.1.10}$$

$$\mathbf{v}(t+\Delta t) = \mathbf{v}(t) + \frac{F(\mathbf{r}(t)) + F(\mathbf{r}(t+\Delta t))}{m}\Delta t + \mathcal{O}(\Delta t^3). \tag{4.3.1.11}$$

This allows us to calculate the velocity at time $t+\Delta t$, once we know the positions of the atoms at $t+\Delta t$ ($\mathbf{r}(t+\Delta t)$), which allows us to calculate the forces at this point.

4.3.2 Periodic Boundary Conditions

One of the prevailing issues with modelling amorphous systems, such as those readily adopted by silica, is their lack of periodicity. Modelling large aperiodic systems quickly becomes computationally infeasible, and requires an understanding of the surface effects at the edge of the simulation. Instead, we can impose some level of periodicity on a scale small enough that is within computational limits, but large enough that the system to be treated as aperiodic. The mechanism for this process is to model a simulation cell bounded in three dimensions, with its images repeated infinitely in three dimensions. Any dynamics in the simulation cell is repeated in all neighbouring cells.

This process means that the cell is 'wrapped' in all modelled dimensions, onto a higher dimensional space. For instance, we can map a two-dimensional surface onto a torus by wrapping along x and y, creating a shape with a single unique face, two unique edges and one unique vertex (see Figure 3.1). This approach comes with complications. Alongside the reduction of system symmetry, we also need to ensure that our simulation cell can effectively tile infinite space, and account for

finite size effects. For computational simplicity, our simulations rely on rectangular unit cells, which readily tile space. The possibility of self-interaction of particles with its copies limits the range at which we can calculate inter-atom forces. As such, we only calculate interactions between each particle and the closest image of each atom, practically limiting the distance at which we calculate forces to half the periodic box length, $L_{PB}/2$.

4.3.3 Thermostats

Thermodynamic simulations of a canonical ensemble (NVT) rely on control of the number of particles (N), the volume of the system (V) , and the temperature (T). In order to control temperature, both our in-house code and our chosen third party software (LAMMPS) rely on the Nosé Hoover thermostat. This thermostat relies on coupling our canonical ensemble to a heat bath, creating an overall microcanonical ensemble (NVE), with heat exchange between the bath and the system maintaining the overall energy, and the temperature of the system. The coupling between the system and the bath is mediated by an additional parameter, ζ, termed thermodynamic friction. This term acts on the velocity of all atoms in the system evenly, accelerating on decelerating them until the temperature converges to the desired value. Including this parameter requires us to modify our equations of motion laid out in 4.3.1.

$$F_{eff}(\mathbf{r}) = F(\mathbf{r}) - \zeta m\mathbf{v}. \tag{4.3.3.1}$$

The magnitude of ζ is dependent on the difference between the target temperature (τ) and the instantaneous temperature (T), as shown in Equation 4.3.3.2.

$$\dot{\zeta} = \frac{N}{Q}(k_B\tau - k_bT). \tag{4.3.3.2}$$

N describes the number of degrees of freedom (with an additional degree for the ζ parameter), and Q, the thermal inertia parameter, describes how strongly the system is linked to the heat bath. Accounting for the effect on the force applied to the system, the velocity Verlet definitions are modified as in Equations 4.3.1.3 and 4.3.1.11.

$$\mathbf{r}(t+\Delta t) = \mathbf{r}(t) + \mathbf{v}(t)\Delta t + \frac{F_{eff}(\mathbf{r}(t)}{2m}\Delta t^2 + \frac{1}{6}b(\mathbf{r}(t))\Delta t^3 + \mathcal{O}(\Delta t^4) \qquad (4.3.3.3)$$

$$\mathbf{v}(t+\Delta t) = \mathbf{v}(t) + \left[\frac{F_{eff}(\mathbf{r}(t+\Delta t))}{m}\frac{F_{eff}(\mathbf{r}(t))}{m} - \zeta(t)\mathbf{v}(t)\right]\frac{\Delta t}{2} + \mathcal{O}(\Delta t^3) \quad (4.3.3.4)$$

Equation 4.3.3.4 is problematic, in that $\mathbf{v}(t+\Delta t)$ depends on itself recursively, and so cannot be solved exactly, however a number of corrections can be utilised to ensure time-reversible trajectories.

4.3.4 Steepest Descent algorithms

In order to find the local energy minimum for a given starting configuration, we want to follow the lines of force down the potential energy surface to the configuration with the lowest potential energy.

Fixed timestep

The simplest steepest descent algorithm involves quenching the system velocity at each timestep, meaning that the equations of motion reduce to Equation 4.3.4.1.

$$\mathbf{r}(t+\Delta t) = \mathbf{r}(t) + \frac{F(\mathbf{r}(t))}{2m}\Delta t^2. \qquad (4.3.4.1)$$

This simplifies calculations considerably, and ensures we always move in a direction which is along the lines of force. From a thermodynamic standpoint, this is equivalent to setting the target temperature of the Nosé Hoover thermostat to 0, such that all of the heat from the system is transferred to the bath. There are, however, disadvantages to this method. It is often slow to find the local minimum, traversing incrementally down the potential surface. In addition, it is sensitive to step size. Too large a timestep, and the minimisation process will overshoot the minimum, too small and the simulation will be slow.

Backtracking algorithms

An alternative to the fixed step method is one where the timestep can fluctuate to satisfy specific conditions. In our in house network generation code, this condition is the Armijo condition, with the step size described in Equation 4.3.4.2.

$$\Delta t_n = \alpha^n \Delta t. \tag{4.3.4.2}$$

α is the Armijo condition coefficient, with a value between 0 and 1, for our purposes set to 0.5.

The acceptance criterion for an Armijo step is if the step moves down the potential gradient:

$$U(\mathbf{r}(t + \alpha\Delta t)) \leq U(\mathbf{r}(t)) + \alpha^n F(\mathbf{r}). \tag{4.3.4.3}$$

It is evaluated iteratively, with the acceptance criteria being that the force gradient after taking a step sized Δt_n is lower than taking a step Δt_0. If the criterion is not met, then $n \to n + 1$, and so a smaller step is evaluated, to the limit that as $n \to \infty$, $\Delta t_n \to 0$. The advantages of this method are efficient step size selection, leading to faster convergence, and a lower likelihood of overshooting the minimum as it searches within the proposed step for an alternative energy endpoint.

However, there is an additional computational overhead to evaluating multiple points on the potential energy surface, and this method can require more extensive tuning to ensure a viable Armijo condition coefficient to reflect the complexity of the energy surface.

In this work, Armijo methods have been used on a relatively simple energy surface, allowing for a higher α value.

Velocity Quenching

An alternative method is velocity quenching, which takes elements from standard MD and steepest descent approaches. It relies on allowing the system to evolve as an NVE system, without any controls on velocity, allowing potential energy to be converted into kinetic energy. When kinetic energy approaches a maximum, and

so the potential energy approaches a minimum, all velocity is quenched, and the system is again released. This method has the advantage of a more rapid approach to the minimum, with the retained kinetic energy resulting in fast motion down the force gradient. Quenching velocity at the maximum ensures the system's kinetic energy does not cause it to overshoot the minimum.

4.4 Potential Models

A variety of potential models are evaluated to model silica systems, with varying computational complexity allowing evaluation the accuracy of computationally cheaper models as predictors of more accurate, computationally expensive calculations.

4.4.1 Harmonic Systems

The simplest potential model applied uses harmonic springs to connect each node to its nearest neighbours, with the force derived from the compression or stretching of the springs. The energy of a stretch is given by

$$U_{ij} = \frac{1}{2}k_r(r_{ij} - r_0)^2, \tag{4.4.1.1}$$

with r_{ij} as in the distance between nodes i and j, r_0 is the ideal bond distance, and k_r is the bond force constant. r_0 is defined trivially for the system, whereas k_r can either be determined with respect to known bond stretching behaviour, or can be used as a more free parameter, balanced with other potentials as discussed for graphene in Chapter 2.

4.4.2 Angle Control

Angle constraints are handled by a cosine/squared function, approximating a three body term.

The form of the potential is

$$U_{ijk} = \frac{1}{2}k_\theta[cos(\theta_{ijk}) - cos(\theta_0)]^2, \tag{4.4.2.1}$$

where θ_{ijk} is the angle formed between species ijk, and θ_0 is the ideal system angle ($\pi/3$ for a hexagonal net). The potential is similar in form to the harmonic potential above, with k_θ replacing k_r and cosine terms replacing radial terms. As for harmonic potentials, k_θ can be related back to the three body terms derived from experimental data, or used to balance forces.

4.4.3 Repulsive Terms - Lennard Jones

For simple systems, bond and angle constraints are sufficient to ensure atoms do not overlap. However, for more complex systems, additional potentials may be required to ensure that atoms remain physically separated.

The repulsive potential selected in a shifted Lennard-Jones 6-12 potential. This applies between selected pairs of like, unbonded atoms for computational efficiency. The Lennard-Jones potential provides a compromise between hard shell approaches used in the geometric treatment of ideal zeolites[90, 92], and softer harmonic interactions. An important point of note is that the gradient of the potential at $r_0 - \Delta r$ is dependent on r_0. The smaller r_0, the more the form of the potential resembles a hard shell.

$$U_{ij} = \begin{cases} 4\epsilon \left[\left(\frac{\sigma}{r}\right)^{12} - \left(\frac{\sigma}{r}\right)^{6} \right] + \epsilon & r < r_0 \\ 0 & r \geq r_0 \end{cases} \tag{4.4.3.1}$$

In Equation 4.4.3.1, U_{ij} denotes the potential energy of an ij interaction, with ϵ as the depth of the potential well at $r = r_{min}$, and σ is the distance at which

$$4\epsilon \left[\left(\frac{\sigma}{r}\right)^{12} - \left(\frac{\sigma}{r}\right)^{6} \right] = 0, \tag{4.4.3.2}$$

given as $2^{1/6}\sigma = r_0$.

The potential energy and its first differential (negative force gradient) equal zero at the cutoff point, which is sufficient for steepest descent algorithms.

4.4.4 Repulsive Terms - Coulombic Repulsion

An alternative repulsive force field used is a modified coulombic potential. This potential has the advantage of not decaying in energy to zero at the cutoff, which has been useful as a basic model for repulsions between like atoms in heteronuclear systems. This, however, comes with the strong caveat that it should only be used in situations where r is constrained by other forces in the system at $r \ll r_{cut}$, as both the forces and energy are undefined at $r = r_{cut}$. As such, if used carefully, this potential is suitable for steepest descent methods.

$$U_i j = \begin{cases} \frac{q_i q_j}{\epsilon r_{ij}} & r < r_0 \text{ and } i = j \\ 0 & r \geq r_0 \text{ or } \ i \neq j \end{cases} \tag{4.4.4.1}$$

The charges on the ion species i, j are defined using q_i and q_j. ϵ is the relative permitivity, which for unitless calculations is a metric for controlling the steepness of the potential.

4.4.5 Tangney-Scandolo (TS) potential

The potential forms introduced to this point are highly generic, controlling the fundamental network topology. In order to focus on a specific system, for example silica, the next step in our escalating potential model is to use a higher level potential, based on empirical data and parameterised for silica.

At this point, we need to look for potentials specific to the systems we are modelling, in this case silica. As XRD data is limited for silica bilayers, we have opted to use bulk silica as an approximation. We expect to see similar chemical behaviour for our low dimensional systems. Using these potentials we negate surface effects, assuming that full coordination within the structure is sufficient as a global structure descriptor (*i.e.* fully coordinated oxygen atoms at the surface of the bilayer are treated the same as oxygen atoms within a bulk silica structure).

There are a variety of empirical models for silica available; we have selected a Tangney-Scandolo potential as the code for such a potential is easily obtainable, and it has been used in previous work[67] to good effect.

As a starting point, SiO_2 is best described as an ionic system. As with a range of MO_2 structures, SiO_2 is correctly predicted by Paulings rules to have a local metal ion coordination of 4, forming vertex sharing SiO_4 tetrahedra. SiO_2 structures show strong short range ordering, forming recognisable vertex-sharing SiO_4 tetrahedra indicative of anion ordering. As such, the starting point for an efficient computational model would describe the balance of interactions between each pair of ions, accounting for the charges and other contributions to the interactions. This balance of interactions can be reduced to an 'effective pair potential', such as seen in the Fumi-Tosi potential.

$$U(r_{ij}) = \frac{Q_i Q_j}{r_{ij}} + B_{ij} e^{-\alpha_{ij} r_{ij}} - \sum_{n=6,8,10} \frac{C_n^{ij}}{r_{ij}^n} f_n(r_{ij}) \qquad (4.4.5.1)$$

In this equation, $U(r_{ij})$ denotes the interaction energy between two ions i and j, as a function of the distance between the two species, r_{ij}. It is worth noting this is a distance, rather than a vector, resulting in no angle dependence for the interactions, as expected for an system with ionic interactions. The pure electrostatic energy is given by the product of the charges, Q_i and Q_j, divided by the distance between them. Short range interactions resulting from an effective ion size are accounted for by the B_{ij} and a_{ij} terms, which produce a parameterised exponential decay of ion contact force with r_{ij}. Dispersion interactions are quantified by C_n^{ij}, and damped by $f_n(r_{ij})$.

As more accurate structural information became available, parametrisation of the effective pair potentials was favoured over *ab initio* methods, with parameters refined against available structural data to create a wide range of pair potentials specialised for different crystal structures.

Additional degrees of freedom can be attained by moving towards a Morse Stretch form (Equation 4.4.5.2), which has more detailed terms with respect to describing the pair potentials and was found to be more transferable between different phases.

$$U_{ij} = \frac{Q_i Q_j}{r_{ij}} + D_{ij} \left[e^{\gamma_{ij}[1-(r_{ij}/r_{ij}^0)]} - 2e^{\gamma_{ij}/2[1-(r_{ij}/r_{ij}^0)]} \right] \qquad (4.4.5.2)$$

In this equation, the parameters are as in the Fumi-Tosi potential, with the additional terms D_{ij}, the dissociation energy for interactions between i and j, and

q_O	-1.38257
q_{Si}	2.76514
D_{O-O}	2.4748×10^{-4}
D_{Si-O}	1.9033×10^{-3}
D_{Si-Si}	-2.08460×10^{-3}
γ_{O-O}	12.07092
γ_{Si-O}	11.15230
γ_{Si-Si}	10.45517
r^0_{O-O}	7.17005
r^0_{Si-O}	4.63710
r^0_{Si-Si}	5.75038

Table 4.1: Values for the Morse Stretch potential parameterised for silica, given in a.u.(elementary charge, Hartrees, Hartrees per Bohr radius, and Bohr radii respectively for this table)

γ_{ij} is the force constant at the minimum of the well. The parameterised values for the TS potential are listed in Table 4.1, in atomic units.

Polarisability

Effective potentials can only go so far in describing covalent systems, in that they are at their core ionic models which account for the size of the ions. Instead, to accurately understand the more localised nature of charges, an additional degree of freedom must be included. This is the polarisability of the atoms. We can understand polarisability as the process by which charge is delocalised from the atom centres, mimicking an electron cloud about a more ionic core. The simplest perturbation is a dipole, implemented by separating two equal and opposite charges on opposite ends of a fixed rod, centred on the atom and free to rotate in space. This allows us to effectively model the fluctuations of dipoles on each atom, but comes with computational complications. In order to conduct molecular dynamics on the dipole, the rod must have a mass. This means that the energy effects of the dipole can be broken down into three terms:

$$E_{dipole} = E_{charge-dipole} + E_{dipole-dipole} + E_{KE} \tag{4.4.5.3}$$

From these terms, $E_{charge-dipole}$ and $E_{dipole-dipole}$ are physically realisable terms, but E_{KE} is a so called 'fake' term, in that it has no physical equivalent. We

have kinetic energy terms for these rods, which are not 'real'. Incorporating these dipoles in the same way as other charges in the system can result in unphysical phenomena, with transfer of kinetic energy from the ions to the to dipoles. As such, the orientation of these dipoles are minimised independently of the system in a incremental manner.

First, the ion positions and dipole values are fixed. Then, the dipoles are able to vary, and their energy minimised by velocity quenching methods. The timestep for this process is shorter than for the ion dynamics, as the masses involved are significantly smaller, and so larger step sizes would not lead to effective minimisation. Once dipoles have been minimised, they are frozen in space. The ions are then released, with the dipoles treated as static. This process is repeated for each molecular dynamic step, effectively separating the dipole and ion systems.

For our implementation of the Tangney-Scandolo potential, dipoles are induced on oxygen atoms only, by electrostatic induction (Equation 4.4.5.4) or short-range forces (Equation 4.4.5.5).

$$\mathbf{P}_i = \alpha E(\mathbf{r_i}) \tag{4.4.5.4}$$

$$\mathbf{P}_i^{SR} = \alpha \sum_{j \neq i} \frac{q_j \mathbf{r}_{ij}}{r_{ij}^3} f_{ij}(r_{ik}) \tag{4.4.5.5}$$

$$f_{ij}(r_{ij}) = c \sum_{k=0}^{4} \frac{b r_{ij}^k}{k!} e^{-b r_{ij}} \tag{4.4.5.6}$$

In Equation 4.4.5.4, α is the polarisability of the ion and $E(\mathbf{r_i})$ denotes the electric field of particle i at position $\mathbf{r_i}$.

The short-range contribution in Equations 4.4.5.5 and 4.4.5.6 are derived from Madden *et al.*[132], with $\mathbf{r}_{ij} = \mathbf{r}_i - \mathbf{r}_j$, f_{ij} is a variation on a Tang-Toennies function, with b and c are parameters denoting the short range damping parameters and amplitude of the short-range interaction respectively.

The total dipole moment on each ion is obtained by iteratively solving for the dipoles to achieve self-consistency within the electric field, which includes contributions from other dipoles and charges in the system.

This process is described in 4.4.5.7, with n as the iteration step, $\mathbf{E}^{n-1}(\mathbf{r}_i)$ is an average of the electric field at the previous three steps, and includes both the field from the ions and the surrounding dipoles.

This polarization scheme can never be perfectly converged, leading to oscillations in energy, but at low temperature these become negligible.

$$\mathbf{P}_i^n = \alpha \mathbf{E}^{n-1}(\mathbf{r}_i) + \mathbf{P}_i^{SR} \tag{4.4.5.7}$$

4.5 Implementation

Our aim over this work is to generate a broad range of diverse configurations, and by treating these configurations as silica bilayer systems, to understand the feasibility of a range of bilayer structures beyond the subset visualised by experimental investigation. To this end, we have laid out a series of escalating potentials, to scan across a broad range of configurations with the aim of gleaning sufficient information from computationally 'cheap' calculations to predict the phase-space behaviour of more computationally 'expensive' calculations. Figure 4.1 shows the design of this process, indicating points at which we identify phase space to discard before moving to the next higher level potential. This allows us to limit our use of 'expensive' calculations to areas of the phase space we predict to be close to energetic minimum, allowing us be selective in our higher level calculations and better use our computational time.

In order to scan through a wide range of structures with simple potentials, we needed a highly optimised means of calculating simple potentials. For this purpose, we used LAMMPS (Large-scale Atomic/Molecular Massively Parallel Simulator). LAMMPS allows for fast calculations, with a database of well optimised potentials, and efficient use of neighbour lists for potentials which act within a cutoff radius. Additional potentials can be added to the LAMMPS repositories, but for our purposes the potentials provided were sufficient. Although LAMMPS comes with a wide range of potentials, modifying them in a way which maintains their efficiency is particularly difficult, and the lack of flexibility within the code (for instance, in

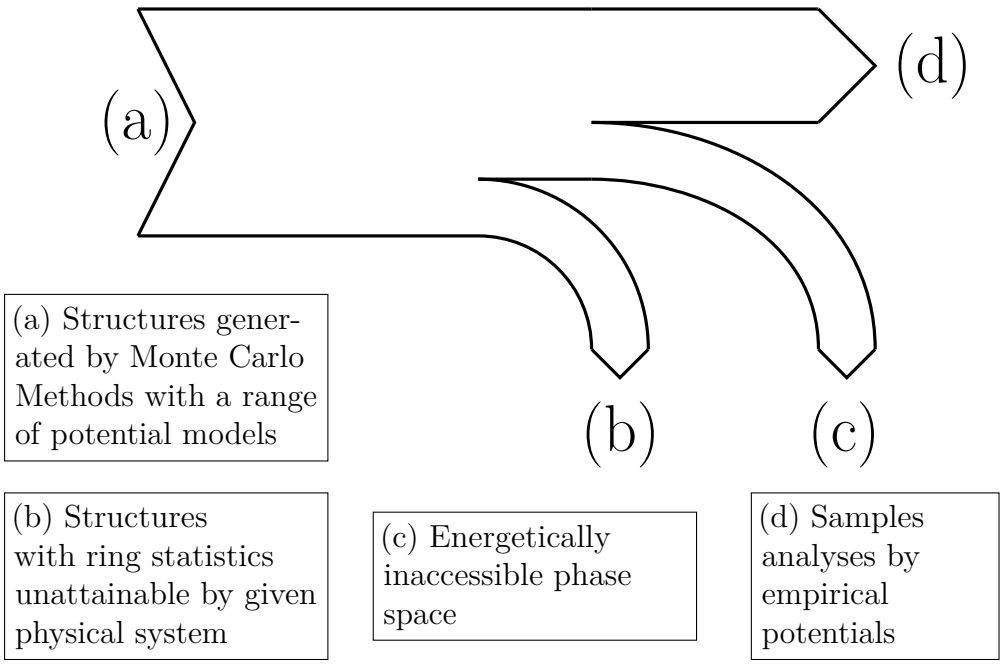

Figure 4.1: Graphic to demonstrate our experimental design for a high throughput approach, with areas where structures are discarded are labeled.

direct declaration of atom pairs, or in the memory usage of pair calculations) limits our usage to lower level potentials. In addition, our approximations to the system result in a high degree of connectivity, which is not well understood by LAMMPS parallelisation algorithms. In particular, the OpenMP and CUDA implementations of the code frequently give different results to single core versions. However, we have mitigated these issues by consistently conducting only single core calculations. In addition, the results of LAMMPS simulations are never taken in isolation, but instead as the basis from which to run higher level potentials. A small sample set was confirmed against our in-house code for silica systems, with only harmonic bonds described, which returned similar results.

5

Network Generation

Contents

5.1 Motivation

In Chapter 2, I have discussed some of the history and nature of the structures of interest for this work. For each of the atomic systems (namely graphitic systems, boron nitride planar systems and silica bilayers), nodes and edges have definitive definitions, and each have different building units, energetics and physical properties. However, as described in Chapter 3, we can unite the disordered configurations formed by these chemical systems under a common approach, namely network theory, a branch of mathematics in which this diverse range of 2D and pseudo-2D structures as a collection of nodes and edges.

Our implementation (Figure 4.1, Section 4.5) relies on the generation of a wide range of amorphised networks, with the aim of naturally covering a broad section of the phase space by design of interatomic potentials.

In this chapter, I discuss the underlying basis for network generation of our three atomic systems, alongside metrics to quantify their disorder. I have built on previous work[133, 134] to establish a range of models to fit the structures of interest for this work, which rely on a central network theory approach, adorned with different chemically realisable atoms and potentials. This allows us to generate a diverse range of structures with an understanding of their underlying network characteristics.

5.2 Periodic Monte Carlo Approach

As has been established in Chapter 3 , we can understand two-dimensional and pseudo-two-dimensional system as networks of rings on a flat surface, made of nodes and edges. We can then decorate these systems with atoms and provide potentials to describe their interactions, approximating molecular systems at a low level. Network Monte Carlo methods have a proven track record for generating such structures, in particular for two-dimensional structures[57, 133–135].

Our methodology relies on a bond switching algorithm, starting from an ideal crystal of tessellated hexagons, forming a network of nodes and edges as described in Section 3.3. The connectivity of the structure is then modified using a 2D analogue of the Wooten, Winer and Weaire (WWW) algorithm[136–138], a standard method to generate 3D vitreous glasses.

These stepwise modifications amorphise the crystalline lattice, approximating a continuous random network (CRN). The system is relaxed after each modification using the steepest descent methods described in Section 4.3.4.

CRN models can accurately replicate a range of experimental observables, including bond length and angle distributions, radial distribution functions, electronic band gaps, and Raman spectra as applied to other systems such as three-dimensional amorphous carbon, binary glasses, and biological polymers[91, 139–143]. The stepwise WWW approach can be easily adapted for two- and pseudo two-dimensional systems, as demonstrated in studies of amorphous graphene and silicon[57, 144]. In two-dimensions, this method generates Stone-Wales[16] (5577) defects, as identified in graphene and silica bilayer samples[20, 32, 62]. Introduction of a large number of defects overlaps these (5577) defects, to allow a broader ring size distribution.

5.2.1 Cost Functions

Once we have amorphised a system from the crystalline state, we can then anneal it using Monte Carlo methods, with the degree of disorder related to the Metropolis criterion therein. The Metropolis criterion relies on a cost function, which although usually energetic, can take other forms. Published methods[133] presented novel

methods allowing for the control of the cost functions. By establishing target values for the Aboav-Weaire parameter (α, Section 3.2.3), the relative predominance of each ring size (p_n, Section 3.2.2) and the second moment of the ring distribution (μ_2, Section 3.2.4), it is possible to ensure selective formation of structures possessing key characteristics. The cost function derived from these metrics is given in Equation 5.2.1.1, with the Metropolis condition given by Equation 5.2.1.2.

$$\chi = k \mod \alpha - \alpha_t + \frac{|\mu - \mu_t|}{\mu_t} + \sum_{n \in R} \frac{|p_n - p_n^t|}{p_n^t}. \tag{5.2.1.1}$$

$$P = min[1, e^{-\Delta\chi/T}]. \tag{5.2.1.2}$$

This method provides a way to explore specific areas of the phase space without having to tune a range of potential parameters to arrive there in a more 'natural' manner. Using experimental values for α, p_n and μ_2 as targets, it is possible to explore the phase space of structures which share these metrics, with the aim of understanding why the experimental structures settle at these values. With sufficient metrics included in this search, we would expect to narrow the phase space of interest to better approximate the structure of the broader phase space from which experimental snapshots are sampled. Using methods such as these has enabled us to gain a better understanding of the physical manifestations of these metrics, and glean some understanding of their limits beyond the snapshots provided by experimental data.

There are however limitations to this approach. With insufficient target metrics, we cannot be certain how closely the samples we generate reflect the true experimental distribution. The values we set as targets are not directly physically realisable traits, but rather more nuanced values with complicated inter-dependencies. In addition, the energetics and physical structure of these systems are more complicated than might be expected. Without potential models designed to reflect the experimental systems, it becomes difficult to use internal energy as a target value for the MC cost function. The result is structures which do not necessarily reflect the physical constraints placed on the system by their chemistry, such as distributions in bond lengths and angles.

Although we do examine structures generated using this method later in this work (Chapter 9), the majority of structures in this thesis are built from potential models.

5.2.2 Potential Models

The starting point for our work has focused on networks with low level potentials parameterised loosely for graphene using a Keating potential, with the relative bond and angle force constants determined experimentally[145]. By incorporating different potential models and manners of adorning atoms to systems before amorphisation, I have been able to provide an alternate approach, whereby the energy of the system evaluated by the Monte Carlo simulations is tuned for a specific system, with the aim of creating systems whose energetics and physical structures better reflect different system types. The focus of this work has been silica bilayer systems, but I also demonstrate in passing potential applicability for heteronuclear systems such as boron nitride, and the option to apply higher level potential such as Tersoff potentials, although implementation is somewhat contrived (Appendix A).

The method I have developed relies on incorporating a third party API, namely LAMMPS[146] (Large Atomic/Molecular Massive Parallel Simulations), which offloads any energy and force calculations to external software, allowing a wide range of user-defined potential models. The advantage of this method is that well established LAMMPS potentials from literature can be easily incorporated, without the requirements for low level changes to the code by the user.

As the focus of this method is control over how the system is adorned, rather than over the network statistics (as was our focus in Equation 5.2.1.1), it is possible to evaluate the same underlying dual network (Figure 5.1) with different methods for adorning it. Two examples of this process are shown in Figure 5.2, with (a) representing a graphene system and (b) a triangle raft system, both built on the same underlying network shown in Figure 5.1. This feature lends itself to parallelisation, allowing for simultaneous evaluation of the same dual network using different potential models. This process works on the basis that the systems have the same underlying network structure, but will react differently to distortions to the

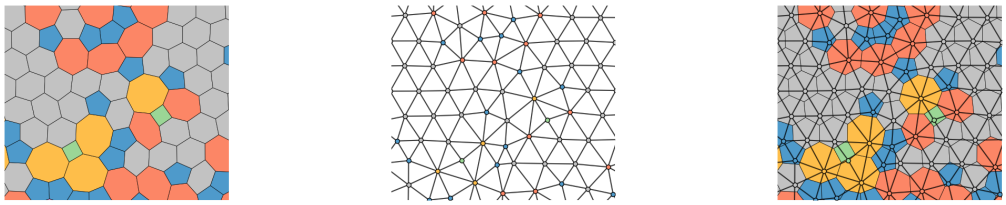

(a) Atomic network **(b)** Ring network **(c)** Dual relationship

Figure 5.1: Panel (a) gives an example of a 3-coordinate periodic network with disordered ring structure. Nodes and edges are shown, and the rings formed by their connections are coloured by size. Panel (b) gives the corresponding ring network, with nodes representing the centre of each ring and coloured by degree, and edges linking edge-sharing rings. Panel (c) shows the dual relationship between the networks and its underlying ring connectivities.

underlying connectivity as a result of the potential models used. One structure type must be selected as the directing structure, and all others follow its determinations. As such, the algorithmic steps involved are:

1. A Stone-Wales defect into the structure is proposed
2. Energies are calculated for N parallel systems, each of which are adornments of different potential models to the same proposed underlying network structure
3. The defect is accepted or rejected based on the energy of one potential model, the 'leading structure'
4. All N structures are updated dependent on the Metropolis condition of the leading structure.

(a) Graphitic System **(b)** Triangle Raft System

Figure 5.2: Panels (a) and (b) show two distinct ways of adorning the same network, (a) with carbon atoms to form a graphitic net, and (b) with silicon and oxygen atoms to form a triangle raft, analogous to silica bilayers

5.3 Potential Models

5.3.1 Graphene-like

Graphene is the simplest adornment to our network. Positioning a C atom at each node, and defining each edge as a bond is sufficient to describe the system. The potential used for the system is a simplified Keating potential, as described in Chapter 4. The potential is as follows:

$$U = U_{ij} + U_{ijk}, \tag{5.3.1.1}$$

where

$$U_{ij} = \frac{1}{2}k_r(r_{ij} - r_0)^2 \tag{5.3.1.2}$$

and

$$U_{ijk} = \frac{1}{2}k_\theta[cos(\theta_{ijk}) - cos(\theta_0)]^2. \tag{5.3.1.3}$$

The bond force constant (k_r) is set at 0.800 units, and the angle force constant (k_θ) at 0.200 units for this example. θ_0 is set at 120°, and r_0 at 1 unit. This ensures a similar balance of potentials to experimental values, determined from X-ray scattering to be $k_\theta/k_r \simeq 0.2$[36, 147, 148].

Under these conditions, we can calculate the isolated ring energies of ring sizes $4 \geq n \geq 12$, based on the ideal internal angles of each ring size. This is provided in Figure 5.3, compared against a loose fit of $k(n - \langle n \rangle)^2$. We can see that the

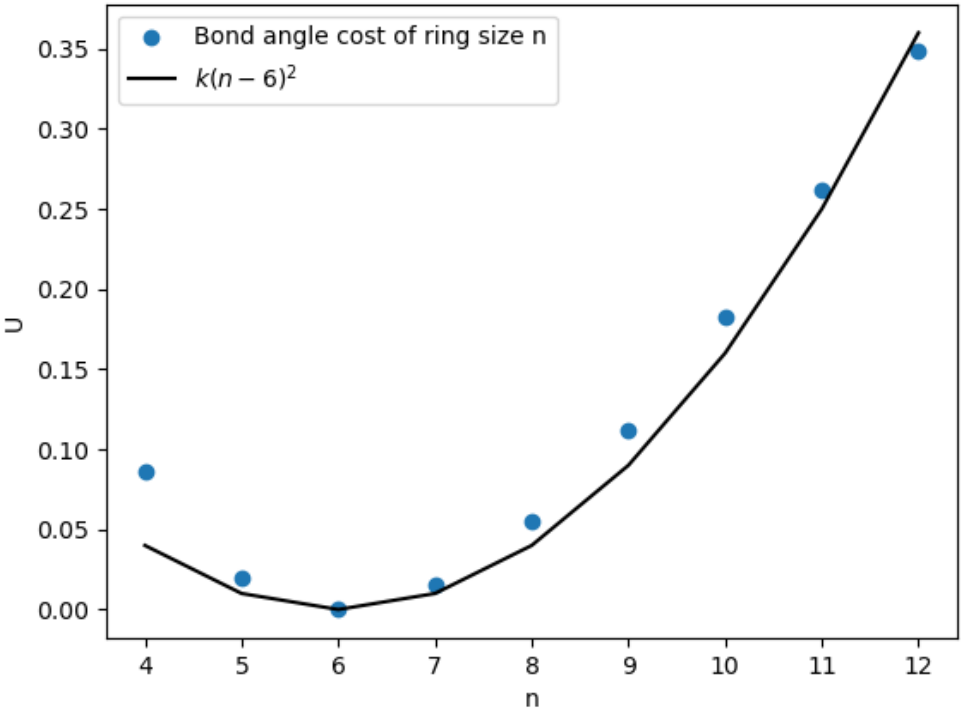

Figure 5.3: Isolated ring energy for ring size, n, resulting from the difference between the ideal Keating angle, $\pi/3$, and the regular internal ring angle, $\frac{(n-2)\pi}{2n}$

energy of an ideal hexagonal ring is 0, with the energetic cost of forming a ring size n scaling roughly with $(n - \langle n \rangle)^2$. Notably, $n = 4$ (square) rings show a significant deviation from this trend, having a higher energetic cost.

5.3.2 Boron Nitride layer-like

For our purposes, Boron Nitride (BN) sheets are structurally very similar to graphene networks [149]. BN sheets, like graphene sheets, map a single atom to the site of each network node, with the main difference being the identity of this atom; the binary nature of BN necessitating an alternating arrangement of boron and nitride atoms.

In the absence of reliable scattering data for BN surfaces, we assume that there is a similar balance of bond and angle forces to graphene, and so the same force constants are used as a basis. In order to try to maintain a high degree of canonical B-N bonding, it is important that the energy of homonuclear bonds (non-canonical) are higher than that of heteronuclear bonds (canonical). In higher level potentials, this would be accounted for by partial atomic charges, but as coulombic forces act at significant range, truncating these effects complicate the model significantly, putting it beyond the timescales required for a high throughput approach. In addition, full charges cloud our initial potentials and so move us away from our initial graphitic model assumption into a more unknown potential we have less control over. Instead, I have opted to use a short range coulombic force, which will only affect nearest neighbours, defined exclusively as bonded atom pairs. This was accomplished by using a cut version of the coulombic potential (as described in Section 4), with a cutoff distance of $r_{Qcut} = 2r_{BN}$. This ensures that bonded atoms will not be able to escape this repulsive force by escaping to $r = r_{Qcut}$. A secondary effect of this method is that the bond lengths of homonuclear bonds are lengthened slightly, as would be expected for weaker N-N and B-B interactions, which is also an assumption in lower-level Tersoff potentials[150].Incorporating only repulsive, rather than attractive and repulsive forces as produced by a full coulombic potential, significantly simplifies the computations involved.

To modulate the effect of this coulombic potential, five charges were selected, between $q = 0.1$ units to $q = 5.0$ units.

$$U = U_{ij} + U_{ijk} + U_Q, \tag{5.3.2.1}$$

where

$$U_{ij} = \frac{1}{2}k_r(r_{ij} - r_0)^2, \tag{5.3.2.2}$$

$$U_{ijk} = \frac{1}{2}k_\theta[cos(\theta_{ijk}) - cos(\theta_0)]^2, \tag{5.3.2.3}$$

and

$$U_Q = \begin{cases} \frac{q_i q_j}{\epsilon r_{ij}} & r < r_{Qcut} \text{ and } i = j \\ 0 & r \geq r_{Qcut} \text{ or } \ i \neq j \end{cases} \tag{5.3.2.4}$$

Where i, j represent the atomic species, with only boron-boron and nitrogen-nitrogen interactions accounted for.

This approach can also be used more generally to simulate structures where even ring sizes are experimentally favoured, such as aluminosilicate bilayers[151, 152].

5.3.3 Approximations to Silica Bilayers - 'Triangle Raft' methods

'Triangle Raft' (TR) networks are a two-dimensional model of silica structures, first construed by Shackelford and Brown in 1982[153] as a method for visualising Zachariasen structures analogous to bubble rafts. As Zachariasen structures have since been realised as analogous to graphene[5] and silica bilayer structures[21, 154], TR systems have also found use as a representation for these systems[134, 135].

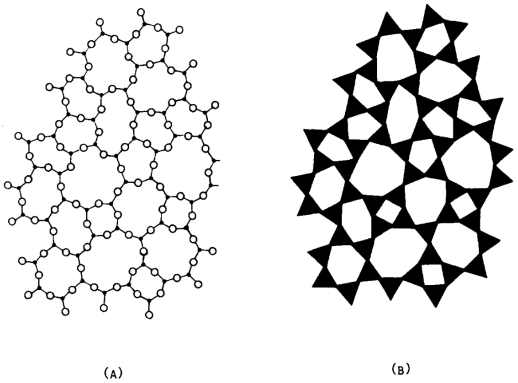

Figure 5.4: Triangle Raft representation (B) of a Zachariasen schematic (A), reproduced from literature[153]

These networks rely on a 2D projection of the bilayer as its basis, resulting in vertex sharing SiO_3 triangles, thus preserving the degree of freedom inherent in the Si-O-Si linkage (See Figure 5.4). For our implementation, these triangles are more than representations of known structures, they are used as a way to account for the degree of freedom within our energetic and structural modelling of the system. As such, we describe these triangles as being held together by harmonic bonds, as shown in Figure 5.5. These systems have been shown to produce structures comparable to experimental structures[155].

As such, the ability to build systems on the basis of a triangle raft system will hopefully open a better understanding of the energetics of silica bilayers as a function of their ring structure, and move towards methods to build more realistic bilayer structures.

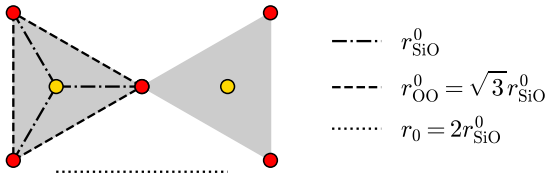

Figure 5.5: Graphic to show the potential model constructed for triangle raft units, with silicon (Si) atoms in yellow and oxygen (O) atoms in red. Dashed O-O harmonic bonds enforce the edges of the triangle, while Si-O dot-dashed harmonic bonds maintain the Si atom position in the centre of the triangle, reproduced from[155]

.

In order to better understand the bond potentials which produce results best fitting experimental results, I have evaluated a range of repulsive parameters, as laid out in Table 5.1.

The parameters selected seek understand the effect repulsive parameters play on the structures formed. Sample 1 adopts a more flexible approach, allowing a broader degree of flexibility based on previous work on high throughput processes within the Wilson group, derived work on zeolite frameworks (Chapter 2) which describe repulsions between oxygen atoms as hard-shell with a radius of $\simeq$ 2.7Å[90, 92]. While these methods preclude the need for Si-Si repulsive parameters, they are included for completeness. Sample 2 is a modification to this approach, with the aim of minimising the energy of the Si-O-Si angles at 180°, as used in previous triangle raft generation methods[155]. Again, these methods should preclude the need for O-O repulsions, but they are included for completeness.

Samples 3-6 seek to strike a balance between these approaches, with r_0(SiSi) set to maintain Si-O-Si angles at 180° where possible, while the repulsive r_0(OO) is increased from 2.7Å (the value taken for hard shell calculations) in increments of 0.1Å. Sample 6 is a limiting case, where r_0(OO) is set to a greater value, significantly increasing the energetic cost of forming rings $n = 4$ but not $n > 4$. The aim of this sample is to understand the effect of applying pressure on the configuration to adopt ring sizes larger than 4, increasing the relative predominance of p_5 at the cost of p_4.

The oxygen-oxygen repulsive parameters are visualised in Figure 5.6, for ring sizes $n = 4, 5, 6$. The successive coloured shells indicate the distance within which a Lennard-Jones short range interaction is felt by the reference oxygen atom. The

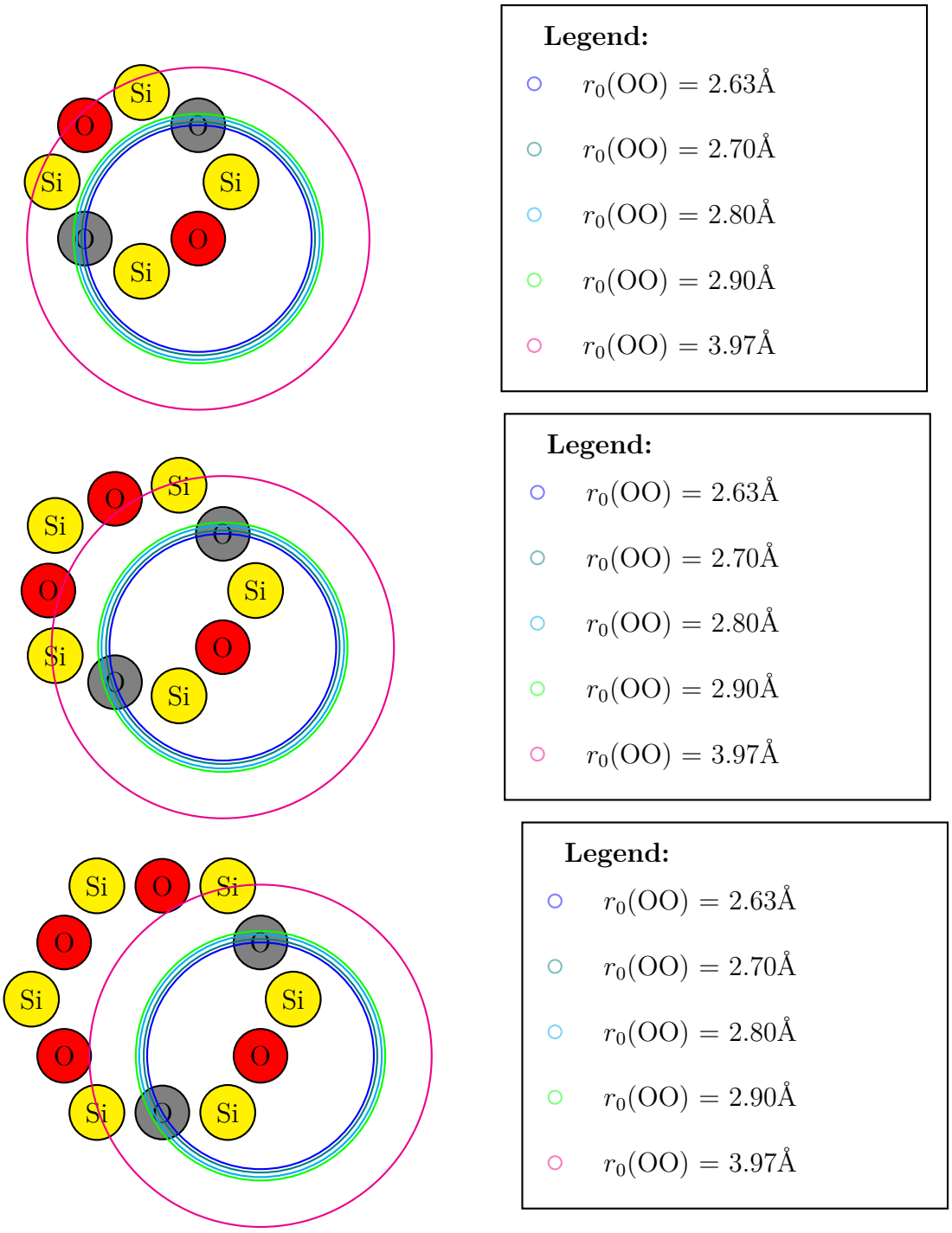

Figure 5.6: Graphic to show proposed $r_0(\mathrm{OO})$ values for 4,5,6 membered rings. As can be seen, $r_0 < 2.90$Å results in no energetic cost to forming regualr four membered rings. $r_0 < 3.97$Å has an energetic cost to forming four membered rings, but not five membered rings

Sample	r_{cut} (Si-Si)			r_{cut} (O-O)		
	a.u.	Å	Reduced units	a.u.	Å	Reduced units
Sample 1	4.9624	2.63	r_{OO}	4.9624	2.63	r_{OO}
Sample 2	5.7334	3.04	$2r_{SiO}$	4.9624	2.63	r_{OO}
Sample 3	5.7334	3.04	$2r_{SiO}$	5.1023	2.70	$1.03r_{OO}$
Sample 4	5.7334	3.04	$2r_{SiO}$	5.2912	2.80	$1.07r_{OO}$
Sample 5	5.7334	3.04	$2r_{SiO}$	5.4772	2.90	$1.10r_{OO}$
Sample 6	5.7334	3.04	$2r_{SiO}$	7.5050	3.97	$1.51r_{OO}$

Table 5.1: Simulation parameters used for our six samples, in terms of atomic units, angstroms (Å) and reduced units in terms of the harmonic oxygen-oxygen ($r_{OO} \simeq 2.63$Å) and silicon-oxygen ($r_{SiO} \simeq 1.52$Å) bond lengths. N.B. the literature r_{SiO} in three dimensions is $\simeq 1.609$, but for two-dimensional simulations we use a projection of these tetrahedral bond lengths onto the basal plane of the bilayer; r_{OO} is unchanged.

neighbouring atoms are shown in grey, as they are harmonically bonded to the reference atom, they are exempt from short range forces. With a $r_{cut} < 2.9$Å, we can see that there is no energetic cost to forming an ideal four membered ring. However, for $r_{cut} = 3.97$Å, there is a direct energetic cost, which we would expect to disfavour four membered rings. By comparison, in ordered five and six membered rings a cutoff of $r_{cut} = 3.97$Å does not impinge on the ideal cross-ring oxygen oxygen displacements, and so we expect that this potential will not disfavour five or six membered ring formation.

The range of allowed ring sizes was set at 4-12, slightly greater than the observed experimental range ($4 \geq n \geq 10$). This is because we are interested in how the parameters selected can affect the limits in ring sizes formed. We would expect that a reliable potential would reproduce experimental systems without these constraints.

Figure 5.7 visualised the energy cost of forming an isolated ring size n, assuming ideal trigonal SiO_3 units, with the energy calculated for the repulsive terms. We can see that, for isolated regular polygons, Samples 2,3,4 and 5 give identical energy profiles. Sample 1 shows no energy cost to form regular isolated rings of any size, whereas Sample 5 has a strong energetic penalty for forming four membered rings. It is worth noting, however, from these profiles that to maintain ideal trigonal units, the bridging oxygen atoms must be distorted into or out from the ring, which is expected to have significant effects on the surrounding rings.

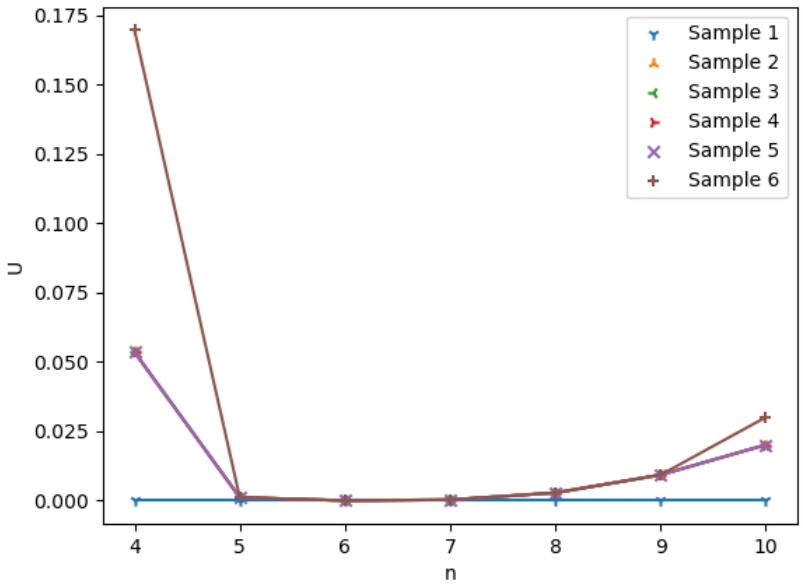

Figure 5.7: Isolated ring energy for ring size, n, assuming ideal bond lengths and evaluating based on the repulsive terms only.

5.4 Computational Considerations

5.4.1 Computational time considerations

Calculations were conducted on 400 ring (800 node) and 1600 ring (3200 node) systems, with the CPU time for a range of systems provided for reference in Table 5.2. Computationally, minimising triangle raft structures is significantly more

System	System Size	Number of Atoms	CPU Time/100 Monte Carlo Steps
Graphene	400 rings	800	≃30 seconds
Graphene	1600 rings	3200	≃80 seconds
Triangle Raft	400 rings	2000	≃ 100 seconds
Triangle Raft	1600 rings	8000	≃200 seconds
Boron Nitride	400 rings	800	≃50 seconds

Table 5.2: Computational Cost of potential models used as a function of potential model and system size. Times derived for one thread of Intel E5-2698 CPU.

intensive than simpler systems, in part due to the addition of additional atoms, but also due to the highly connected nature of the system. As might be expected, Boron Nitride-like systems sit between triangle raft and simple graphene systems in complexity, with the addition of coulombic terms increasing the computational load.

Calculation times do not scale linearly with atom count with the LAMMPS software due to fixed costs within the code.

5.4.2 Local vs Global Minimisation considerations

We also need to consider the effect of the additional degree of freedom in TR system for our minimisation protocol. For previous work[124], minimisations have been conducted locally (*i.e.* energy was evaluated only for atoms within a range of 5 edge lengths from any introduced defect). This simplification was based on investigations into graphene have shown that graphene is particularly capable of absorbing the structural distortion of introducing a Stone-Wales (SW) defect in a small local radius, significantly improving computational performance[35]. For our TR models, we need to understand whether this assumption holds. To understand the comparative behaviour of bilayer systems, we have evaluated the effect of a single Stone Wales defect in an otherwise crystalline structure, and allowing the system to minimise only within a local area. This was achieved by fixing the atom coordinates of all atoms outside of radius r from the SW defect.

Images to show the effect of constraining the area over which the structure can minimise are given in Figures 5.9 and 5.10. We can see that with our potentials, both systems benefit from allowing a greater percentage of the system to relax. However, there are distinct differences in the energy distributions around the defect between these two potential models. For graphene, we see that energy decreases regularly and radially from the defect; however, for our triangle raft systems, there is a pronounced angular dependence. Looking closer, we can see that this is reflected in percolating structural changes in the triangle raft system, in particular in the oxygen atoms. Oxygen atoms move in a concerted manner, generating subtle structural ripples which percolate through the entire cell. This is similar to the distortions hypothesised for hexagonal networks[67, 87], but is more directed. Examining closely, we can see that these structural distortions percolate across the periodic boundary.

The comparative effect on the energy as a function of the percentage of the unit cell around the defect is presented in Figures 5.9 and 5.10. These graphs present

the percentage of the energy of the defect which remains after allowing a given percentage of the periodic unit cell to relax. 100% is taken as the energy of the system with only the atoms in rings directly involved in the SW defect to relax; 0% is the energy once the whole periodic cell has been relaxed, giving a lower threshold that any given defect can be minimised to using our potentials.

Comparing (a) and (b), using a graphene potential we can see that 99% of the defect energy can be absorbed by allowing only a small fraction (< 0.05) of the cell to relax. By contrast, a significantly higher fraction of the cell is needed to accommodate 99% of the energy of a SW defect in a triangle raft system. We also see an inflection point in the energy of the triangle raft system with about 82% of the periodic cell allowed to relax; this corresponds to the radius at which the local radius surrounding the defect within which atoms are free to minimise reaches across the unit cell, allowing concerted structural changes which percolate across the periodic boundary. The inflection indicates that allowing structural changes to percolate across the periodic boundary is an important factor in minimising the energy of the system. This comes at a significant computational cost, as we must now simulate the dynamics of significantly more atoms; however, without minimising across the entire cell after the introduction of each defect, we cannot expect to get reliable energy values.

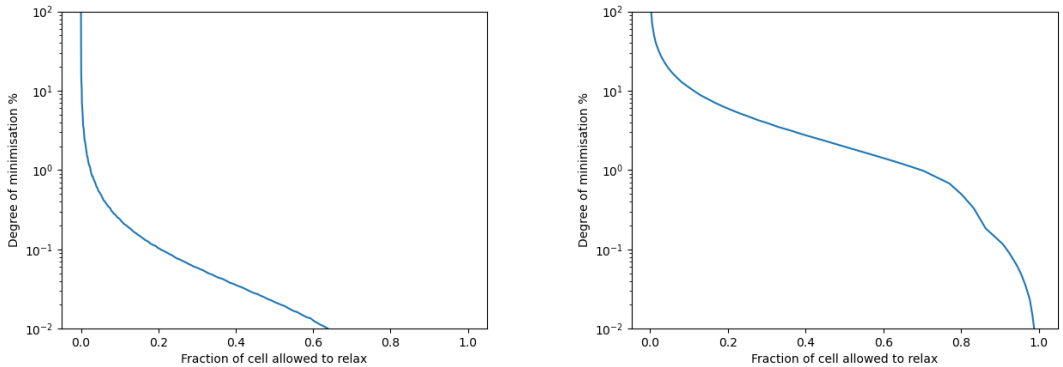

(a) Graphene potential model **(b)** Triangle raft potential model

Figure 5.8: Minimisation profile of a single defect in an otherwise crystalline hexagonal network, using a graphene potential (a) and a triangle raft potential (b). The energy is a presented as the percentage of the isolated defect energy which can be absorbed as a function of the fraction of the cell which is allowed to react to the distortion.

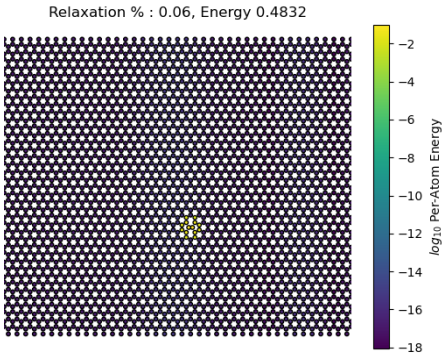

(a) Per atom energy with 0.06% of the system allowed to relax

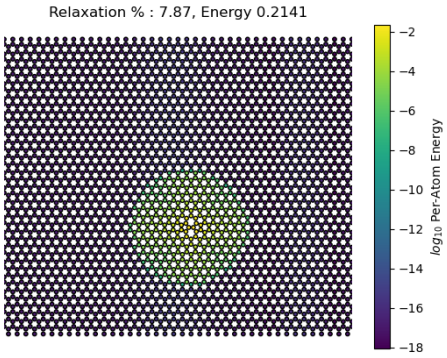

(b) Per atom energy with 7.87% of the system allowed to relax

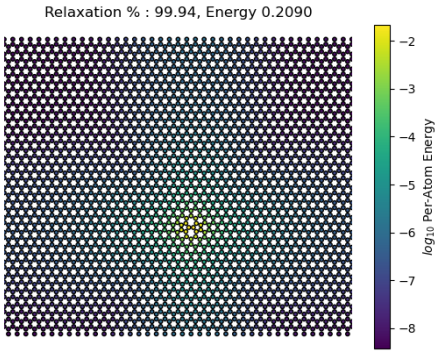

(c) Per atom energy with 99.94% of the system allowed to relax

Figure 5.9: Per atoms energies for a graphene system, locally minimised at different radii about the single SW defect, allowing a given % of atoms to relax

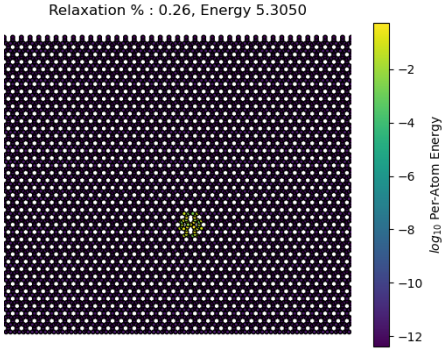

(a) Per atom energy with 0.26% of the system allowed to relax

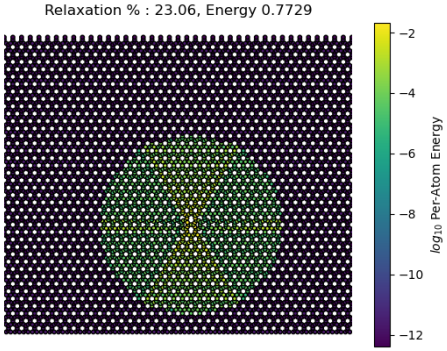

(b) Per atom energy with 23.06% of the system allowed to relax

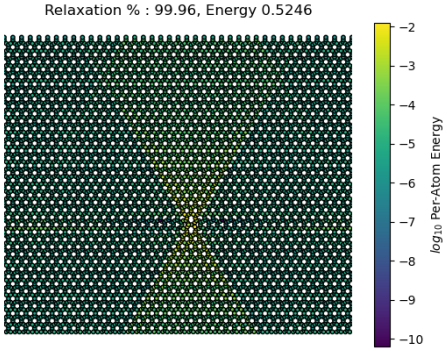

(c) Per atom energy with 99.96% of the system allowed to relax

Figure 5.10: Per atoms energies for a graphene system, locally minimised at different radii about the single SW defect, allowing a given % of atoms to relax

5.5 Metrics

A wide range of metrics are utilised to understand the effect of using different potential models to shape the formation of amorphised networks.

5.5.1 Disorder as a function of Monte Carlo generation 'temperature'

The ring structures produced by amorphisation at a given Monte Carlo 'temperature' are given in Figures 5.11,5.12 and 5.13. We can see that raising the 'Temperature' allows for the formation of more disordered, less enthalpically favourable structures, as would be expected and reflected in previous work[133]. From an experimental standpoint, these graphics are similar to those understanding increasing disorder at a crystalline-amorphous interface[61].

'Temperature' is a useful simulation parameter, but has limited use in understanding the nature of structures, and does not directly correlate to the structural ring statistics due to higher level structural factors. However, it gives a qualitative indication of the level of disorder present for an overview of the structures present. It is a function of these structures forming with enthalpy as a target, rather than a direct metric such as p_6, that the results show a level of disorder at a given 'temperature'. As such, rolling mean averages are used.

Figure 5.11 shows such a plot for a simple graphene system. We can see that at low Monte Carlo 'temperature', the sample is crystalline ($p_6 = 1$), meaning no dispersion in the size of the rings present. As we increase the generation 'temperature', we introduce disorder into the system, as p_6 decreases to $\simeq 0.2$, indicative of the introduction of more Stone-Wales (SW) defects, forming more entropically but less enthalpically favourable structures. This process can be decomposed into two regions: The first, $0.8 < p_6 < 1.0$, where this disorder is composed solely of $n = 5, 7$ rings, and the second, $0.2 < p_6 < 0.8$, where $n = 4, 8, 9, 10$ rings are also adopted. We expect this to be a result of the higher energetic costs of ring formation as we move away from $n = 6$. We can see that even at low p_6, the composition of large ring sizes ($n > 10$) is still very low.

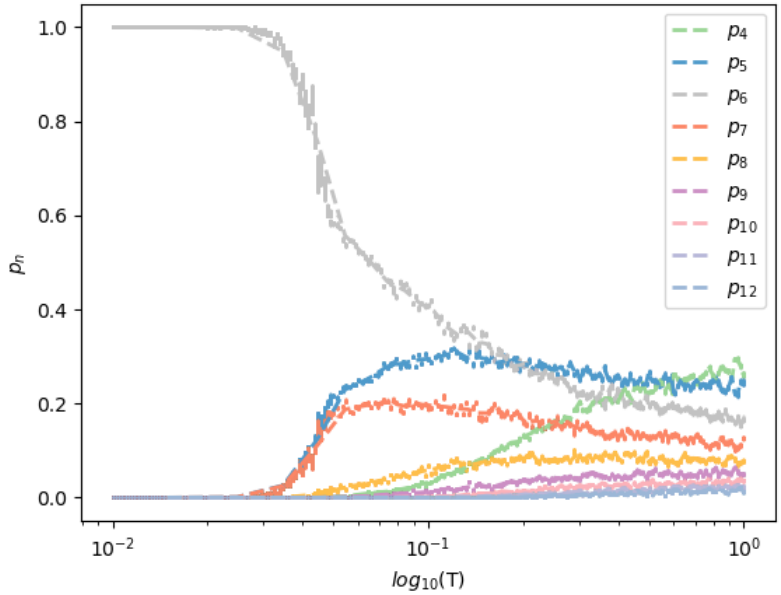

Figure 5.11: Plot to show the effect of Monte Carlo moves on a graphene network across a range of 'temperatures' ($10^{-2.00} \rightarrow 10^{0.00}$ units). Ring fractions are coloured by ring size, with simulation values shown with scatter points and a rolling average plotted for clarity.

Boron Nitride (BN) systems follow a similar pattern, with an increase in 'temperature' resulting in increased disorder. However, modulating the coulombic repulsion has significant impact on the structure of these plots.

Increasing the localised atomic charges increases the MC temperature required to introduce SW defects. This is because SW defects introduce a 5577 defect into a previously crystalline 6666 arrangement. Whereas a crystalline system with even rings can be arranged such that all bonds are canonical, introducing odd membered rings as in a SW defect means that this is no longer possible, and so each defect introduces non-canonical bonds.

If we examine the difference between BN $q = 0.1$ units (a), which closely resembles the graphene system (Figure 5.11), and $q = 5.0$ units (e), we can see that changing q also impacts the balance of ring populations at a given p_6. In particular, we can see the region in which the system is composed solely of five, six and seven membered rings shrinks, with p_4 following p_5 and p_7 more closely with p_6.

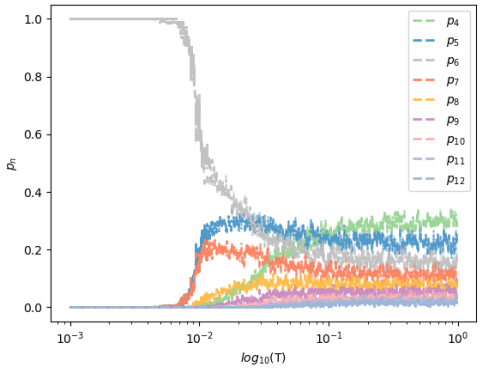

(a) BN : q=0.1 Units

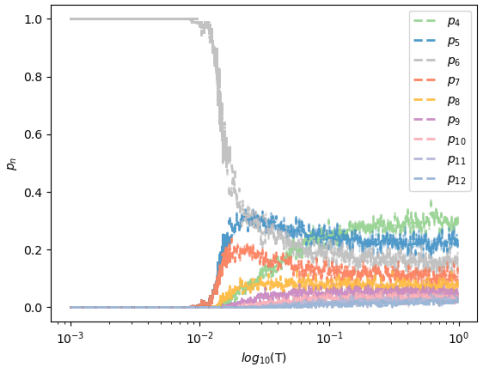

(b) BN : q=0.5 Units

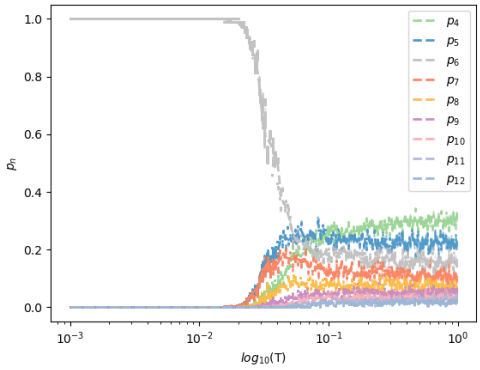

(c) BN : q=1.0 Units

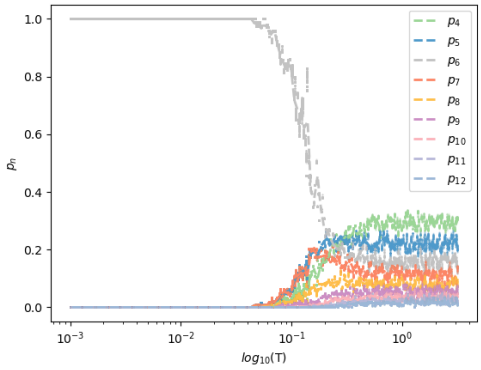

(d) BN : q=2.0 Units

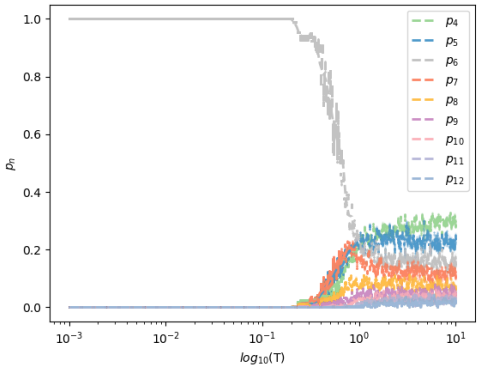

(e) BN : q=5.0 Units

Figure 5.12: Plot to show the effect of Monte Carlo moves on a BN network, with atomic charges from 0.1 to 5.0 units, across a range of 'temperatures' commensurate with displaying a range of ring statistics. Ring fractions are coloured by ring size, with simulation values shown with scatter points and a rolling average plotted for clarity.

For the different triangle raft samples, we see very similar behaviours of p_n with temperature. There are slight differences in the prevalence of crystalline structures, and different p_6 limits found within the given temperature range.

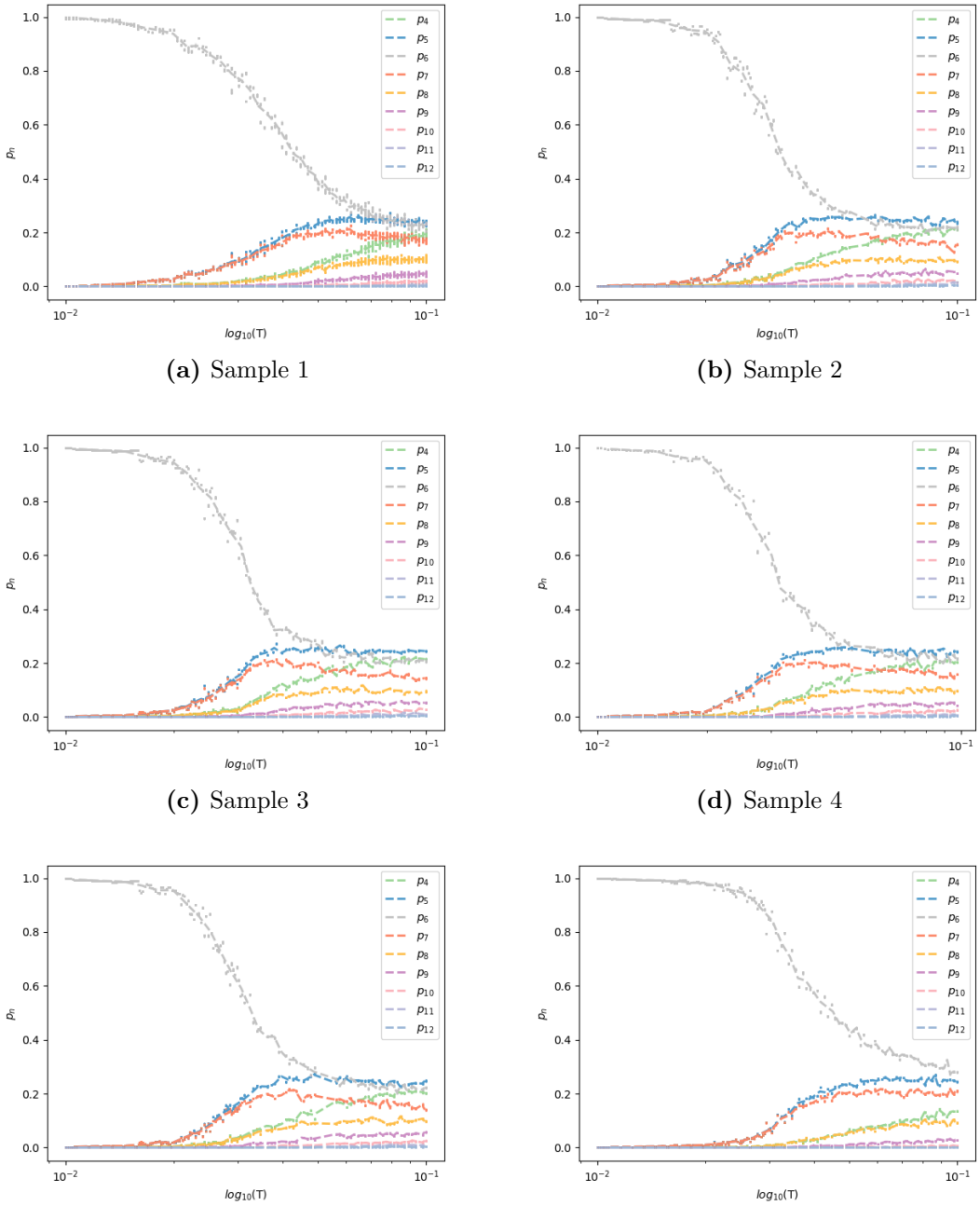

(a) Sample 1 **(b)** Sample 2

(c) Sample 3 **(d)** Sample 4

(e) Sample 5 **(f)** Sample 6

Figure 5.13: Plot to show the effect of Monte Carlo moves on different triangle raft potential networks across a range of 'temperatures' ($10^{-2.00} \rightarrow 10^{-1.00}$ units). Ring fractions are coloured by ring size, with simulation values shown with scatter points and a rolling average plotted for clarity.

We can see that a narrower temperature range is required to explore the phase space of triangle raft networks of $0.2 > p_6 \geq 1.0$.

5.5.2 Trends in ring composition with disorder

The Monte Carlo 'temperature' is metric used to indicate the level of disorder introduced by Monte Carlo moves. However, it is an incomplete measure of the structure of the system, and the differing nature of the systems explored mean that our axes are scaled differently. This makes comparison difficult, and can cloud the effects present. For our systems, p_6 is a far more identifiable metric. As such, for comparisons between samples, I have visualised the proportion of $p_{n\neq6}$ against p_6, to evaluate how the ring structure evolves as a function of disorder. These are visualised in Figures 5.14, 5.15 and 5.16.

From these figures, we can get a qualitative understanding of the means by which the structures distribute disorder through different ring sizes.

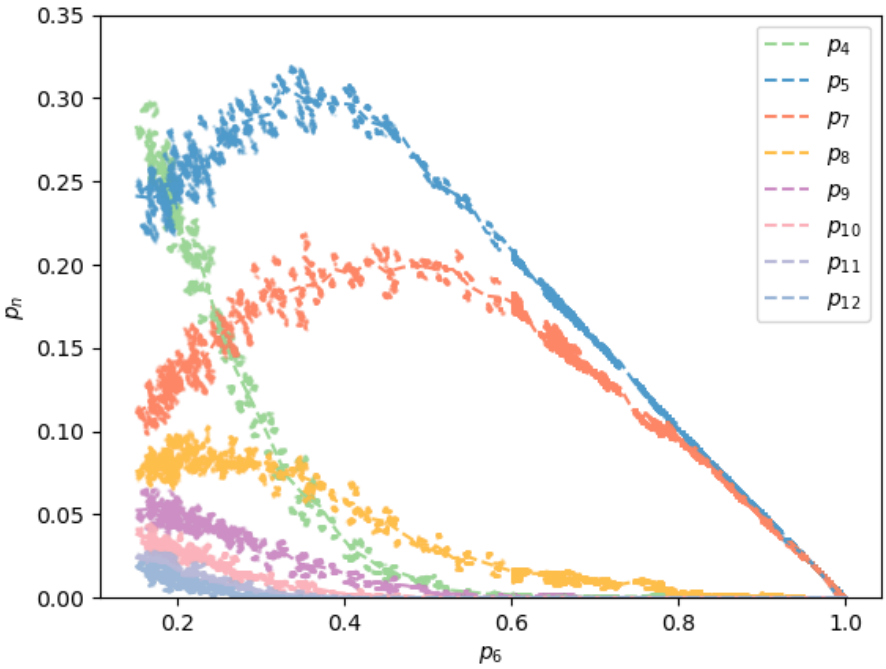

Figure 5.14: Visualising the composition of rings sized $n \neq 6$ of a graphene network as a function of p_6

For our simple graphene system in Figure 5.14, we can see more clearly that for $1.0 < p_6 < 0.8$, disorder is composed only on 5- and 7- membered rings.

Moving to lower p_6, we can see that 8-membered rings are introduced before 4-membered rings, likely as a result of the increased enthalpic cost of the internal angles (Figure 5.3). Below $p_6 = 0.5$, the fraction of four membered rings increases rapidly as the ring distribution flattens out, and seven and five membered rings are replaced by four and $n > 7$ rings.

For our BN systems in Figure 5.15, we can see that with low charges, the ring distribution approximates to a graphene system. Increasing the charge acts to reduce the range over which the system is composed of 5-, 6- and 7- membered rings, introducing 4- and 8- membered rings such that system composition shows more consistent trends with p_6. Although 5- and 7- membered rings remain the most common ring sizes, their relative predominance shrinks, with the enthalpic terms favouring a higher proportion of even membered rings with canonical bonding, shifting the balance between the higher bond angle energy term of forming more strained rings (Figure 5.3) and the lower coulombic cost of forming canonical bonds in even membered rings.

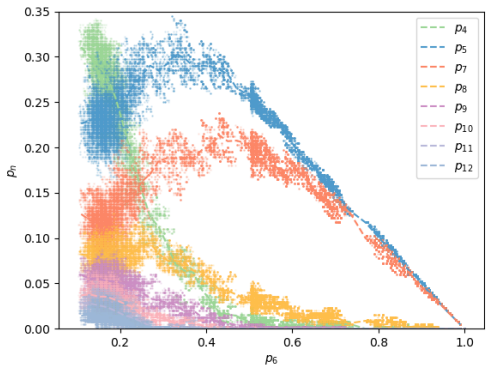

(a) BN : q=0.1 Units

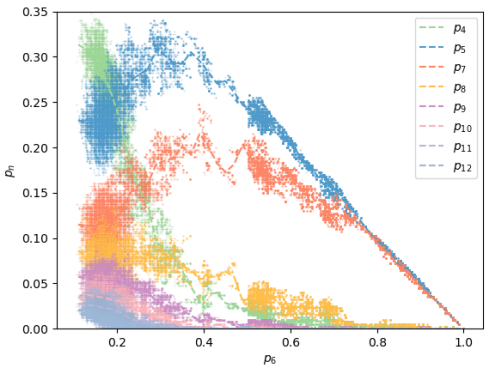

(b) BN : q=0.5 Units

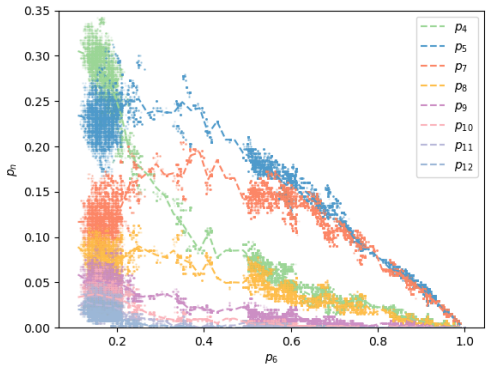

(c) BN : q=1.0 Units

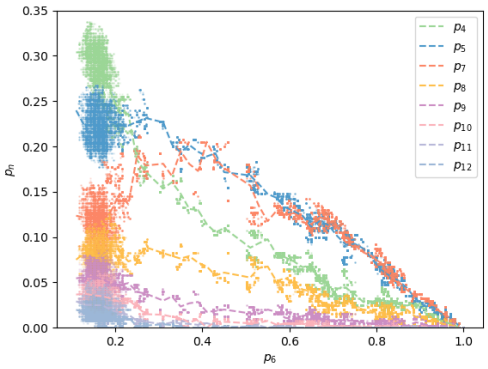

(d) BN : q=2.0 Units

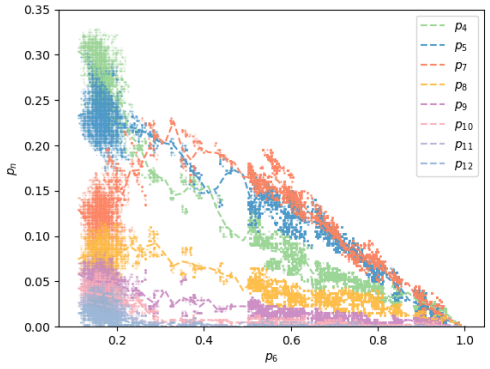

(e) BN : q=5.0 Units

Figure 5.15: Visualising the composition of rings sized $n \neq 6$ of a BN network as a function of p_6 and charge

Across our six potential models for bilayer silica, we see similar results, with little noticeable change in the ring proportions in reaction to the changes in repulsive terms. The greatest difference is within Sample 6, where the temperature range used is not sufficient to access structures of $p_6 < 0.26$; however within the range

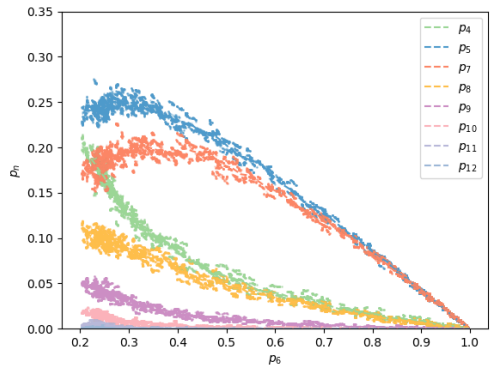

(a) Sample 1

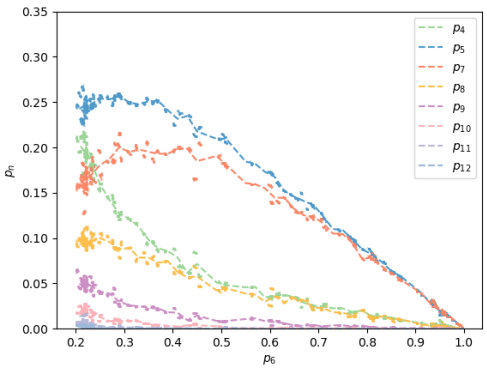

(b) Sample 2

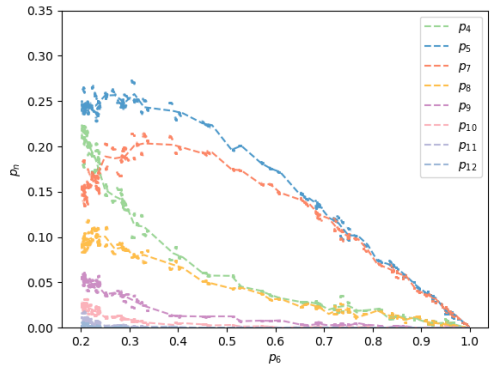

(c) Sample 3

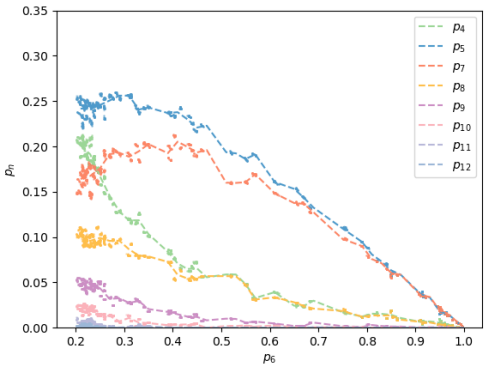

(d) Sample 4

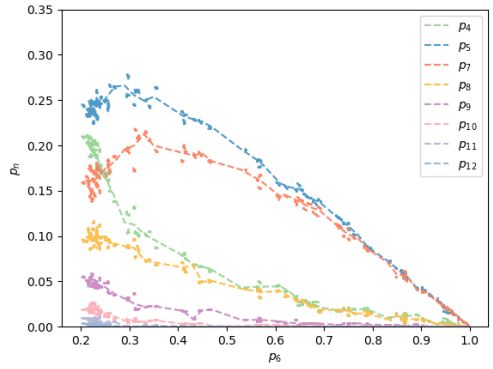

(e) Sample 5

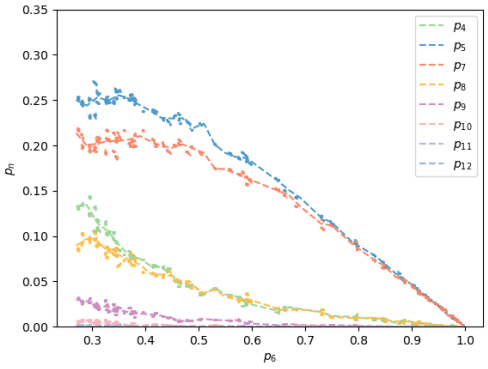

(f) Sample 6

Figure 5.16: Visualising the composition of rings sized $n \neq 6$ of a BN network as a function of p_6 and LJ parameterisation

used it maps well onto the other structures.

5.5.3 Comparisons to maximum entropy solutions

The generation of a structure using MC systems is a balance between the system entropy and enthalpy. Changing the potentials applied alters this balance, introducing different enthalpy considerations which can bias the system from the highest entropy solution. Comparison to the maximum entropy ring distribution, as defined by a Lemaître's law (Section 3.2.4), gives an indication of the enthalpic effects on a structure and how they may cause deviations from the maximum entropy solution.

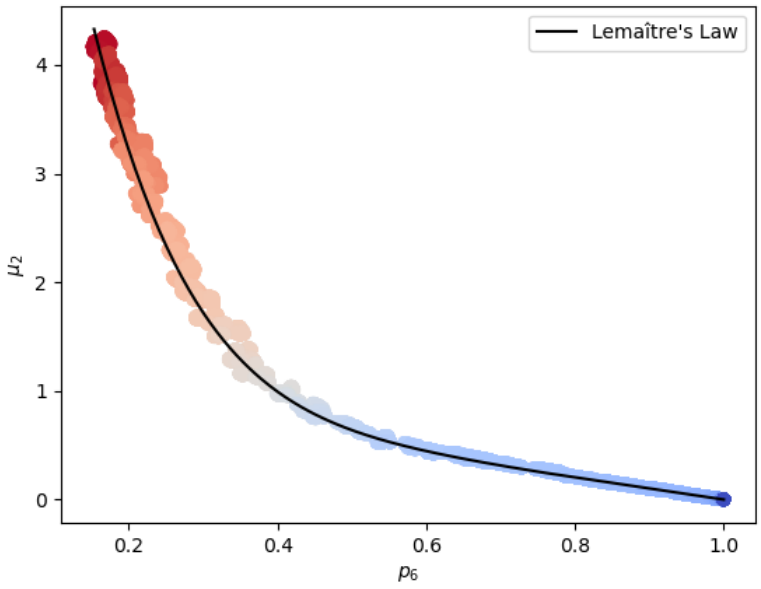

Figure 5.17: Lemaître's law plot for a graphene system, comparing structures formed to the maximum entropy solution, coloured by Monte Carlo generation 'temperature'.

Our model of graphene follows the maximum entropy distribution closely (Figure 5.17), whereas our BN (Figure 5.18) and triangle raft (Figure 5.20) systems approximate to maximum entropy solutions at high and low p_6, but deviate significantly at intermediate p_6. This makes our BN and triangle raft systems notable, as Lemaître's law is generally well obeyed by CRN networks, and so worth of further analysis.

BN structures show a charge dependent deviation from the maximum entropy solution. At $q < 1.0$ units, the ME solution well approximates the system; however for $q \geq 1$ units, the systems break from this trend, sitting at a higher variance.

For $q = 1.0$ units (Figure 5.19), we can see a stronger prevalence of even membered rings, especially apparent at higher p_6, where we see four and eight membered rings, not present in the ME solution. This indicates that our potential model does bias the system towards more heteronuclear, canonical bonding. Similarly, for our triangle raft systems (Figure 5.21), we can visualise the discrepancy from the ME solution with a set of ring distributions. The difference at $n > 6$ tends to slightly favour n =even rings, and larger rings than would be entropically expected. Below $n = 6$, we see a stronger preference for $n = 4$ than the ME solution predicts. We can rationalise this by considering the additional degree of freedom afforded by the oxygen bridge between Si atoms.

5.5.4 Even and Odd ring distributions

Of particular note for our BN systems, we would like to have an understanding of the ratio of even to odd rings. This is because in a BN system only even membered rings can be composed of solely canonical bonds. The limits of these scenarios would be a haekelite $5-7$ system, with $p_{n=even} = 0$, and a procrystal system, with $p_{n=even} = 1$. To this end, I have visualised the relative fractions of $p_{n=even}$ and $p_{n=odd}$ rings for all of the systems ($p_{n=odd}/p_{n=even}$), as a function of p_6. Visualising the structures in this manner, we can evaluate the effectiveness of our BN systems at biasing the system towards even ring sizes.

Figure 5.22 shows the odd to even ratio for graphene systems. As would be expected, our graphene-style potential follows the maximum entropy solution closely. Starting at $p_{odd}/p_{even} = 0$ for a $p_6 = 0$ system, the fraction increases as 5 and 7 membered rings are introduced, and drops off at low p_6 as larger ring sizes become more accessible, mirroring the p_5 and p_7 trends in Figure 5.14.

For our BN structures (Figure 5.23), we confirm the trend we noted in q in Section 5.5.2 with q, namely a notable difference between structures generated with $q < 1.0$ units and those generated with $q > 0.1$ units. For systems with $q < 1.0$, we can see that the systems largely follow the maximum entropy solution, with slight deviation towards a lower $p_{n=odd}/p_{n=even}$. Systems generated with $q > 1.0$ sit at

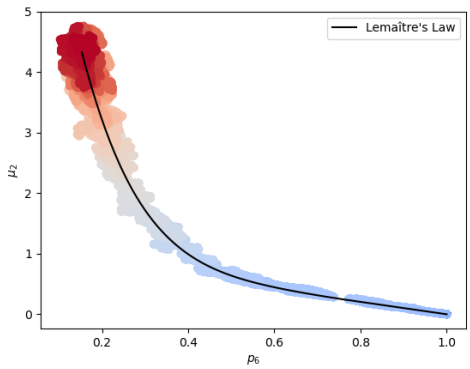

(a) BN : q=0.1 Units

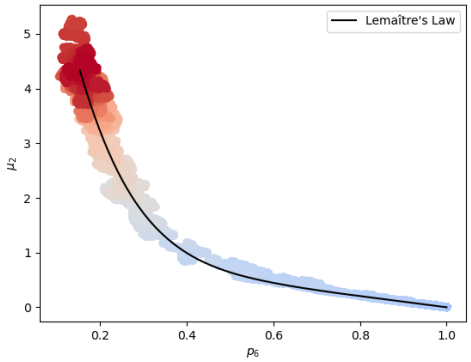

(b) BN : q=0.5 Units

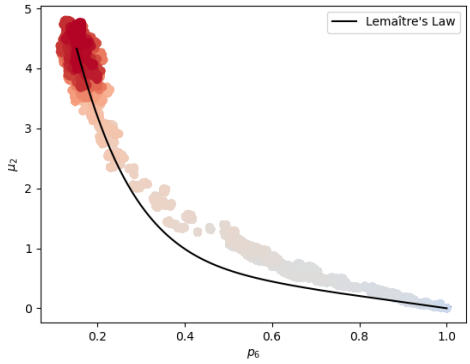

(c) BN : q=1.0 Units

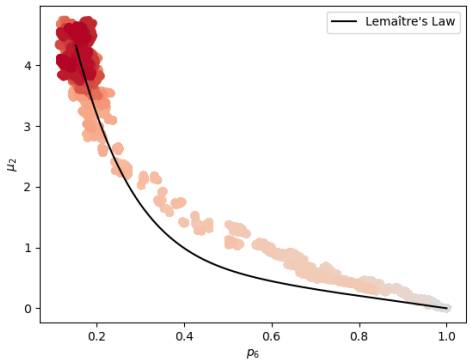

(d) BN : q=2.0 Units

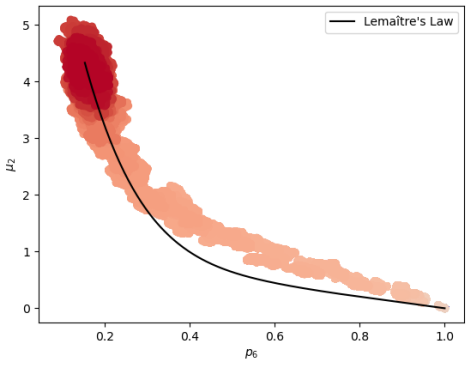

(e) BN : q=5.0 Units

Figure 5.18: Lemaître's law plot for BN systems as a function of charge, comparing structures formed to the maximum entropy solution

a lower $p_{n=odd}/p_{n=even}$, indicative of a higher even ring proportion. Interestingly, moving from $q = 1.0 \rightarrow q = 5.0$ has a minimal effect, especially compared to moving from $q = 0.5 \rightarrow q = 1.0$.

Figure 5.24 shows two configurations for a BN potential at $q = 0.1$ units (a)

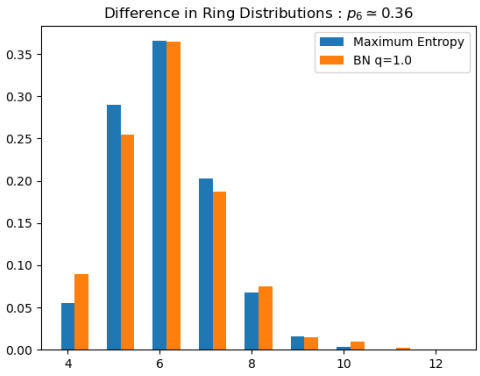

(a) Ring distribution for a $q = 1.0$ unit BN system at $p_6 = 0.36$

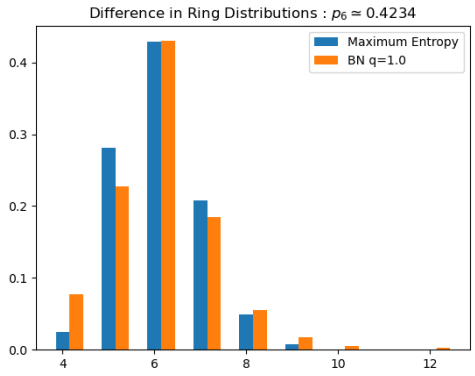

(b) Ring distribution for a $q = 1.0$ unit BN system at $p_6 = 0.4234$

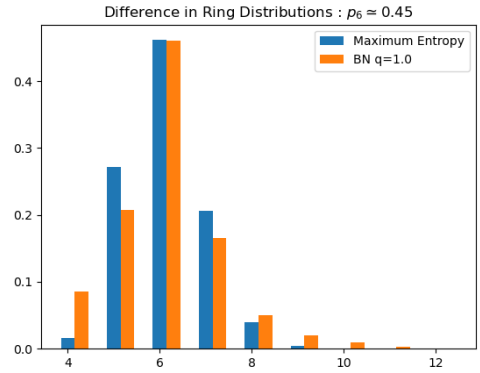

(c) Ring distribution for a $q = 1.0$ unit BN system at $p_6 = 0.45$

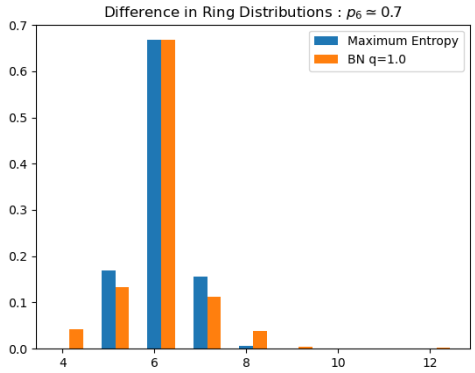

(d) Ring distribution for a $q = 1.0$ unit BN system at $p_6 = 0.70$

Figure 5.19: Ring distributions for a $q = 1.0$ BN system, produced at $p_6 = 0.36, 0.4234, 0.45, 0.7$

and $q = 5.0$ units (b). We can see that while (b) is composed of more even membered rings, its is visibly more strained, with the coulombic effect dominating contributions to the enthalpic terms.

All triangle raft structures (Figure 5.25) follow a similar trend, diverging from the maximum entropy ratios fro $0.25 \geq p_6 < 1.0$, likely mostly driven by the divergence of p_4, p_5 from their maximum entropy solutions as noted in Figure 5.21.

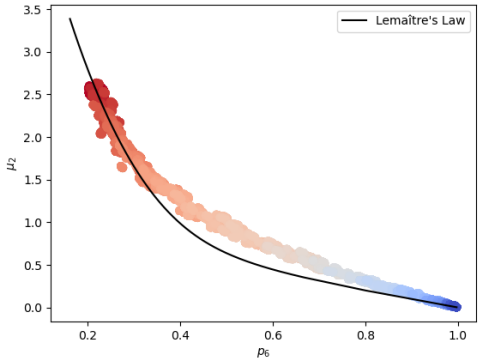

(a) Sample 1

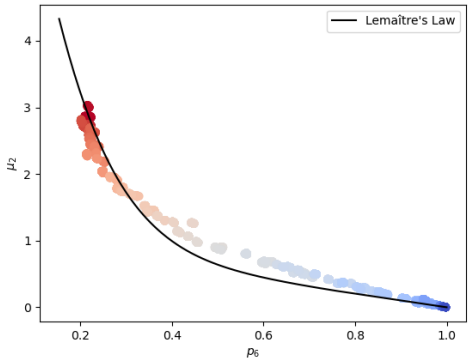

(b) Sample 2

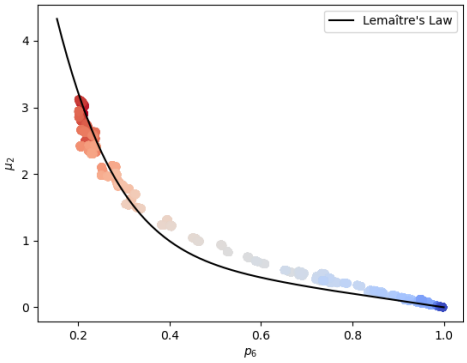

(c) Sample 3

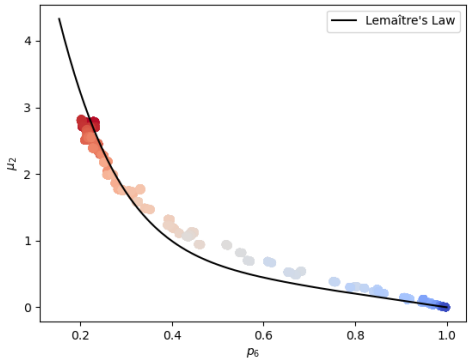

(d) Sample 4

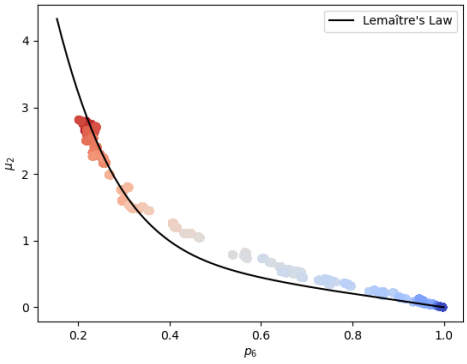

(e) Sample 5

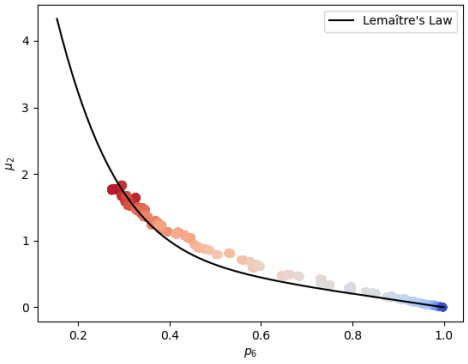

(f) Sample 6

Figure 5.20: Plot to show the effect of Monte Carlo temperature on triangle raft networks for samples 1 through 6

5.5.5 Assortativity as a function of disorder

Network metrics such as the degree assortativity are used to quantify the local ordering of rings in a network. The metrics themselves are not directly realisable,

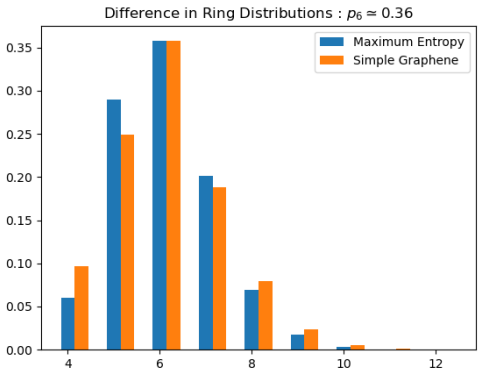

(a) Ring distribution for Sample 1 triangle raft network at $p_6 = 0.36$

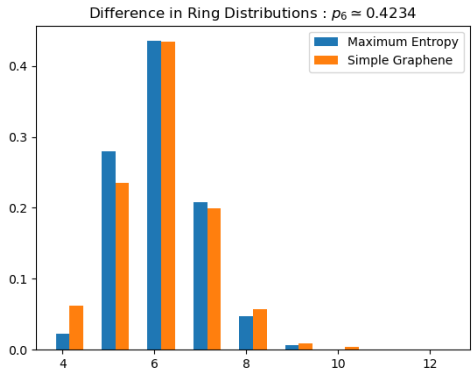

(b) Ring distribution for Sample 1 triangle raft network at $p_6 = 0.4234$

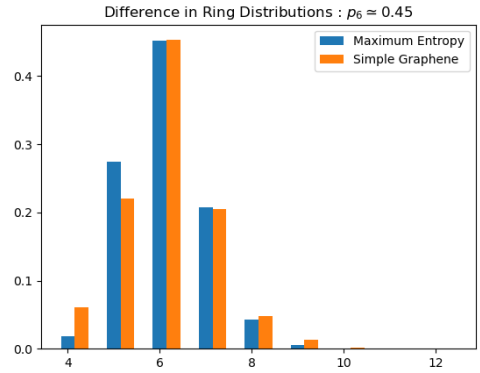

(c) Ring distribution for Sample 1 triangle raft network at $p_6 = 0.45$

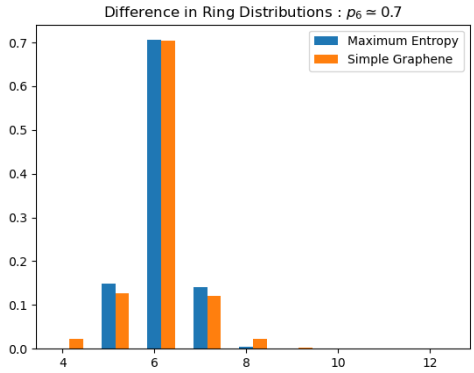

(d) Ring distribution for Sample 1 triangle raft network at $p_6 = 0.70$

Figure 5.21: Ring distributions for a $q = 1.0$ BN system, produced at $p_6 = 0.36, 0.4234, 0.45, 0.7$

but rather rely on evaluating the surroundings about each ring. As such, visualising structures directly gives only a qualitative understanding of these metrics, meaning justifying changes beyond broad arguments is difficult.

Figures 5.26, 5.27 and 5.28 present the network assortativity as a function of p_6. We can see that all of these networks are disassortative, with assortativity values r lying between $-0.35 < r < -0.10$. The results in Figure 5.26 are similar to literature results[124], which utilised similar bond switching Monte Carlo methods, across slightly broader p_6 limits.

This work posited that this variation could be split into to regimes. At the high p_6 limit, defects are effectively isolated, and r approximates to its value for an

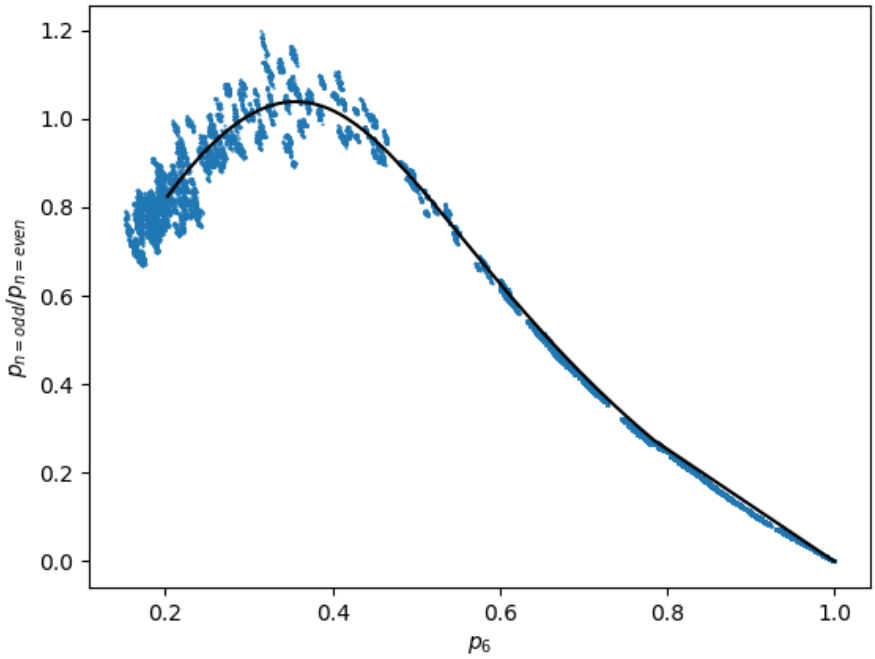

Figure 5.22: Even vs odd ring characteristics for a graphene-style potential

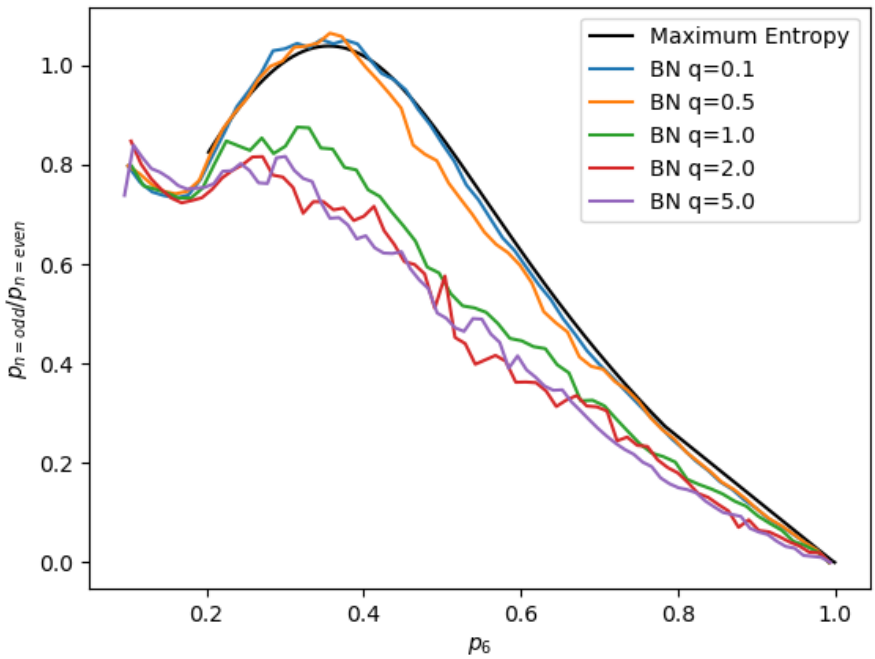

Figure 5.23: Even vs odd ring characteristics for a BN potential at different values for q

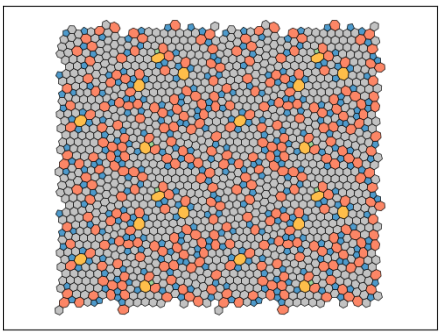

(a) BN $q = 0.1$

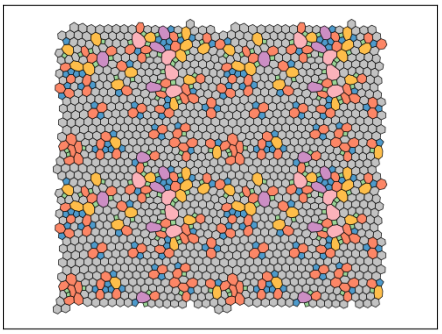

(b) BN $q = 5.0$

Figure 5.24: Different BN structures $q = 0.1$ to $q = 5.0$, at $p \simeq 0.6$ (0.6125, 0.5975)

isolated defect, $-\frac{1}{4}$. Moving to low p_6, the networks go through a "phase transition" to truly amorphous networks. Both the graphene and BN systems show these domains, with a minimum in r, and a high p_6 assortativity of $r \simeq -0.25$. Increasing q for the BN structures shifts the p_6 at which the gradient changes to a lower value. In contrast, triangle raft systems generated by bond switching methods deviate from this trend, returning a negative trend in assortativity with lower p_6. Unlike our graphene and BN systems, increasing the disorder in the network increases the disassortativity across all p_6, showing only one of the two regimes present in the BN and graphene networks.

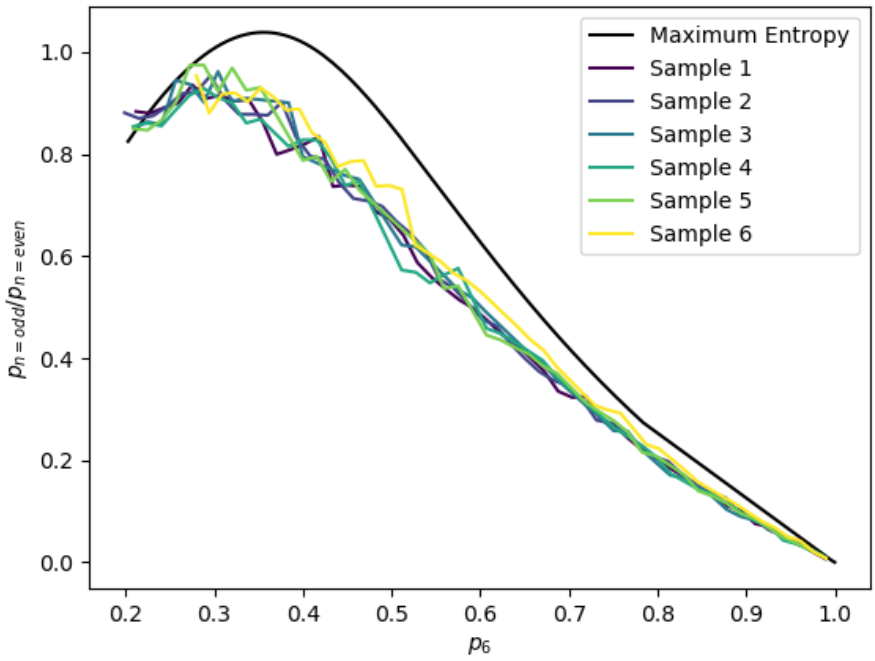

Figure 5.25: Even vs odd ring characteristics for different triangle raft samples

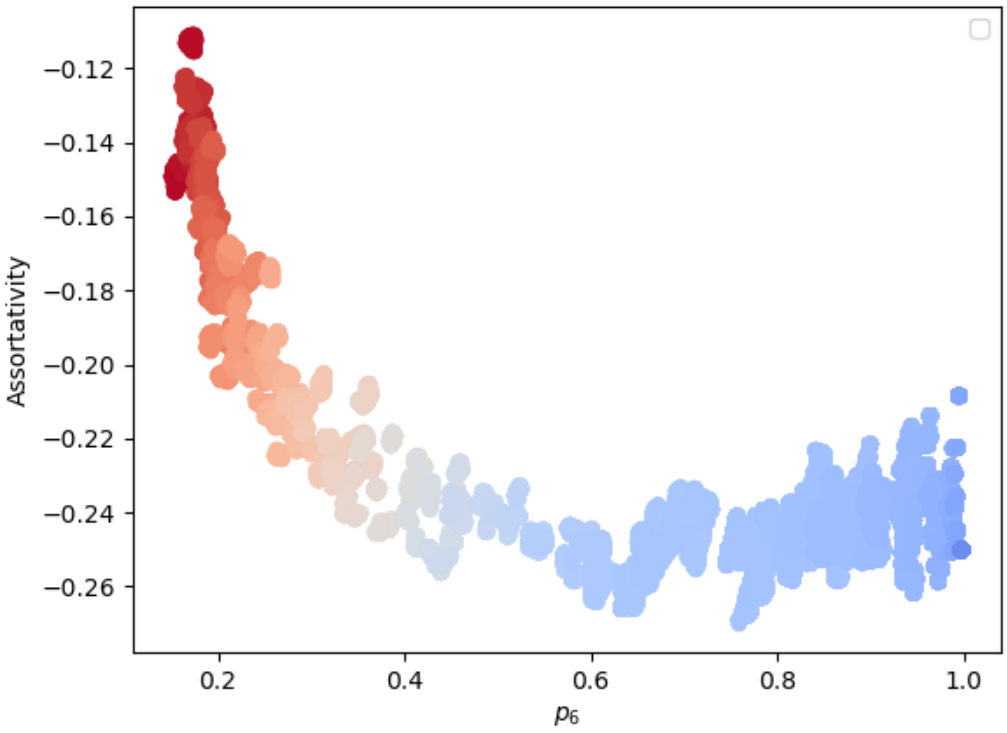

Figure 5.26: Assortativity across p_6 for a graphene system

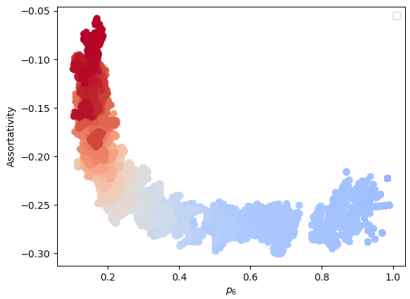

(a) Assortativity for $q = 0.1$ unit BN system

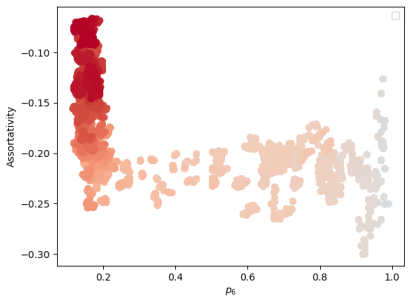

(b) Assortativity for $q = 2.0$ unit BN system

Figure 5.27: Assortativity for BN systems, given at different charges ($q = 0.1$, $q = 2.0$ units)

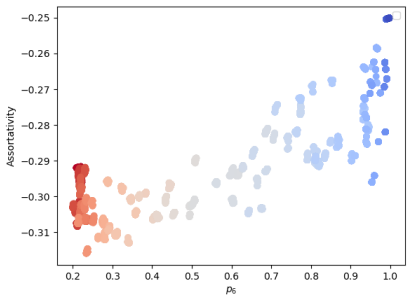

(a) Assortativity for triangle raft Sample 2

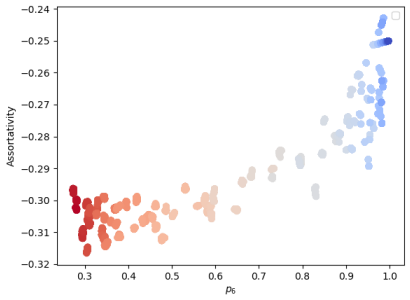

(b) Assortativity for triangle raft Sample 6

Figure 5.28: Assortativity for triangle raft structures (Sample 2, 6)

5.5.6 Energy as a function of disorder

The energy of the system is an interesting metric to understand the enthalpic effects of each potential model. We can visualise the energy of the network, U, as a function of p_6 or μ_2, as in Figure 5.29.

Taking graphene as an example, we can see that there is a non-linear correlation with p_6, which which it is difficult to pick out a quantifiable fit. However, visualising against μ_2 gives a good linear fit. This a novel finding, implying that the width of the ring distribution can be related directly to the energy, U, of the system. Our visualisation against p_6 gives us an energy against only variable, whereas μ_2 has an additional level of detail. One possible interpretation of this result can be

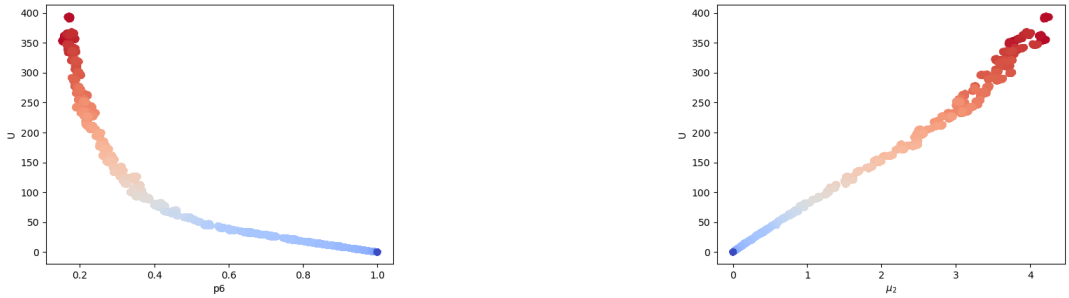

(a) **(b)**

Figure 5.29: Graphene energy as a function of p_6 (a) and system variance (b), in arbitrary units

derived from Figure 5.3 and our definition for μ_2,

$$\mu_2 = \sum_{4 \leq n \leq 12} (n-6)^2 p_n. \tag{5.5.6.1}$$

If we assume that the energy of a ring size n is independent of its surroundings, and is proportional to $(n-6)^2$ (which loosely fits our results in Figure 5.3), then the energy becomes

$$U = \sum_{4 \leq n \leq 12} \epsilon (n-6)^2 p_n = \epsilon \mu_2. \tag{5.5.6.2}$$

The assumption of this approach, that the energy of a ring is independent of its surroundings, is surprising, and there may be further refinement required to this interpretation. It is particularly surprising in light of the differing values for assortativity. It is worth noting that a potential of this form was introduced in by Aste and Sherrington in 1999 to as a means of quantifying the enthalpy cost of forming cells of a given shape, defined as the 'topological distance'[156] $E = \mu_2 N$. This energy function was defined only 'in the spirit of minimalism', but has since been used for later work on silica bilayers as an approximation to energy[157].

This empirical relationship also applies to the BN (Figure 5.30) and triangle raft methods (Figure 5.31). However, the correlation appears weaker, and only holds for BN up to $\mu \simeq 3$, beyond which it breaks down. The gradient of these functions varies with the potential model used, as shown in Table 5.3. We can see that all the triangle raft samples behave similarly to graphene except sample

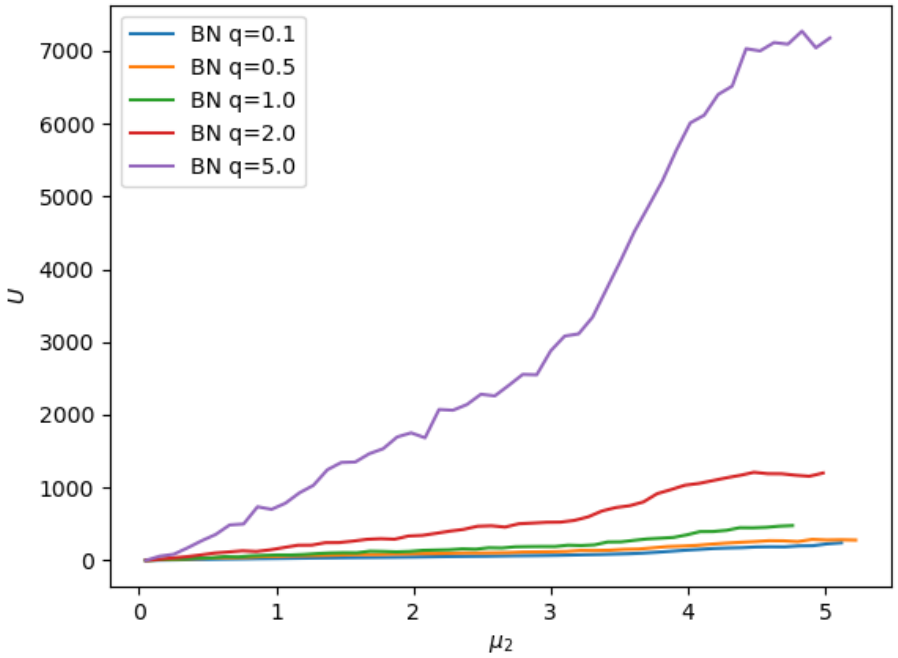

Figure 5.30: Energy, U, of BN systems as a function of system variance. Energy is in arbitrary units.

6, which has a significantly higher gradient. We can rationalise this by referring back to Figure 5.7, which shows significantly a higher energy of formation for four-membered rings. Given we have seen that our samples behave similarly with respect to ring distributions, this higher gradient can be traced back to the higher energy cost of forming the same proportion of four-membered rings as seen in the other samples. The gradient of the BN systems sit above the graphene system, and rise steeply with q, as might be expected from the formulation of the BN potential, which is effectively a graphene potential with repulsive charges overlaid, and so cannot reach lower energies than the graphene potential alone.

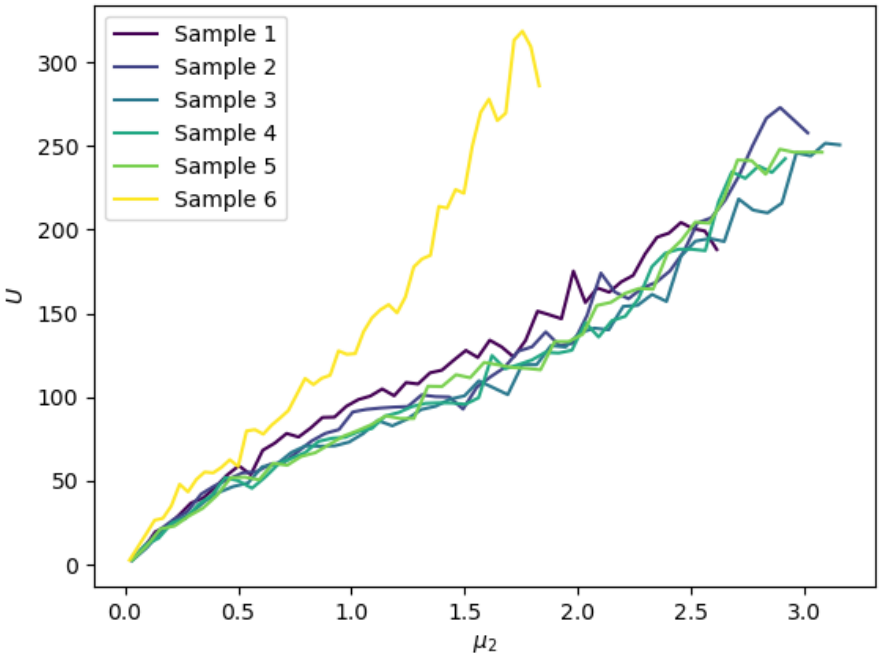

Figure 5.31: Energy, U, of Triangle Raft systems as a function of system variance. Energy is in arbitrary units.

5.5.7 Charge Based Interpretations

Work on large defects in triangle raft ring growth networks (Chapter **??**) has drawn comparisons between how such networks accommodate large rings, and similar profiles for charged fluids. As such, one potential avenue of research is by understanding a system of rings as a charged fluid. Here, we have used our significant structural database as a tool for evaluating the basis of this method; using ring size as a approximation to particle charge.

An electrostatic approach comes with the advantage of using well defined, static ring statistics, as each particle is assigned a charge at the start of the simulation, and the system can thermalised and quenched to different temperatures to achieve different levels of disorder. Alternatively, a switching method similar to that discussed in this Chapter, based on charges rather than connectivity, could also be applied. We learn from assortativity measurements that our the ring network node degree is disassortative, meaning that the systems have a preference for surrounding

System	Gradient	r^2
Graphene	0.0246	0.996
Triangle Raft Sample 1	0.0259	0.970
Triangle Raft Sample 2	0.02479	0.972
Triangle Raft Sample 3	0.0233	0.974
Triangle Raft Sample 4	0.0240	0.969
Triangle Raft Sample 5	0.0250	0.979
Triangle Raft Sample 6	0.0477	0.976
Boron Nitride $q = 0.10$	0.0294	0.991
Boron Nitride $q = 0.50$	0.0541	0.981
Boron Nitride $q = 1.00$	0.0847	0.993
Boron Nitride $q = 2.00$	0.2182	0.989
Boron Nitride $q = 5.00$	1.0882	0.976

Table 5.3: Gradient of linear regression fit to U/per node (arbitrary units) as a function of μ_2, within the range $\mu_2 < 3.0$

large rings with small rings, and vice versa, which fits well with our understanding of charged systems. For our work, the mean ring size is 6 (as determined by Euler's law, Section 3.2.2), and so the charges we assign to rings are centred about this value, in order to ensure the system is charge balanced. The charge of the particle representing a ring of size n becomes $q = n - 6$. Systems based on this construction are charge balanced, and charges are said to sit at the centre of mass of each ring. For our work, the sizes of the particles used is less important, as they will largely affect dynamics; we are interested more in understanding the stability of charged systems based on our structures of known disorder and energy, with the assumption that for the structures from our database, the particle overlap is zero.

The enthalpies of such systems are complicated by the nature of ring-ring interactions. As our systems rely on introducing defects into systems, each step of our simulations maintain charge balancing but do not maintain the ring distribution. Comparing between ring distributions, we can see that there is a strong correlation between system μ_2 and electrostatic energy, mirroring that of the harmonic systems (Section 5.5.6).

We expect a general negative trend with energy when we introduce charges into the system. This is because each SW defect introduced charges four particles (Figure 5.32). As such, if we examine the interaction between these new charges,

we see two repulsive like-charge interactions and four attractive unlike-charge interactions (Figure 5.33). In addition, the repulsive interactions act at greater distances, resulting in a significant energy decrease with each defect introduced. The effect of this decrease should be predictable towards the crystalline limit, with isolated defects having a reliable energy. However, as noted in Section 5.4.2, the minimisation dynamics differ between graphene and triangle raft models, resulting in differences between the energy introduced per defect in each potential model.

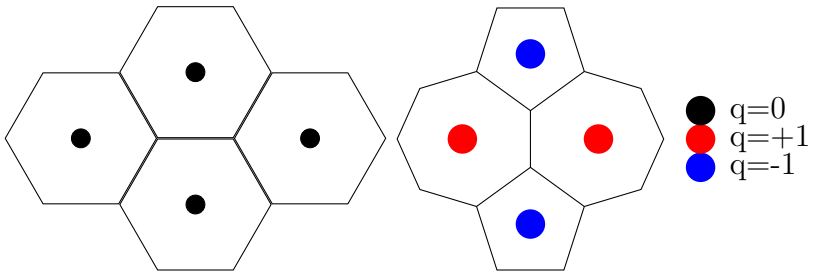

Figure 5.32: Graphic to show the effect of introducing a Stone Wales defect into a ideal hexagonal system on our charged approximation.

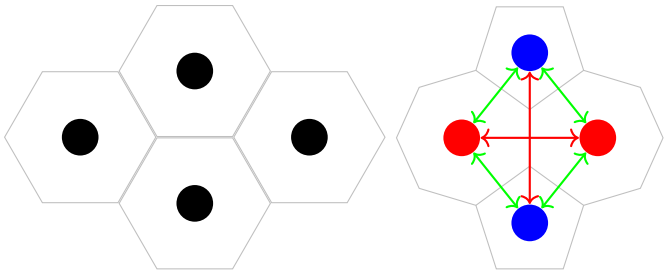

Figure 5.33: Graphic to show the effect of introducing a Stone Wales defect into a ideal hexagonal system on our charged approximation, with favourable electrostatic interactions shown in green, and unfavourable in red.

An notable result is the strong correlation of this energy with sample variance (Figure 5.35), which shows strong similarities to Figures 5.29 and 5.31 (reproduced with a line of best fit in Figure 5.34). In particular, it is surprising that the energy is independent of assortativity, which varies significantly with μ_2. We can assume that the correlation follows the empirical Equation 5.5.6.1, although there is no *ab initio* reason why this may be. Electrostatic energies show a good correlation with the harmonic energy (Figure 5.36), indicating that this approach has promise as an alternative method for modelling disordered ring networks.

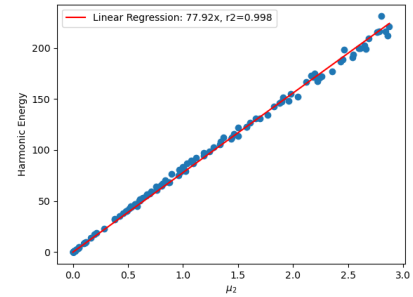

(a) Graphene

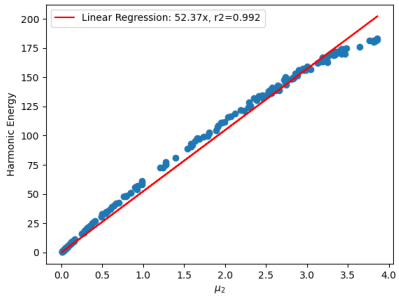

(b) Triangle Raft

Figure 5.34: Harmonic energy as a function of μ_2, fitted to linear regression for graphene (a) and triangle raft (b). Energy units are arbitrary.

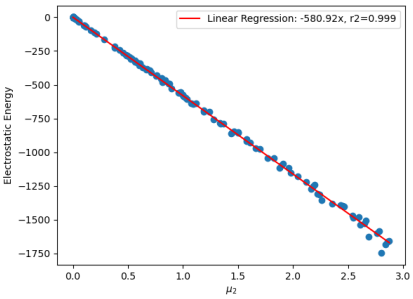

(a) Graphene

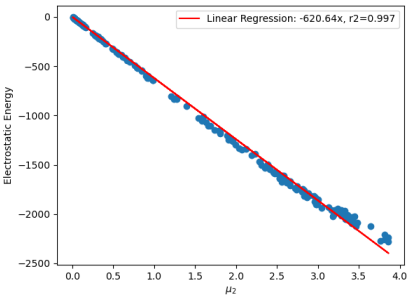

(b) Triangle Raft

Figure 5.35: Electrostatic energy as a function of μ_2, fitted to linear regression for graphene (a) and triangle raft (b). Energy units are arbitrary.

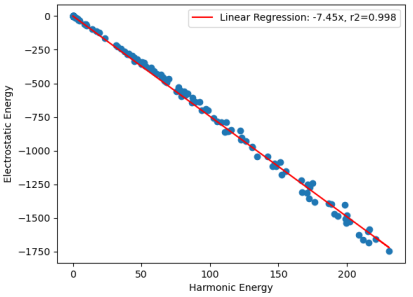

(a) Graphene

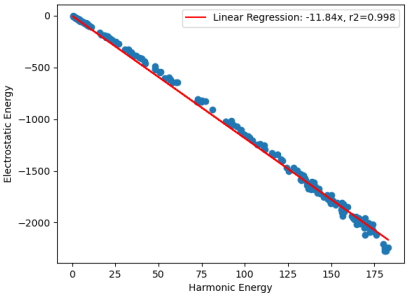

(b) Triangle Raft

Figure 5.36: Electrostatic energy as a function of harmonic energy, fitted to linear regression for graphene (a) and triangle raft (b). Energy units are arbitrary.

A complete electrostatic model would need further method development, in particular surrounding particle size effects, and efforts to reconstruct a network from charged particle positions. As such, for our systems, the electrostatic-only equivalent systems are generated and evaluated, with an understanding that this would be only one part of a more complicated potential model for such systems.

5.6 Comparison to experimental silica bilayer structures

Its has been shown that triangle raft methods can approximate the ring structures seen in amorphised silica systems[134, 158]. Using a range of parameters, we have been able to generate samples which resemble experimental structures.

The seven samples we will be using for comparison are seen in Table 5.4, with summaries of their ring and network statistics. These experimental ring distributions are derived from experimental images, as referenced in the table. As direct imaging give refined silicon atom positions, connectivity is inferred from nearest-neighbour relations, from which a network can be established. However, this is an intensive process, and has high resolution requirements for the experimental data. As such, we have fewer amorphous samples, and they encompass lower areas than crystalline samples, which are easier to identify at lower resolution because of their higher symmetry. This limits the extent to which we can rigorously test our models. In particular, the samples collected often do not conform to our mean ring size expectations, $\langle n \rangle = 6$. This is a result of the limited size of our samples, and can complicate our comparisons as the samples cannot be said to be 'complete'. The ring statistics of the experimental samples are compared to the maximum entropy distributions directly in Figure 5.37, at the p_6 value of the experimental sample.

As each sample is unique, it is difficult to determine overarching trends from ring distributions alone. We can, however, see two general trends across these samples. The first is that there are discrepancies between the maximum entropy solution, and the second is that there are consistently more 4-membered rings than would be expected from the maximum entropy solution. We can investigate general differences between the samples and the maximum entropy distribution using Lemaître's law, as in Figure 5.38.

All of the experimental samples sit above the Lemaître's law curve, with the extent to which they deviate varying significantly between samples. Comparing to our triangle raft simulation results (Figure 5.38b), we can see that some of the

	p4	p5	p6	p7	p8	p9	p10	$\langle n \rangle$	μ_2	α
Exp. sample (a) [Sample A[4]]	0.04	0.27	0.42	0.21	0.05	0.01	0.002	6.00	0.94	0.33
Exp. sample (b) [Sample C[6]]	0.04	0.28	0.45	0.16	0.07	0.01	0	5.97	0.94	0.36
Exp. sample (c) [Sample A[6]]	0.04	0.29	0.47	0.10	0.10	0	0	5.94	0.95	0.31
Exp. sample (d) [Sample B[6]]	0.08	0.25	0.42	0.20	0.03	0.03	0	5.95	1.15	0.36
Exp. sample (e) [Sample B[4]]	0.03	0.26	0.45	0.20	0.04	0.004	0.002	5.98	0.84	0.30
Exp. sample (f) [159]	0.0379	0.2744	0.4448	0.1609	0.0757	0.0063	0.0	unknown	0.946	0.32
Exp. sample (g) [4]	0.0383	0.2725	0.4189	0.2117	0.0495	0.0068	0.0023	6.00	0.933	0.33

Table 5.4: Experimental Sample Data

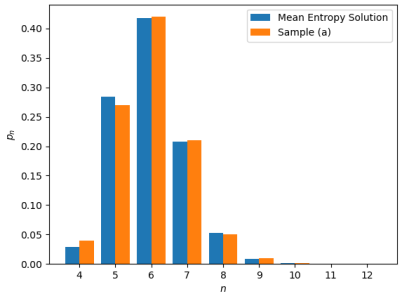

(a) Sample (a)

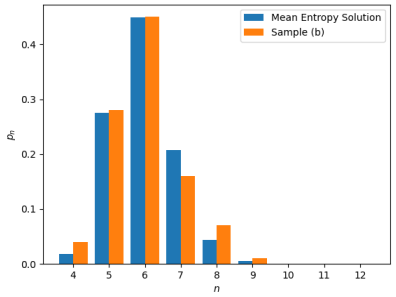

(b) Sample (b)

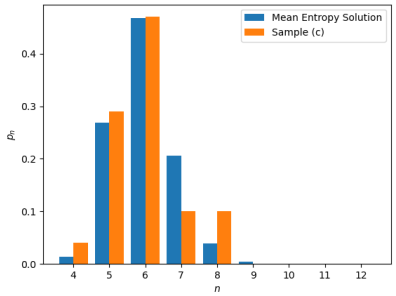

(c) Sample (c)

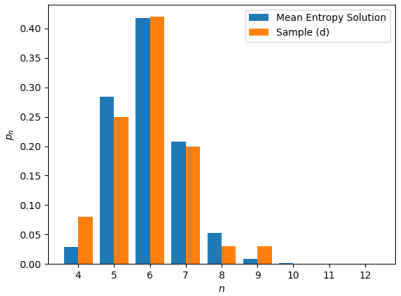

(d) Sample (d)

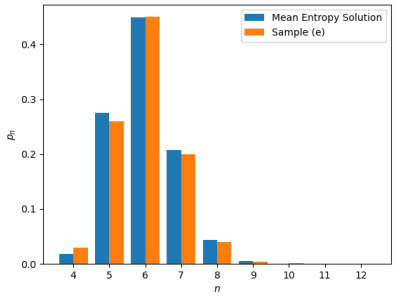

(e) Sample (e)

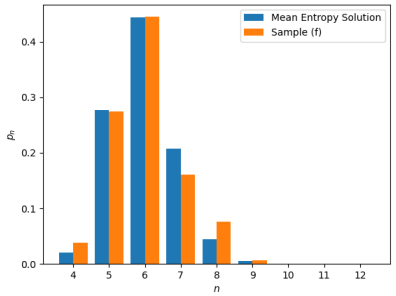

(f) Sample (f)

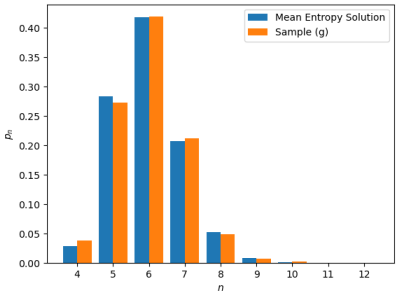

(g) Sample (g)

Figure 5.37: Comparison of experimental samples (a-g) to maximum entropy solutions at the sample p_6

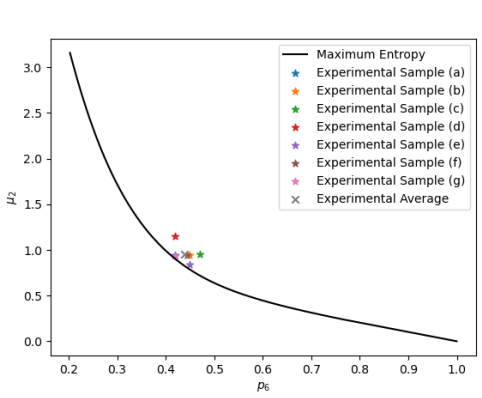

(a) Experimental samples compared to Lemaître's law

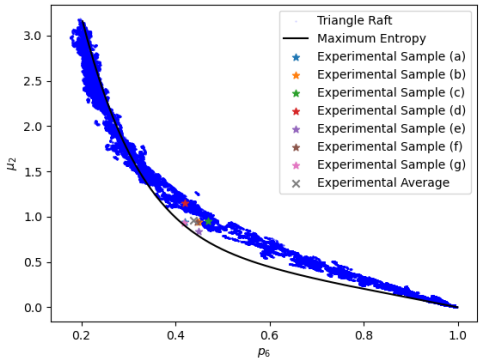

(b) Experimental samples compared to Lemaître's law, with triangle raft samples overlaid in blue

Figure 5.38: Experimental samples compared to Lemaître's law, with triangle raft simulations provided for comparison

experimental results fit well within the range of our simulations, with others sitting between the maximum entropy curve and our triangle raft simulations.

Having identified the relative predominance of 4-membered rings as a key difference between our experimental samples and the maximum entropy distributions, we need to find a metric to quantify this. At a given p_6, $2p_4 + p_5$ must be constant, in order to maintain the mean ring size, $\langle n \rangle = 6$. As such, we can visualise p_4/p_5 as a metric to understand the relative predominance of 4 relative to 5 membered rings. Figure 5.39 shows that all experimental samples have a higher proportion of 4-membered rings than the maximum entropy solution, as expected from the ring statistics in Figure 5.38. Our simulation results in (b) show an even greater proportion of 4-membered rings, with one experimental sample (Sample d) within the range, and all others lying between the maximum entropy solution and our triangle raft methods.

This indicates potential for our models as predictors for experimental results. In particular, adding the additional degree of freedom on moving from a triangle raft structure to simulating a full bilayer may further refine our models towards experimental results, although such simulations are significantly more computationally demanding, and so are beyond the scope of this work.

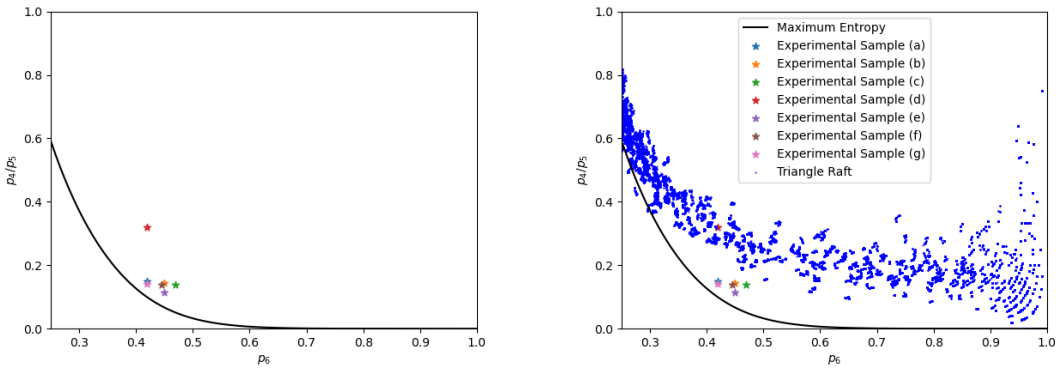

Figure 5.39: Relative predominance of 4 compared to 5 membered rings, with simulation results for comparison

Previous work[124] has shown that, for ring growth methods, triangle raft networks systems well approximated the Aboav-Weaire parameters for experimental structures, and provide similar ring statistics. However, the formation mechanism of formation for ring growth systems in previous work is significantly different from the methods discussed above, reliant on a non-equilibrium MC simulation with local energy minimisation, as compared to our equilibrium MC with global energy minimisation. Figure 5.40 shows Aboav-Weaire coefficients for all triangle raft networks, showing values lower than expected from ring growth methods and experimental results, but in line with other simulations[154]. This is an indication our simulations result in too little structural ordering, which is an interesting investigation for future work. As noted in [124], increasing the bond force constant increases the disassortativity of the network. It is likely that the difference in our simulation is that our potential model relies on $12-6$ Lennard-Jones repulsive terms, whereas previous work[134] has used steeper $24-12$ repulsive terms, which are not readily available in LAMMPS. Whilst for the Keating potential investigated in [124] allows for clear delineation of the angle and bond force constants, triangle raft methods operate by a different mechanism, with both angle and bond length constraints imposed by a combination of the rigid triangle rafts and the short range repulsive terms. As such, changing the short range repulsive potential has an unknown effect on the balance of angle and bond potentials. Scaling the repulsive

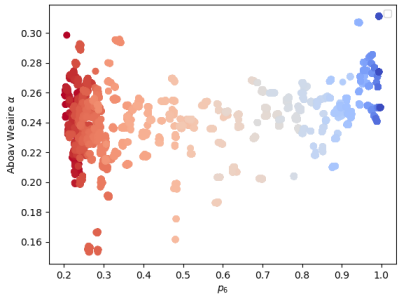

(a) Aboav-Weaire coefficient for triangle raft Sample 1

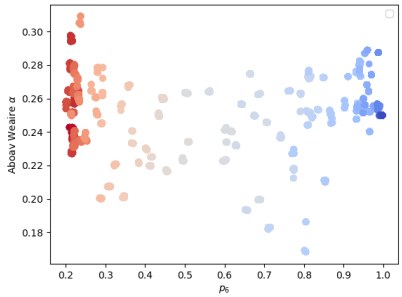

(b) Aboav-Weaire coefficient for triangle raft Sample 2

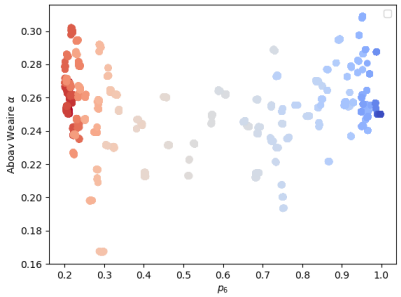

(c) Aboav-Weaire coefficient for triangle raft Sample 3

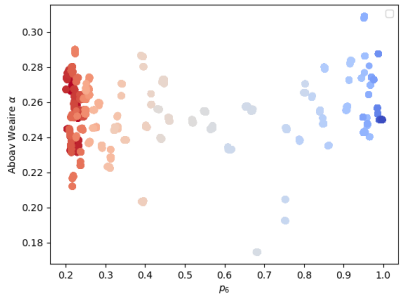

(d) Aboav-Weaire coefficient for triangle raft Sample 4

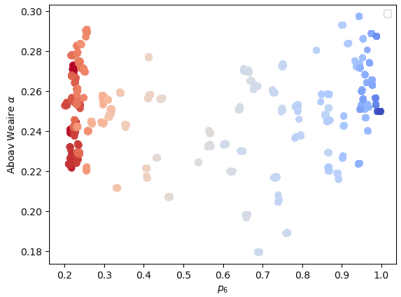

(e) Aboav-Weaire coefficient for triangle raft Sample 5

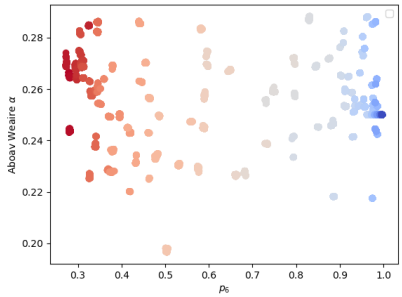

(f) Aboav-Weaire coefficient for triangle raft Sample 6

Figure 5.40: Aboav-Weaire coefficients for triangle raft Samples 1-6

terms to better resemble the stiffer $24 - 12$ terms would likely have the effect of bringing increasing the disassortativity within the experimental range, but further parameter testing in this vein is beyond the scope of this thesis.

5.7 Conclusions

We have established three models for potential energy for work in this thesis, and matched them to physical systems. For each, we have evaluated their computational tractability and adapted our approach accordingly, minimising across the whole periodic cell system. Using these potentials, we have generated systems across a range of disorder, from $0.2 \lesssim p_6 \leq 1.0$, and analysed the resulting structures. The metrics we have used include standard measurements of maximum entropy distributions and local ordering parameters, alongside system-specific metrics to understand in more detail the effect of our potentials on the systems they generate. We have demonstrated capability of biasing systems (*e.g.* BN) towards a lower proportion of odd membered rings, and noted that triangle raft networks exhibit a noticeable bias towards even membered rings, likely as a result of the bridging oxygen atoms. Evaluating the energy of our systems showed good linear correlation with the ring distribution variance, μ_2, for all systems (within the range $0 \leq \mu_2 \leq 3$). A novel interpretation of the system, which understands the systems of rings as a charged fluid, has been proposed, with single point energy calculations conducted on the basis of ions sited at the centre of mass of each ring, with charge equal to $q = (n - \langle n \rangle)$. The energies produced also form a strong linear correlation with μ_2.

Finally, we have made explicit comparison of our amorphous triangle raft systems to experimental silica bilayer distributions, noting that experimental samples tend to sit above the Lemaître curve, in part as a result of a greater proportion of 4-membered rings. The triangle raft systems show similar trends, however the assortativities are lower than expected.

6
Biological Networks

Contents

6.1 Motivation

The networks generated as described in Chapter 5 have a myriad of potential uses for modelling physically realisable networks. An example of such a network is the cell structure of the corneal endothelium, a collagen network in the eye. These biological networks are important in understanding and predicting the changes in the networks in the eye with various external factors (diabetes, age, contact lens use), to determine their influences on eye health. The metrics generated from the experimental data were evaluated, and comparable metrics are collected from our networks to compare with experimental data.

6.2 The network structure of the corneal endothelium

The Journal of Chemical Physics

RESEARCH ARTICLE | FEBRUARY 03 2023

The network structure of the corneal endothelium

Bryan Xuan ; Oliver Whitaker ; Mark Wilson

J. Chem. Phys. 158, 055101 (2023)
https://doi.org/10.1063/5.0134667

The Journal of Chemical Physics ARTICLE scitation.org/journal/jcp

The network structure of the corneal endothelium

Cite as: J. Chem. Phys. 158, 055101 (2023); doi: 10.1063/5.0134667
Submitted: 12 November 2022 • Accepted: 29 December 2022 •
Published Online: 3 February 2023

Bryan Xuan, Oliver Whitaker, and Mark Wilson[a)]

AFFILIATIONS

Department of Chemistry, Physical and Theoretical Chemistry Laboratory, University of Oxford, South Parks Road, Oxford OX1 3QZ, United Kingdom

[a)]Author to whom correspondence should be addressed: mark.wilson@chem.ox.ac.uk

ABSTRACT

A generic network model is applied to study the structure of the mammalian corneal endothelium. The model has been shown to reproduce the network properties of a wide range of systems, from low-dimensional inorganic glasses to colloidal nanoparticles deposited on a surface. Available extensive experimental microscopy results are analyzed and combined to highlight the behavior of two key metrics, the fraction of hexagonal rings (p_6) and the coefficient of variation of the area. Their behavior is analyzed as a function of patient age, the onset of diabetes, and contact lens wearing status. Wearing contact lenses for ~10 years is shown to change the endothelium structure by the equivalent of ~30 years contact lens-free. Model network configurations are obtained using a Monte Carlo bond-switching algorithm, with the resulting topologies controlled by two potential model parameters (the bond and angular force constants) and the Monte Carlo temperature. The effect of systematically varying these parameters is investigated. In addition, the effect of constraining the ring size distribution is investigated. The networks generated with relatively weak bond force constants are shown to correlate best with the experimental information. The importance of extracting the full ring size distribution (rather than simply the fraction of hexagons) is discussed.

I. INTRODUCTION

The cornea is a transparent avascular membrane comprised mainly of collagen molecules which form the anterior section of the eye.[1,2] The membrane forms a crucial barrier to both infection and structural damage and is constructed from five distinct layers. In this paper, we are concerned with one of these layers, the corneal endothelium, which can be readily imaged and which adopts a honeycomb-like structure. Such structures are common across a range of systems, from the atomic level of ultra-thin materials[3–5] through colloids,[6,7] foams,[8,9] and epithelial cells,[10,11] all the way to geological rock formations.[12] The maturing of network science as a field has led to new ways of thinking about and quantifying complex networks,[13] driven largely by interest in abstract networks such as the internet or social media.[14,15] The corneal endothelium is potentially another example of such a network. At a fundamental level, the endothelium structures (as well as those systems listed above) appear to map onto a percolating network of rings or, equivalently, to an array of connected nodes, and hence they are governed by the same fundamental laws. For the percolating ring network description, for example, the structure can be characterized (at one level) by determining the number of rings of different sizes, where the ring size corresponds to the number of edges in each ring. In addition, the areas of the rings can be measured, and their deviation from ideal regular polygons can be quantified, for example, by determining the coefficient of variation (CV) of the area. Experimental evidence suggests that the structure of the corneal endothelium is affected not only by aging[16–26] but also by other factors, such as the onset of diabetes,[27–30] smoking status,[31] or the prolonged wearing of contact lenses.[32–35] The most common network properties, which are tracked experimentally, are the cell density, the distribution of ring sizes (cellular polymegethism), and the distribution of the areas of those rings, in particular distortions away from their ideal (symmetric) shapes (cellular pleomorphism). These systems may show additional structural complexity. The rings in a given ring size distribution may be arranged in an effectively infinite number of ways. For chemical systems, it is intuitive that some configurations would be expected to be energetically favorable. For example, at the nearest-neighbor length scale, it is reasonable to assume that large rings will tend to be located next to small rings. It is also likely that structural ordering may persist beyond the nearest-neighbor length scale.

In this paper, we aim to make connections between the experimental information available for the corneal endothelium structure and network theory to demonstrate how better to quantify their structure, thus allowing connections to be made to a wide

range of related systems. The connections made may help rationalize some experimental observations, for example, by quantifying how corneal damage from non-aging mechanisms correlates with that resulting from aging alone. In addition, the construction of model networks allows insight into any ordering of the rings, which may be quantified again by reference to network theory using assortativity.[36–38]

The outline for this paper is as follows: In Sec. II, the background to the required network theory is summarized. In Sec. III, the methods used will be discussed. Section IV will contain the results, dividing into the analysis of the experimental information, the construction and analysis of model networks, and finally a discussion of the links between the two. Finally, conclusions will be drawn.

II. BACKGROUND

The network topology is described by Euler's formula, $N + V - E = \chi$, where N, V, and E are the number of rings, vertices, and edges, and χ is the so-called Euler characteristic, which depends on the global topology of the system. Consider a network constructed from nodes with a range of coordination numbers, c, with the fraction of each given by x_c. As a result, the mean coordination number is $\langle c\rangle = \sum_c c x_c$. The number of edges is then $E = \frac{V}{2}\langle c\rangle$ and the mean ring size is $\langle k\rangle = \frac{V}{N}\langle c\rangle$. Euler's formula may then be rewritten as

$$\langle k\rangle = \frac{2\langle c\rangle\left(1 - \frac{\chi}{N}\right)}{\langle c\rangle}. \tag{1}$$

As a result, for $\langle c\rangle = 3$ (nodes of degree three) and $\chi = 0$ (corresponding to an infinite plane), the mean ring size, $\langle k\rangle = 6$.

The next level of available information is given by the ring size distribution, p_k (the distribution of different ring sizes in a given network). Lemaître *et al.* demonstrated how many three-coordinate networks can be described by a maximum entropy distribution.[39] In summary, the entropy of the probability distribution is $S = -\sum_k p_k \log p_k$, and the system is subject to three constraints; $\sum_k p_k = 1$, $\sum_k k p_k = \langle k\rangle$, and $\sum_k \frac{p_k}{k}$ = constant. The first two constraints correspond to the distribution being normalized and the requirement of a fixed mean ring size. The third constraint is a little more mysterious and was originally justified by the ring areas, although it can be fully justified by considering the ring adjacencies.[40] As a result, the distribution can be summarized through the variance, $\mu_2 = \langle k^2\rangle - \langle k\rangle^2$, and the plot of μ_2 vs p_6 is known as Lemaître's law.

For a more constrained system of three types of rings, $k = \{5, 6, \text{and } 7\}$ only, the constraint that $\langle k\rangle = 6$ requires that $p_5 = p_7$, and so,

$$\begin{aligned}\mu_2 &= \sum_{k=5}^{7} k^2 p_k - \left\{\sum_{k=5}^{7} k p_k\right\}^2 = \sum_{k=5}^{7} k^2 p_k - 36 \\ &= 5^2 p_5 + 6^2 p_6 + 7^2 p_7 - 36 = 74 p_5 + 36 p_6 - 36. \end{aligned} \tag{2}$$

The distribution given by p_k is normalized such that $p_5 + p_6 + p_7 = 1$, and so $2p_5 = 1 - p_6$. As a result,

$$\mu_2 = 37(1 - p_6) + 36 p_6 - 36 = 1 - p_6. \tag{3}$$

In this case, therefore, the Lemaître curve is simply linear at p_6, and a single measurement of p_6 fully defines the ring size distribution, *including* the precise number of 5- and 7-membered rings.

For a less constrained distribution, in which both smaller and larger rings are permitted, μ_2 may become larger and depend on p_6 in a non-linear fashion. Again, however, if the ring sizes follow a maximum entropy distribution, then measuring p_6 alone still fully defines the fractions of the remaining ring sizes, $p_{k'}(k' \neq 6)$. Configurations that do not sit on the Lemaître curve may do so either because of a finite system size effect or because the ring size distribution does not reflect the maximum entropy solution (i.e., enthalpic effects are significant). It is worth noting that not all ring size distributions fit on this curve. The most obvious examples are (ordered) crystalline networks, such as the complete tiling of space by $\{4-, 8-\}$membered or $\{3-, 12-\}$membered rings, respectively (see Ref. 41 and references therein). Recent work has shown how so-called procrystalline structures, in which sites on an ordered lattice are linked by a disordered array of bonds, may also "violate" Lemaître's law.[42]

The ring size distribution does, however, give an incomplete picture of the overall network structure. The rings in a given distribution may be arranged in an arbitrarily (infinite) number of ways. It is, however, physically reasonable to assume that some configurations will be energetically favored over others. For example, large rings should tend to be nearest-neighbors to small rings. For systems with chemical bonds, the background to this behavior is clear, as the relatively obtuse bond angles associated with larger rings need to be "offset" by the more acute angles associated with smaller rings in order to avoid significantly strained bonds and/or angles. The magnitude of any such nearest-neighbor ordering can be quantified. Historically, the mean ring size around a given ring was determined, leading to the Aboav–Weaire law.[43,44] In that case, the degree of association is characterized by a single parameter (usually given the symbol α). However, the limits of this parameter are unclear, and obtaining it requires a linear fit (which may not be appropriate) and is heavily dependent upon (potentially small numbers) of small and/or large rings.[45] Furthermore, the parameter is not zero for a totally disordered network. An alternative metric is the assortativity, r, commonly employed in network theory and which has clear limits (of ± 1), a value of $r = -1$ corresponding, for example, to a fully disassortative network.[36] In the present work, we shall refer exclusively to assortativity.

III. METHODS

The chosen method for generating randomized ring size distributions is via a bond-switching algorithm, a Monte Carlo stochastic sampling approach originally developed by Wooten, Winer, and Weaire to generate models for silica glass in three dimensions.[46] Analogous approaches have been employed for 3-coordinate and, in one instance, 4-coordinate planar atomic systems.[47,48] In the present work, the starting configuration is an ideal hexagonal net (equivalent to a graphene sheet or a honeycomb). To amorphize the network, links between neighboring nodes are switched, and the change in potential energy of the system is calculated. The potential energy is a relatively simple function of the atom positions. Incorporating switches, which reduce the network potential energy with greater probability, biases the search toward low-energy networks. The original hexagonal lattice is thermalized using a large number of random

bond switches to generate a random network with high energy that has no "memory" of the original ordered lattice. The system is then annealed at a finite temperature, T, by accepting moves according to the Metropolis criterion,[49]

$$P = \min\left[1, e^{-\Delta U/k_B T}\right]. \quad (4)$$

ΔU is the change in energy resulting from the proposed move. The net effect will be to accept more moves, which reduce the system energy and hence generate a physically acceptable network structure.

The bond-switching move (known as a T1 switch[50] or, more recently, as a Stone–Wales defect[51]) augments the ring size of two rings and decrements two others, preserving the mean ring size.

The system energy is determined using a specified potential model; here, a simplified two-dimensional version of the Keating potential[52] augmented with a restricted bending (ReB) potential[53] of the form

$$U = \sum_{i,j\in\text{bonds}} \frac{k_r(r_{ij} - r_0)^2}{2} + \sum_{i,j,k\in\text{angles}} \frac{k_\theta\left(\cos\theta_{ijk} - \cos\theta_0\right)^2}{f\left(\theta_{ijk}\right)}, \quad (5)$$

where r_0 is the equilibrium separation between neighboring nodes and θ_0 is the equilibrium angle between pairs of neighboring nodes, and k_r and k_θ are the respective bond and angle force constants, which control the relative magnitudes of the bond length and angular components of the total potential energy. The equilibrium bond length was set equal for all interaction types, and the equilibrium angles were set to $2\pi/3$ radians, appropriate for the three-coordinate nodes. The function $f\left(\theta_{ijk}\right) = 2\sin^2\theta_{ijk}$ for the ReB potential [setting $f\left(\theta_{ijk}\right) = 1$ recovers the simplified Keating potential]. The ReB angle potential maintains ring convexity. The addition of the sine term in the denominator causes the potential to diverge as bond angles approach linearity and so prevents the bond pairs from "inverting." The rationale for choosing the relatively simple potential of this form is that a key aim is to obtain results for generic systems that capture the essential physics while remaining computationally tractable to allow a high-throughput approach. The simplicity of the chosen potential model means that the network topology and the shape of the contributing rings are controlled by just three parameters, the bond length and angle force constants (k_r and k_θ, respectively), and the system temperature, T. In fact, the system is further constrained in the sense that the energy scale imposed by the choice of force constants is linked to the available thermal energy. Put simply, increasing the force constants can be "offset" by increasing the temperature. As a result, the key network properties can be systematically varied by varying, say, k_r, the ratio k_θ/k_r and T. The expectation would be that varying the ratio k_θ/k_r could help transform the system from one, which is more like atomic material (i.e., length dominated) to a foam (angle dominated). For example, Wooten *et al.* suggested values for k_θ/k_r of 0.2[54] and 0.285,[46] respectively, to study amorphous Si and Ge while Martin investigated the properties of a range of ZnS structure semiconductors, using $k_\theta/k_r = 0.294$–0.079,[55] and Kumar *et al.* modeled amorphous graphene with $k_\theta/k_r = 0.2$.[56] k_r and k_θ are systematically varied with $k_r = \{0.010.10.2, 0.4, 0.6, 0.8, 1.0\}$ and $k_\theta = \{0.1, 0.15, 0.2, 0.25, 0.3\}$. As an additional control, the range of rings "allowed" to form is varied, with three systems considered. In the first, the ring sizes are unconstrained, while in the other two, the ring sizes are constrained to be between 5- and 7-membered and 4- and 8-membered (termed $\{567\}$ and $\{45\,678\}$, respectively).

IV. RESULTS

A key motivation in the present work is an attempt to link state-of-the-art models and techniques to existing experimental results. As a result, Sec. IV A will present a survey of the available experimental data, focusing on the key extracted topological parameters and highlighting any possible trends. Section IV B will focus on the simulation model results and how these may relate back to the experimental data.

A. Interpretation of the experimental data

The most common experimental data presented are in the form of the fraction of hexagons, p_6, less commonly given with a more complete analysis of the ring size distribution, the ring areas, and the coefficient of variation (CV) of the area, $CV = \sigma_A/\bar{A}$, where σ_A and $\bar{A}$ are the standard deviation and mean area, respectively.

1. Trends in p_6

Figure 1(a) shows a schematic to highlight the range of p_6 values obtained from the experiment. The data are subdivided into those obtained as a function of patient age,[16–26] contact lens usage,[32–35] onset of diabetes,[27–30] and "other" [here, covering smoking behavior, non-human species (here, dogs, rabbits, and mice), and the behavior of transplanted tissue[22,31,57–61]]. A large spread of p_6 values is obtained, ranging from $p_6 \sim 0.36$–0.88. The most significant factor affecting p_6 appears to be aging ($p_6 \sim 0.39$–0.88). The wearing of contact lenses and diabetes show a similar, but smaller, range ($p_6 \sim 0.54$–0.71 and $p_6 \sim 0.52$–0.68, respectively). The points labeled "other" cover the range $p_6 \sim 0.36$–0.83.

As discussed in the introduction, a range of different systems show this type of ring structure and display different ranges of values for p_6.[40] For example, colloidal nanoparticles distributed on a surface show $p_6 \sim 0.35$–0.69 depending on the packing fraction, while thin layers of silica and graphene show $p_6 \sim 0.42$–0.46 and ~ 0.55–0.95, respectively. For reference, the Poisson–Voronoi limit, which corresponds to a random distribution of points on a surface (or, equivalently, the limit as the packing fraction of the colloids on a surface tends to zero), corresponds to $p_6 \sim 0.295$. Even more extreme distributions can be obtained by considering, for example, geographical entities, such as county boundaries of political constituencies, which show relatively low values of p_6 ($p_6 \sim 0.21$–0.28).[40] Figure 1(b) shows the spread of experimentally determined p_6 values on a Lemaître curve (a plot of the standard deviation of the ring size distribution, μ_2, against p_6) *assuming* the presence of 5-, 6-, and 7-membered rings only (which, recall from Sec. II, imposes a *linear* relationship of $\mu_2 = 1 - p_6$). The figure also shows the ideal Lemaître curve obtained from the maximum entropy solution for an unconstrained ring size distribution. The ideal curve is linear for $p_6 \gtrsim 0.6$, for which the networks are dominated by 5-, 6-, and 7-membered rings only. The curve deviates from linearity for $p_6 \lesssim 0.6$, as the networks contain a broader range of ring sizes.

Experimental data obtained as a function of patient age are shown in Fig. 2(a). The data are subdivided by the nation of

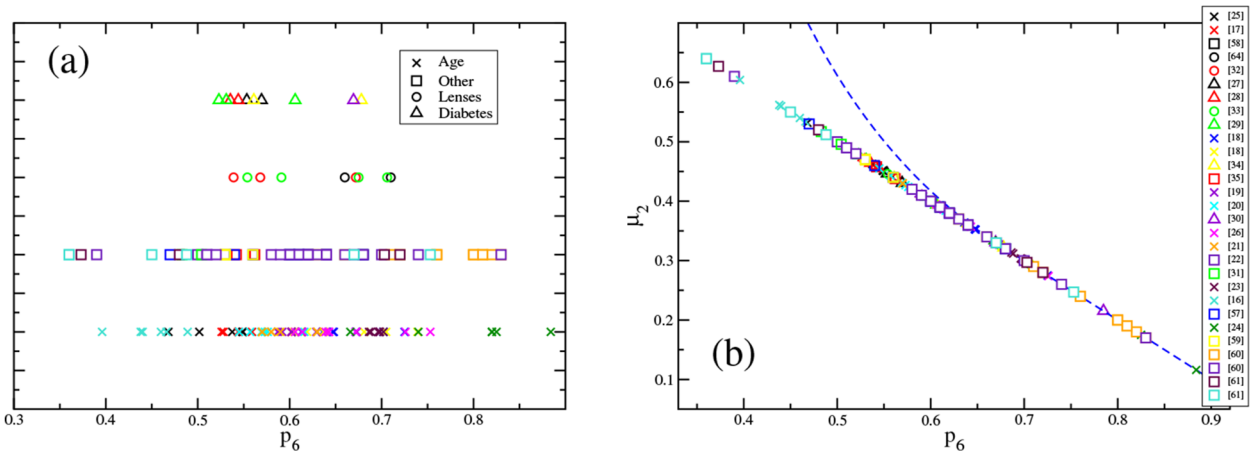

FIG. 1. Alternative views of the experimental observations of the fraction of hexagons, p_6, in the corneal endothelium. In panel (a), the data are subdivided in terms of patient age (×), contact lens wearing (○), diabetic status (△) and "other" (□)—see text. The four divisions are offset along the ordinate axis for clarity. In panel (b), the same data are shown on a Lemaître curve showing the variance, μ_2, assuming a constrained system containing only 5-, 6-, and 7-membered rings (giving $\mu_2 = 1 - p_6$). The dashed line shows the maximum entropy solution, assuming an unconstrained ring size distribution. The respective references are shown in the legend and apply to both panels.

origin of the patient, with the published standard deviations shown as error bars.[16–22,25,62,63] In the majority of cases, the fraction of six-membered rings decreases as a function of time (and this is the over-arching trend in all cases). The aging of the network appears to be correlated with its degradation away from an ideal hexagonal network. The figure also highlights the mean average curve, calculated as a simple unweighted average of all the data shown. The mean shows a steady decline in p_6 to $t \sim 35$ years, followed by a leveling off. One possibility is that this corresponds to the value of p_6 below which rings of sizes other than 5-, 6-, and 7-membered are required [which would correspond to the value at which the Lemaître curve shown in Fig. 1(b) deviates from the linear constrained maximum entropy solution].

Figure 2(b) shows additional data to that shown in panel (a) obtained for mice over their lifespan.[22] In order to allow comparison with the data obtained for humans, the abscissa are normalized by the approximate lifespans (taken as $t_{\text{lifespan}} \sim 80$ years for humans and ~2.5 years for mice, respectively). The data obtained from mice show a reduction in p_6 at long times ($t/t_{\text{lifespan}} \gtrapprox 0.1$) but show a rise at short times, corresponding to the continued eye development in mice *post partum*. The implication is that the networks degrade relatively little over the lifespan of the animal, and the rate of change is related to the animal lifespan (and hence metabolic rate).

Figure 2(c) shows the result of an attempt to generate a "universal" curve for the change in p_6 with age. Each experimental data are normalized such that $p_6 = 1$ at $t \to 0$, corresponding to starting from an ideal hexagonal net. p_6 shows a near-linear decrease to a reduced age of $t_{red} \sim 0.4$ (corresponding to $t \sim 32$ years in humans) with a gradient $dp_6/dt \sim -0.0046$ year^{-1}. Beyond this age, some groups show a further (slower) decrease in p_6, while others appear to have reached a limiting value.

In addition to the passage of time, external factors such as contact lens wearing, smoking status, or the onset of diabetes may affect cornea endothelium structure. Figure 3(a), for example, shows the mean average temporal behavior of p_6 on aging [from Fig. 2(a)] compared to two studies in which the effect of contact lens wearing is investigated.[32,33] In both cases, the fraction of hexagonal cells is determined as a function of the period for which the lenses have been worn. Lee *et al.*[33] studied the effect of wearing soft contact lenses in the age group $t \sim 25$–31 years with between zero and $\Delta t \sim 14$ years of continual wear, while Chang *et al.*[32] considered a group in the age range $t \sim 23.6$–27.0 years with between zero and 8.3 years wear. In both cases, the fraction of hexagons appears to decrease significantly over a ten year time-scale. For context, Fig. 3(b) shows the same data displaced along the time axis by the mean age of the participants and compared to the mean average behavior of the aging data from Fig. 2(a). It is clear that the fraction of six-membered rings falls more rapidly for contact lens wearers when compared with the aging process alone. To quantify the effect, a simple linear fit to the whole datasets produces rates of change of $dp_6/dt = -0.0113$ and -0.0152 year^{-1} for the data of Lee *et al.*[33] and Chang *et al.*,[32] respectively, compared with $dp_6/dt = -0.0046$ year^{-1} for the aging process (see above). The endothelium network also appears more disordered as a result of contact lens wearing in older patients. Figure 3(b) shows the data of Nieuwendaal *et al.*,[34] who report a change from $p_6 \sim 0.68 \pm 0.06$ to $\sim 0.56 \pm 0.07$ for humans in the age range ~41–42 years. Figure 3 also shows data from Bourne *et al.*,[57,58] who studied changes in the endothelium morphology in transplanted corneas up to ~20 years post-surgery. The rate of change is $dp_6/dt = -0.0081$ year^{-1}, comparable to the effect of contact lens wearing and significantly higher than that attributable to aging alone. Overall, therefore, wearing contact lenses for ten years appears to lead to an equivalent change in the corneal endothelium structure of ≃30 years by aging alone. Similarly, the transplanted corneas age the equivalent of ≃20 years over the ten-year timescale.

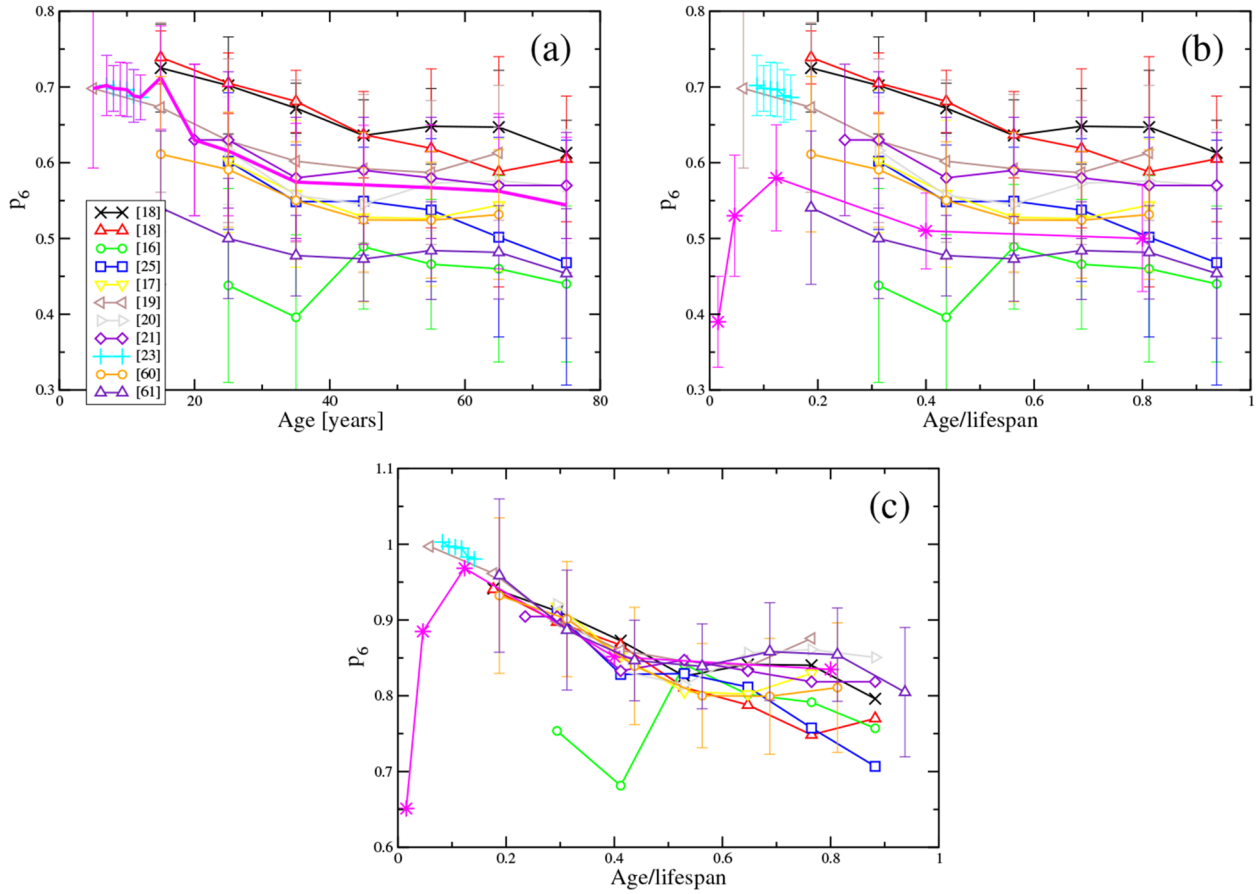

FIG. 2. Experimental data showing the change in the fraction of hexagons, p_6, with patient age. In panel (a), the data are shown for human subjects. The thick magenta line shows the mean average behavior. In panel (b), the human patient data are shown as a function of a reduced time obtained by dividing by a typical life expectancy (here, $t_{exp} \simeq 80$ years). For comparison, the figure also shows data for mice (from Ref. 22) divided by their life expectancy of $t_{exp} \simeq 2.5$ years. In panel (c), the data from (b) are shown (again as a function of reduced age) but normalized such that $p_6 \to 1$, as $t \to 0$. In all cases, the respective references are shown in the legend.

The effect of the onset of diabetes appears more subtle. Taşli *et al.*[30] find a change from $p_6 = 0.7849 \pm 0.0656$ to 0.6694 ± 0.0717 for patients with and without diabetes. In this study, the mean ages of the control and diabetic patients were $t = 59.6$ and 61.4 years, respectively. Chowdhury *et al.* see a smaller change, from $p_6 = 0.5694 \pm 0.0700$ to 0.5534 ± 0.0582 for the control and diabetic patients in a younger age group of $t = 53.7 \pm 7.0$ and 53.3 ± 6.0 years, respectively.[27] Kim and Kim[28] studied the effect of diabetes grouped by patient age (from $t \sim 40$ to $t > 80$ years), showing a small further decrease in p_6 in older diabetic patients. For example, patients in the $t = 40$–49 years group showed $p_6 = 0.554 \pm 0.020$ and 0.555 ± 0.020 for the control and diabetic groups, respectively, while patients of age $t > 80$ years showed $p_6 = 0.530 \pm 0.020$ and 0.508 ± 0.020. It appears, therefore, that the effect of the onset of diabetes becomes more significant with patient age.

Smoking status appears to lead to a similar (small) change. Golabchi *et al.*[31] report a change from $p_6 = 0.5042 \pm 0.0861$ to 0.4829 ± 0.0848 for the control and smoking groups (mean ages, $t \sim 46.39$ and 48.61 years, respectively). Again, in terms of aging timescales, this implies the corneal endothelium in the eye of a smoker will age the equivalent of ≃17 years over a ten year timeframe.

2. The effect of using p_6 only

Figure 1 shows a range of p_6 values obtained from experimental investigations. In panel (b), the data are shown in the form of a Lemaître curve (i.e., as the variance, μ_2, vs p_6, which, as described above, highlights the deviation of the ideal (maximum entropy) curve from linearity for $p_6 \lesssim 0.6$ and which corresponds to networks containing both 4-membered rings and rings larger than 7-membered). In panel (a), the data are sub-divided by the focus of the experiment (aging, the wearing of contact lenses, and the onset of diabetes), while panel (b) shows the data sub-divided by patient nationality and includes data obtained for diabetic dogs,[60] injured rabbits,[61] and aging mice.[22] Figure 4(a) shows a Lemaître curve, highlighting experimental data for which a more complete distribution of ring sizes has been published.[18,26,60,61,64–66] The relatively

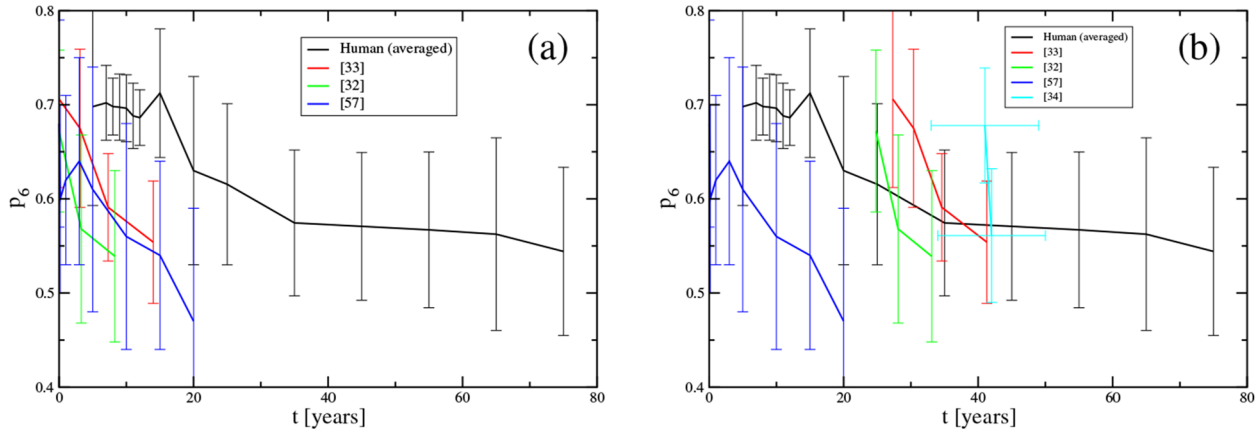

FIG. 3. Experimental data for the time dependence of the fraction of hexagons, p_6. The solid black line shows the mean average behavior of human patients (as shown in Fig. 2). The red and green lines show the effect of contact lens wearing over time, while the blue line shows the analogous change in transplanted corneas. In panel (a), time corresponds to the patient age for the black line but the time since the starting wearing contact lenses or since the transplant for the three other lines. In panel (b), the data for contact lens wearing have been offset along the abscissa by the mean age of the patients on beginning contact lens use. In both cases, the respective references are shown in the legend.

small system sizes lead to relatively large error bars, making it difficult to draw definitive conclusions. For example, the finite system size need not lead to a mean ring size of six. It is clear, however, that the vast majority of the observations for $p_6 \gtrsim 0.6$ sit on the linear region of the Lemaître curve. It is reasonable to expect that the error bars associated with the small system sizes will be larger for the more diverse distributions of ring sizes (smaller p_6). As noted above (Sec. II), it is entirely possible for ring size distributions to not sit on the maximum entropy solution if non-entropic (enthapic) effects are significant. It remains to be seen if this is the case here.

3. Cell areas

Figure 5(a) shows the variation of the cell area coefficient of variation, CV, with human patient age (data from Refs. 16–23, 25, 26, 67, and 68). CV rises gradually, and near-linearly, with age with mean gradient $d(CV)/dt \sim 0.001\ \text{year}^{-1}$. The increase in CV is potentially indicative of both the broadening of the ring size distribution (the fall in p_6) and a reduction in ring regularity. Figure 5(b) shows the same data normalized for lifespan and including additional data for cats[68] and mice.[22] The smaller mammals show a similar *change* in CV over their respective lifespans. The magnitude

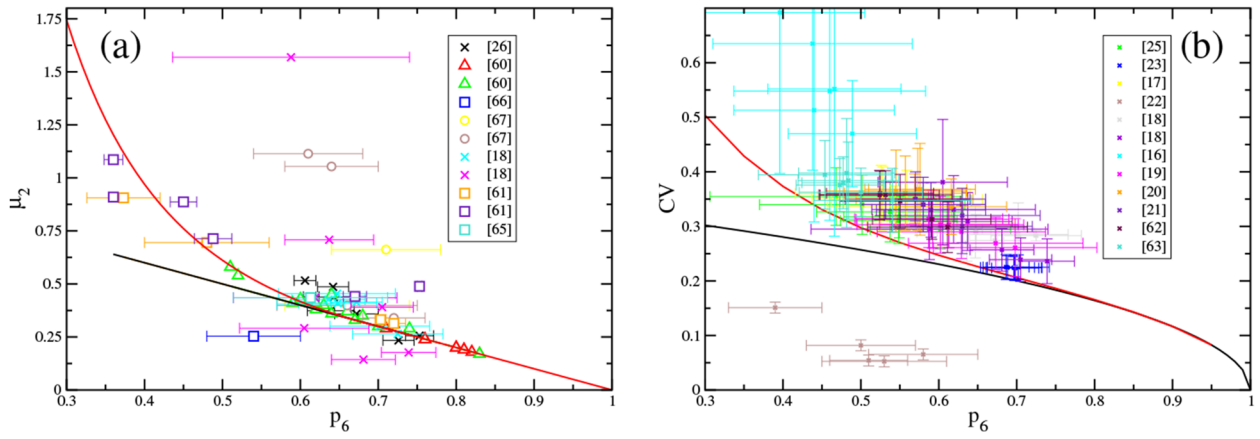

FIG. 4. Experimental data for (a), the variance, μ_2, and (b), the coefficient of variation of the area, CV $(=\sigma_A/\bar{A})$, for which more complete ring size distribution data are available. In both panels, the ideal (maximum entropy) solutions for the constrained 5-, 6-, and 7-membered ring systems and the unconstrained ring size systems are shown as black and red solid lines, respectively. In both cases, the respective references are shown in the legend.

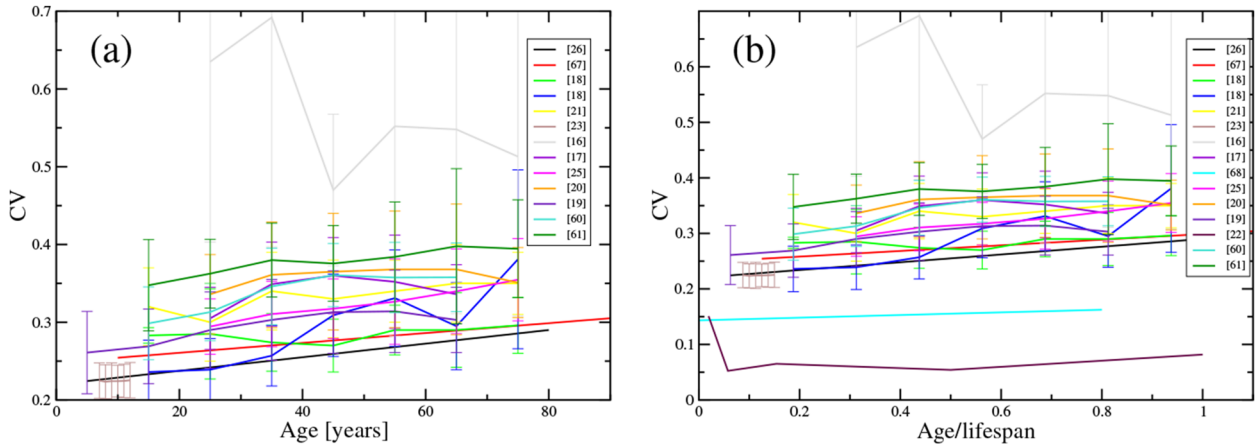

FIG. 5. Experimental data showing the change in the coefficient of variation of the area, *CV*, as a function of human patient age. In panel (a), the abscissa is shown in years, while in panel (b), the abscissa is shown divided by lifespan (as in Fig. 2), and additional data for mice[22] and cats[68] are shown. In both cases, the respective references are shown in the legend.

of the CV appears to reduce with mammal lifespan. Figure 4(b) shows the experimental CV against the fraction of hexagons, p_6. The figure also shows the analytic maximum entropy solutions (see the Appendix) determined for the constrained 5-, 6-, and 7-membered ring systems and for the unconstrained ring size distribution, assuming that the polygons adopt their ideal areas. The experimental data show a CV whose dependence on p_6 effectively mirrors the analytic ideal solution but is systematically larger, perhaps reflecting the distortions of the contributing polyhedra from their ideal (regular) shapes.[69]

B. Model behavior

1. p_6 and CV

As outlined in Sec. III, the networks obtained from the bond-switching algorithm are controlled by three parameters; the bond length and angle force constants (k_r and k_θ, respectively), and the Monte Carlo temperature, T. Varying these parameters allows us to control the level of disorder and topology of the generated networks. Figure 6 shows the Lemaître curve obtained over the full range of $\{k_r, k_\theta, \text{and } T\}$ investigated here. As the Monte Carlo temperature increases, the distribution of ring sizes becomes broader, corresponding to a higher μ_2 (lower p_6). At low T, the network corresponds to a near-ideal hexagonal net ($p_6 = 1$) with a correspondingly vanishingly small CV. As T increases, the fraction of hexagons falls (corresponding to the formation of networks dominated by hexagons with isolated 5- and 7-membered ring defects). The figure also shows the analytic (maximum entropy) solutions for the constrained $\{567\}$ and $\{45\,678\}$ rings system and the unconstrained ring size distribution. As discussed in Sec. II, the $\{567\}$ constrained system shows a linear dependence with $\mu_2 = 1 - p_6$. The $\{45\,678\}$ system shows a non-linear dependence but sits below the ideal maximum entropy solution at very low p_6 ($p_6 \lesssim 0.45$), as even larger rings ($k > 8$) become entropically favored.

Figure 7(a) shows the values for the CV of area obtained from the simulation models for all values of $\{k_r, k_\theta, \text{and } T\}$ investigated. The figure shows the ideal values calculated from both Eqs. (A2) and (A6) (see the Appendix). As $p_6 \to 1$, $CV \to 0$, as the network is comprised exclusively of ideal hexagons. As p_6 falls, CV increases, simply reflecting the dispersion of polygon areas imposed by the presence of 5- and 7-membered rings. For the constrained system, $CV \to \frac{|A_5 - A_7|}{A_5 + A_7} \sim 0.36$ as $p_6 \to 0$ (i.e., for a system composed of

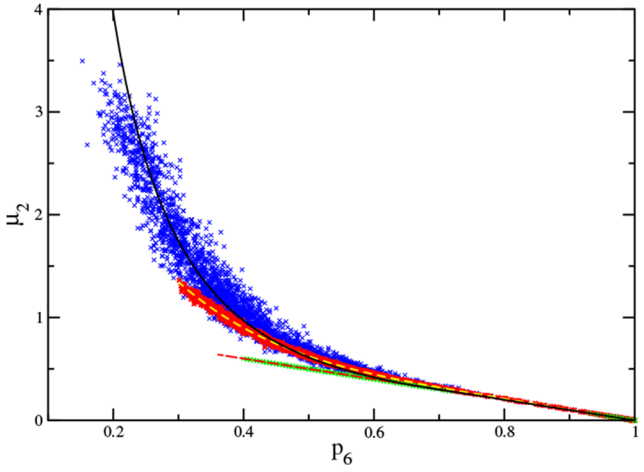

FIG. 6. Lemaître curve plot of the variance, μ_2, against the fraction of hexagons, p_6, obtained from the models at three levels of constraint. The green, red, and blue points show data collected from models constrained to have 5-, 6-, and 7-membered rings only, 4- to 8-membered rings (inclusive) only, and unconstrained ring size distributions, respectively. The ideal (maximum entropy) solutions for the constrained 5-, 6-, and 7-membered ($\{567\}$) ring systems, constrained $\{45\,678\}$ ring systems, and unconstrained ring size systems are shown as dashed red, dashed yellow, and solid lines, respectively.

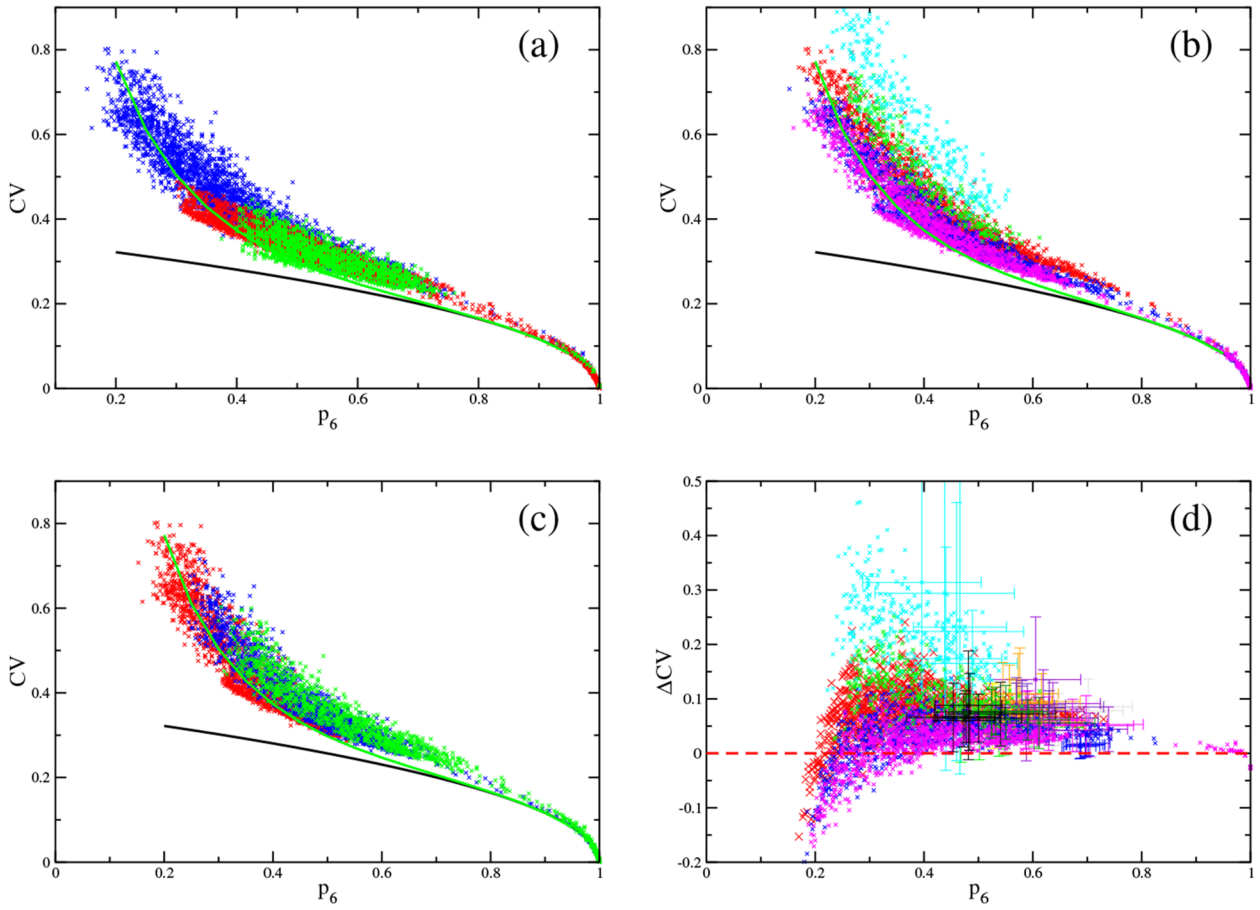

FIG. 7. The coefficients of variation for the polygon area obtained from the simulation models. Panel (a) shows the values obtained from the models at three levels of constraint. The green, red, and blue points show data collected from models constrained to have 5-, 6-, and 7-membered rings only ($\{567\}$), 4- to 8-membered rings (inclusive) only ($\{45\,678\}$), and unconstrained ring size distributions, respectively. Panels (b) and (c) show the CV values for fixed values of k_r and k_θ, respectively. Panel (b) key: k_r = 0.01, 0.1, 0.2, 0.6, and 1.0—cyan, green, red, blue, and magenta crosses, respectively. Panel (c) key: k_θ = 0.1, 0.2, and 0.3—red, blue, and green crosses, respectively. In panels (a)–(c), the solid black and green lines correspond to ideal values for the $\{567\}$ constrained and unconstrained systems, respectively. Panel (d) shows the excess CV, ΔCV, at fixed k_r [key as for panel (b)]. Panel (d) also shows the values for ΔCV obtained from the experimental data highlighted in Fig. 4(b) with the same key.

5- and 7-membered rings only). For the unconstrained network, CV continues to rise as p_6 is reduced, reflecting the presence of an increasing diversity of different-sized rings. The obtained model values mirror the ideal curve (see the Appendix) with higher values, reflecting the distortions of the polygons from their ideal areas. As for Fig. 6, data are shown for the three differently constrained systems. As the level of constraint is reduced (corresponding to moving between $\{567\} \rightarrow \{45\,678\} \rightarrow$ unconstrained networks), CV is able to increase more rapidly as p_6 decreases, corresponding to the formation of both smaller and larger rings. The figure also shows the ideal CV curves for both the $\{567\}$ and unconstrained networks (see the Appendix). Figure 7(b) shows the values for the CV for five values of k_r (over all values of k_θ) ranging from k_r = 0.01–1.0. As k_r is reduced (corresponding to making the bonds less strong), CV is observed to deviate from the ideal curves as the greater distribution of bond lengths facilitates more distorted polygons. Figure 7(c) shows the values for the CV for three values of k_θ (over all values of k_r) with k_θ = 0.1–0.3. As k_θ is reduced, CV increases, corresponding to the weaker angular constraint, facilitating greater polygon distortions.

To better see these differences, we can define a difference function as $\Delta CV = CV - CV_{id}$, where CV is obtained from the model or directly from experiment, and CV_{id} is the ideal value assuming regular polygon areas. Figure 7(d) shows ΔCV vs p_6 for the model data, colored by k_r, corresponding to the "raw" CV data shown in Fig. 7(b). As k_r is reduced (corresponding to a weakening of the node–node "bond strength"), ΔCV increases, reflecting the greater polygon distortion. As $p_6 \rightarrow 1$, then $\Delta CV \rightarrow 0$, corresponding to an ideal hexagonal net. At exceptionally low values of p_6 ($p_6 \lesssim 0.25$), ΔCV can become negative, reflecting the presence of larger

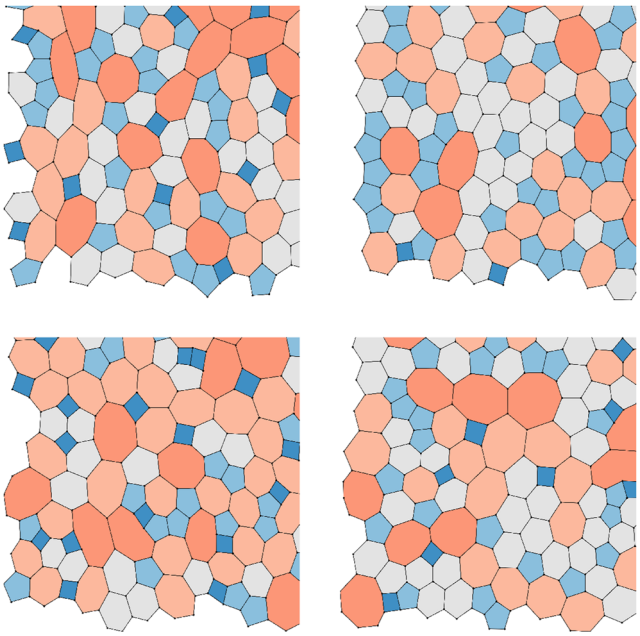

FIG. 8. Molecular graphics "snapshots" showing four configurations, which vary by the ratio of the angular and bond force constants, k_θ/k_r. Different ring sizes are shown in different colors. Key (k_θ/k_r): top left - 0.1, top right - 0.3, bottom left - 0.5, bottom right - 1.5.

rings, which can be more easily distorted. Figure 7(d) also highlights the values of ΔCV obtained from the experimental data [and corresponding to the data shown in Fig. 4(b)]. The observed experimental values appear to correlate most strongly with the simulated values obtained using weaker bond force constants.

2. Nearest-neighbor structure

Figure 8 shows a set of molecular graphics "snapshots" corresponding to different values of k_r and k_θ. The effect of changing the relative strengths of the bond and angular force constants is clear "by eye." The combination of the strongest bond force constant and weakest angular force constant (top left panel, corresponding to $k_\theta/k_r = 0.1$) generates a network with a wider distribution of bond angles. The combination of relatively strong bond and angular force constants (bottom right panel) generates a much more regular-looking network. While the difference in structure is clearly visible in terms of, for example, the deformation of the individual polygons, any difference in nearest-neighbor structure is more difficult to effectively quantify. As noted in Sec. III, the assortativity, r, represents a useful metric for characterizing any nearest-neighbor structural ordering. A further simple measure is to consider the pairwise structure of the ring system, that is, count the number of rings of size k that surround a ring of size k'. These ring adjacencies then build up to form the overall assortativity. However, a simple visualization procedure is flawed for considering the assortativities, as they are complex averages over all ring size pairs.

Figure 9 shows the change in assortativity with p_6 as a function of (a) k_θ at five fixed values of k_r and (b) k_r at three fixed values of k_θ. In all cases, the choice of force constants has a significant effect on the resulting assortativity. The range of assortativities obtained is relatively large, spanning $-0.28 \lesssim r \lesssim -0.10$. For comparison, typical values for related systems include colloids - $-0.25 \lesssim r \lesssim -0.18$, silica - $-0.34 \lesssim r \lesssim -0.32$, graphene - $-0.27 \lesssim r \lesssim -0.22$. At first glance, therefore, it appears that the simulated networks generated here correspond most clearly, as might be expected, to the colloidal networks. At fixed k_θ, an increase in k_r makes the assortativity more negative (corresponding to a stronger preference for small-large neighboring rings), while at fixed k_r, an increase in k_θ appears to have the opposite effect.

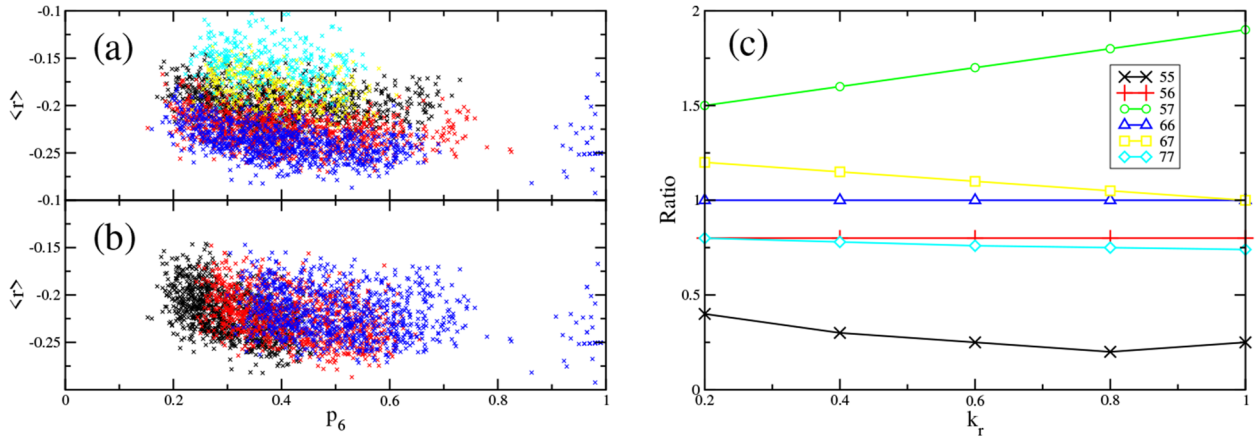

FIG. 9. The left panels show the assortativities, r, at (a) fixed k_r while varying k_θ, and (b) fixed k_θ while varying k_r. Key: (a) $k_r = 0.01$ (cyan), 0.1 (yellow), 0.2 (black), 0.6 (red), and 1.0 (blue). (b) $k_\theta = 0.1$ (black), 0.2 (red), and 0.3 (blue). The right panel (c) shows the nearest-neighbor ring adjacencies for $k_\theta = 0.2$ as a function of k_r displayed as the ratio of the observed number of nearest-neighbor pairs for rings sizes k and k' and the expected number assuming a random distribution of rings. The legend indicates the values of the ring sizes, k and k'.

The precise structural origins of changes in assortativity can be difficult to isolate as all pairs of rings contribute. One potential method is to count the numbers of given nearest-neighbor pairs and compare them to the expected values assuming a random distribution of rings. For example, Fig. 9(c) shows the change in the number of nearest-neighbor ring size pairs, $\{kk'\}$, as a function of k_r at fixed k_θ. Increasing k_r at fixed k_θ increases the number of nearest-neighbor $\{57\}$ pairs with a concomitant reduction in the number of $\{77\}$ pairs, both leading to a more negative assortativity. The effect of changing k_θ at fixed k_r is more subtle.

V. DISCUSSION

The application of a generic model to a key biological problem facilitates an understanding of the network structure in the broader context of related systems. One of the key reasons for wishing to develop a network model is to help interpret the abundance of available experimental data. By systematically varying the model parameters, networks that resemble those observed experimentally have been obtained. Models, which employ relatively weak bond force constants (low k_r), show the most favorable comparison with experimental data, in particular in terms of the polygon areas (as measured by the respective coefficient of variation). This places the corneal endothelium networks in the same "class" as those formed by colloidal nanoparticles deposited on surfaces or by foams on surfaces, as distinct from structures formed by low-dimensional glasses or ultrathin materials.

The most commonly experimentally measured property is the fraction of hexagons, p_6. However, it is clear that it is important to determine the full ring size distribution. For a maximum entropy distribution, the determination of p_6 alone *does* automatically generate the ring size distribution, but non-entropic effects can alter the distribution in a non-trivial fashion. For example, the analysis of the decay of p_6 with patient aging hints at p_6 reaching a potential plateau at $p_6 \sim 0.6$. This value corresponds to the region of the Lemaître curve where the maximum entropy solution deviates significantly from linearity. Supporting values of $p_6 \lesssim 0.6$ requires the stabilization of relatively small (4-membered) and relatively large $(k > 7)$ rings. The implication of a plateau in p_6 with patient age is that the formation of such small and large rings is affected by non-entropic effects.

Finally, connections with more general network theory potentially allow additional structural information to be obtained. The assortativity, for example, quantifies the nearest-neighbor ring structure and highlights a preference for small rings to be neighbors to large rings and vice versa. Experimental observation of large enough samples should allow this key metric to be extracted, including, critically, its behavior with patient aging.

Having noted potential improvements in experimental measurements, coupled with symbiotic model development, it is important to note that the models themselves can be significantly improved. Real corneal endothelia, for example, show polygon areas, which change with patient aging owing to cell recombination effects. Such "moves" can be incorporated as additional potential Monte Carlo rearrangements, and this will form the basis of future work.

VI. CONCLUSIONS

In this paper, a relatively simple bond-switching Monte Carlo method has been applied to generate a wide range of network structures. These networks have been compared to data extracted from the study of the mammalian corneal endothelium. The ability to systematically vary the model parameters allows the structural characteristics of these systems to be assessed alongside analogous network-formers. Indeed, network theory has been most commonly applied to problems more traditionally associated with physics, materials science, and chemistry (or at their respective interfaces). Models employing relatively weak bond force constants have been found to be most appropriate, mapping these systems more clearly onto two-dimensional layers of colloidal nanoparticles. In addition, the work highlights how more useful information could be extracted from experimental investigations, for example, by extracting details of the nearest-neighbor structure.

ACKNOWLEDGMENTS

We are grateful for support from the EPSRC Center for Doctoral Training in Theory and Modeling in Chemical Sciences (TMCS), under Grant No. EP/L015722/1. M.W. is grateful to Dr. Martin Galpin for helpful discussions. This paper conforms to the RCUK data management requirements.

AUTHOR DECLARATIONS

Conflict of Interest

The authors have no conflicts to disclose.

Author Contributions

Bryan Xuan: Data curation (equal); Formal analysis (equal); Investigation (equal); Methodology (equal); Software (equal); Writing – review & editing (equal). **Oliver Whitaker**: Data curation (equal); Formal analysis (equal); Investigation (equal); Methodology (equal); Visualization (equal); Writing – review & editing (equal). **Mark Wilson**: Conceptualization (equal); Formal analysis (equal); Investigation (equal); Methodology (equal); Project administration (equal); Supervision (equal); Validation (equal); Writing – original draft (equal); Writing – review & editing (equal).

DATA AVAILABILITY

The data that support the findings of this study are available from the corresponding author upon reasonable request.

APPENDIX: COEFFICIENT OF VARIATION OF THE AREA

Consider an ideal $k-$ polygon with sides of length $r_0 = 1$. The ideal area is

$$A_k^o = \frac{k}{4\,\tan(\pi/k)}. \tag{A1}$$

We want to determine the coefficient of variation (CV) of the area, $CV = \frac{\sigma_A}{\bar{A}}$, as the ring size distribution changes (i.e., purely as the effect of having a mixture of different areas for the different $k-$ rings). The nth moment of the area is given by $\langle A^n \rangle = \sum_k A^n p_k$, and so

$$CV = \frac{\left[\sum_i p_i A_i^2 - \left(\sum_i p_i A_i\right)^2\right]^{1/2}}{\sum_i p_i A_i}. \tag{A2}$$

Let us assume only 5- to 7-membered rings for simplicity. So

$$\bar{A} = p_5 A_5 + p_6 A_6 + p_7 A_7. \tag{A3}$$

For this system we have the usual constrants of $p_5 = p_7$ (as $\bar{n} = 6$) and $p_5 = \frac{1-p_6}{2}$ as $\sum_i p_i = 1$. As a result,

$$\begin{aligned}\bar{A} &= \frac{(1-p_6)}{2}(A_5 + A_7) + p_6 A_6 \\ &= \frac{(A_5 + A_7)}{2} + p_6\left[A_6 - \frac{1}{2}(A_5 + A_7)\right],\end{aligned} \tag{A4}$$

$$\bar{A^2} = \frac{(A_5^2 + A_7^2)}{2} + p_6\left[A_6^2 - \frac{1}{2}(A_5^2 + A_7^2)\right], \tag{A5}$$

and so CV can be written as

$$CV = \frac{\left\{\frac{(A_5^2+A_7^2)}{2} + p_6\left[A_6^2 - \frac{1}{2}(A_5^2 + A_7^2)\right] - \left(\frac{(A_5+A_7)}{2} + p_6\left[A_6 - \frac{1}{2}(A_5 + A_7)\right]\right)^2\right\}^{1/2}}{p_5 A_5 + p_6 A_6 + p_7 A_7}. \tag{A6}$$

Figure 7 shows CV vs p_6 calculated from both Eqs. (A2) and (A6). As $p_6 \to 1$, $CV \to 0$, as the network is comprised exclusively of ideal hexagons. As p_6 falls, CV increases, simply reflecting the dispersion of polygon areas imposed by the presence of 5- and 7-membered rings. For the constrained system, $CV \to \frac{|A_5 - A_7|}{A_5 + A_7}$ ~ 0.36 as $p_6 \to 0$ (i.e., for a system composed of 5- and 7-membered rings only). For the unconstrained network, CV continues to rise as p_6 is reduced, reflecting the presence of an increasing diversity of different-sized rings.

Equations (A2) and (A6) require values for the ideal ring areas. At the simplest level, the ideal values from Eq. (A1) can be applied. However, other than for the ideal hexagonal net, the ring areas will not actually take these values. An alternative, for example, is to use values of A_5 and A_7 obtained from a single bond switch. This has the advantage that the area is conserved (as a single switch converts four hexagons into two heptagons and two pentagons, and so $4A_6 = 2A_5 + 2A_7$).[70] The ideal curve using these values for A_5 and A_7 is shown in Fig. 7(a) for the constrained system and, significantly, shows little difference from the curve obtained using the ideal areas. In conclusion, the detailed choice of polygon areas has little effect on the predicted CV.

REFERENCES

[1] C. Oyster, *The Human Eye: Structure and Function* (Sinauer Associates Inc., 1999).
[2] D. DelMonte and T. Kim, J. Cataract Refractive Surg. **37**, 588 (2011).
[3] P. Y. Huang, S. Kurasch, A. Srivastava, V. Skakalova, J. Kotakoski, A. V. Krasheninnikov, R. Hovden, Q. Mao, J. C. Meyer, J. H. Smet, D. Muller, and U. Kaiser, Nano Lett. **12**, 1081 (2012).
[4] C. Büchner and M. Heyde, Prog. Surf. Sci. **92**, 341 (2017).
[5] A. W. Robertson, G.-D. Lee, K. He, E. Yoon, A. I. Kirkland, and J. H. Warner, Nano Lett. **14**, 3972 (2014).
[6] J. C. Earnshaw and D. J. Robinson, Phys. Rev. Lett. **72**, 3682 (1994).
[7] C. Allain and L. Limat, Phys. Rev. Lett. **74**, 2981 (1995).
[8] M. Durand, J. Käfer, C. Quilliet, S. Cox, S. A. Talebi, and F. Graner, Phys. Rev. Lett. **107**, 168304 (2011).
[9] M. Tong, K. Cole, P. R. Brito-Parada, S. Neethling, and J. J. Cilliers, Langmuir **33**, 3839 (2017).
[10] M. C. Gibson, A. B. Patel, R. Nagpal, and N. Perrimon, Nature **442**, 1038 (2006).
[11] R. Carter, Y. E. Sánchez-Corrales, M. Hartley, V. A. Grieneisen, and A. F. M. Marée, Development **144**, 4386 (2017).
[12] L. Goehring and S. W. Morris, Phys. Today **67**(11), 39 (2014).
[13] A.-l. Barabási, Nat. Phys. **8**, 14 (2012).
[14] S. Boccaletti, V. Latora, Y. Moreno, M. Chavez, and D.-U. Hwang, Phys. Rep. **424**, 175 (2006).
[15] S. H. Strogatz, Nature **410**, 268 (2001).
[16] P. Mohd Salih, Med. J. Malays. **66**, 300 (2011).
[17] C. Arici, O. Arslan, and F. Dikkaya, J. Ophthalmol **2014**, 852624.
[18] M. Matsuda, R. Yee, and H. Edelhauer, Arch. Ophthalmol. **103**, 68 (1985).
[19] T. Ono, Y. Mori, R. Nejima, T. Iwasaki, T. Miyal, and K. Miyata, Sci. Rep. **11**, 18224 (2021).
[20] S. Rao, P. Sen, R. Fogla, S. Gangadharan, P. Padmanabhan, and S. Badrinath, Cornea **19**, 820 (2000).
[21] H. Yunliang, S. amd Yuqiang, L. Ying-peng, Z. Ming-zhi, D. Lam, and S. Rao, Clin. Sci. **26**, 130 (2007).
[22] S. Jun, A. S. amd Chakravarti, H. Edelhauser, and M. Kimos, Exp. Eye Res. **83**, 890 (2006).
[23] H. Al Farhan, W. Albaow, and W. Masoud, J. Egypt. Ophthalmol. Soc. **107**, 63 (2014).
[24] A. Müller, M. Doughty, and L. Wright, Br. J. Ophthalmol. **82**, 692 (2000).
[25] M. Abdellah, H. Ammar, M. Anbar, E. Mostafa, M. Farouk, K. Sayed, A. Alsmman, and M. Elghobaier, J. Ophthalmol. **2019**, 6370241.
[26] R. Yee, M. Matsuda, R. Schultz, and H. Edelhauer, Curr. Eye Res. **4**, 671 (1985).
[27] B. Chowdhury, S. Bhadra, P. Mittal, and K. Shyam, Indian J. Ophthalmol. **69**, 1718 (2021).
[28] Y. Kim and T. Kim, Sci. Rep. **11**, 8324 (2021).
[29] J. Lee, B. Oum, H. Choi, J. Lee, and B. Cho, Eye **20**, 315 (2006).
[30] N. G. Taşlı, E. Icel, Y. Karakurt, T. Ucak, A. Ugurlu, H. Yilmaz, and E. M. Akbas, BMC Ophthalmol. **20**, 214 (2020).
[31] K. Golabchi, M.-A. Abtahi, A. Salehi, H. Jahanbani-Ardakani, S. Ghaffari, and Z. Farajzadegan, Cutaneous Ocul. Toxicol. **37**, 9 (2017).
[32] S.-W. Chang, F.-W. Hu, and L.-K. Lin, Ophthalmologica **215**, 197 (2001).
[33] J. Lee, S. Park, W. S. amd Lee, B. Oum, and B. Cho, Graefe's Arch. Clin. Exp. Ophthalmol. **239**, 1 (2001).
[34] C. Nieuwendaal, M. Odenthal, J. Kok, H. Venema, J. Oosting, F. Riemslag, and A. Kijlstra, Invest Ophthalmol. Vis. Sci. **35**, 3071 (1994).

[35]M. Odenthal, I. Gan, J. Oosting, A. Kijlstra, and W. Beekhuis, Clin. Sci. **24**, 32 (2005).
[36]M. E. Newman, Phys. Rev. Lett. **89**, 208701 (2002).
[37]R. Noldus and P. V. Mieghem, J. Complex Networks **3**, 507 (2015).
[38]A. Chremos and P. J. Camp, Phys. Rev. E **76**, 056108 (2007).
[39]A. Gervois, J. P. Troadec, and J. Lemaître, J. Phys. A: Math. Gen. **25**, 6169 (1992).
[40]D. Ormrod Morley, A. Thorneywork, R. Dullens, and M. Wilson, Phys. Rev. E **101**, 042309 (2020).
[41]A. Malashevich, S. Ismail-Beigi, and E. I. Altman, J. Phys. Chem. C **120**, 26770 (2016).
[42]D. Ormrod Morley, A. L. Goodwin, and M. Wilson, Phys. Rev. E **102**, 062308 (2020).
[43]D. A. Aboav, Metallography **3**, 383 (1970).
[44]D. Weaire, Metallography **7**, 157 (1974).
[45]J. K. Mason, R. Ehrenborg, and E. A. Lazar, J. Phys. A: Math. Theor. **45**, 065001 (2012).
[46]F. Wooten, K. Winer, and D. Weaire, Phys. Rev. Lett. **54**, 1392 (1985).
[47]V. Meunier, A. G. Souza Filho, E. B. Barros, and M. S. Dresselhaus, Rev. Mod. Phys. **88**, 025005 (2016).
[48]J. M. Greneche and J. M. D. Coey, J. Phys. Fr. **51**, 231 (1990).
[49]N. Metropolis, A. W. Rosenbluth, M. N. Rosenbluth, A. H. Teller, and E. Teller, J. Chem. Phys. **21**, 1087 (1953).
[50]D. Weaire and N. Rivier, Contemp. Phys. **50**, 199 (2009).
[51]A. J. Stone and D. J. Wales, Chem. Phys. Lett. **128**, 501 (1986).
[52]S. von Alfthan, A. Kuronen, and K. Kaski, Phys. Rev. B **68**, 073203 (2003).
[53]M. Bulacu, N. Goga, W. Zhao, G. Rossi, L. Monticelli, X. Periole, D. P. Tieleman, and S. J. Marrink, J. Chem. Theory Comput. **9**, 3282 (2013).
[54]F. Wooten and D. Weaire, J. Non-Cryst. Solids **64**, 325 (1984).
[55]R. M. Martin, Phys. Rev. B **1**, 4005 (1970).
[56]A. Kumar, M. Wilson, and M. F. Thorpe, J. Phys.: Condens. Matter **24**, 485003 (2012).
[57]W. Bourne, Cornea **20**, 560 (2001).
[58]W. Bourne, D. Hodge, and L. Nelson, Am. J. Ophthalmol. **118**, 185 (1994).
[59]M. Matsuda, R. Yee, D. Glasser, D. Geroski, and H. Edelhauer, Arch. Ophthalmol. **104**, 259 (1986).
[60]R. Yee, M. Matsuda, T. Kern, R. Engerman, and H. Edelhauer, Curr. Eye Res. **4**, 759 (1985).
[61]R. Yee, D. Geroski, E. Champeau, L. Meyer, and H. Edelhauer, Invest Ophthalmol. Vis. Sci. **26**, 1191 (1985).
[62]Q. Ul Islam, M. K. Saeed, and M. Mehboob, Saudi J. Ophthalmol. **31**, 86 (2017).
[63]N. Tananuvat and N. Khumchoo, BMC Ophthalmol. **20**, 167 (2020).
[64]K. Carlson, W. Bourne, and R. Brubaker, Invest Ophthalmol. Vis. Sci. **29**, 185 (1988).
[65]M. Doughty, Ophthalmic Physiol. Opt. **18**, 415 (1998).
[66]J. González-Méijome, J. Jorge, A. Queirós, S. Peixoto-de Matos, and M. Parafita, Graefes Arch. Clin. Exp. Ophthalmol. **248**, 1159 (2010).
[67]K. Carlson, W. Bourne, J. McLaren, and R. Brubaker, Exp. Eye Res. **47**, 27 (1988).
[68]T. Chan-ling and J. Curmi, Curr. Eye Res. **7**, 387 (1988).
[69]The data for p_6 and CV given in Table I of Ref. 16 may have been swapped in the original publication.
[70]Assuming $r_0 = 1$ then $A_5 \sim 1.67$ and $A_7 \sim 3.53$.

6.2.1 Summary

This paper was written in collaboration with a fourth year undergraduate student, Bryan Xuan. My role in this project involved co-supervision of significant advice surrounding both the generation of networks and their analysis. I also provided a wide array of networks for analysis and comparison to experimental data, and advised on how best to interpret this data.

The experimental data collected is particularly varied, both in terms of the level of disorder in the systems presented, and the metrics collected. The p_6 range is from $p_6 \simeq 0.36-0.83$. By contrast, previous analysis of silica bilayer networks[5, 134] have focused on a much tighter range of ring statistics for analysis ($p_6 \simeq 0.32 - 0.4448$).

In addition, whereas for chemical systems we have a much clearer understanding of the internal angles of the rings and their side lengths [145], we do not have this information for the networks of the corneal endothelium. This is important because it means we must expand our phase space search to a range of k_r/k_θ values in search of structures which represent experimental values.

6.3 Conclusions

Monte Carlo methods established in Chapter 5 have been employed to create a large dataset of ring distributions, across a range of bond (k_r) and angle (k_θ) force constants. These networks have been compared to experimental data for networks of mammalian corneal endothelium cells, with the aim to correlate experimental images with our network generation parameters. Detailed analysis of experimental data using network metrics allows us to correlate the disorder present to contact lens use, age, diabetic status.

7

Direct Control of Pores in Network Structures: Ring Growth Methods

Work presented in Chapters 5 and 6 has focused on generating structures over a range of disorder, from near crystalline networks through to amorphous continuous random networks (CRNs). Through these chapters, we have had limited direct control over disorder; we cannot introduce rings of a given size, only introduce general disorder, mediated through the nebulous Monte Carlo 'temperature'. These samples have been generated from a zero energy starting point, namely a perfect hexagonal crystal. In this chapter, we select an alternate starting point, using pores of varying size and relaxing a triangle raft style system around them. This allows us to explore areas of the phase space with ring sizes outside the limits observed in experimental amorphous silica bilayers.

Understanding the stability and structural impact of introducing rings of a given size n, or 'pores', is important for predicting the potential of silica bilayers as molecular sieves; recent work[12] has demonstrated and characterised molecular permeation of isolated silica bilayers, hypothesising that each ring size has its own selectivity characteristics.

To this end, a range of ring sizes ($5 \leq n \leq 30$) have been generated as a template for ring growth simulations, which we expect to probe the limits of pore

stability in silica systems. In addition, from these simulations we aim to find an estimation of the concomitant pore density, which is of importance for efficient functional molecular filters. The simulations here utilise a non-equilibrium Monte Carlo method, using the same simple potential models discussed in Chapter 4, with the slight variation of a $12-24$ potential, as opposed to the $6-12$ Lennard-Jones potential described in Chapter 4 (possible implications are discussed in Section 5.6).

7.1 Structural Effects of Inserting large rings into two-dimensional networks

Structural Effects of the Insertion of Large Rings in Two-Dimensional Networks.

Oliver Whitaker,[1] David Ormrod Morley,[1] and Mark Wilson[1]

[1] *Department of Chemistry, Physical and Theoretical Chemistry Laboratory, University of Oxford, South Parks Road, Oxford OX1 3QZ, U.K.*

(Dated: October 10, 2024)

The structural effect of inserting large central rings into a two-dimensional network of three-coordinate nodes is investigated using a ring-growth Monte Carlo procedure. The size of the central ring is systematically varied as is the inherent level of disorder in the surrounding network (as characterised by both the Monte Carlo "temperature" and the fraction of six-membered rings). The effect of the central ring on the overall network topology is analysed in terms of both topological and geometric distances. For larger central rings the first topological shell becomes exclusively populated by four- and five-membered rings which leads to an effective upper limit on the size of central ring which can effectively be accommodated. The topological shells are found to show ordering on significant distances away from the central ring. The effective correlation lengths are determined as a function of both central ring size and level of network disorder, which allows for an understanding of the potential density of large rings which may be accommodated.

I. INTRODUCTION.

Attempting to understand the properties of two-dimensional networks has undergone resurgence in recent years. The dramatic increase in microscopy resolution leading to the observation of graphene[1,2] has started to uncover a potentially vast richness of structure in atomistically-thin systems such as carbon and BN[3–5]. Furthermore, systems such as SiO_2, GeO_2, and related aluminosilicates have been shown to form thin films comprised of bilayers of corner sharing tetrahedra[6–17]. Given the known preponderance of even lower dimensional structures formed by carbon and BN (nanotubes, fullerences...) it is likely that these bilayers show similar structural richness. In the two-dimensional form a key structural requirement is to be able to effectively control the pore sizes and their distribution across the network. Such control is critical if, for example, these films are to be used to control the flow of mixtures of gases.

Significant attention has been paid to highly ordered (crystalline) systems (of which pristine graphene would represent a prime example). However, more recent work has uncovered possible disordered (amorphous) analogues, for example, for carbon[3] and for thin (bilayers) of silica[7,14]. At a fundamental level these systems map onto a percolating network of rings (a-G, for example, is comprised of 5-, 6- and 7-membered rings, whilst bi-SiO_2 shows a broader distribution of ring sizes owing to the greater degrees of freedom afforded by the Si-O-Si bridges). Indeed, two-dimensional networks are commonly observed across all length scales, from the atomic level[7,14,18], to colloids[19,20], foams[21,22], epithelial cells[23,24], geological rock formations[25], drying blood[26], stratocumulus clouds[27] and geopolitical borders[28]. All can all be mapped onto a generic system equivalently described as a collection of tessellating polygons or percolating rings[29]. As a result their structural properties are governed by the same fundamental laws and so an understanding of the properties of a generic network implies understanding of a huge range of different systems across all length-scales.

In this paper one aspect of these networks, namely the effect of inserting a relatively large ring, will be investigated. Particular attention will be paid to any (local) order the presence of a large ring may impose and the length-scales on which any such order vanishes. Effective characterisation of these length-scales through the establishment of a correlation length will allow for an understanding of the density at which such large rings could be effectively templated. In addition, studying the systems across a wide temperature range will establish the dependence of the correlation length on the degree of disorder, potentially in terms of both the distribution of ring sizes and their spatial organisation. Furthermore, establishing the correlation lengths allows the effective interaction of the large rings to be established.

In this paper we focus on bilayers, exemplified by bi-SiO_2, as opposed to less complex two-dimensional networks such as those formed by graphene or boron nitride. Experimental methods to introduce pores into graphene and BN rely on mixed coordination (see, for example, refs.[30–38]), whereas the increased flexibility and diversity in ring sizes observed in the bilayers is expected to be able to accommodate the presence of larger rings whilst maintaining full coordination. Experimental work evaluating gas permeation in bi-SiO_2[39] indicates that rings of a given size may be responsible for the diffusion of specific molecules (*e.g.* six membered rings were likely responsible for heavy water permeation), and so the ability to generate larger ring sizes would be expected to change the permeation characteristics of a given network.

The paper is organised as follows. In section II the background network theory is summarised, including considering the required structural metrics. Section III introduces the methods and models applied to study the problem. Section

IV presents results, broken down into the overall effect on the ring size distribution and structural correlations on different length-scales. Section V presents a discussion to help tie the various intellectual strands together.

II. BACKGROUND.

In this section the background theory covering the nomenclature used to study the networks (including their description as a collection of rings) will be summarised. In addition, the probabilities of finding pairs of neighbouring rings of a given size in a given shell (from the central seed ring) will be discussed.

A. Networks and Rings.

The properties of a percolating network of rings can be deconstructed into different "levels of information". At the simplest level the system is defined by the ring size distribution where the fraction of rings of size k is given by p_k. As a result, the mean of this distribution is,

$$\langle k \rangle = \sum_k k p(k), \tag{1}$$

with second moment,

$$\mu_2 = \langle k^2 \rangle - \langle k \rangle^2. \tag{2}$$

The ring size distribution is, however, a relatively low level of the available information. The rings in any given distribution may be arranged in space in a huge number of different ways, some of which will be entropically and/or enthalpically favoured. The structure around a given ring may be considered in essentially two ways; topologically or spatially. In the former rings surrounding a given ring form numbered shells, whilst in the latter the distance between two rings is simply geometric. Since a key interest here is the effect of a potentially large central ring, we begin by considering the topological relationships.

The number of rings in the shell labelled t away from a ring of size k is given by,

$$K_t(k) = \sum_{k'} N_t(k, k'), \tag{3}$$

where $N_t(k, k')$ is the number of rings of size k' in shell t[40]. In Euclidean space K_t would be expected to be linear in t, such that

$$K_t = At + B(k), \tag{4}$$

for $t \geq \zeta$, where ζ is the ring correlation length. Here, $B(k)$ should depend on the central ring size and A is a measure of the "roughness"[41,42]. Previous reported values of A range from $A = 7.3$ for a two-dimensional network[40], and $A \sim 9.45$ and $A = 11$ for a soap and a Voronoi tessellation respectively[42].

The total number of edges in shell t is

$$M_t(k) = \sum_{k'} k' N_t(k, k'). \tag{5}$$

$$\langle M_t \rangle = \sum_k p(k) M_t(k) = \sum_k \sum_{k'} p(k) k' N_t(k, k') = \sum_{k'} k' p(k') K_t(k') = \langle k K_t \rangle. \tag{6}$$

The latter simply tells us that the mean number of edges in a shell is related to the number of rings in that shell.

The effect of the magnitude of the ring size may be investigated by defining a shell charge $q_t(k)$, given by

$$q_t(k) = \sum_{k'} (\langle k \rangle - k') N_t(k, k') = \langle k \rangle K_t(k) - M_t(k). \tag{7}$$

$$\langle q_t \rangle = \langle (\langle k \rangle - k') K_t \rangle. \tag{8}$$

B. Topological Requirements.

The general topology of a network is described by Euler's formula, $N + V - E = \chi$. Here, N, V and E are the number of rings, vertices and edges, and χ is the Euler characteristic, a function of the global topology of the system. For a general network constructed from nodes with a range of coordination numbers, c, with proportion x_c, the mean coordination number, $\langle c \rangle = \sum_c c x_c$. Here the number of edges is $E = \frac{V}{2}\langle c \rangle$ and the mean ring size is $\langle k \rangle = \frac{V}{N}\langle c \rangle$ and so Euler's formula may then be rewritten as

$$\langle k \rangle = \frac{2\langle c \rangle \left(1 - \frac{\chi}{N}\right)}{\langle c \rangle}. \tag{9}$$

In the present work the network is constructed exclusively from nodes of degree three and so $\langle c \rangle = 3$ and $\chi = 0$ (corresponding to an infinite plane), resulting in a mean rings size, $\langle k \rangle = 6$.

A more useful level of available information is given by the ring size distribution, p_k, the distribution of different ring sizes in a given network. Lemaître *et al.* employed a maximum entropy method to determine the distributions with the entropy given by $S = -\sum_k p_k \log p_k$[43]. The system is subject to three constraints; $\sum_k p_k = 1$, $\sum_k k p_k = \langle k \rangle$, and $\sum_k \frac{p_k}{k}$ =constant. The first two correspond to the distribution being normalised and the fixed mean ring size. The third constraint was originally justified through constraining the ring areas, although it can be fully rationalised by considering the ring adjacencies[44]. The distributions obtained from the maximum entropy solutions can be summarised through the variance (equation 2) and the plot of μ_2 *v.* p_6 is known as Lemaître's law. For $p_6 \gtrsim 0.5$ the distributions are dominated by 5-, 6- and 7-membered rings and so μ_2 shows a linear dependence on p_6 ($\mu_2 = 1 - p_6$). For a distribution in which both smaller and larger rings are permitted, μ_2 becomes larger and depends on p_6 in a non-linear fashion. Configurations not sitting on the Lemaître curve do so either due to a finite system size effect or because of enthalpic effects meaning the ring size distribution does not reflect the maximum entropy solution. Obvious examples are crystalline networks. For example, space can be completely tiled by $\{4-, 8-\}$membered or $\{3-, 12-\}$membered rings respectively (see ref.[45] and references therein). In addition, so-called procrystalline structures, in which the sites are ordered but linked by a disordered array of bonds, may also 'violate' Lemaître's law[46].

C. Ring adjacency probabilities within a shell.

For a given ring size distribution in a given shell the probability of an $k-$membered ring being adjacent to a ring of size k' can be calculated and compared to the values extracted from the model configurations. In general, the probability of an k-ring being next to a k'-ring is,

$$P_{kk'}^{(t)} = \frac{n_k^{(t)}}{k_{cent}} \frac{n_{k'}^{(t)} - \delta_{kk'}}{k_{cent} - 1}, \tag{10}$$

where $n_k^{(t)}$ is the absolute number of $k-$membered rings in shell t. For the first shell ($t = 1$) the number of rings is equal to the size of the central ring, k_{cent}, and so $\sum n_k^{(1)} = k_{cent}$.

The probability of a 4-ring being next to a 4-ring is,

$$P_{44}^{(1)} = \frac{n_4^{(1)}}{k_{cent}} \frac{n_4^{(1)} - 1}{k_{cent} - 1}, \tag{11}$$

and the probability of a 4-ring being next to a 5-ring is,

$$P_{45}^{(1)} = \frac{n_4^{(1)}}{k_{cent}} \frac{n_5^{(1)}}{k_{cent} - 1} \equiv P_{54}^{(1)}. \tag{12}$$

If we assume that the first shell contains 4- and 5-rings only then $p_4^{(1)} = \frac{n_4^{(1)}}{k_{cent}}$ and $p_4^{(1)} + p_5^{(1)} = 1$, where $p_n^{(t)}$ is the fraction of $k-$membered rings in shell t, and so $P_{TOT} = P_{44}^{(1)} + P_{45}^{(1)} + P_{54}^{(1)} + P_{55}^{(1)} = 1$.

III. POTENTIAL MODELS AND METHODS.

The method for growing the ring systems from a specified seed (here, a ring whose size can be controlled) has been presented in detail in ref.[47]. In summary, the original systems to be grown were SiO_2 bilayers (two layers of

corner-linked SiO_4 tetrahedra). The presence of a mirror symmetry plane between the upper and lower layers means that the system maps exactly onto a two-dimensional network of vertex-sharing [SiO_3] triangles. For simplicity each [SiO_3] unit is modelled via harmonic potentials which act between the three Si-O and three O-O nearest-neighbour pairs and so,

$$U_{\alpha\beta} = \frac{k}{2}\left(d_{\alpha\beta} - d^0_{\alpha\beta}\right)^2, \tag{13}$$

where k is a bond force constant, $d_{\alpha\beta}$ is the interatomic separation and $d^0_{\alpha\beta}$ the equilibrium interatomic separation between species $\alpha\beta$. The triangular geometry requires that $d^0_{\rm OO} = \sqrt{3}\, d^0_{\rm SiO}$. The angle between neighbouring triangle (which controls the strain associated with the formation of different ring sizes) is governed by a shifted/cut 24-12 potential of the form:

$$U = \begin{cases} \epsilon\left[\left(\frac{r_0}{r}\right)^{24} - 2\left(\frac{r_0}{r}\right)^{12}\right] + \epsilon, & r \le r_0 \\ 0, & \text{otherwise} \end{cases} \tag{14}$$

where ϵ is a constant and r is the Si–Si distance between atoms in neighbouring [SiO_3] triangles. r_0 controls the Si–O–Si angle, denoted ϕ_0, which can be related to the internal angle in the ring, θ_0, by $\phi_0 = 60^\circ + \theta_0$. The ideal hexagonal lattice is taken as the zero of energy and so $\phi_0 = 180^o$ and hence $r_0 = 2r_{SiO}$. As a result, the formation of rings whose internal angle deviates from θ_0 (which corresponds to an ideal hexagon) will result in an energetic penalty. The network is grown from a central seed (here a ring whose size is termed k_{cent}). The triangles on which to build the next rings are then established and the probability of constructing rings of different sizes is determined. Trial ring systems (within a given specified range of ring sizes) are built and their geometries optimised to determine the energy change. As a result, the probability of adopting a ring of size n can be determined as

$$P_n = \frac{e^{-(E_n - E_0)/T}}{\sum_n e^{-(E_n - E_0)/T}}, \tag{15}$$

in which E_n and E_0 correspond to the energy of the trial structure and the lowest energy of *all* trial structures respectively. T is a "temperature" which controls the ease by which the potential energy landscape can be explored (and hence controls the forming ring distribution). At low T acceptance moves are dominated by the energy term and hence the lowest energy rings are selected, which will depend on the local environment (*i.e.* they will not necessarily be hexagons). At high T the acceptance probabilities for different ring sizes are approximately equal, and the rings selected are more random. The "temperature" is the key parameter for controlling the distribution of ring sizes in the networks.

System sizes containing a total number of rings as 500, 1000, 2000, 5000 and 10000 were used throughout. A range of temperatures were employed from $T^* = 10^{-5}$ to $T^* = 5\times10^{-3}$. Central rings sizes from $k_{cent} = 5$ to $k_{cent} = 35$ were considered. Taking a Si-O nearest-neighbour separation as $\sim$1.61Å then these large rings correspond to diameters between $\sim$4.4-35.8Å.

IV. RESULTS.

The effect of the central (seed) ring is first considered in terms of the distribution of ring sizes. The direct structural effects are then considered both in terms of the geometrical and topological shells, then the structures of the individual shells are analysed.

A. Network Images.

Figure 1 shows four example "snapshots" generated at low temperature ($T^* = 10^{-5}$) for four central ring sizes of k_{cent} =10, 16, 25 and 35. In all cases the structural effects of the presence of the central ring are clear. For the smallest central ring size shown, $k_{cent} = 10$, for example, the first shell ($t = 1$) contains only 5- and 6-membered rings. The next largest central ring size shown, $k_{cent} = 16$, shows a mix of 4-, 5- and 6-membered rings. The largest central rings ($k_{cent} = 25, 35$), however, show only 4- and 5-membered rings in $t = 1$. For $k_{cent} = 25$ the first shell itself appears highly ordered with clear chains of 4-, 5-, 4-, 5-... rings. For $k_{cent} = 35$ the first shell also contains a number of neighbouring 4-membered rings which appear to place strain on the central ring, distorting it away from the ideal circular geometry. Ordering effects at longer length-scales are also apparent. For the three larger central ring sizes

shown, for example, the second shell ($t = 2$) appears dominated by relatively large ($k \geq 7$) rings. Furthermore, the ordering effect of the larger central rings clearly percolates beyond even the second ($t = 2$) topological shell with an excess of 5-membered rings evident in the third ($t = 3$) shell for $k_{cent} = 35$, for example. In addition to the apparent ordering of the rings in concentric topological shells, it is also clear that the larger rings appear highly distorted.

The overall impression portrayed by the images shown in figure 1 is that the central (seed) ring may have a significant structural effect on the surrounding system, manifest in the sizes of rings in concentric shells, the distribution of rings in those shells, and the ordering of rings in those shells. As a result, it is instructive to understand the length-scales over which any structural effects are significant.

B. Distributions.

A common method for displaying the distribution of ring sizes is via a Lemaître curve, a plot of the second moment of the ring size distribution, μ_2, against the fraction of six-membered rings, p_6. Figure 2(a) shows the Lemaître curve with data from all configurations generated for $N_{rings} = 500$ at all temperatures along with the ideal curves generated using the constrained $\{567\}$ and unconstrained distributions. At high p_6 the ideal constrained and unconstrained curves are equivalent as these networks are comprised mainly of $5-$, $6-$ and $7-$membered rings. In this regime (corresponding to $p_6 \gtrsim 0.6$) the dependence of μ_2 on p_6 is near-linear, with $\mu_2 \simeq 1 - p_6$. As the size of the central ring increases the calculated moments move away from the expected behaviour. Under the simulation conditions considered rings of the size $4 \leq n \leq 12$ are reasonably expected to be favoured. As a result, the forced introduction of a significantly larger (central) ring would be expected to affect the distribution of the remaining rings. Figures 2(b) and (c) show the mean average second moments for each temperature and for a range of ring sizes respectively and which clearly shows the departure from the ideal Lemaître curve with increasing ring size. Increasing temperature corresponds to moving along the Lemaître curve to lower p_6 (figure 2(b), corresponding to greater disorder). Figure 2(c) highlights the increasing "drift" from the ideal ME curve with increasing k_{cent}. The deviation from the ME solution simply arises from the enforced presence of a large central ring distorted the ideal distribution. For $k_{cent} \gtrsim 12$ the probability of a ring of that size forming at random is close to zero which forces a non-ME solution.

The degree of deviation from the ME solution is, of course, system size dependent. To highlight this figure 2(d) Lemaître curve with for four system sizes plotted for $k_{cent} = 30$ and $T = 0.003$. As the system size increases from $N_{rings} = 500 \longrightarrow 1000 \longrightarrow 2000 \longrightarrow 10000$ the second moment "moves back" towards the ME solution. Figure 2(e) shows the *difference* between the mean calculated second moment and that generated using a ME solution, $\Delta\mu_2 = \langle\mu_2\rangle - \mu_2^{ME}$, generated for six different central ring sizes. $\Delta\mu_2$ is shown as a function of $\sqrt{N}$ which is directly proportional to the radius of the growing structure. This behaviour allows a length-scale over which the distribution tends to the ME solution to be established. For example, the typical standard deviation for μ_2 in an infinite periodic system is of the order of ~ 0.15 which is highlighted in figure 2(e). However, small changes in this standard deviation lead to large changes in the predicted correlation length-scales over which the system returns to the ME distribution, making this an unreliable method of assessing these length-scales.

C. Ordering.

The images shown in figure 1 strongly hint at significant ordering imposed by the presence of a central seed ring. The potential structural order imposed by the central seed ring can be considered in two ways; geometric, in which the distance between rings is a simple length, and topological, in which rings form a series of concentric shells about the seed. In this section we consider the ordering in geometric and topological terms before considering any ordering within specific shells.

1. Geometric shells.

Figure 3 shows the spatial radial distribution functions (rdf), $g(r)$, calculated using the centres of mass of the rings and taken relative to the centre of mass of the central seed ring. Panels (a) and (b) show the rdfs determined at low and high temperature at six different central ring sizes. At both temperatures the effect of the central ring size is clear with the first peak (corresponding to the first coordination shell) shifting to higher r as k_{cent} increases. At the lowest T it appears that, for the smallest central rings ($k_{cent} = 5, 10$), the ordering extends to very long range, indicating potentially significant crystalline order. For larger central rings the ordering appears less dramatic at long range. In all cases, even at the highest T studied, the rdfs show significant structure at low r. Figure 3(c) shows a set of total rdfs (corresponding to $T^* = 0.003$) with the abscissa scaled in terms of the ideal radius of the central

ring, $R_{cent} = r_0/2\sin(\pi/k)$, where r_0 is the bond length. The shell structure focussed on the central ring is clear in all cases and appears to become more pronounced as k_{cent} increases. For example, the long-range order appears more pronounced at high k_{cent}. Figure 3(d) shows $g(r)$ for $k_{cent} = 30$ determined over a range of temperatures. The extension of significant ordering to high r is evident, particularly at intermediate temperatures ($T^* = 5 \times 10^{-4}, 10^{-3}$ respectively). At the highest temperatures studied the ordering becomes near "washed-out" at $r/r_0 \sim 14$.

Figure 4 shows the rdfs for $k_{cent} = 30$ at two temperatures with the respective breakdowns into contributions from each ring size, $g_\alpha(r)$, with $\alpha = 4 - 10$. The breakdown highlights the origin of the structure in the rdfs at low r. The peak at lowest r arises from the presence of $4-$, $5-$, (and a relatively small number of) $6-$membered rings. The next-nearest-neighbour peak arises from correlations with larger $n-$membered rings ($n \geq 7$). Even at the highest temperature studied, there is significant ordering on the next length-scale, corresponding to correlations with $4-$ and $5-$membered rings.

It is worth noting that, when averaged over a number of configurations, successive shells show a circular symmetry. Individual configurations (such as those shown in figure 1) may show significant distortions of the central ring, with these distortions averaged out over more than one configurations.

An alternative distribution function which may act to highlight the shell structure about the central ring may be defined by weighting in terms of the ring charge (see, for example, ref.[40]), $q_k = 6 - k$, where k is the ring size,

$$\rho G_q(r) = \sum_i (6 - k_i)\delta(\mathbf{r_i} - \mathbf{r_{cent}}), \tag{16}$$

where the sum is over all rings *excluding* the central ring, $\mathbf{r}_i$ is the position of the centre of mass of the ring i, and $\mathbf{r}_{cent}$ is the location of the centre of mass of the central ring. Figure 5(a) shows $G_q(r)$ calculated for $k_{cent} = 30$ over a range of temperatures. The alternating small, large, small ... ring structure is evident as alternating positive ($\langle n_t \rangle < 6$) and negative ($\langle n_t > 6$) peaks. As would be expected, an increase in temperature results in a smoothing of these features and a more rapid decay of the peak envelope. Figure 5(b) shows $G_q(r)$ as a function of k_{cent} determined at high temperature, with figure 5(c) showing the same functions with the abscissa scaled as previously (figure 3(d)). The oscillations in $G_q(r)$ are significantly stronger than in $g(r)$ as the effect of the oscillatory shells of small and large rings is effectively "amplified" by the presence of small ($k = 4$) and large ($k \geq 8$) rings. The weighting of the components of $G_q(r)$, by shell charge, means that this function effectively mimics the concentration-concentration Bhatia-Thornton function[48,49].

The clear shell structure evident in figure 5 emphasizes how the ring structure may map onto a model dominated by electrostatic interactions. For a system in which the inter-ionic interactions are dominated by Coulomb (electrostatic) terms, the asymptotic behavior of the total pair-correlation functions $rG_q(r)$ is given by

$$rG_q(r) \propto \exp(-a_0 r)\cos(a_1 r - \theta), \tag{17}$$

where a_0, a_1 and θ control the rate of decay of the oscillations, their frequency and phase shift respectively. a_0 is related to the correlation length as $\zeta = 1/a_0$, which is a further measure of the extent of structure imposed by the presence of the central ring. Figures 6(a) and (b) show examples of $\ln|rG_q(r)|$ as a function of the geometric distance from the central ring along with the fitted lines used to extract the correlation length. Panel (a) shows the function for a single central ring of size $k_{cent} = 30$ at seven temperatures, whilst panel (b) shows the function at a fixed temperature of $T^* = 0.003$ at six central ring sizes. Figures 6(c) and (d) show the obtained correlation lengths, ζ, as a function of both T and k_{cent}. For with $k_{cent} = 5, 10$ the behaviour appears more complex owing to extensive crystallisation at low temperatures (and as is clear in the rdfs shown in figure 3). The decrease in ζ with T for $k_{cent} \gtrsim 15$ corresponds to a more rapid decay to a standard amorphous structure on moving radially outwards from the central ring. Panels (c) and (d) also highlight the ideal topological length-scales associated with an *ideal* hexagonal lattice. At high temperatures the correlation length extends to between shells $t = 2 - 4$ (in an ideal hexagonal lattice) with a relatively weak dependence on k_{ncent}. At low temperatures the correlation lengths spread to $t > 4$.

2. Topological shells.

Figures 7(a) and (b) show the evolution of the mean rings size as a function of the topological shell t for a range of central ring sizes, k_{cent}, and at high and low temperature. The effect on the topological structure of the central ring is clear even at the highest temperature studied. For central rings with $k_{cent} > 6$ successive topological shells show mean ring sizes which are $\langle n_t \rangle < 6$, $\langle n_t \rangle > 6$... corresponding to shells containing more small, large, small... rings. As expected, the magnitude of this effect becomes larger as k_{cent} increases. For $k_{cent} < 6$ the reverse trend is observed. To highlight this figures 7(c) and (d) show the mean ring size in successive shells as a function of k_{cent} at both low and high T. Each line in figures 7(c) and (d) shows the change in the corresponding peak heights in figures

7(a) and (b). Similar trends are observed over the range of temperatures studied but are clearer at high T. The mean ring size in the first shell ($t = 1$) appears to tend to a limit of $\langle n_1 \rangle \sim 4.5$ at high k_{cent}. The mean ring size of the second shell ($t = 2$) continues to rise at a near-constant gradient of $d\langle n_2 \rangle / dk_{cent} \sim 0.06$ for $k_{cent} \gtrsim 16$ at high T and ~ 0.12 at low T, indicative of stronger ordering in the ring structure in successive topological shells at low T. For the third shell ($t = 3$) the mean ring size decreases with $d\langle n_3 \rangle / dk_{cent} \sim -0.016$, whilst for the fourth shell ($t = 4$), $d\langle n_4 \rangle / dk_{cent} \sim +0.013$, and the fifth shell ($t = 5$), $d\langle n_5 \rangle / dk_{cent} \sim -0.005$. For shells further out the mean ring size is ~ 6 with no significant change with k_{cent}.

In Euclidean space the number of rings in a given topological shell (K_t) would be expected to be linear in t (equation 4) with gradient A. The parameter A is a measure of the "roughness" of the shell structure. An ideal hexagonal net, for example, would give $A = 6$. Any rings for which $k \neq 6$ necessarily generate a deviation from the ideal value. Figure 8 shows the dependence of the parameter A shown in (a) as a function of the temperature for six values of k_{cent}, and (b) as a function of k_{cent} for seven values of the temperature. At low T ($T \lesssim 0.001$) A varies from $A \sim 6.5 - 7$. At high T the A values increase significantly to $A \sim 8 - 8.3$ simply corresponding to the higher levels of disorder present. The dependence on k_{cent} at fixed T appears much weaker and more subtle. At low temperature the disorder induced by the central ring increases with k_{cent} then falls for the largest ring size studied, $k_{cent} = 30$. At the highest temperatures studied the level of disorder actually falls as k_{cent} increases. In those cases the larger rings impose greater ordering (a narrower distribution of ring sizes) in successive shells.

The values of A vary between $A \sim 6.3 - 8.3$ depending on both k_{cent} and T, compared with published values of $A = 7.3$ for a two-dimensional network[40], and $A \sim 9.45$ and $A = 11$ for a soap and a Voronoi tessellation respectively[42]. Temperature (and hence the overall level of ring size disorder) appears a much more significant factor in determining the roughness than the central ring size itself. Furthermore, the range of values obtained for the roughness remain significantly smaller than those obtained for significantly more distorted networks.

i. First shell.

Figures 7(c) and (d) show how the mean ring size in the first shell ($t = 1$, directly neighbouring the central ring) reaches a limit of $\langle n_1 \rangle \sim 4.5$ at high k_{cent}. To further break this down figure 9 shows the fraction of different ring sizes in the first topological shell as a function of the central ring size, k_{cent}. Figures 9(a)-(c) shows the fraction of each ring size at three temperatures whilst panels (d)-(g) show the same data for different ring sizes, p_k, for $k = 4 - 7$ over a range of temperatures. At low T there are clear regimes of first shell structure. For large central rings ($k_{cent} \gtrsim 24$) the first shell is comprised *almost* exclusively from 4− and 5−membered rings, with a very small minority of 6−membered rings. Furthermore, the ratio of 4− and 5−membered rings is ∼50:50 (see below). For $12 \leq k_{cent} \lesssim 24$ the first shell is comprised of 4−, 5− and 6−membered rings only. For $k_{cent} \sim 11$ the first shell is comprised of 5−membered rings only. For $k_{cent} \lesssim 11$ the nearest-neighbour shell is comprised mainly of 5- and 6-membered rings, with 7-membered rings only present for $k_{cent} = 5$ (*i.e.* when the central ring is smaller than the required mean ring size). For $k_{cent} = 6$ the first shell is comprised exclusively of 6-membered rings, indicating the formation of a crystalline (graphene-like) structure.

As the temperature increases (panels (a)⟶(b)⟶(c) in figure 9) the magnitude of the excess of 5-membered rings (and an associated "dip" in the number of 4-membered rings) for $k_{cent} = 10$ decreases. At the highest temperature studied the fraction of 5-membered rings effectively plateaus at $k_{cent} \sim 10$ with $p_5 \sim 0.3$. For larger central rings at intermediate temperatures the first shell is still comprised mostly from 4− and 5−membered rings, although and small number of 6−membered rings are stabilised. At the highlest temperature studied more 6− and 7−membered rings are present with the number of 4−membered rings reaching a plateau at $p_4 \sim 0.55$.

It is clear from figure 7(c) and (d) and figure 9 that the fraction of 4- and 5-membered rings in the first shell increases as the central ring size increases. Indeed, at the lower temperatures the first shell becomes entirely composed of 4- and 5-membered rings. In this regime the presence of rings larger than 5-membered in the first shell can be considered as defects. To further break down the first shell structure one can consider the observed frequency of given pairs of nearest-neighbour rings in the first shell ($\{k, k'\}$) compared to a given random distribution. For the specific case of the first topological shell,

$$P^{(1)}_{k,k'} = \frac{n^{(1)}_k}{k_{cent}} \left\{ \frac{n^{(1)}_{k'} - \delta_{kk'}}{k_{cent} - 1} \right\}, \tag{18}$$

where the Kronecker-δ is required to account for "like" ($k = k'$) pairs. Figure 10 shows the differences between the observed and random frequencies of nearest-neighbour pairs in the first topological shell, $\Delta P^{(1)}_{k,k'}$. Across all temperatures the number of 4- and 5-membered ring pairs is greater than expected ($\Delta P^{(1)}_{4,5}$ is positive) from a random distribution, with concomitant fewer 4-,4-membered and 5,5-membered pairs ($\Delta P^{(1)}_{4,4}$ and $\Delta P^{(1)}_{5,5}$ are negative). At low

temperature $\Delta P^{(1)}_{k,k'}$ becomes effectively "saturated" for $k_{cent} \gtrsim 20$, indicative of the formation of a near-ideal first shell of 4-, 5-, 4-, 5-...membered rings (see the images in figure 1).

ii. Longer Range.

Figure 11 shows the distribution of ring sizes in successive shells for $k_{cent} = 5$, 10 and 35 at high and low T. The individual ring size fractions at each temperature make up the mean size information shown in figure 9. Considering first the trend as k_{cent} increases at low temperature. As k_{cent} increases the ring size distribution of the first topological shell ($t = 1$) shifts to higher $\langle k \rangle$. For $k_{cent} = 5$ the mean ring size in the first shell is unique in that $\langle k \rangle_1 > 6$. In addition, as k_{cent} increases, the separation in the $t = 1$ and $t = 2$ distributions becomes greater and a clear $\langle k \rangle_1 < 6$, $\langle k \rangle_2 > 6$, $\langle k \rangle_3 < 6$ ... structure emerges (see also figure 1). As the temperature, and hence level of network disorder, increases each central ring size shows a broadening in each distribution. However, the percolating shell structure is still very much in evidence for $k_{cent} = 35$ and the first shell structure remains visible for both $k_{cent} = 5$ and $k_{cent} = 10$.

V. DISCUSSION.

The results presented show that the spatial influence of the central ring may be estimated in a number of ways. Correlation lengths may be estimated from the apparent deviation of the ring size distribution from the maximum entropy solution. However, these values have significant underlying uncertainty and rely on the ME solution as being most applicable. A more successful method is to appeal to the analogy of the ring distribution to a system controlled by electrostatic interactions and to consider the decay of the pair distribution functions, here weighted by the shell charges.

It is clear that the presence of a (relatively large) central ring has a significant effect on the surrounding network topology, regardless of the underlying temperature (and hence level of disorder). The most dramatic effect is observed in the first ($t = 1$) coordination shell. For large central rings at low temperature this shell becomes exclusively constructed from 4- and 5-membered rings. At higher temperatures the 4- and 5-membered rings still dominate, with a small number of larger rings attaching to the central ring. The structures preferentially adopted in the first topological shell ($t = 1$) can be rationalised relatively simply in terms of ideal individual ring geometries. Figure 12 shows a schematic highlighting the key angles about a central ring of size k_{cent}. For the central ring, the external angle is given by, $\theta_{cent} = \frac{2\pi}{k_{cent}}$ radians, and the internal angle by $\alpha_{cent} = \pi\left(1 - \frac{2}{k_{cent}}\right)$ radians. For the first shell, an $n-$membered ring offers an effective curvature, β_n, given (in radians) by

$$\beta_n = \pi\left(\frac{n-4}{2n}\right), \tag{19}$$

which is the difference between 90^o (*i.e.* no curvature) and the external angle of the $k-$membered ring. As a result, a 4-membered ring ($k = 4$) shows no curvature (*i.e.* a chain of squares forms a simple straight line). The next largest ring, $k = 5$, induces a curvature of 18^o per ring and the next, $k = 6$, a curvature of 30^o per ring. As a result, a first shell comprised exclusively from 6- or 5-membered rings could surround a 6-membered ring (*i.e.* forming an ideal hexagonal net) and a 10-membered ring respectively. To surround a central ring of size $k_{cent} > 10$ requires a smaller curvature per ring than the 18^o afforded by the 5-membered rings. This can only be (realistically) achieved by the introduction of 4-membered rings into the first coordination shell. The most circular central ring can be accommodated by alternating 4- and 5-membered rings in the first shell. Placing two 4- or 5-membered rings as neighbours in the first shell forces a significant deviation from the circular symmetry of the central ring (see, for example, the configurations highlighted in figure 1). Overall, therefore, the reduction in entropy associated with the ordering of the first shell is countered by the enthapic contribution associated with retaining the near-circular geometry of the central ring.

VI. CONCLUSIONS.

In this paper the structural effect of inserting large central rings into a two-dimensional network of three-coordinate nodes has been investigated. The networks were grown from the central ring using a ring-growth Monte Carlo procedure with the size of the central ring being systematically varied. In addition, the level of disorder in the surrounding network (which is characterised by both the Monte Carlo "temperature" and the fraction of six-membered rings) has been systematically varied. The effect of the central ring on the overall network topology has been analysed in terms of both topological and geometric distances. For larger central rings the first topological shell has been found to become exclusively populated by four- and five-membered rings which leads to an effective upper limit on the size

of central ring which can effectively be accommodated. The topological shells have been found to show ordering on significant distances away from the central ring. The effective correlation lengths have been determined as a function of both central ring size and level of network disorder, which has allowed for an understanding of the potential density of large rings which may be accommodated.

ACKNOWLEDGEMENTS

We are grateful for support from the EPSRC Centre for Doctoral Training in Theory and Modelling in Chemical Sciences (TMCS), under grant EP/L015722/1. This paper conforms to the RCUK data management requirements.

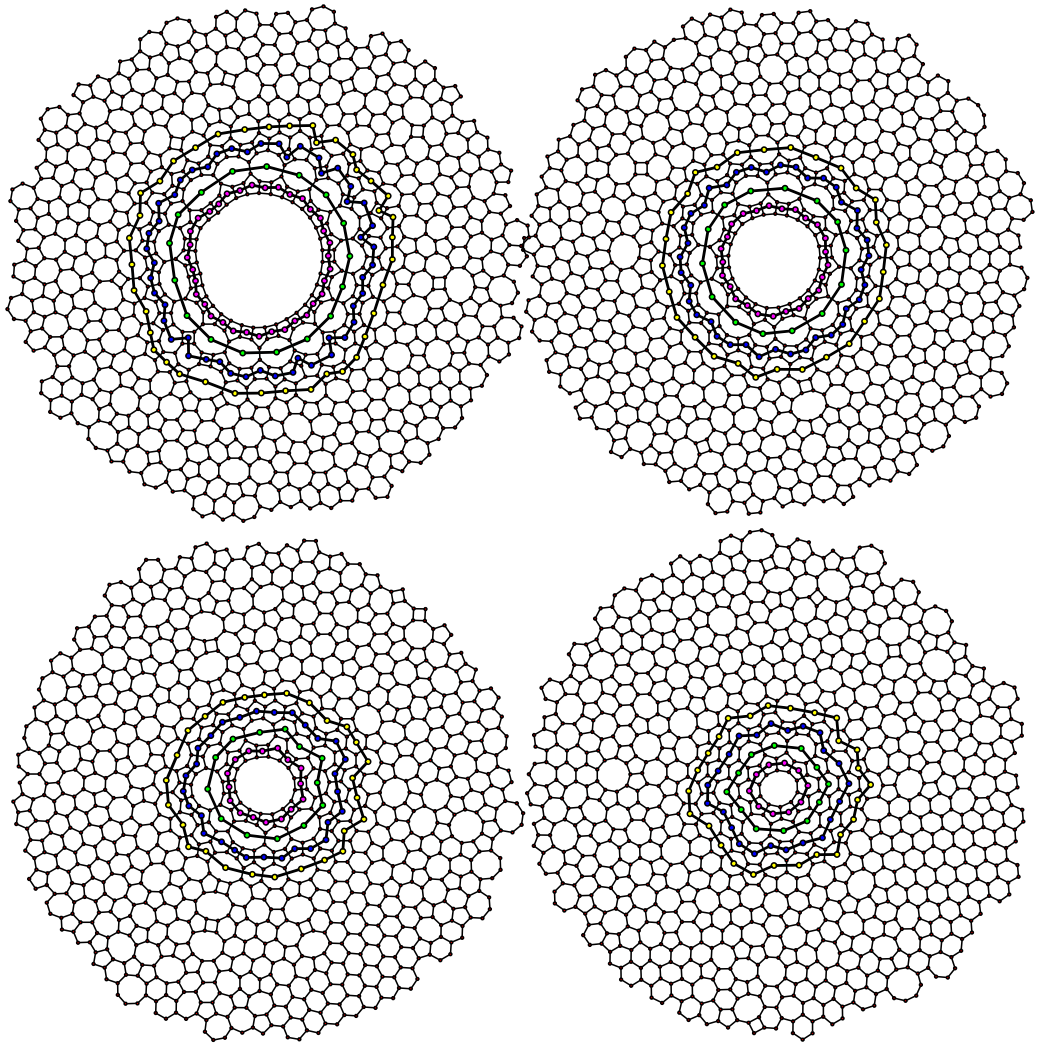

FIG. 1. Molecular graphics "snapshots" generated for four different central ring size seeds. Top left, $k_{cent} = 35$, bottom left, $k_{cent} = 16$, bottom right, $k_{cent} = 10$, top right, $k_{cent} = 25$. All four configurations are obtained at low temperature ($T^* = 10^{-5}$). In each case the centres of mass of successive topological shells are highlighted. Key: $t = 1$ - magenta, $t = 2$ - green, $t = 3$ - blue, $t = 4$ - yellow. In each case the centre of mass is each ring is shown joined to the neighbours in the same topological shell to highlight the shell structure.

[1] K. S. Novoselov, A. K. Geim, S. V. Morozov, D. Jiang, Y. Zhang, S. V. Dubonos, I. V. Grigorieva, and A. A. Firsov, Science **306**, 666 (2004).

[2] A. Neto, F.Guinea, N.M.R.Peres, K.S.Novoselov, and A.K.Geim, Rev. Mod. Phys. **81**, 109 (2009).

[3] C.-T. Toh, H. Zhang, J. Lin, A. S. Mayorov, Y.-P. Wang, C. M. Orofeo, D. B. Ferry, H. Andersen, N. Kakenov, Z. Guo, *et al.*, Nature **577**, 199 (2020).

[4] K. S. Novoselov, A. K. Geim, S. V. Morozov, D. Jiang, Y. Zhang, S. V. Dubonos, I. V. Grigorieva, and A. A. Firsov, Science **353**, arc9439 (2016).

[5] A. Pakdel, C. Zhi, Y. Bando, and D. Golberg, Materials Today **15**, 256 (2012).

[6] D. Löffler, J. J. Uhlrich, M. Baron, B. Yang, X. Yu, L. Lichtenstein, L. Heinke, C. Büchner, M. Heyde, S. Shaikhutdinov, *et al.*, Phys. Rev. Lett. **105**(14), 2 (2010), arXiv:1408.1149.

[7] P. Y. Huang, S. Kurasch, A. Srivastava, V. Skakalova, J. Kotakoski, A. V. Krasheninnikov, R. Hovden, Q. Mao, J. C. Meyer, J. H. Smet, *et al.*, Nano Lett. **12**, 1081 (2012).

[8] L. Lichtenstein, C. Buchner, B. Yang, S. Shaikhutdinov, M. Heyde, M. Sierka, R. Włodarczyk, J. Sauer, and H. J. Freund, Angew. Chemie - Int. Ed. **51**(2), 404 (2012).

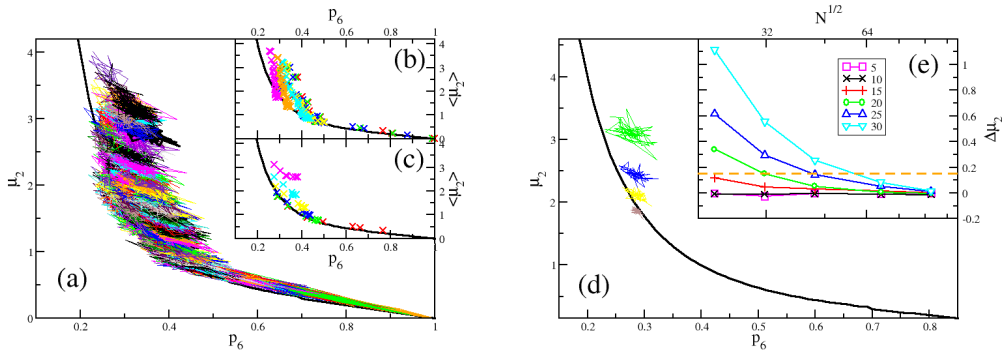

FIG. 2. Panels (a)-(d) show the Lemaître curve for exclusively three-coordinate nodes with the data from the present simulations. In panels (a)-(c) the black line shows the maximum entropy (ME) solution. Panel (a) shows all data for 7 values of the central ring size, k_{cent}, and 7 values of the temperature, T^*. Panels (b) and (c) show the respective trends with respect to T^* and k_{cent}. Panel (b) shows the mean values for each simulation at fixed temperature, varying k_{cent} and panel (c) the mean values at fixed k_{cent} and varying T^*. Panel (d) shows the effect of increasing the system size for $k_{cent} = 30$ and $T^* = 0.003$. Key: green, blue, yellow and brown lines correspond to systems of size 500, 1000, 2000 and 10000 rings respectively. Panel (e) shows the difference between the mean second moment and the ME value for six values of k_{cent} as indicated in the legend. The dashed line highlights a typical ME standard deviation which may be used to define a correlation length as described in the text.

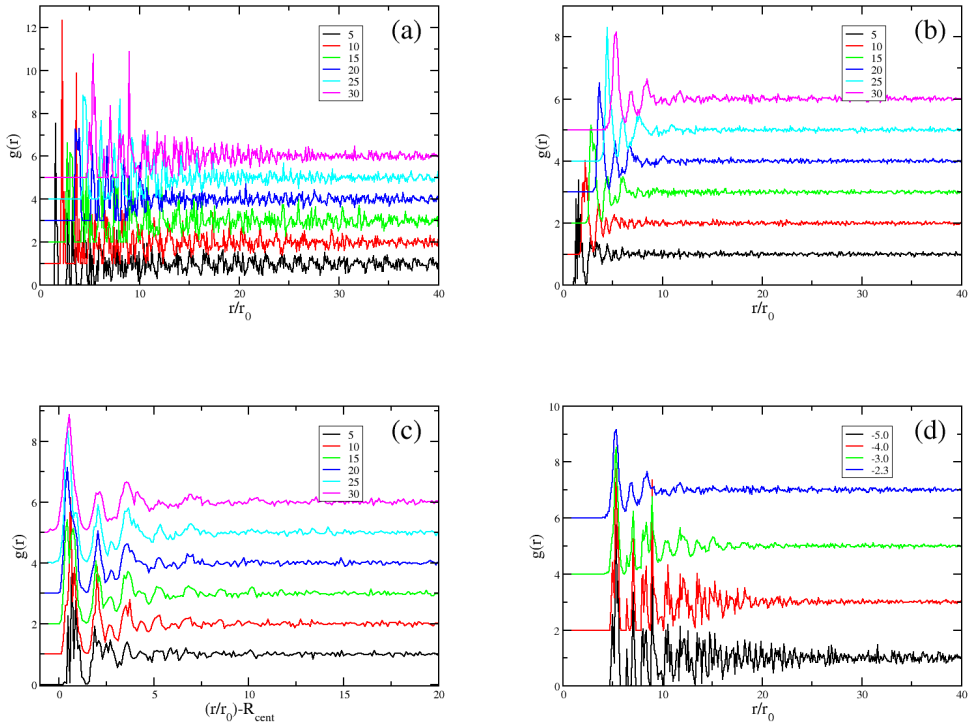

FIG. 3. Geometric radial distribution functions (rdfs), $g(r)$, determined with respect to the centre of mass of the central (seed) ring. In all cases the length-scales are "normalised" in terms of the bond length, r_0. In all cases successive functions are shifted along the ordinate axis for clarity. Panels (a) and (b) show the rdfs at low and high temperature ($T^* = 10^{-5}$ and 5×10^{-3} respectively) for six sizes of the central ring (k_{cent}) as indicated in the legends. Panel (c) shows the rdfs at $T^* = 0.003$ for six values of k_{cent} in which the abscissa is shifted in terms of the radius of the central ring, R_{cent}. Panel (d) shows the rdfs for a single large central ring, $k_{cent} = 30$, at four temperatures (as shown in the legend).

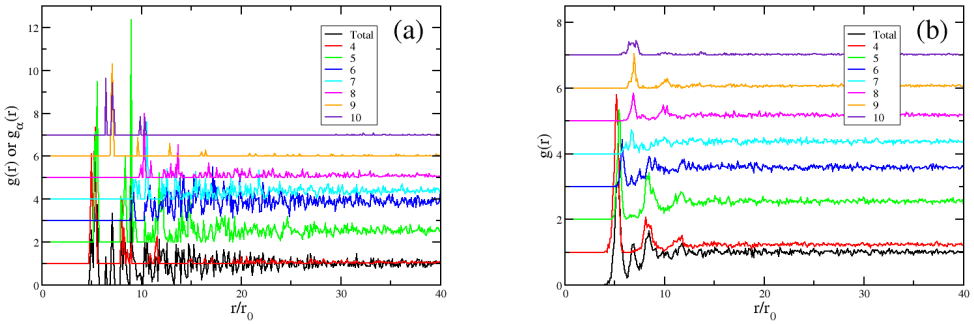

FIG. 4. Radial distribution functions, $g(r)$, determined at three temperatures along with the breakdown into respective contributions from different ring sizes, α, denoted $g_\alpha(r)$, where $\alpha = 4 - 10$ as indicated in the legend. In all cases successive functions are shifted along the ordinate axis for clarity.

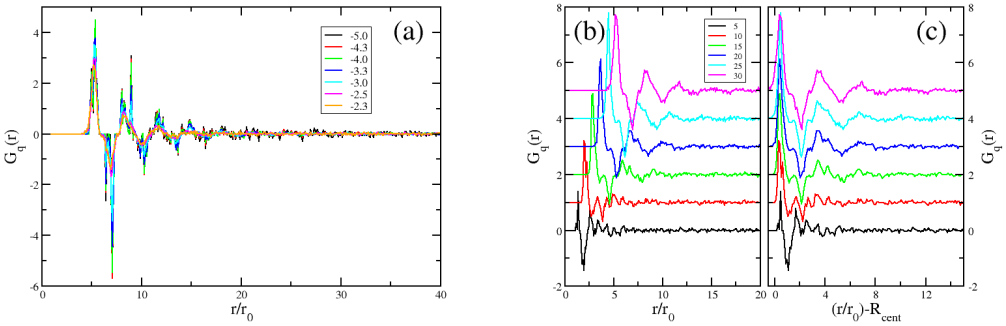

FIG. 5. Ring charge radial distribution functions, $G_q(r)$, determined for (a) $k_{cent} = 30$ at seven temperatures as indicated in the legend and, (b) for $T^* = 0.005$ at six values of k_{cent} as indicated in the legend. In panel (c) the abscissa is shifted in terms of the radius of the central ring, R_{cent}.

[9] L. Lichtenstein, M. Heyde, and H. J. Freund, J. Phys. Chem. C **116**(38), 20426 (2012).
[10] L. Lichtenstein, M. Heyde, and H. J. Freund, Phys. Rev. Lett. **109**(10), 1 (2012).
[11] M. Heyde, S. Shaikhutdinov, and H. J. Freund, Chem. Phys. Lett. **550**, 1 (2012).
[12] C. Büchner, *Adding a Novel Material to the 2D Toolbox: Properties and Transfer of a Silica Bilayer*, Ph.D. thesis (2016).
[13] C. Büchner, L. Liu, S. Stuckenholz, K. M. Burson, L. Lichtenstein, M. Heyde, H. J. Gao, and H. J. Freund, J. Non. Cryst. Solids **435**, 40 (2016).
[14] C. Büchner and M. Heyde, Prog. Surf. Sci. **92**, 341 (2017).
[15] C. Büchner, S. D. Eder, T. Nesse, D. Kuhness, P. Schlexer, G. Pacchioni, J. R. Manson, M. Heyde, B. Holst, and H. J. Freund, Phys. Rev. Lett. **120**(22), 226101 (2018).
[16] P. K. Roy, M. Heyde, and A. Heuer, Phys. Chem. Chem. Phys. **20**, 14725 (2018).
[17] A. L. Lewandowski, P. Schlexer, C. Büchner, E. M. Davis, H. Burrall, K. M. Burson, W. D. Schneider, M. Heyde, G. Pacchioni, and H. J. Freund, Phys. Rev. B **97**(11), 115406 (2018).
[18] A. W. Robertson, G.-D. Lee, K. He, E. Yoon, A. I. Kirkland, and J. H. Warner, Nano Lett. **14**, 3972 (2014).
[19] J. C. Earnshaw and D. J. Robinson, Phys. Rev. Lett. **72**(23), 3682 (1994).
[20] C. Allain and L. Limat, Phys. Rev. Lett. **74**(15), 2981 (1995).
[21] M. Durand, J. Käfer, C. Quilliet, S. Cox, S. A. Talebi, and F. Graner, Phys. Rev. Lett. **107**, 168304 (2011).
[22] M. Tong, K. Cole, P. R. Brito-Parada, S. Neethling, and J. J. Cilliers, Langmuir **33**, 3839 (2017).
[23] M. C. Gibson, A. B. Patel, R. Nagpal, and N. Perrimon, Nature **442**, 1038 (2006).
[24] R. Carter, Y. E. Sánchez-Corrales, M. Hartley, V. A. Grieneisen, and A. F. M. Marée, Development **144**, 4386 (2017).
[25] L. Goehring and S. W. Morris, Phys. Today **67**(11), 39 (2014).
[26] D. Brutin, B. Sobac, B. Loquet, and J. Sampol, J. Fluid Mech. **667**, 85 (2011).
[27] F. Glassmeier and G. Feingold, PNAS **114**(40), 10578 (2017).
[28] G. Le Caër and R. Delannay, J. Phys. I Fr. **3**, 1777 (1993).

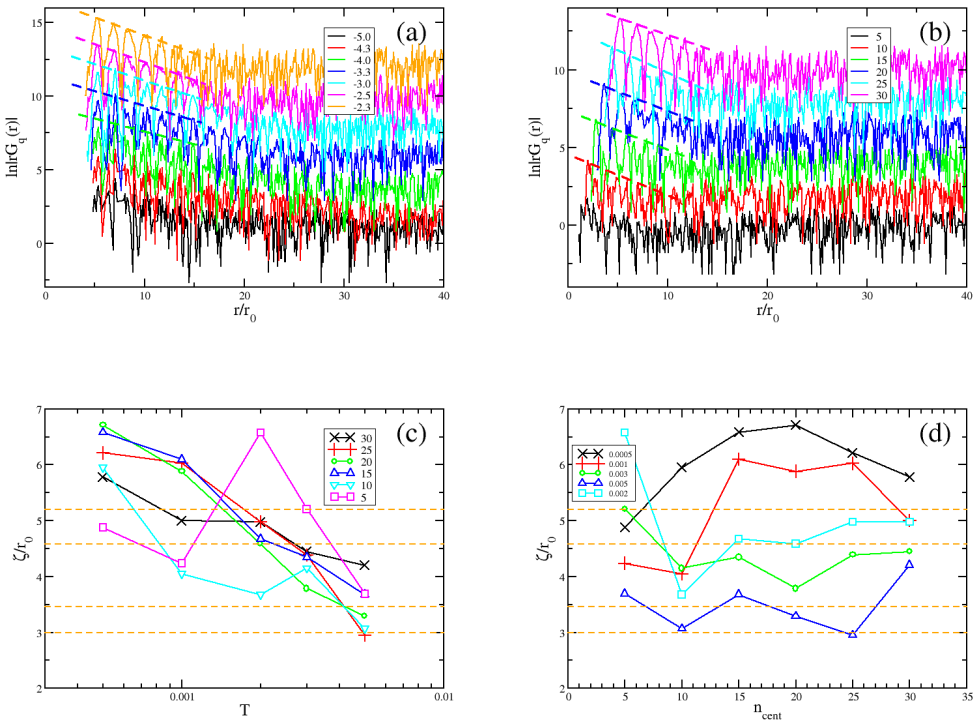

FIG. 6. Panels (a) and (b) show the ring charge radial distribution functions, $G_q(r)$, as ln$|\ rG_q(r)\ |$, in order to highlight the extraction of the correlation length from the envelope gradients (dashed lines). Panel (a) shows the function for a single central ring size ($k_{cent} = 30$) at seven temperatures, as indicated by the legend, whilst panel (b) shows the function at a fixed temperature of $T^* = 0.003$ for six central rings sizes, again as indicated by the legend. The dashed lines in panels (a) and (b) highlight example fits to equation 17. Panels (c) and (d) show the respective values of the correlation length, ζ, shown in units of the bond length, r_0. Panel (c) shows ζ as a function of temperature for six central ring sizes (as indicated in the legend) and panel (d) shows ζ as a function of k_{cent} at five temperatures (again, as indicated in the legend).

[29] G. Schliecker and S. Klapp, Europhys. Lett. **48**, 122 (1999).
[30] S.P.Koenig, L.Wang, J.Pellegrino, and J.S.Bunch, Nat. Nanotechnol. **7**, 728 (2012).
[31] K.Celebi, J.Buchheim, R.M.Wyss, A.Droudian, P.Gasser, I.Shorubalko, J.-I.Kye, and C. H.G.Park, Science **344**, 289 (2014).
[32] S.C.O'Hern, M.S.H.Boutilier, J.-C.Idrobo, Y.Song, J.Kong, T.Laoui, M.Atieh, and R.Karnik, Nano. Lett. **14**, 1234 (2014).
[33] S.P.Surwade, S.N.Smirnov, I.V.Vlassiouk, R.R.Unocic, G.M.Veith, S.Dai, and S.M.Mahurin, Nat. Nanotechnol. **10**, 459 (2015).
[34] S.M.Gilbert, G.Dunn, A.Azizi, T.Pham, B.Shevitski, E.Dimitrov, S.Liu, S.Aloni, and A.Zettl, Sci. Rep. **7**, 15096 (2017).
[35] J.P.Thiruraman, K.Fujisawa, G.Danda, P.M.Das, T.Zhang, A.Bolotsky, N.Perea-López, A.Nicolaï, P.Senet, M.Terrones, *et al.*, Nano. Lett. **18**, 1651 (2018).
[36] K. Zhao, X. Li, and Q. Wang, Phys Chem Chem Phys **21**(246), 246 (2019).
[37] P.Cheng, M.M.Kelly, N.K.Moehring, W.Ko, A.-P.Li, J.C.Idrobo, M.S.H.Boutilier, and P.R.Kidambi, Nano. Lett. **20**, 5951 (2020).
[38] J.Liu, L.Jin, F.I.Allen, Y.Gao, P.Ci, F.Kang, and J.Wu, Nano. Lett. **21**, 2183 (2021).
[39] D.Naberezhnyi, L.Mai, N.Doudin, I.Ennen, A.Hütten, and E.I.Altman, Nano. Lett. **22**, 1287 (2022).
[40] M. Sadjadi and M. F. Thorpe, Phys. Rev. E - Stat. Nonlinear, Soft Matter Phys. **94**(6), 1 (2016).
[41] C. Oguey and N. Rivier, J. Phys. A Math. Gen. **34**, 6225 (2001).
[42] T. Aste, K.-Y. Szeto, and W.-Y. Tam, Phys.Rev.E **54**, 5482 (1996).
[43] A. Gervois, J. P. Troadec, and J. Lemaitre, J. Phys. A **25**, 6169 (1992).
[44] D. Ormrod Morley, A. Thorneywork, R. Dullens, and M. Wilson, Phys. Rev. E pp. 1–13 (2020).
[45] A. Malashevich, S. Ismail-Beigi, and E. I. Altman, J. Phys. Chem. C **120**, 26770 (2016).
[46] D. Ormrod Morley, A. L. Goodwin, and M. Wilson, Phys. Rev. E **102**(6), 1 (2020).
[47] D. Ormrod Morley and M. Wilson, Mol. Phys. **117**(21), 3148 (2019).
[48] A.B.Bhatia and D.E.Thornton, Phys.Rev.B **2**, 3004 (1970).
[49] P.S.Salmon, Proc: Maths and Phy. Sci. **437**, 591 (1992).

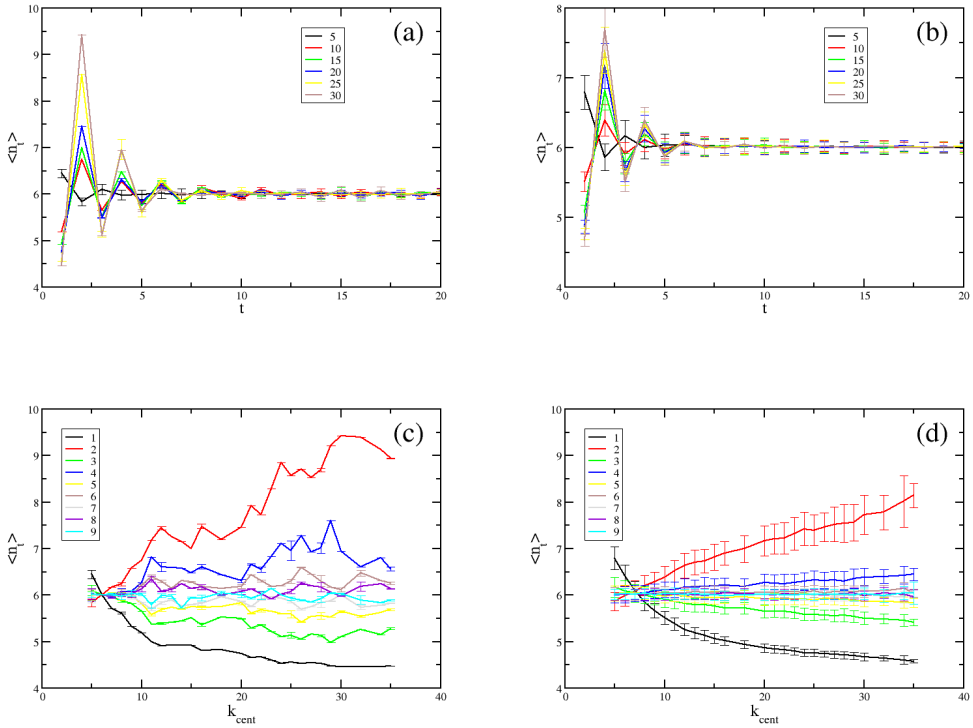

FIG. 7. Panels (a) and (b) show the mean ring size, $\langle n_t \rangle$, as a function of the topological shell, t, shown for six central ring sizes as indicated in the legend and at (a) $T^* = 10^{-5}$, and (b) $T^* = 0.005$. Panels (c) and (d) show the mean ring size in successive topological shells (t, as indicated in the legend) as a function of the size of the central ring, k_{cent} at the same two temperatures.

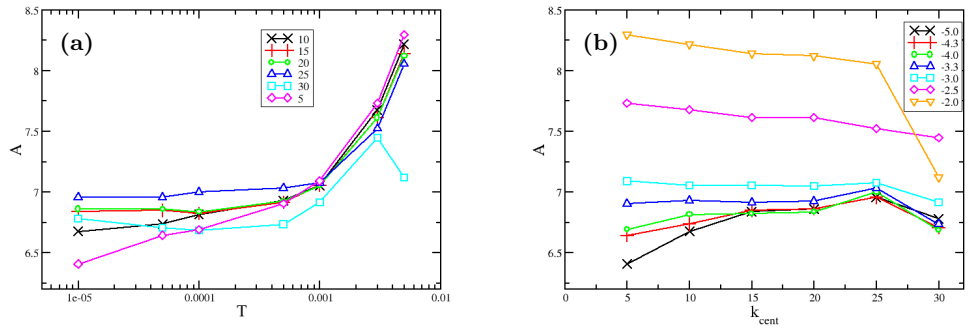

FIG. 8. The gradients, A, to the fit of the number of rings in each shell, K_t, against t such that $K_t = At + B$. Panel (a) shows A as a function of the temperature, T (shown on a log scale) for six values of the central ring size, k_{cent} (as indicated by the legend). Panel (b) shows A as a function of k_{cent} at six temperatures (again, as indicated by the legend).

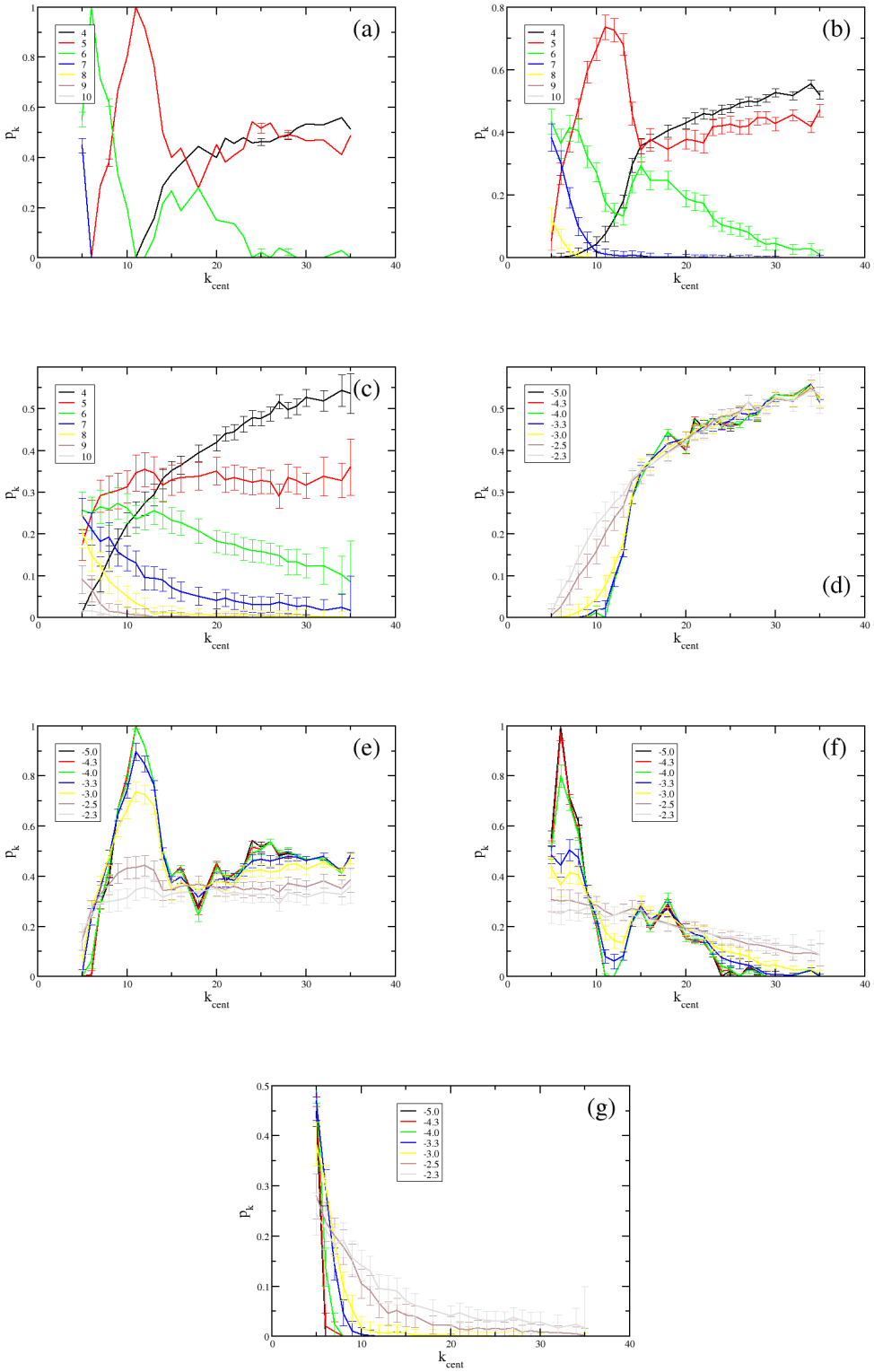

FIG. 9. The fraction of each ring sizes n (as indicated in the legend) in the first topological shell about the central ring, shown as a function of the central ring size, k_{cent}. Panels (a)-(c) show the fractions, p_n, at low, intermediate and high temperatures ($T^* = 10^{-5}$, 10^{-3}, and 5×10^{-3} respectively). Panels (d)-(g) show the changes in the fractions of $4-$, $5-$, $6-$ and $7-$membered rings int the first topological shell over seven temperatures (as indicated in the legends, on a log scale).

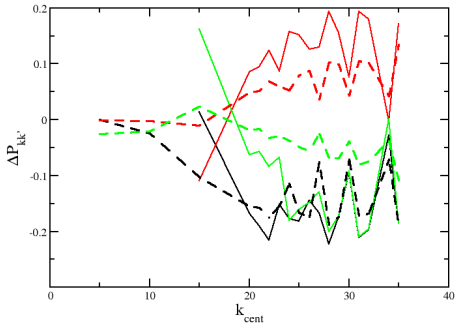

FIG. 10. Difference in the probability of a ring of size k being adjacent to a ring of size k' in the first ($t = 1$) topological shell, compared to a random distribution, $\Delta P^{(1)}_{kk'}$. The black, red and green lines correspond to $\Delta P^{(1)}_{44}$, $\Delta P^{(1)}_{45}$, and $\Delta P^{(1)}_{55}$ respectively. The solid and dashed lines correspond to $T^* = 10^{-5}$ and $T^* = 5 \times 10^{-3}$ respectively.

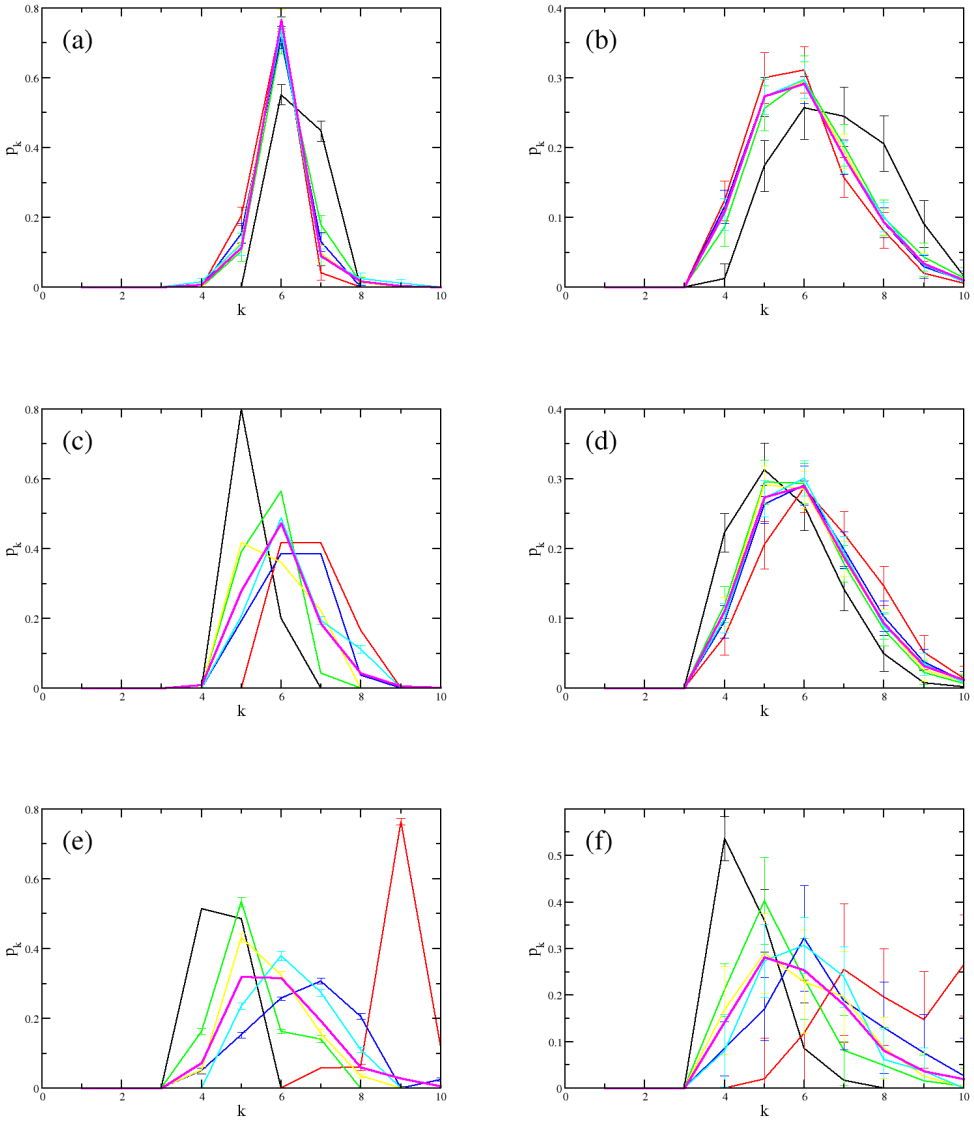

FIG. 11. Ring size distributions in successive topological shells. The black, red, green, blue, yellow, cyan and magenta lines correspond to $t = 1, 2, 3, 4, 5, 6$ and 7 respectively. Panels (a) and (b) are for $k_{cent} = 5$, panels (c) and (d) for $k_{cent} = 10$, panels (e) and (f) for $k_{cent} = 35$. Panels (a), (c) and (e) [left] are for $T^* = 10^{-5}$ and panels (b), (d) and (f) [right] are for $T^* = 5 \times 10^{-3}$.

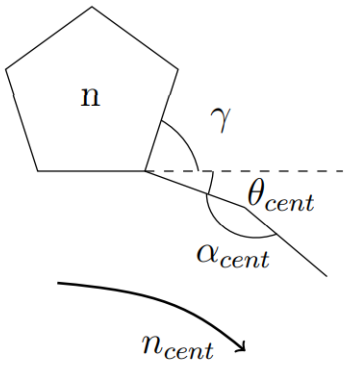

$$\gamma = \frac{2\pi}{n}$$

$$\theta_{cent} = \frac{2\pi}{n_{cent}}$$

$$\alpha_{cent} = \pi(1 - \frac{2}{n_{cent}})$$

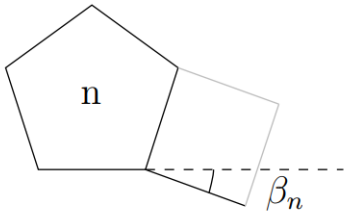

$$\beta_n = \frac{\pi}{2} - \gamma = \pi(\frac{n-4}{2n})$$

FIG. 12. Schematic to highlight the relationship between the external angle of the central ring, θ_{cent}, and the angles associated with the rings in the first topological shell.

7.2 Conclusions

A range of directed ring growth structures have been presented, using central ring templates ranging from small ($n = 5$) through larger rings ($10 \leq n \leq 30$), which are beyond the range of ring sizes so far found in amorphous systems. The simulations use a ring growth Monte Carlo method to introduce disorder into structure. The effect of the central ring size on the surrounding system is evaluated in terms of the distribution of rings surrounding the central templated ring, both in terms of the geometric distance and topological distance. With larger central ring size, these systems show significant ordering, especially close to the central ring size. Effective correlation lengths have been determined to evaluate the upper density of large rings that the system can accommodate.

8

Direct control of pores in network structures: Periodic "node evaporation" methods

8.1 Motivations

Chapter 7 focused on a novel application of a published[124, 135] approach to silica bilayer structural generation. This method utilises ring growth dynamics, starting from a seed whose ring size is predetermined. The structure is defined as vertex sharing SiO_3 'triangles', forming a $SiO_{1.5}$ layer, as described in Section 5.3.3. Rings are sequentially grown around the initial ring by adding SiO_3 corner-sharing 'rafts', in a non-equilibrium process (*i.e* once a ring has been formed, it cannot be broken). The size of the new ring added is determined by a Monte Carlo process : rings of size 4-10 are trialled and the local energy of the system is probed, with the energies fed into a probability distribution to select the ring chosen. As such, a range of disordered structures can be generated by varying the Monte Carlo temperature, and the central ring size. The minimisation process is a local approach, whereby only the atom in the proposed ring and directly adjacent rings are allowed to relax. As additional rings are grown from the edges of the structure, there are always under-coordinated sites at the edges of the system.

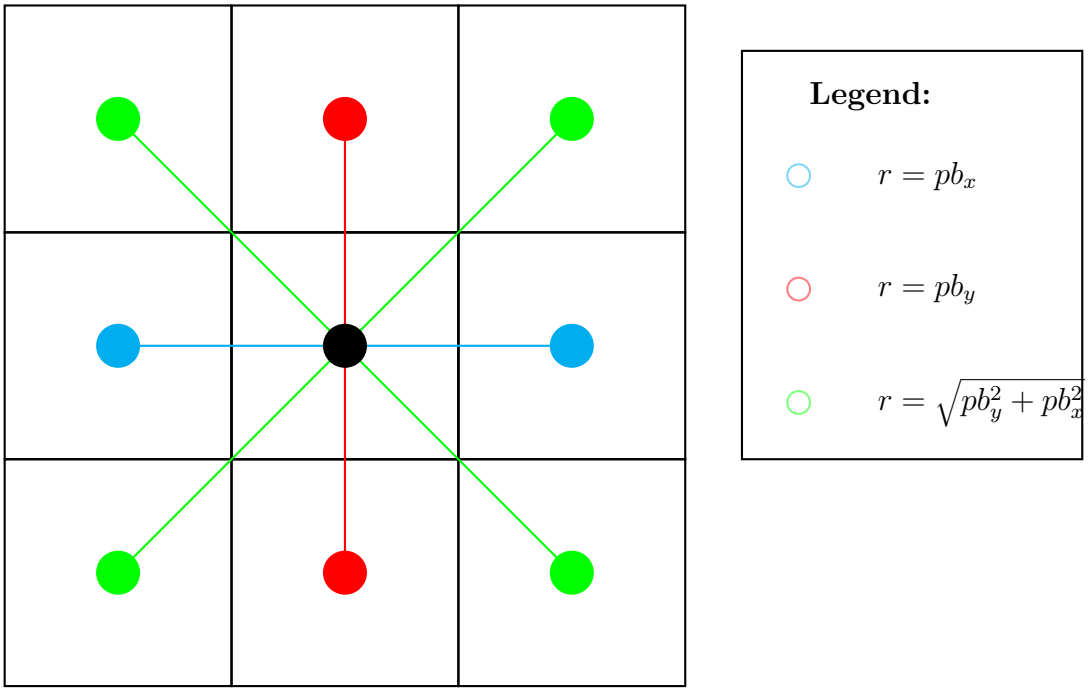

Figure 8.1: Graphic to show the nearest neighbour pores in the periodic environment

Whilst this ring growth method is a reliable means for generating large pores and understanding the behaviour of bilayer systems, there is scope to build on this approach. Firstly, we would like to generate periodic systems. This allows us to understand the effect of using potentials which rely on longer range interactions and full coordination, and so may be strongly influenced by the surface effects at the edges of the ring growth systems. Using periodic systems would allow us to understand the medium to long range interactions between pores.

By nature of having cubic periodic systems of dimensions (pb_x, pb_y), any ring in the unit cell would be surrounded by eight identical rings, with two at $r = pb_x$, two at $r = pb_y$, and four at $r = \sqrt{pb_y^2 + pb_x^2}$, as shown in Figure 8.1. As such, introducing a pore into these systems gives us a 'pore density', and by varying the size of the system, we change (pb_x, pb_y), and so can understand the ability of the structure to accommodate multiple pores.

Secondly, we would like to employ an equilibrium process to relax the system around the pores. This would ensure that the system can relax globally (which is particularly important for triangle raft structures as noted in Section 5.4.2),

and so approximate a thermodynamic product.

8.2 Periodic Node Evaporation

In order to fulfil these requirements, I have designed a software to generate periodic systems, into which large pores can be inserted in a precise, user defined manner. The software relies on a GUI, allowing the user to visualise the networks as it is being created. The user can select nodes to 'evaporate' from the surface, resulting in mixed coordination nodes on the internal surface. Once the required number of nodes have been evaporated, the user ends the pore creation process, and potential connections between undercoordinated nodes are evaluated. My algorithm for this process relies on our understanding of the underlying network. In order for two undercoordinated nodes to connect together, reforming rings, they must have originally been members of the same ring. As such, it is possible to pick a random starting node, and evaluate which of the remaining undercoordinated nodes were originally members of the same rings as this node. Where there are two candidates, two paths can be created, one moving clockwise and one anticlockwise around the internal surface. This process returns up to two potential connection pathways, resulting in two options for pore creation.

As an example, Figure 8.2 shows the effect of removing six nodes from an ideal hexagonal net. The removal of this hexagon of nodes results in the formation of six under-coordinated (two-coordinate) nodes (Figure 8.2b). Full three-coordination may be reestablished by joining these nodes as shown in Figure 8.2c. In this example, therefore, a relatively large ring of size k = 12 has been formed which is "balanced" by the concomitant formation of three four-membered rings (and hence the mean ring size remains, as it must, as six). Nodes can be removed in any number of ways.

8.2.1 Pathological structures

For a given user generated structure, there at most two connection pathways which return fully coordinated solutions. There are pathological solutions where fewer than two connection pathways are feasible. The first type are coordination disallowed

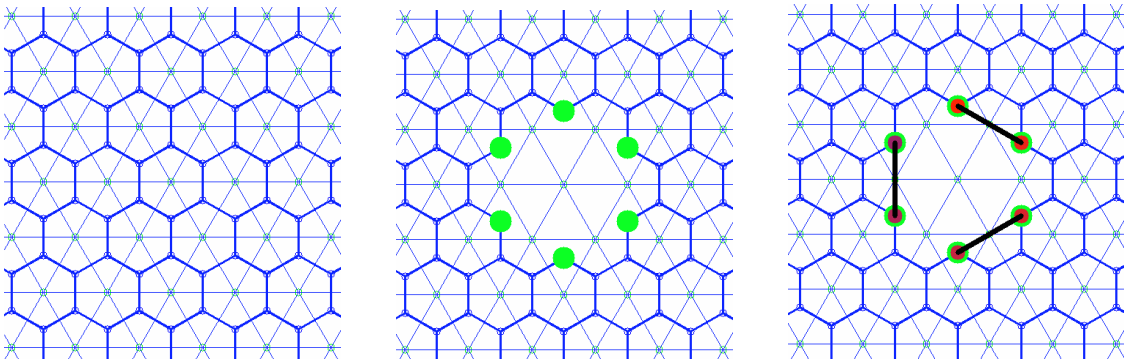

Figure 8.2: Graphic to show the pore evaporation process, starting with a pristine lattice (a), followed by evaporation of 6 nodes, leaving to a pore surrounded by undercoordinated nodes, shown in green (b). Finally the structure created by coordinating the remaining nodes with new bonds, shown in black (c)

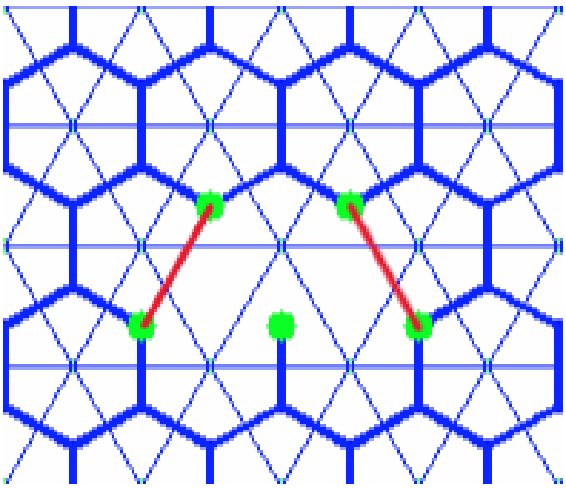

Figure 8.3: Graphic to show a pathological configuration which is coordination disallowed.

solutions. These are more common where a node is reduced to single coordination by evaporating two neighbouring nodes, or where there are uncoordinated nodes which share an edge. An example is given in Figure 8.3, where the presence of the single coordinate node means that this 'walk' round the internal surface cannot maintain full three coordination.

The second type are ring size disallowed configurations. All experimental evidence points to an absence of three membered rings for graphene and silica bilayer systems. Figure 8.4 shows an example where the network cannot be reconnected without forming three membered rings.

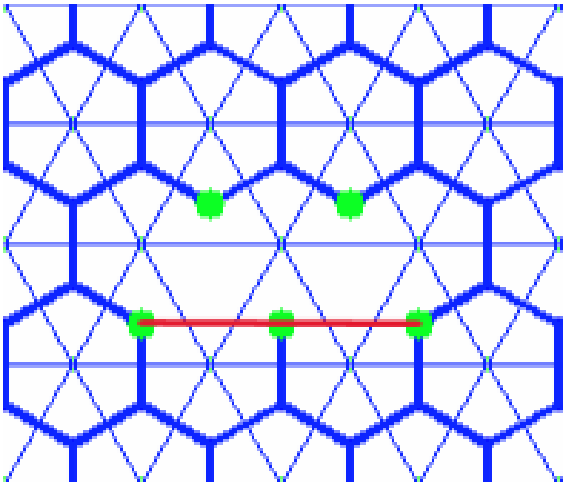

Figure 8.4: Graphic to show a pathological configuration which is ring-size disallowed.

Whilst each user generated structure can only form one of two final configurations, there are a number of user generated structures which can produce a given ring size. Examples of three different ways of forming a ring of size $n = 24$ are shown in Figure 8.5.

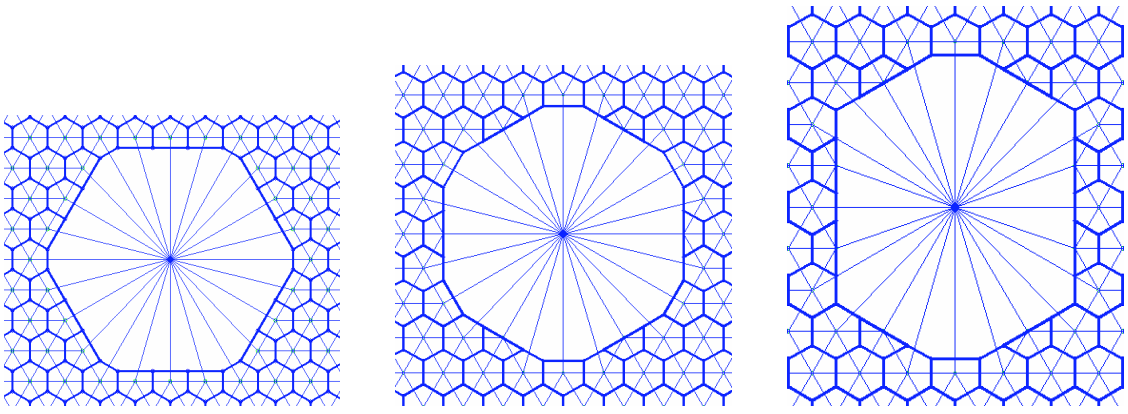

Figure 8.5: Three different pores generated using the periodic node evaporation GUI, each with the same central ring size (24), but different numbers of compensating 4 and 5 membered rings.

These structures have the same pore size, but their ring distributions and pore shapes are very different, with (a) consisting of only 4 and 6 membered rings about the pore, (b) consisting of only 5 and 6 membered rings about the pore, and (c) incorporating 4, 5 and 6 membered rings about the pore.

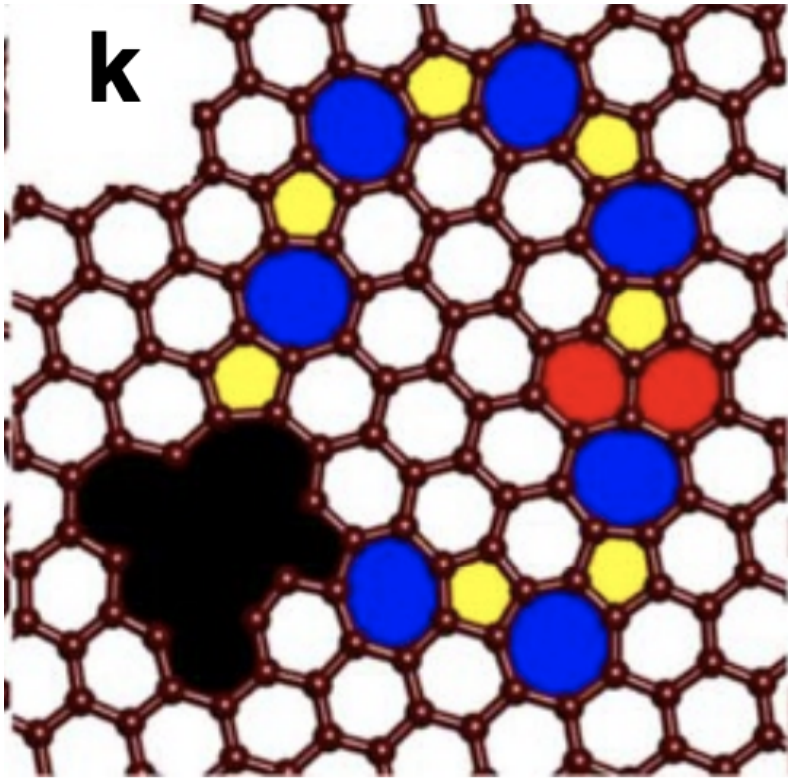

Figure 8.6: Image of an experimental graphene 'pore', generated by irradiation of crystalline graphene with an electron beam, showing potential under-coordination. Reproduced from literature[3]

8.2.2 Experimental Comparisons

The periodic node evaporation technique is similar to the effect of experimental processes to generate pores in graphene[3, 24, 160, 161]. In these experiments, the resulting structures may be under-coordinated, as seen in Figure 8.6.

By contrast, our network structures maintain three coordinate sites, and as such this process creates strained structures, with distorted node-node angles and distances (see Figure 8.2c).

8.2.3 Effect of pore on natural area

Removing nodes also reduces the number density, changing the periodic lengths in x and y. The minimum energy structure depends on the potential model used. For consistency, we have used the graphene potential (as in Chapter 5), as the simplest potential model evaluated in this thesis. Using this potential, we search the

energy surface around the initial periodic boundary conditions (pb_x^0, pb_y^0) to find the minimum energy cell dimensions using the graphene potential. Assuming the energy surface is continuous with respect to the lattice dimensions, we can approximate the energy surface in two dimensions by calculating single point energies at N values for the periodic boundary conditions (pb_x, pb_y) about the initial periodic boundary conditions (pb_x^0, pb_y^0). For our work, we have used $N = 100$, with the dimensions on the surface described in Equation 8.2.3.1;

$$(pb_x - pb_x^0)^2 + (pb_y - pb_y^0)^2 = 0.0001pb_x^0. \tag{8.2.3.1}$$

This gives a simplified energy surface about (pb_x^0, pb_y^0), which we can then use to approximate the force gradient at (pb_x^0, pb_y^0). Moving down the force gradient using Equation 4.3.4.1 moves us towards a local minimum in energy across (pb_x, pb_y).

This minimum energy structure arrived at by this method is treated as our minimised defect. However, it is worth noting at this stage that this is a reference only, and with not be the minimum energy structure for all potential models used.

8.2.4 Zeolite Formation

An interesting avenue opened by this method is the generation of structures with multiple pores of finely controlled size. In particular, we have been able to reproduce a wide array two-dimensional structures on demand. One such example is that of pseudo-two-dimensional zeolite structures. An example of AFI and AFO structures generated by this method is shown below in Figure 8.7, (a) and (b) respectively. By using this method, we can recreate the (100) projections of a subset of zeolites, which can then be adorned with atoms for further analysis. The AFO example in particular makes clear the importance of a preminimisation and rescaling, showing unrealistic four membered ring shapes. The zeolite structures selected for this treatment were selected based on an analysis of their underlying CBUs and Tiling, as discussed in Section 2.4. These structures are explored in more detail in Chapter 9, where their potential as silica bilayer structures is evaluated.

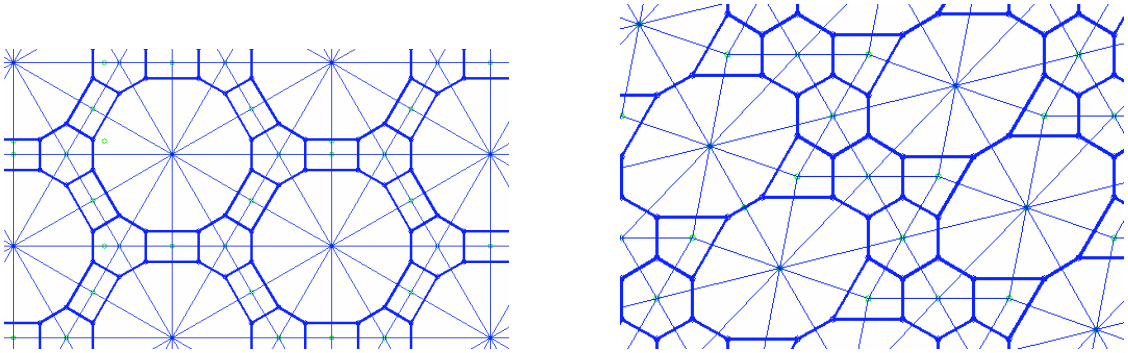

(a) (b)

Figure 8.7: Graphic to show pore evaporation process resulting in AFI (a) and AFO (b)

8.3 Relaxing Network about Pore template

Having created a periodic systems, we can use the models built and evaluated in Chapter 5 to introduced disorder, which acts to minimise the energy of the system with respect to its ring distribution and local ordering. The pore introduced via the node evaporation process is treated as fixed, and so it is not involved in any of the defect generation steps described in Section 5.2. The bond switching will act to reduce the distortion created by the presence of the large ring; without the constraint of fixing the large ring, the simplest way to reduce strain would simply be to minimise the size of the largest ring. The process does however involve the rings neighbouring the pore in the switching process. Preliminary work on a limited number of graphitic networks generated using different shaped pores indicated that, over sufficient simulation time, the pores approached a similar structure. This implies that the final configuration is invariant to initial pore shape over longer time scales, but further analysis is required for confirmation of this feature.

8.4 Monte Carlo simulations on periodic pore template

Whilst similar work in Chapter 7 has focused on varying the size of the pore, this work focuses primarily on the periodic nature of this new approach, and so a single pore size has been chosen, which has then been used as a template in a range of

system sizes, to understand the medium- to long-range interaction between pores. As such, I have replicated the same pore in six periodic square environments of cell size 70 to 370 rings (140 to 740 nodes, starting from 10×10 and 20×20 lattices respectively). The discrepancy between the cell dimensions in x × cell dimensions in y indicates half the number of nodes removed in the pore evaporation process. In addition to these six square configurations, a single hexagonal configuration was included for comparison. Table 8.1 shows the respective dimensions (number of rings along periodic x boundary × number of rings along periodic y boundary), alongside ring, node and pore count, with pore orientation and concomitant 'pore density' in pores per 1000 rings. The hexagonal system contains two pores, in order to maintain periodic cell angles at $\pi/2$ for ease of simulation.

Cell dimensions	No. Rings	No. Nodes	No. Pores	Pores/1000 rings	Pore Environment
10× 10	70	140	1	14.28	Square
12× 12	114	228	1	8.77	Square
10× 20	140	280	2	14.28	Hexagonal
14× 14	166	332	1	6.02	Square
16× 16	226	452	1	4.42	Square
18× 18	294	588	1	3.40	Square
20× 20	370	740	1	2.70	Square

Table 8.1: Characteristics of the periodic cell sizes, into which our pore template is introduced.

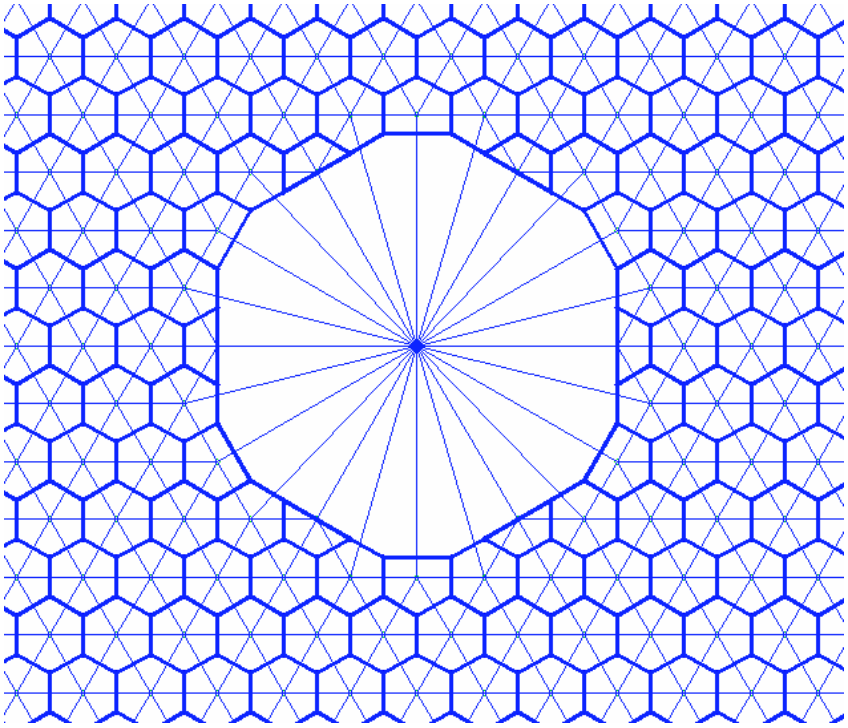

Figure 8.8: Pore of size 24 selected as the template for simulations of different periodic system sizes

The ring size selected for this analysis was $n = 24$, representing a ring significantly outside of the naturally occurring range of observed silica bilayer and graphene behaviours, but within the limits of previous work (Chapter 7, ring sizes $n = 5 - 30$). This will be a starting point for work on inter-pore effects, as we expect rings of this size to require significant system reordering to fully minimise them, which will likely have a longer range impact.

The pore chosen is shown in Figure 8.8, composed of the 24 sided pore, compensated by 6 4-membered rings and 6 5-membered rings. Two potential models have been chosen for Monte Carlo minimisation from Chapter 5, the graphene-like potential, and triangle raft Sample 1. We hope to understand the effect of these potentials on the templated pore structure, and the mechanisms by which they minimise the energy of the system by introduction of disorder.

As has been previously noted, experiments on graphene which evaporate atoms from the surface invariably result in mixed coordination for larger pores, whereas experiments for silica have not clarified the coordination environments around larger

defects in the structure, usually brought about by poorer coverage. With this in mind, our graphene system is unlikely to replicate experimental results, and so is treated as an alternative network approach, rather than predictive of graphene behaviour.

8.4.1 Network Images

Figures 8.9 and 8.10 show 'snapshots' of two pore environments, cubic and hexagonal, with (a) and (c) showing lower temperature simulations, and (b) and (d) showing higher temperature simulations. The introduced pore is shown in black, and the rings are coloured by edge count. Figure 8.9 shows results using a graphene potential, while Figure 8.10 uses a triangle raft potential.

Focusing first on our graphene potential, we can see that at low temperature there is clear structural ordering around the pore. In particular, there are a predominance of five membered rings bordering the pore, which tend to link together to form a smooth ordered pore surface. This is particularly visible in the low temperature hexagonal images (Figure 8.9 c), where we can see up to 9 sequential five membered rings. These chains are broken up by larger and smaller ring sizes, in order to maintain the internal angle of our 24 sided pore. As described in Figure 12 within Section 7.1, the curvature of the ideal polygons are easily defined, with four membered rings allowing for straightening of ring edges, or even concave sections.

These concave sections have a high energetic cost, but due to a limitation of the Keating potential, the energy of angles either side of π are identical, *i.e* $U(\pi + \delta) = U(\pi - \delta)$. This results in a lower energetic cost than would be experimentally expected for reflex angles, allowing for the formation of concave structures. An alternative potential would be a MARTINI style potential, defined as

$$U_{ijk} = \frac{1}{2}k\frac{(cos(\theta_{ijk}) - cos(\theta_0))^2}{sin^2(\theta_{ijk})}. \tag{8.4.1.1}$$

Whilst this function also exhibits symmetry in π, it is asymptotic at $\theta = \pi$, with the force gradient tending to negative infinity at $\theta \to \pi$. It seems likely that such a potential would sufficiently disfavour reflex angles with a sufficiently short

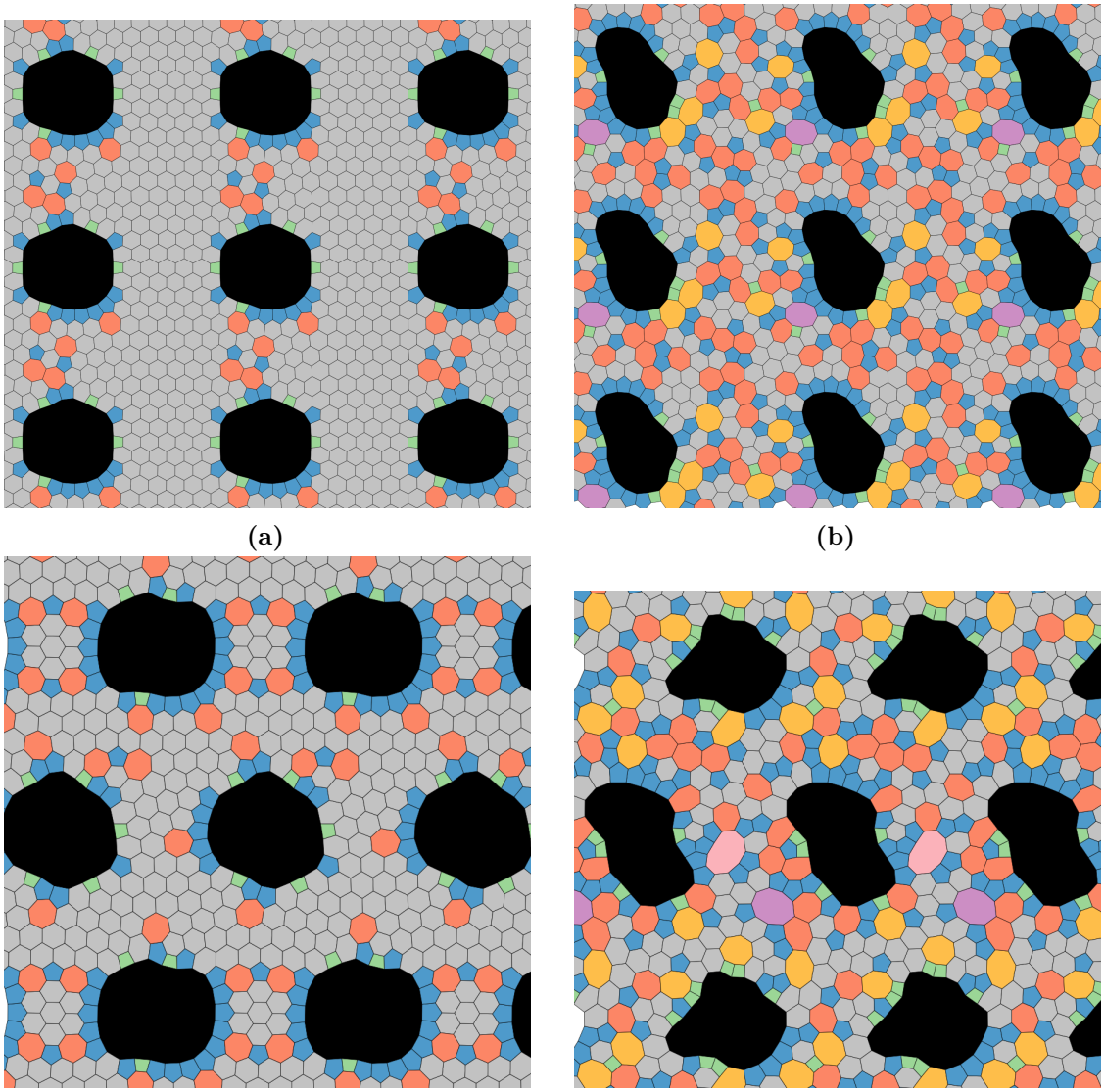

Figure 8.9: Ring structures under different generation temperatures and pore arrangement using a simple graphene potential

simulation timestep; however, as this potential was added to LAMMPS in April 2024, it was not a viable option for this work.

Moving on to triangle raft images, we can see that with angles mediated by internuclear repulsion and rigid SiO_3 units, we do not see such concave pores, and where there are reflex angles they are significantly closer to π. In general, we see significantly more disorder at a given temperature than the graphene systems, which we can understand based on the lower energy cost of Stone Wales (SW) switches in triangle raft systems as a result of the flexibility in the bridging oxygen

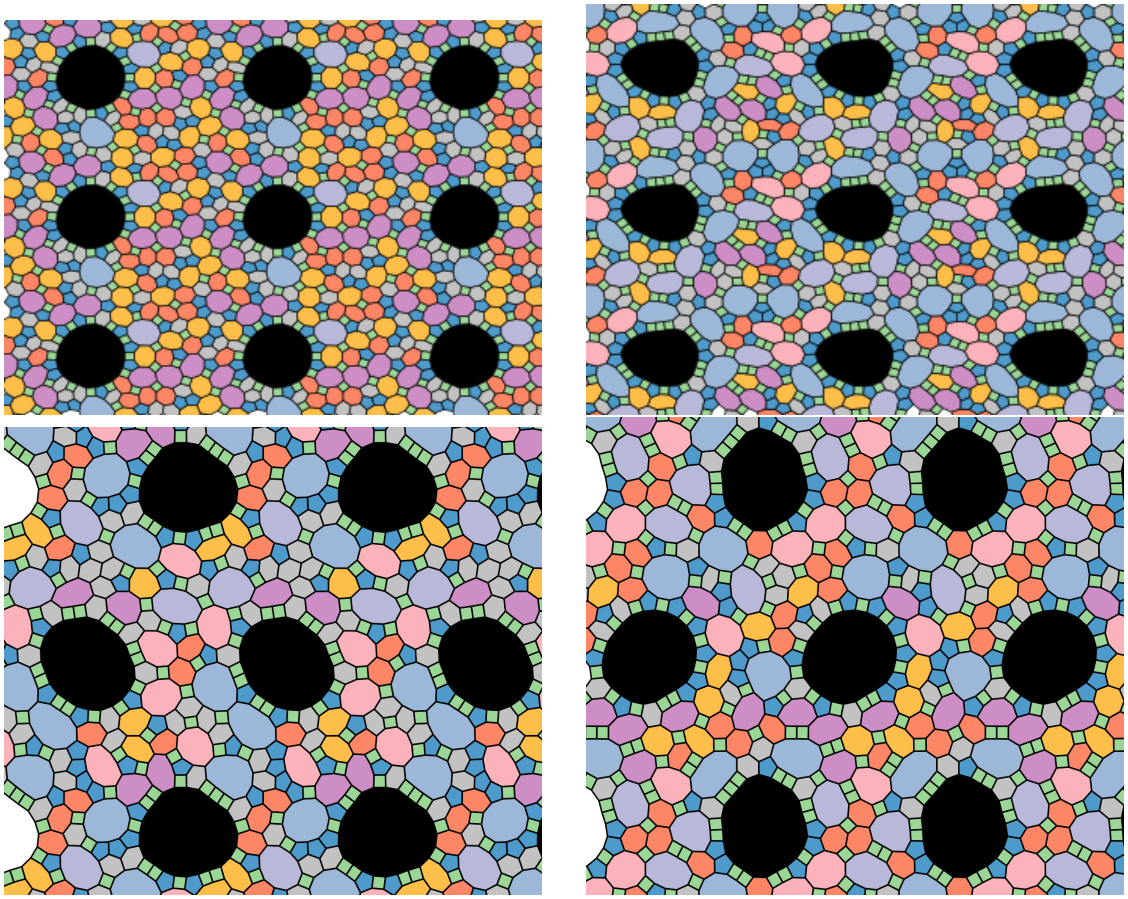

Figure 8.10: Ring structures under different generation temperatures and pore arrangement using a triangle raft potential

atoms. In particular, although ring sizes $10 \leq n \leq 12$ are allowed for graphene systems, they are only realised in our triangle raft systems, and become increasingly prevalent with higher 'temperature'.

Around the large pore, there are a high proportion of four membered rings, which are often paired to create more linear sections. Although the first 'shell' around the pore can contain ring sizes up to $n = 7$, it is dominated by 4 and 5 membered rings, and there is a clear second shell of larger, $n \geq 7$ ring, which are often edge sharing.

The shapes of the pores appear more regular across ring size and temperature for the triangle raft systems, approximating to regular polygons.

It is difficult to glean an understanding of ordering from these images, beyond the very clear ordering in the first shell, and so further analysis is required to better understand these correlations, as in Chapter 7.

8.4.2 Ring Distributions

For all our work on networks, we have used Lemaître's law as a tool to understand how close our networks are to maximum entropy ring distributions.

As has been noted in Chapter 2, the experimentally observed ring limits for experimental silica bilayers are $4 \leq n \leq 10$, with a narrower ring distribution for graphene. Artificially introducing a pore by pore evaporation is expected to cause deviation from the maximum entropy solution.

Figure 8.11 shows a Lemaître curve with data for our templated pore systems, with (a) showing results generated using a graphene potential and (b) using a triangle raft potential. Colouring the markers by periodic system size shows that larger periodic sizes occur at lower disorder, and fit closer to the maximum entropy solutions than smaller periodic system sizes.

We can rationalise this in the same manner as in Chapter 7 B; with increased system size, the relative effect of our pore template reduces, as its contribution decreases relative to the bulk. This pattern is particularly clear in the graphene systems, where we also see a concomitant increase in the maximum recorded p_6 value, resulting in part from the same effect. As N increases, $p_{24} = \frac{1}{N}$ decreases, and so does its contribution to variance, $\mu_2 = \langle n^2 \rangle - \langle n \rangle^2$. Applying this logic to the maximum p_6 value, we expect the p_6 to be at its theoretical maximum when only the template pore is used, and the rest of the system is crystalline (*i.e.* the starting point for our simulations). In the template, there are 13 rings where $n \neq 6$ (24 membered pore, 6 4-membered rings and 6 5-membered rings). For our 140 and 3140 atom systems, this puts the p_6^{max} values at $\frac{70-13}{70} = 0.81$ and $\frac{1570-13}{70} = 0.99$ respectively, which lines up well with our observations.

Looking closer at Figure 8.11, we can see that the triangle raft systems (b) sit at greater disorder, as noted in Section 8.4.1. They also sit closer to the maximum entropy solution, although this may in part be a result of the very low p_6 values, in which regime p_6 becomes a worse system descriptor as it is no longer describing the ring fraction of a predominant ring size. Of particular interest is the difference between square and hexagonal pore orientations at the same pore

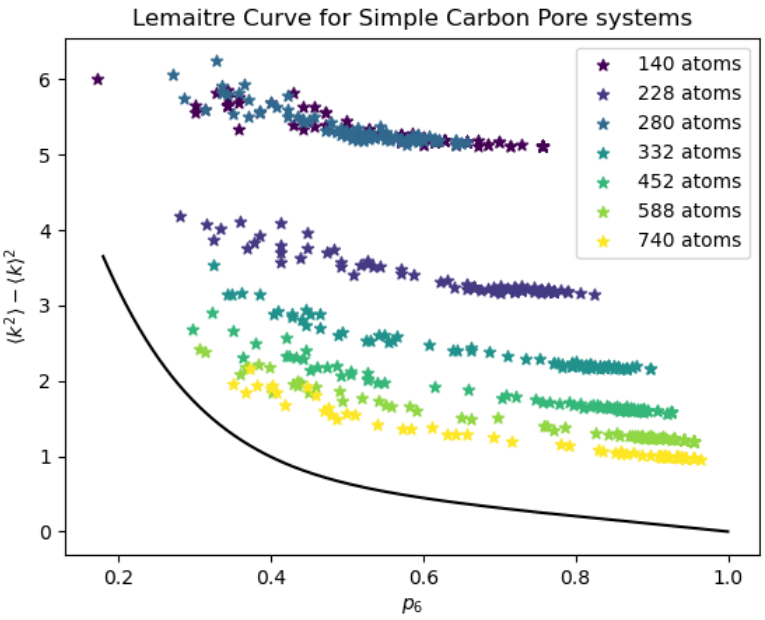

(a)

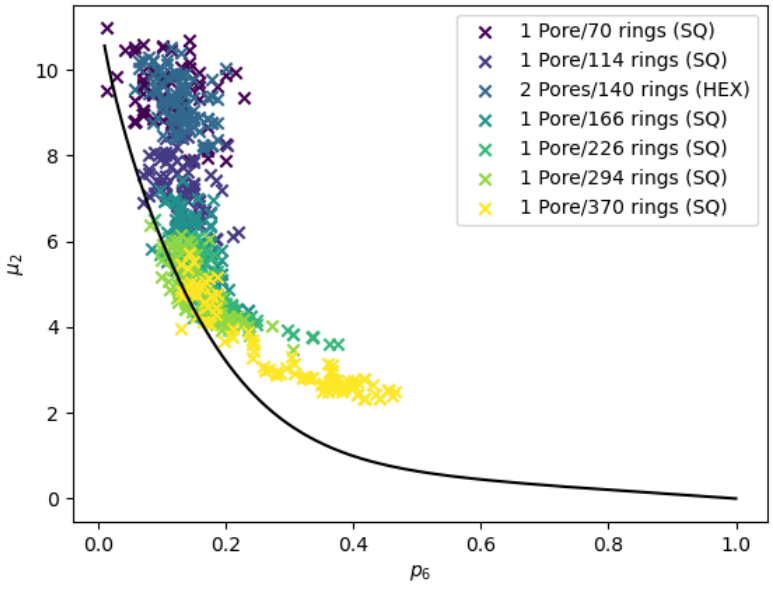

(b)

Figure 8.11: Lemaître plots, differentiating between systems generated using graphene potential (a) and triangle raft potential (b). Points coloured by the size of the periodic system.

density. Examining both the graphene and triangle raft results, we can see that the 2 Pores/280 rings and 1 Pore/140 rings (which have the same pore density) occupy the same space in these figures, indicating that pore orientation does not noticeably affect the global ring distribution.

We expect that a significant amount of this deviation from the maximum entropy solution can be explained by the contribution of the very large pore. These systems have the same central pore, a 24-membered ring surrounded by 6 4-membered rings and 6 5-membered rings, to maintain local coordination environments. This created an initial distortion of the system away from the natural distribution of ring sizes, forming a sample with artificially high variance, skewed by the presence of the very large ring. As such, if we are interested in how the bulk system relaxes around our pore template, we would like to isolate the contributions to μ_2 and p_6 from the pore template, so we can understand to what extent the bulk system's reaction to the large pore follows the maximum entropy ring distribution. At high n, this is a simple process, as we can simply remove the $n = 24$ ring from consideration. However, we cannot simply exclude the pore, as this would alter the average ring size, and so our mean node coordination number. Instead, we need to exclude a set of rings which have a mean ring size $\langle n \rangle = 6$, and as such we need to include 4- and 5-membered rings to balance the size of the pore. There are a discrete number of combinations of four and five membered rings which we could exclude from our μ_2 and p_6 values. We have selected three; compensate for the pore with only 4-membered rings (9 4-membered rings), compensate using our initial template (6 4-membered rings, 6 5-membered rings) and compensate using only 5-membered rings (18 5-membered rings).

Figures 8.12 and 8.13 show the results of these compensations on the graphene and triangle raft results respectively. We can see for both systems, any degree of compensation shows significantly better fit to the Lemaître curve for the bulk sample surrounding the pore, indicating that outside of the template, the system behaves similarly to our graphene and triangle raft systems generated in Chapter 5. In particular, this implies that local ordering about the pore does not significantly

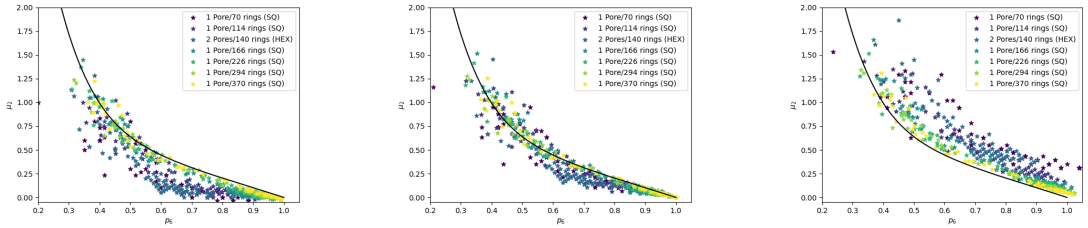

(a) **(b)** **(c)**

Figure 8.12: Lemaître plots for systems using graphene potentials, adjusted by removal of 9 4-membered rings (a), 6 4-membered and 6 5-membered (b), and 18 5-membered (c) rings.

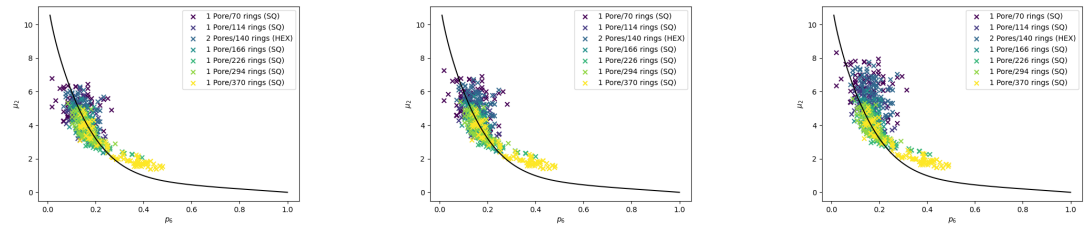

(a) **(b)** **(c)**

Figure 8.13: Lemaître plots for systems using triangle raft potentials, adjusted by removal of 9 4-membered rings (a), 6 4-membered and 6 5-membered (b), and 18 5-membered (c) rings.

affect the network with respect to the variance in the ring distribution at a given p_6. A limited number of systems in Figure 8.12 (c) show $p_6 > 1.0$ after the compensations, as a result of the systems having fewer than 18 5-membered rings, meaning $p_5 < 0$, and so $\sum_{n \neq 5} p_n > 1$.

We can see that moving from (a) $\rightarrow$ (b) $\rightarrow$ (c) for both potential models moves the values to higher p_6 and higher μ_2. The shift in p_6 is a function of the number of rings present in each adjustment; from (a) to (c), nine additional rings are removed, resulting in a higher adjusted p_6. The shift in μ_2 is derived from the greater 'moment' of four membered rings; removing 5-membered rings has a lower effect on the 'width' of the distribution, as measured by μ_2.

The graphene potential shows best fit to the maximum entropy solution for (b), whereas the triangle raft potential shows best fit for (a). We can explain this qualitatively with reference to Figures 8.9 and 8.10, which show graphene and

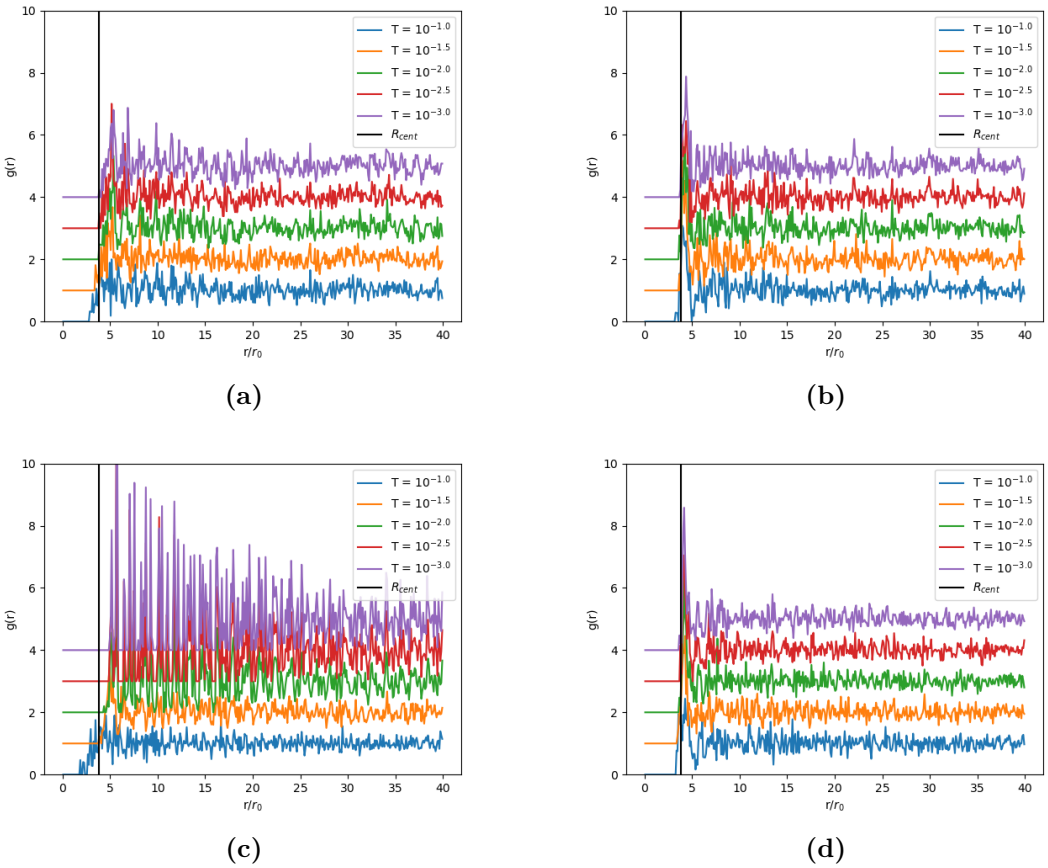

Figure 8.14: Geometric radial distribution functions (rdfs), g(r), at 5 different 'temperatures', determined with respect to the centre of mass of the central (seed) ring. In all cases the length-scales are "normalised" in terms of the bond length, r_0. Panels (a) and (b) show systems with 228 nodes, (c) and (d) show systems with 740 nodes. Panels (a) and (c) are graphene systems, (b) and (d) are triangle raft systems. The ideal polygonal radius, R_{cent}, of the pore is marked with a black line

triangle raft pores to have more 5-membered and 4-membered nearest neighbour rings respectively.

8.4.3 Geometric Analysis

Figure 8.14 shows the spacial radial distribution functions (g(r)), calculated using the centres of mass of the rings and taken relative to the centre of mass of the central ring. These figures are for two system sizes, 228 and 740 nodes respectively, at a range of temperatures with both potential models.

Examining the nearest neighbours of the pore (first peak in the g(r)), we see a clear trend in the distance to the nearest neighbour with 'temperature' for graphene

systems, which is not true of triangle raft systems. At low 'temperature', the nearest ring sits further from the centre of the pore than the ideal radius, as would be expected as the nearest neighbour distance is the radius of both the pore (R_{cent}) and the rings in the first shell. However, increasing 'temperature' results in a gradual lowering of the distance to the first shell, until at high 'temperature' the distance is lower than R_{cent}. There is also a system size effect, with the first shell of the larger 740 node system found at a greater distance than the smaller 228 node system. For triangle raft systems, the distance to the first shell remains constant across 'temperature' and system size.

Looking beyond the nearest neighbours, we see no long range ordering at high 'temperature' for either potential model or periodic system size. At lower 'temperature', for triangle raft systems we see a narrowing of the first peak, and a better defined second peak; however, beyond this point the systems show no clear ordering. For graphene systems however, lowering the 'temperature' results in crystalline structures close to the pore at large system size (b), with some level of ordering also noticeable for smaller system sizes (a).

We can examine these trends further by delineating the contributions of each ring size to the g(r) distribution at a given 'temperature'. Figures 8.15 and 8.16 show decompositions of g(r) for two different system sizes, 228 nodes in (a) and (b), and 740 nodes in (c) and (d), for high 'temperatures' in (a) and (c) and low 'temperatures' in (b) and (d), for the graphene and triangle raft potentials respectively.

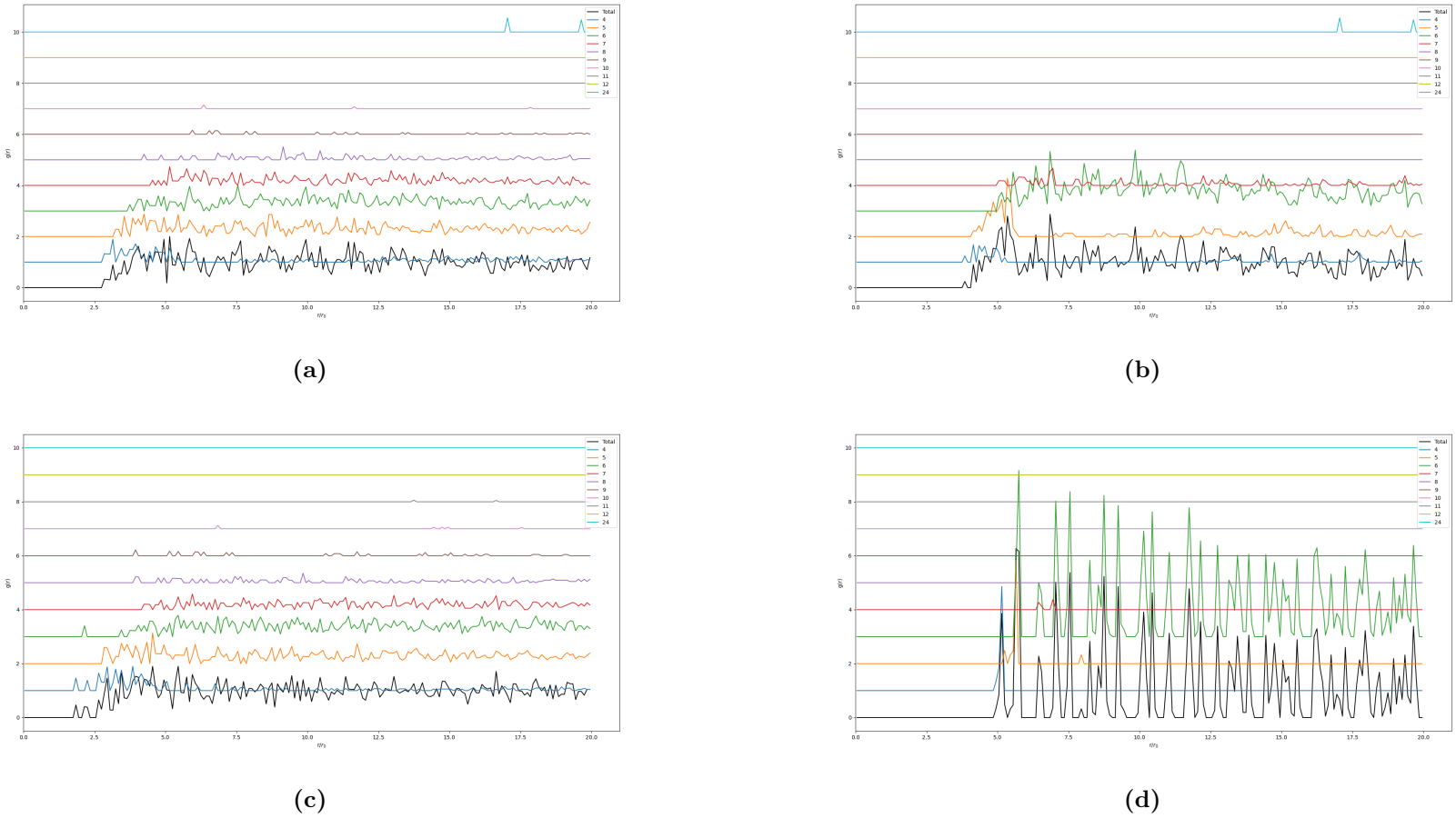

Figure 8.15: Geometric radial distribution functions (rdfs), g(r), broken down into the contributions of each ring size for graphene systems, determined with respect to the centre of mass of the central (seed) ring. In all cases the length-scales are "normalised" in terms of the bond length, r_0. Panels (a) and (b) show systems with 228 nodes, (c) and (d) show systems with 740 nodes. Panels (a) and (c) are high 'temperature' systems, (b) and (d) are low 'temperature' systems.

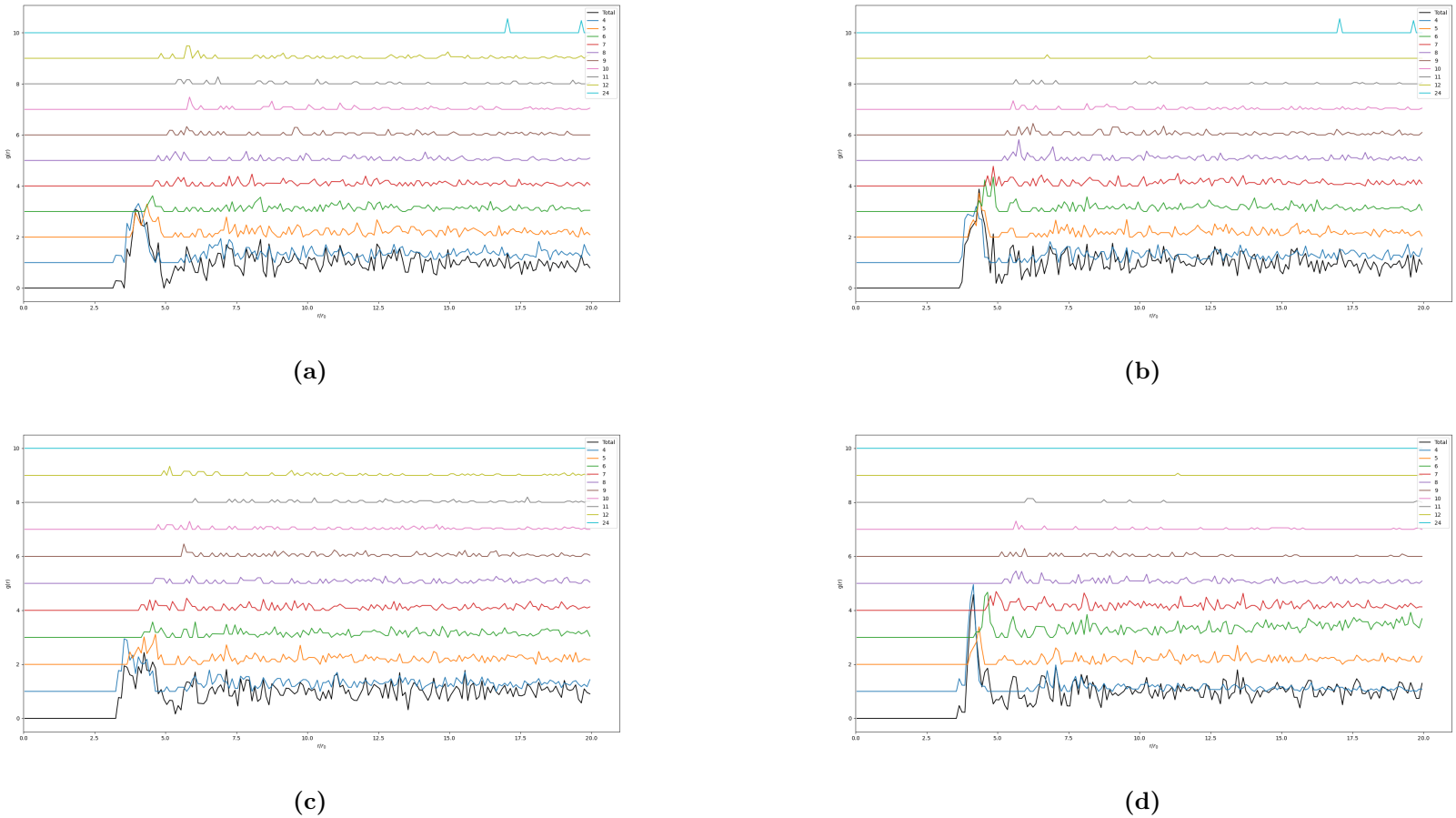

Figure 8.16: Geometric radial distribution functions (rdfs), g(r), broken down into the contributions of each ring size for triangle raft systems, determined with respect to the centre of mass of the central (seed) ring. In all cases the length-scales are "normalised" in terms of the bond length, r_0. Panels (a) and (b) show systems with 228 nodes, (c) and (d) show systems with 740 nodes. Panels (a) and (c) are high 'temperature' systems, (b) and (d) are low 'temperature' systems.

For both potential modes, the general trend is that larger rings are introduced further from the pore. We can also see the introduction of the two nearest pores for the smaller system at the same distance for both systems, as this is defined by the periodic cell size, however for all systems this has no noticeable effect on the g(r). However, there are significant differences between the behaviours of these systems.

Beginning with graphene systems in Figure 8.15, we can see a reduced range of ring sizes for the lower 'temperature' simulations, with $4 \leq n \leq 10$ for high 'temperature' systems and $4 \leq n \leq 7$ for low 'temperature' systems. At higher 'temperature' in (a) and (c), the nearest neighbour peak is very broad, likely as a result of the concave structures visualised in Figure 8.9. As a result it is difficult to get a clear understanding of the composition of the rings neighbouring the pore, as they are situated across a range of r/r_0. There appears to be no ordering in ring sizes for these disordered systems, with the proportion of each ring size varying consistently and randomly with r/r_0, resembling an amorphous system. The lower 'temperature' systems show a clearer nearest neighbour peak. For the smaller system (b), this first peak contains mostly 5-membered rings, alongside a considerable contribution from 4-membered and 6-membered rings, and a small contribution from 7-membered rings. Beyond the clear ordering in the first shell, 6-membered rings predominate, with 5-membered and 7-membered rings present in low concentrations and without order. The larger system (d) shows strong peaks, with the highly ordered structure resulting in splitting of the nearest neighbour peaks into the 4-membered (initial peak) and 5- and 6-membered (second peak) ring contributions. The second shell is composed of mostly 6-membered rings, with a small 7-membered contribution. Beyond these two peaks, the g(r) is composed almost exclusively of 6-membered rings at regular, ordered positions, indicative of a crystalline structure.

Moving to the triangle raft systems in Figure 8.16, we see a broader range in ring sizes across all temperatures, with the full range of allowed ring sizes, $4 \leq n \leq 12$ present across (a)-(d). There are fewer $n \geq 10$ rings at lower temperature. All systems have 4-membered rings as the largest contributor the first peak. Decreasing the 'temperature' (a) $\rightarrow$ (b) and (c) $\rightarrow$ (d) narrows the first peak, and as such

excludes ring sizes $n > 6$ from the nearest neighbours, whereas (a) and (c) both have contributions from $n \geq 7$ in their first peaks. Where second peaks are identifiable, they tend to be composed of more $n > 6$ rings. There is little order to any of the ring contributions beyond the first (and in some cases second) peaks.

The shell charge correlation function, $G_q(r)$ has been defined in Section 7.C.1. (equation 16 therein) as a means to separate $n < 6$ and $n > 6$ contributions to g(r). The $G_q(r)$ curves for system sizes of 228 nodes in (a,b), and 740 nodes in (c,d), are shown using potential models for graphene and triangle raft models in (a,c) and (b,d) respectively in Figure 8.17.

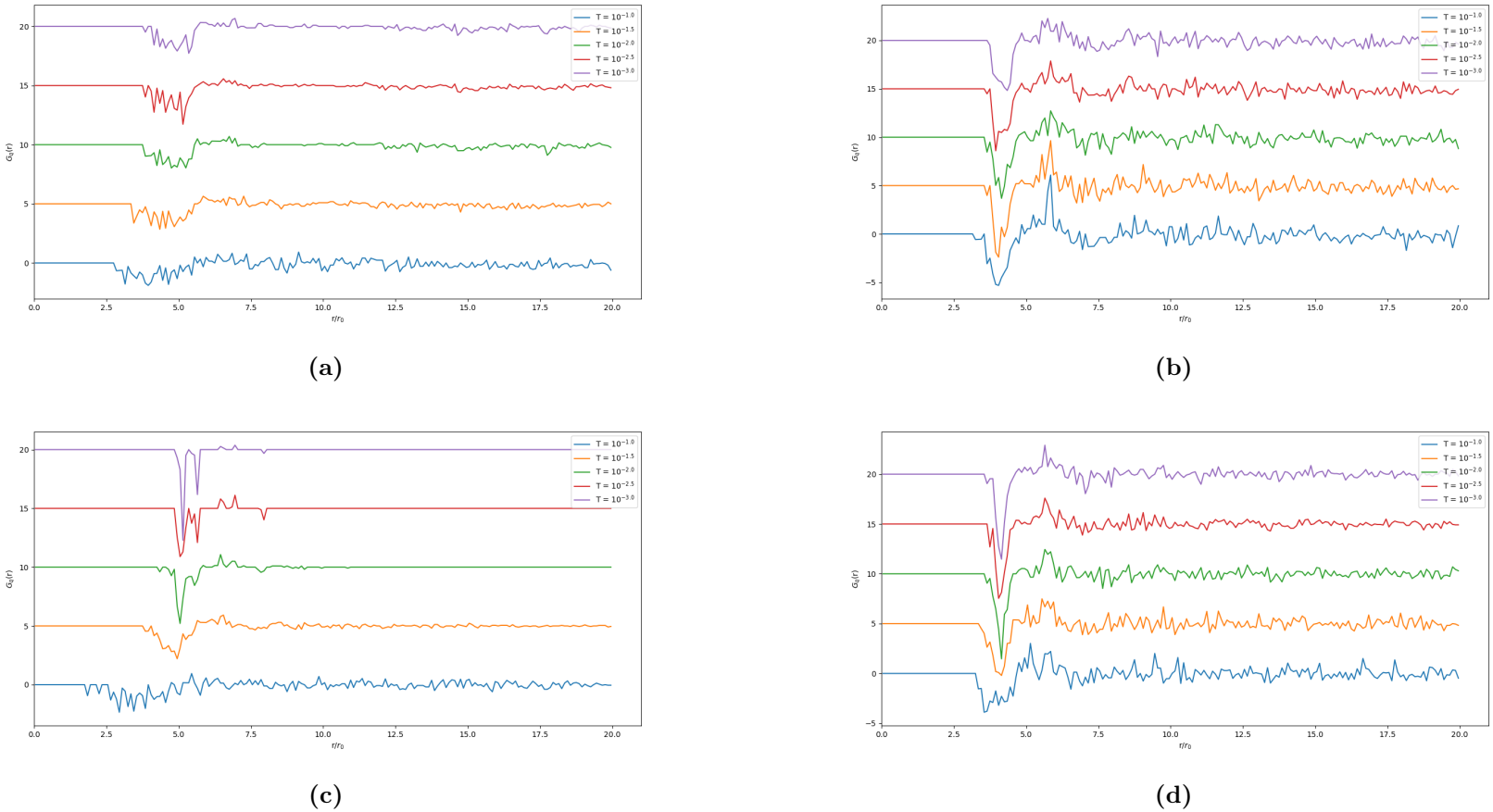

Figure 8.17: Weighted geometric radial distribution functions, $G_q(r)$ with 'temperature', determined with respect to the centre of mass of the central (seed) ring. In all cases the length-scales are "normalised" in terms of the bond length, r_0. Panels (a) and (b) show systems with 228 nodes, (c) and (d) show systems with 740 nodes. Panels (a) and (c) are generated using a graphene potential, (b) and (d) are generated using a triangle raft potential.

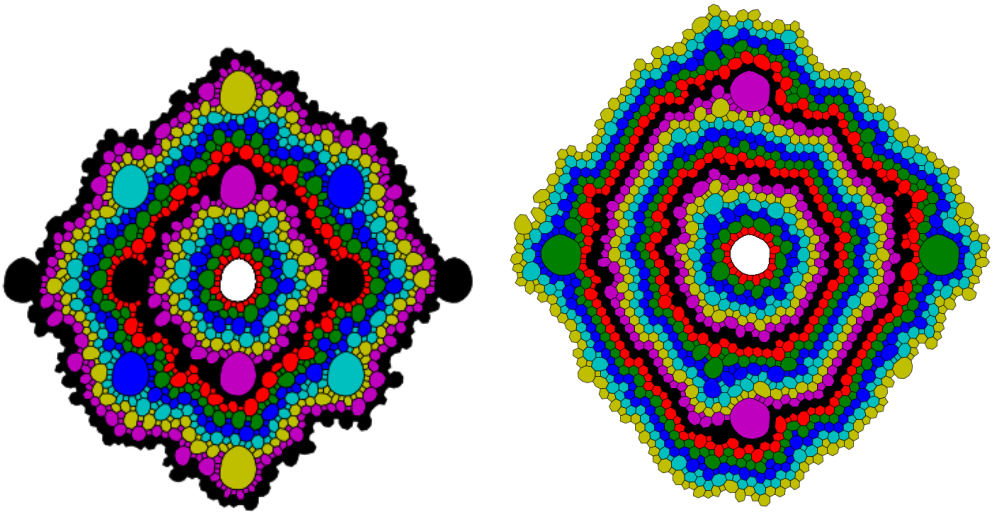

(a) (b)

Figure 8.18: Topological view of ordering about a pore for triangle raft systems of size 228 (a) and 740 (b) nodes, coloured by shell number

For our graphene systems (a,c), we see an initial negative peak, beyond which the system is effectively damped, with the level of 'noise' dependent on the simulation 'temperature'. By contrast, our triangle raft systems show much a stronger first negative peak, followed by a noticeable second positive peak. No ordering is discernible beyond this peak. These graphs indicate increased ordering in triangle raft over graphene systems.

8.4.4 Topological Analysis

Two examples of a shell interpretation of 228 (a) and 740 (b) node structures are given in Figure 8.18, with the central pore coloured white and each successive shell coloured to distinguish them. Both samples extend to 20 shells. For these images, we need to account for multiple images of the periodic cell to encompass for cell ordering that extends beyond the limit of each periodic cell. For instance, Figures 8.18 (a) and (b) include 12 and 4 additional periodic cells, respectively.

As we are interested in the ring size ordering in each shell, we can also colour these shells by their mean ring size, as in Figure 8.19. These images show clear ordering, but are limited in their scope, and broader analysis is needed to fully describe general behaviour with shell count.

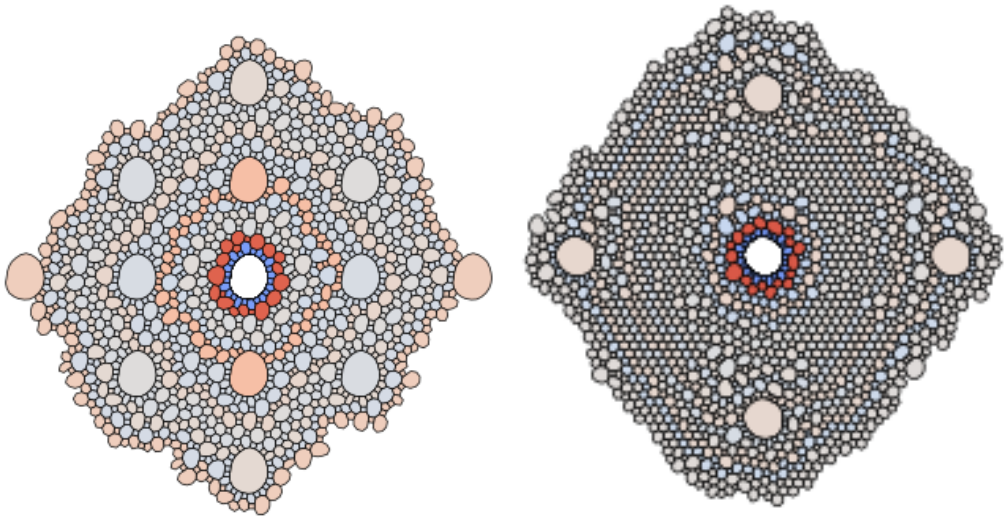

(a) **(b)**

Figure 8.19: Topological view of ordering about a pore for triangle raft systems of size 228 (a) and 740 (b) nodes, coloured by the mean ring size of the shell, from blue ($\langle n \rangle = 4$) to red ($\langle n \rangle = 8$)

Figure 8.20 shows the evolution of mean ring size as a function of topological shell. We see very clear trends in the mean ring size with shell count away from the pore. Averaging over five seeds gives the error bars, which are higher for the triangle raft systems. For all systems, it is clear that $n < 6$ rings are favoured in the first shell, and that there are more $n > 6$ rings than $n < 6$ rings in the second shell. However, there are clear system size and potential model effects.

Focusing first on graphene systems (a,c), we see that the behaviours of the first three shells is the same between our periodic system sizes, but beyond this point their behaviours diverge, with unpredictable behaviour for the smaller system size (a), whereas the larger system size (c) has $\langle n \rangle \simeq 6$ from shells 3-10.

For triangle raft systems, we see significant long range shell ordering across all temperatures, with the effect more pronounced at smaller system size (b).

We can examine the effect of neighbouring pores by identifying the shells that they are present in. Figure 8.21 shows the same graphs with only the low 'temperature' $10^{-3.0}$ unit result, with the population of pores overlaid in red. Having pores present in a shell significantly affects the $\langle n \rangle$ values, especially for smaller systems (a,b), where neighbouring pores are closer, at which distance there are

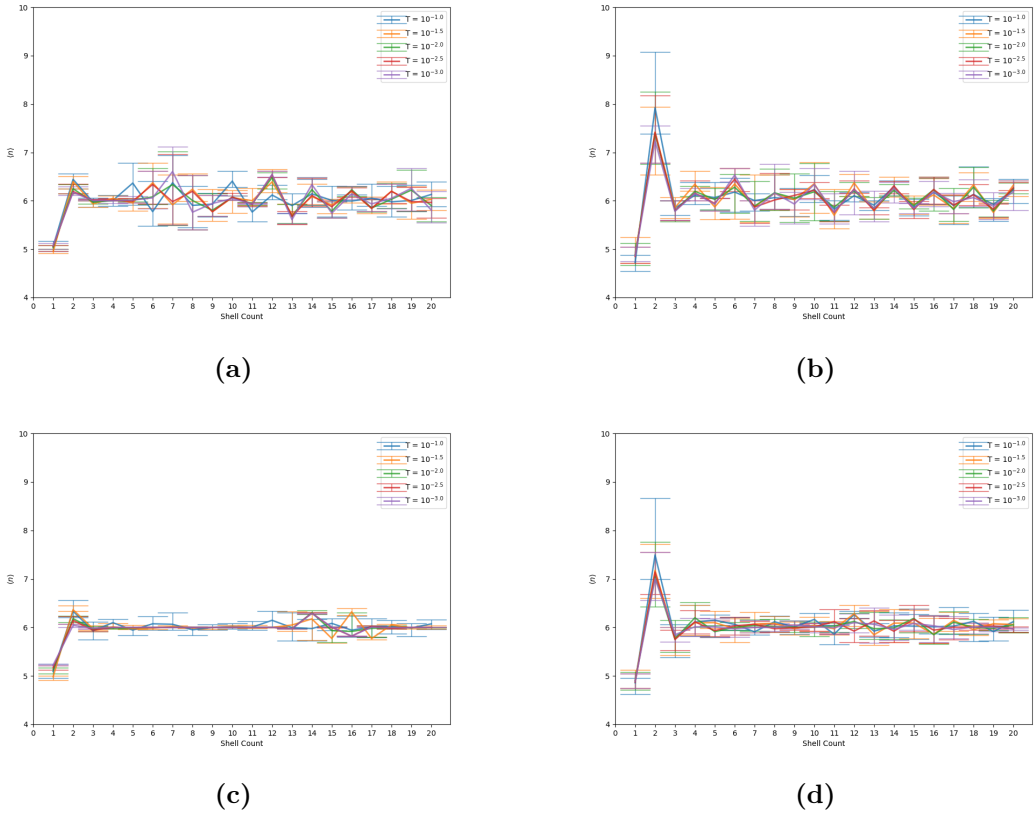

Figure 8.20: Mean ring size $\langle n \rangle$, as a function of topological shell averaged across 'temperature'. .Panels (a) and (b) show systems with 228 nodes, (c) and (d) show systems with 740 nodes. Panels (a) and (c) are generated using a graphene potential, (b) and (d) are generated using a triangle raft potential.

fewer rings per shell. Isolating the effect of the pore explains the differences between Figure 8.20 (a) and (c); we can see that for both systems, neighbouring pores are responsible for moving $\langle n \rangle$ away from 6.

It is notable that, for the same system size, these pores occur at smaller shell count for triangle raft systems as opposed to graphene systems, despite the pores being the same physical distance apart, as enforced by the cell periodicity. This is likely a result of the larger rings ($n \geq 10$) present in triangle raft systems, which increase the volume of some shells, and the large area disparity between these rings and $n < 6$ rings resulting in less regular shell shapes.

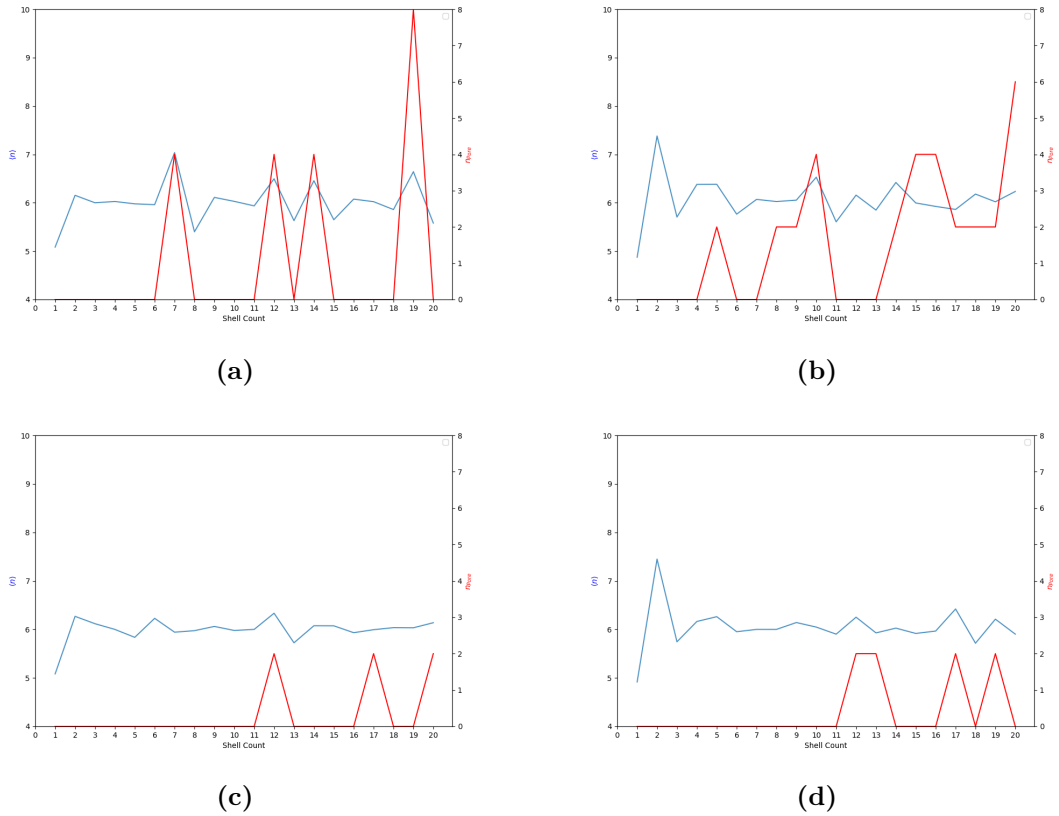

(a) **(b)** **(c)** **(d)**

Figure 8.21: Mean ring size $\langle n \rangle$, as a function of topological shell at a single low 'temperature' in blue, with the number of pores from neighbouring periodic cells in each shell plotted in red. .Panels (a) and (b) show systems with 228 nodes, (c) and (d) show systems with 740 nodes. Panels (a) and (c) are generated using a graphene potential, (b) and (d) are generated using a triangle raft potential.

8.4.5 Characterising the Central Pore

One key metric for understanding the impact and utility of a pore in experimental applications is its area; we expect that pore area with directly correlate with its selectivity for molecular permeation.

Figure 8.22 presents the area of the pores averaged across all periodic system sizes and seeds with 'temperature', for graphene (a) and triangle raft networks (b) respectively. The units of the area are in r_0^2, where r_0 is the ideal inter-node distance, taken as 1 for graphene and $2r_{SiO}$ for triangle raft models. These systems behave differently with 'temperature', with the triangle raft ring area largely consistent across 'temperature', whereas the graphene system shows a negative trend with temperature. The implication of this figure for the triangle raft system is that the

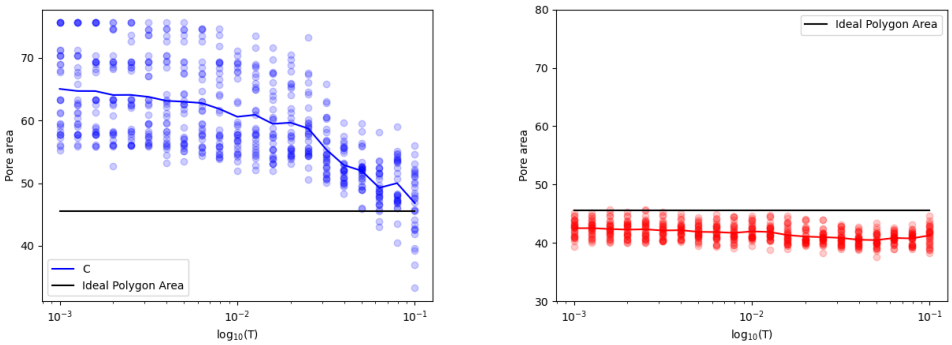

(a) (b)

Figure 8.22: Area of the pore formed using graphene potential (a) and triangle raft potential (b) with temperature across all system sizes, in r_0^2. The area of a regular polygon side length r_0 is shown for comparison

disorder surrounding the central pore does not affect the size or shape of the pore, and neither does the periodic system size, as these results are captured across the full range of periodic environments. The area sits consistently $\simeq 0 - 5r_0^2$ below the ideal polygon area. In contrast, the disorder surrounding the graphene system acts to reduce the size of the pore, at low 'temperature' resulting in pores $\simeq 10 - 30r_0^2$ larger than the ideal polygon area, with the area shrinking within $\simeq 10r_0^2$ either side of the ideal area at higher 'temperature'.

We can gain an insight into this effect by directly examining single structures, as in Figure 8.23, which shows a graphene (a) and triangle raft (b) pores at the same axis scaling. From these images, we can see that our triangle raft pore is smaller, as expected from Figure 8.22. Examining the environment surrounding the pore, we see that all of the rings neighbouring the pore are elongated away from the pore. All of the bridging oxygen (O) atoms between the silicon (Si) atoms which make up the pore are displaced into the void created by the pore, shortening the Si-Si distances for the edges which make up the ring and twisting the SiO_3 units to deform the first shell of rings about the pore. This mechanism is not available for our graphene systems, instead at low disorder we see longer carbon-carbon (C-C) bond lengths for C atoms involved in the pore ($\simeq 1.2r_0$).

Figure 8.9 indicated that at greater disorder, the graphene pores become more concave. We can evaluate this effect using the shape regularity coefficient (SRC),

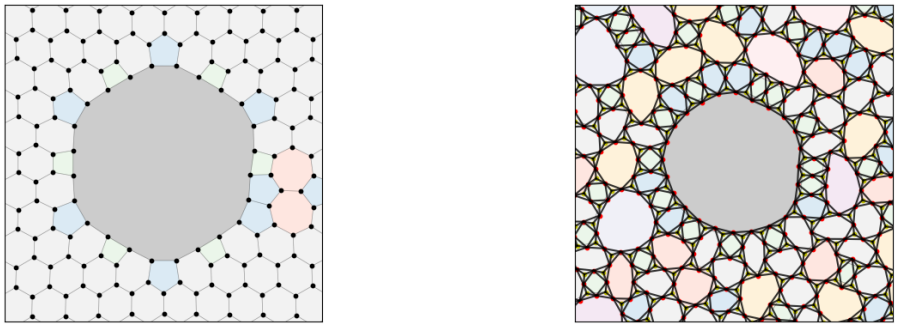

(a) **(b)**

Figure 8.23: Image of the ring network surrounding the pore for graphene (a) and triangle raft (b) for single, low disorder configurations. Oxygen (O) atoms are shown in red for the triangle raft system, with rings coloured for clarity. The axes scaling for both images is the same, to allow for direct comparison

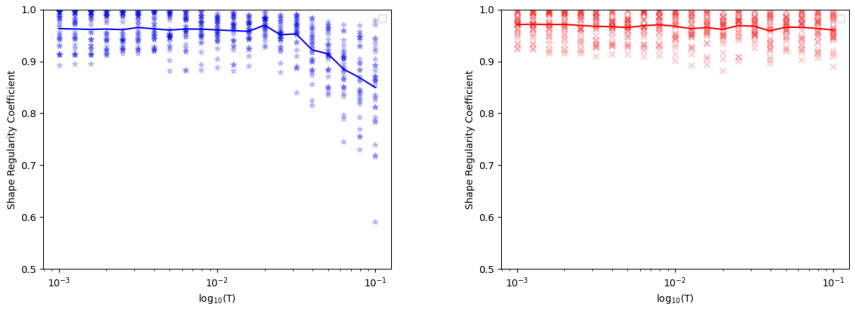

[h!] **(a)** **(b)**

Figure 8.24: Shape Regularity Coefficient (SRC) of the pore formed using graphene potential (a) and triangle raft potential (b) with 'temperature' across all system sizes.

as defined in Section 3.2.6. Figure 8.24 shows the SRC values for graphene (a) and triangle raft (b) networks with 'temperature'. We can see that there is a wider range in SRC for graphene systems at low 'temperature', likely resulting from the lower distortion about the pore in these systems as discussed in Section 8.4.1, which result in less even curvature about the pore.

Whereas for the triangle raft system SRC is nearly invariant with 'temperature', the graphene systems show a drop in SRC over the range $T = 10^{-1.5} \rightarrow 10^{-1.0}$, as the systems become more concave.

We have noted that for pore networks, the physical size of the pore has

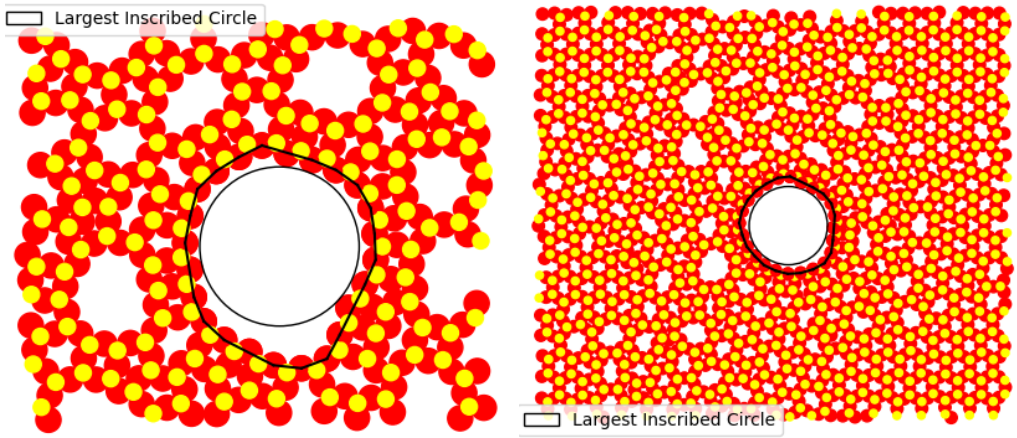

Figure 8.25: Graphics to show the largest inscribed circle for two triangle raft pores at different periodic system sizes, with (a) at 140 nodes and (b) at 740 nodes. Oxygen atoms are shown in red with a radius 1.35Å, silicon atoms are shown for ease of visualisation. The oxygen atoms which make up the edge of the pore are connected, and the largest inscribed circle visualised.

implications for its porous characteristics. In particular, we are interested in the largest free sphere (the maximum diameter of a sphere that can pass through the pore system without colliding with the atoms of the framework). This is particularly important for silica bilayer systems, which have been hypothesised to show diffusion characteristics based on ring size[12]. For triangle raft systems, we have noted that the oxygen (O) atoms bordering the pore are displaced towards it, effectively reducing its area. For our evaluation, similar to work on zeolite pore size[92], we treat the O atoms as hard spheres with contact radius $r = 1.35$Å. Figure 8.25 shows a representation of this process at small (a) and larger (b) periodic system size.

Figure 8.26 shows the largest inscribed circle for our triangle raft networks across 'temperature', as compared to that of an ideal triangle raft 24-membered ring shown in black. The pore size does show a reduction with temperature, indicating that less ordered systems with the same pore size may have different diffusion characteristics to more ordered systems. There is also a high degree of variability, indicating that other factors such as system size may have some impact; however, it appears that introducing a pore allows for a large ($\simeq$ 16Å diameter) area through which diffusion is possible. For reference, this is $\simeq 5-6$ times larger than the

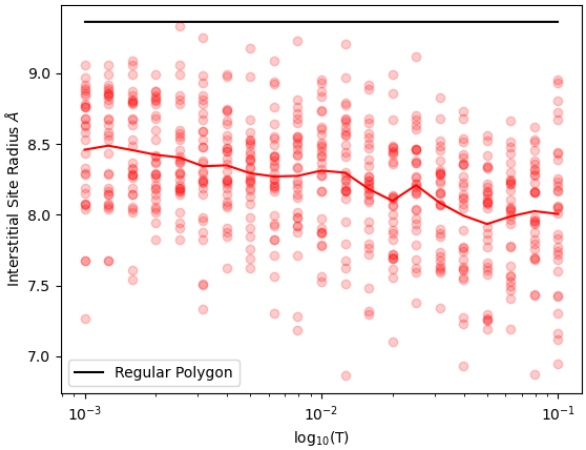

Figure 8.26: Largest inscribed circle for the pore in triangle raft networks in Å, with a oxygen hard shell radius of 1.315Å. The largest inscribed circle for an ideal triangle raft 24-membered ring is provided in black for reference.

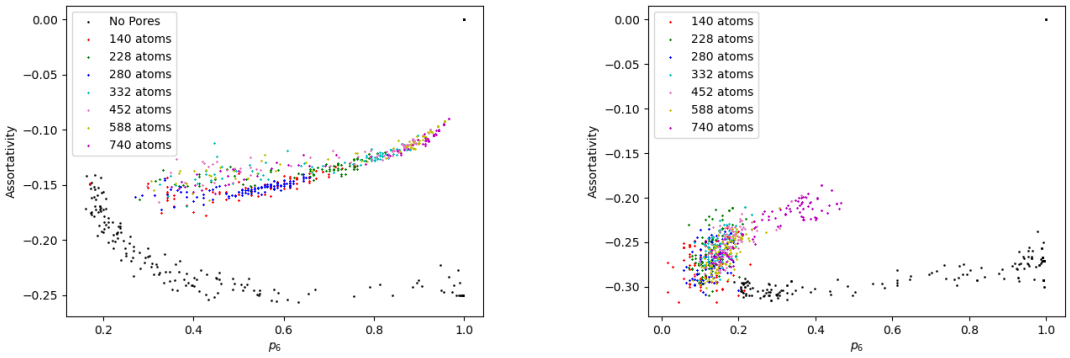

(a) **(b)**

Figure 8.27: Assortativity values, differentiating between systems generated using graphene potential (a) and triangle raft potential (b). Points coloured by the size of the periodic system.

theoretical largest inscribed circle for a 6-membered ring.

8.4.6 Assortativity as a function of disorder

In Section 5.5.5, we discuss using assortativity to quantify local ordering. We can also use these techniques to understand local ordering in our pore networks. Figure 8.27 shows the results from Section 5.5.5 for graphene (a) and triangle raft (b) networks in black, as compared to the different sized pore templated networks. We can see that for both systems, the pores behave similarly to each other, but very

differently to the untemplated amorphous systems.

Beginning with the graphene systems, we can see that the pore systems follow the opposite trend to the untemplated amorphous systems, becoming more assortative with decreasing disorder. This is initially counter intuitive; we have noted significant ordering of smaller rings around the large pore, which would imply significant disassortativity. However, in ordering rings into 'shells' around the large pore, we force like-sized rings to neighbour each other.

If we examine the first shell in Figure 8.9, we can see that the five membered ring shares edges with two other like sized 5-membered rings, with one connection to the dissimilarly sized 24 sided ring, and two connections to the similarly sizes 6-membered rings. We can identify from this that the intra-shell connections tend to be assortative, while inter-shell connections are more dissortative, by virtue of the alternating $\langle n \rangle < 6$, $\langle n \rangle > 6$, $\langle n \rangle < 6$ ... nature of successive shells. As such, associative ordering is more pronounced where there is a less extensive shell network. As noted in Section 8.4.4, graphene systems show significantly lover range shell ordering, and as such appear more assortative that triangle raft systems, which have greater ranger ordering, with larger disassortative inter-shell contributions. It is also notable that the assortativity of both the graphene and triangle raft systems tend to their untemplated amorphous values at low p_6, as the effect of the pore becomes 'washed out' by global system disorder.

8.4.7 Energy as a function of disorder

Section 5.5.6 analysed the energy of amorphised systems as a function of system ring size variance, and found that both the graphene and triangle raft systems showed linear behaviour of energy U in variance μ_2, such that $U = \epsilon\mu_2$, where ϵ is a potential specific constant which is related to the energy of a single Stone Wales defect.

Figure 8.28 shows the linear trend from the untemplated systems in Section 5.5.6 as compared to the templated pore systems, coloured by system size, for graphene (a) and triangle raft (b) systems. The graphene and triangle raft systems have very different behaviours, although both systems show a lower per-atom energy for

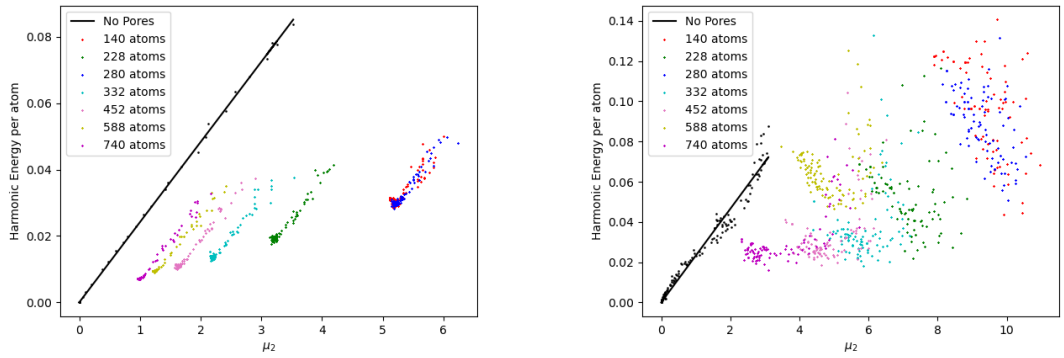

Figure 8.28: Final structure energy values U as a function of system variance μ_2, differentiating between systems generated using graphene potential (a) and triangle raft potential (b). Points coloured by the size of the periodic system.

templated pore systems compared to the untemplated system. We can rationalise this as the disproportionate effect of the large pore on μ_2; the large ring is a low energetic cost means to significantly raise μ_2 with minimal global distortion.

The correlations in energy for the two potentials belie more fundamental differences between the samples. Examining first the graphene systems, the templated results are separated in μ_2, with smaller system sizes at greater μ_2, as expected from the relative ring proportion of the large ring, and as noted in Section 8.4.2. For each sample there is a very good fit in U with μ_2, with approximately the same gradient as the untemplated systems. This implies that the pore systems react in the same manner to the introduction of disorder to the untemplated systems, *i.e.* the pore has no meaningful effect on how the system energetics evolve with disorder. We can rationalise this by considering Figure 8.20, which shows that the pore is well accommodated locally (within the first and second shell), meaning the effect of the pore is localised. As such, it behaves more like a surface vacancy.The energy of the pore behaves as a localised, fixed energy, and the system is amorphised effectively independent of it. By contrast, our triangle raft systems do not show such a clear trend, with significantly more sample specific variance, especially within small system sizes. It appears that introducing pores

has a significant effect on the energetics of the system, as might be expected from the notable ordering introduced by the pore in triangle raft systems.

In particular, the energies of these systems are significantly higher than the graphene equivalent systems. This may in part be a result of our definition of the natural area of the system, which as discussed in Section 8.2.3 is defined relative to the graphene system. As we have noted in this work (Section 8.4.5), pores adopt significantly lower areas in triangle raft systems, and as such the triangle pore systems likely are not simulated at their natural areas, which would impose additional energetic costs to the simulations. In particular, generally smaller system sizes ($N_{nodes} = 140, 228, 280$) and $N_{nodes} = 588$ sit at higher energy than $N_{nodes} = 332, 452, 740$, although there is a great deal of variation and so definitive conclusions are difficult to draw. The energy of the $N_{nodes} = 588$ system sits at significantly higher energy than other larger system sizes. We expect this effect to be periodic size dependent; if the pores are spaced such that their long range ordering overlaps unfavourably, we expect the system as a whole to have a higher energy. Equilibriating medium- to long-range ordering is a challenge for our simulation methods, as local minima arising from strong ordering close to the pore may not result in the most stable longer-range ordering. With increased simulation time and tuning of the thermalisation, we may be able to better stabilise these systems, and this is an interesting avenue for future work.

Examining the trends in energy with disorder at each system size, for larger system sizes ($N_{nodes} = 740, 452, 332$), we see a positive trend in energy with ring size variance (μ_2), as would be expected from the untemplated samples. However, the correlation is weaker than in our untemplated systems, and the gradient does not match the untemplated systems;the gradients are lower than our untemplated systems, indicating that it is significantly easier to introduce disorder into pore systems than untemplated systems. This is likely a result of the ordering present in the system, which mean that defects which overlap well with this ordering resulting in a lower energetic cost.

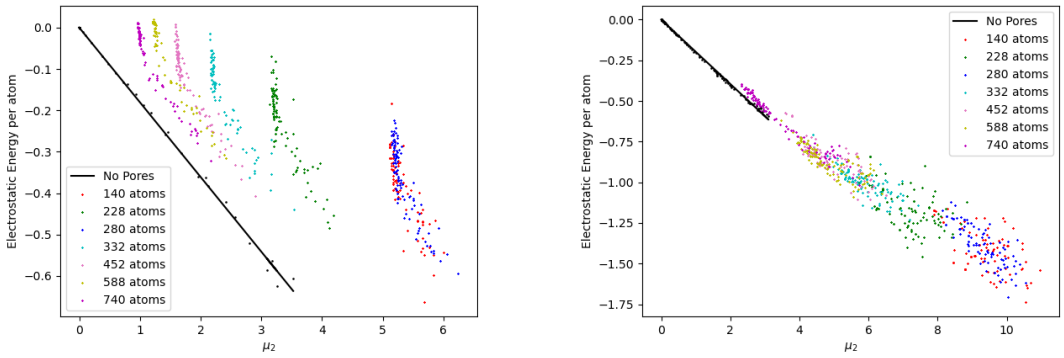

Figure 8.29: Electrostatic energy values as a function of system variance μ_2, differentiating between systems generated using graphene potential (a) and triangle raft potential (b). Points coloured by the size of the periodic system.

The smaller system sizes, $N_{nodes} = 228, 280, 140$, and $N_{nodes} = 588$, show the opposite trend, with negative gradients indicating that increasing disorder stabilises the system. We would expect that for smaller system sizes, establishing a short- to medium- range shell system is particularly important to 'screen' the distortion created by each pore from other pores. As such, a negative gradient here implies that greater ring variance is required to establish this ordering, and lower the system energy.

8.4.8 Charge Based Interpretations

An alternative approach to the energetics of these systems is an electrostatic one, as described in Section 5.5.7. Untemplated systems show linear correlation between the electrostatic energy and μ_2, as shown by the black markers in Figure 8.29, which also shows the electrostatic energies of the graphene (a) and triangle raft (b) systems, coloured by system size.

Examining first (b), the triangle raft systems, we can see good agreement with the gradient predicted by the untemplated system; where there is deviance from the trend, the energies of the templated pore networks are higher than would be expected, indicating that they have not minimised down to the expected levels. This dispersion away from the trend is more pronounced for smaller systems. The

general agreement to this fit implies that triangle raft pore systems show potential to be modelled as charge-based systems, as they have consistent energetic behaviour with μ_2, even when the system deviates from the maximum entropy solution as discussed in Section 8.4.2. Agreement to this fit implies that ordering about the pore is close to that expected for a charged fluid.

Our graphene structures (a) do not follow the same relationship, instead consistently sitting at higher energy, showing two distinct regions with disorder. At lower disorder, the gradient is steeper than the untemplated system, with an inflection point at intermediate disorder, beyond which the gradient approximates to that of the untemplated system. In the latter region, the pore behaves energetically similarly to a charged particle, however in the former region, the shape and ordering around the pore do not map well onto an electrostatic model. In particular, we noted in Sections 8.4.3 and 8.4.5 that the pore size was larger than that of an ideal polygon with edge size r_0 at lower disorder, with pore size shrinking with disorder (Figure 8.22). The size effect present will likely have a significant effect on the energy of the pore, although the shape of the pore is more concave at higher disorder, complicating this effect.

The system energies deviate significantly from those predicted by the untemplated systems. However, as we have noted in Sections 8.4.7 and 8.4.4, the pores in graphene systems appear to behave less like rings and more like vacancies. As such, methods such as our electrostatic model which rely on 'ring charges' are less likely to well approximate these systems.

8.5 Conclusions

A novel method for introducing large rings, termed pores, into periodic systems is presented. This method allows for direct evaluation of the effect of large ring density on the stability of the system, accounting for inter-pore interactions. The form of this method is compared to experimental processes for forming 'nanopores' in graphene. The capabilities of this method to produce zeolite structures are introduced. This technique is used to introduce a single large pore ($n = 24$) into

the center of seven different sized periodic systems, with the systems then relaxed about this pore using the Monte Carlo approach and potentials for graphene and the triangle raft system from Chapter 5. The impact of the on the surrounding system is evaluated in terms of the distribution of rings surrounding the central templated ring, both in terms of the geometric distance and topological distance. Approximations are made to evaluate the ring distribution variance for the bulk system surrounding the pore, which is shown to approximate to Lemaître's curve for both graphene and triangle raft systems. Local ordering around the ring is shown to be signficantly different for graphene and triangle raft systems, with triangle raft systems showing longer range order. For graphene systems, the central pore shows concave regions at high disorder, with the edges of the central pore elongated, while triangle raft systems show consistent pore size with disorder, with a largest inscribed circle $\simeq 16$Å in diameter. Global assortativity measurements show pore systems as more assortative than bulk systems, which is proposed to result from the intra-shell ordering about the pore, which brings like-sized rings together. Energy values derived from the simulation potentials and from charge-based approaches as in Chapter 5 indicate that pores in graphene systems act similar to surface vacancies, whereas pores in triangle raft systems behave more like large rings.

9

The High Throughput Construction and Analysis of Bilayers of Tetrahedra.

9.1 Motivations

Throughout this work, we have highlighted to the relevance of our models to silica bilayers, constructed of vertex-sharing SiO_4 tetrahedra. In this work, we use our results from Chapter 5 as a basis for building a dataset of network structures, to which we can apply higher level potentials, following the workflow described in Section 4.5. The presence of a mirror plane allows bilayer structures to exactly map onto a two-dimensional network of three-coordinate nodes, with the same characteristics as those we have discussed earlier in this work. In particular, we are interested in the energetic behaviour of systems with cell area, which we treat as a variable, in order to determine the maximum and minimum stable areas occupied by our structures. This work aims to bridge the gap between hard-shell simulations of silica systems, which are used as the basis of zeolite modelling, and higher level, more accurate, system-specific empirical potentials.

9.2 The High Throughput Construction and Analysis of Bilayers of Tetrahedra.

The High Throughput Construction and Analysis of Bilayers of Tetrahedra.

Oliver Whitaker,[1] David Ormrod Morley,[1] and Mark Wilson[a1]

[1] *Department of Chemistry, Physical and Theoretical Chemistry Laboratory, University of Oxford, South Parks Road, Oxford OX1 3QZ, UK*

A method for generating siginficant numbers of network configurations is developed appropriate to bilayers of systems such as SiO_2, GeO_2 and aluminosilicates. The presence of a mirror plane allows the bilayer structures to exactly map onto a two-dimensional network of three-coordinate nodes (equivalent to a percolating network of edge-linked rings). A bond switching algorithm is employed to generate disordered (amorphous) network topologies (characterised by the ring size distribution and the nearest-neighbour connectivities, as measured by the Aboav-Weaire Law and assortativity). Bilayer configurations are generated from these networks and energy minimisations are performed using a hierachy of potential models; a purely harmonic potentials, a harmonic potential and an inter-tetrahedral repulsive term, a rigid-ion model, and a polarizable-ion model. The harmonic potential shows a flexibility window whose extend depends on the magnitude of the inter-tetrahedral repulsive term. Distortions of the bilayer networks are characterised with reference to both the ideal (hexagonal) crystal and the amorphous networks. In addition, a "pore evaporation" algorithm is developed and used to generate a range of potential zeolitic networks. These networks, which are ordered but contain significant numbers of non-hexagonal rings, provide a useful contrast to the disordered networks.

[a] mark.wilson@chem.ox.ac.uk

I. INTRODUCTION.

Recent developments in experimental techniques have shown how inorganic thin films, which consist of *bilayers* of network-forming materials such as SiO_2, GeO_2 and aluminosilicates, may be effectively synthesised[1,2]. Whilst such films have most commonly been synthesised in a disordered (amorphous) state, partially crystalline films have also been observed[3]. Such materials have potential applications in, for example, catalysis and gas separation (see ref.[4] and references therein). However, whilst the experimental investgations generate highly detailed information regarding the bilayer structures, they are time and resource consuming and it is difficult to extract any truly statistical information regarding the relative stability of different network topologies. For highly distorted systems, continuous random networks appear commonplace in nature being observed in chemical, biological and physical systems, such as crystallite grains[5–8] or cellular structures[9–13], foams[13–20] and geological phenomena such as the Giant's Causeway[21].

Synthetic pathways developed to date have allowed thin films of SiO_2 to be deposited on metallic[1,4,22–29] or graphitic[30] substrates, with advanced imaging techniques allowing for atomic resolution of the structure. A subset of the films deposited show structures which can be interpreted as based on bilayers of corner-sharing SiO_4 coordination polyhedra (CP). Such bilayers are stable (in a chemical sense) as all the Si and O atoms are 4- and 2-coordinate respectively (*i.e.* there are no "dangling" bonds). For both amorphous and crystalline films a mirror plane houses a layer of O atoms which act as bridges between the two monolayers[31,32]. The pseudo-two dimensional nature of the bilayers allows the ring structures to be *directly* observed, constructed from the network of Si atoms. The ideal crystalline system is a percolating net of six-membered rings, and amorphous systems are constructed from 4- to 10-membered rings[33,34]. The experiments allow near-atomistic resolution of the surface structure. However, whilst the information obtained is highly detailed, it is statistically limited in the sense that, although the location of thousands of atoms may be impressively resolved, this is still significantly fewer than the thermodynamic limit (*i.e.* $N < N_A$).

The novelty of these near-2D bilayer networks has spawned a number of (complementary) computational studies, both *ab initio*[35,36] and classical[31,37]. The atomistic resolution offerred by experiment allows these configurations to be used directly in the simulation models. However, these are limited both in size and number, and can contain defects or areas which could not be fully imaged. Furthermore, the configurations are necessarily aperiodic, requiring the application of sliding boundary conditions for effective simulation[38]. As a result, computational techniques are preferable for generating configurations. To this end a number of complementary techniques have been developed, including quenching a liquid confined to two dimensions[31], bond switching Monte Carlo[39,40], and growth of triangular rafts[40,41].

The network structure can be described at a number of "levels". At the first the ring distribution, p_n, describes the proportion of rings in the network of size n. The distributions are constrained by Euler's formula for connected planar graphs, such that the mean ring size must be equal to six, $\langle n \rangle = 6$. The second involves the ring correlations, that is, the tendency (if any) of rings of different sizes to be adjacent to one another. The ring distributions themselves contain no information as to how these rings are spatially arranged. Information on the nearest-neighbour ring structure has, historically, been investigated using an empirical Aboav-Weaire law[5,6], which, in one form, may be written as

$$nm_n = \langle n \rangle^2 + \mu_2 + \langle n \rangle (1 - \alpha)(n - \langle n \rangle), \tag{1}$$

where m_n is the mean ring size for the rings neighbouring a ring of size n and $\mu_2 = \langle n^2 \rangle - \langle n \rangle^2$, the second moment. As a result, the parameter α in equation 1 contains information regarding nearest-neighbour ordering. For example, a larger value of α indicates an increased tendency of small rings to be adjacent to large rings. Nature appears to favour $\alpha \sim 0.2 - 0.3$ suggesting a strong tendency for large rings to be positioned next to small rings[42]. The Aboav-Weaire law has been used (in particular, in a chemistry context) to quantify local ordering. There are, however, issues with its application, in particular the requirement for equation 1 to give a good linear fit, and the potential for "outliers" (*i.e.* very small or, more likely, very large rings) to greatly affect the fit. In addition, the value of the parameter α does not have clear physical bounds. For example, a truly random network shows $\alpha = -\mu_2/\langle n \rangle$ and hence depends upon the width of the ring size distribution[43].

What is required, therefore, are methods to generate large numbers of possible bilayer structures which can then be sorted. The existence of the mirror plane in the bilayers means that the network topology maps directly onto a two-dimensional net. A modelling strategy, therefore, is to generate the basic topologies using this (highly computationlly-efficient) mapping. These networks can then be sorted as required (for example in terms of the level of disorder or in terms of the nearest-neighbour structure), converted into full bilayer configurations, and then investigated further using higher-level (and hence less computationally-efficient) models. This hierarchical strategy allows potential new structures to be effectively identified and investigated for possible useful properties. For example, the concept of the *flexibility window* is significant in considering zeolite properties[44,45], in particular in helping to ratioanlise the ability of these systems to form networks which differ significantly in density whilst maintaining lattice energies close to that of the crystalline ground state.

The structure of this paper is as follows. In section II the methods used are summarised, namely the bond-switching Monte Carlo technique used to generate the basic network topologies, along with the method by which the bilayers are generated and the potential models used. In addition a method for generating arbitrary pore distributions (termed "pore evaporation") is described, allowing for a rich array of potential zeolitic crystal structures to be investigated. Section III contains the core results, focussed first on the ideal hexagonal-net-based crystal, before branching into introducing non-six-membered rings, firstly as potential zeolitic structures, and secondly as fully disordered (amorphous) structures. Section IV discusses the results and links the different networks whilst section V draws conclusions.

II. METHODS.

A. Bond-Switching Monte Carlo.

The fundamental coordination polyhedra (CP) for the silica bilayers are vertex-sharing tetrahedra with O atoms at the vertices and the Si atoms at the centre, as is the case for the bulk condensed phases at ambient pressure. In the bilayers these CP are arranged such that three of the vertices are connected to tetrahedra in the same layer, with one vertex shared between layers (a "bridge"). The bridging oxygen atoms enforce a symmetry plane between the upper and lower layers and means that the two layers are mirror images. As a result, the bilayer structure can be mapped onto two-dimensions, retaining all key information such as the ring statistics and connectivities[41]. Here we wish to produce large numbers of configurations with controlled ring statistics and topologies. To that end, working with this reduced representation is sufficient to fully describe the bilayer network topology. It provides a highly computationally efficient method for generating networks with the required *topology*. Each network topology can then be converted back to a full bilayer configuration whose structure may be refined as required.

The two-dimensional network configurations are generated using a bond-switching Monte Carlo (MC) technique as originally developed by Wooten, Winer and Weaire[46] (described fully in ref.[39]). In this method a starting configurations (here a perfect hexagonal lattice) undergoes a series of transformations in which neighbouring pairs of atoms are swapped. In the present work MC moves are used which preserve the three-coordinate nodes (and hence the overall coordination number remains fixed at three throughout). As a result, each MC move introduces a Stone-Wales defect into the lattice (increasing the size of two rings by one and reducing the size of another two by one). Each bond "flip" is followed by a geometry optimisation in which the system energy is driven towards a local energy minimum. Here a simplified Keating potential[47–49] is utilised as an example of a relatively simple models which contains two- and three-body interactions and allows for rapid energy minimisation. Note that the choice of potential model is not critical as it is merely a means to ensure that the two dimensional network evolves in an energitically reasonable fashion. Geometry optimisation is achieved via a steepest descent algorithm which can be applied locally to the bond switch (with significant reduction in computational cost).

The use of a MC procedure introduces a "temperature" parameter, which controls the moves allowed in which the system energy becomes more positive. As a result, the MC temperature and the rate at which this MC temperature is reduced effectively contol the level of disorder. The MC procedure described generates entropically-driven configurations consistent with a maximum entropy (ME) analysis. As a result, the disorder may be effectively characterised by the fraction of a single given ring size, usually the fraction of six-membered rings, p_6, since these are dominant (particularly at low temperature). Alternatively, the ME distribution automatically links the second moment of the ring size distribution, μ_2, to the fraction of six-membered rings, known as the Lemaître law[50,51]. In addition to using the MC temperature, the network properties may be controlled using a *cost function*. For example, the network properties determined may be compared to the target parameters (here the fraction of $k-$membered rings, p_k^t, the second moment, μ_2^t, and the Aboav-Weaire paremater, α_t), with cost function,

$$\chi = k|\alpha - \alpha_t| + \frac{|\mu_2 - \mu_2^2|}{\mu_2^t} + \sum_{k\in\mathbb{R}} \frac{|p_k - p_k^t|}{p_k^t}, \tag{2}$$

where k is a scaling parameter[39]. Further control can be applied by constaining the distribution of allowed ring sizes. In the present work we use two contrained networks. In the first only 5-, 6- and 7-membered rings are allowed (termed 5-7 constrained) and in the second rings of size $n = 4 - 10$ are allows (termed 4-10 constrained). For the 5-7 constrained system the second moment becomes linear in p_6, with $\mu_2 = 1 - p_6$.

B. Pore Evaporation.

To allow even greater comtrol over network formation a method of so-called *pore evaporation* has been developed in which identified nodes in a given lattice can be systematically removed. Nodes are removed from an ideal net with the remaining under-coordinated notes reconnected to reestablish both full coordination and the required ring connectivity. As an example, figure 1 shows the effect of removing six nodes from an ideal hexagonal net. The removal of this hexagon of nodes results in the formation of six under-coordinated (two-coordinate) nodes (figure 1b). Full three-coordination may be reestablished by joining these nodes as shown in figure 1c. In this example, therefore, a relatively large ring of size $k = 12$ has been formed which is "balanced" by the concomitant formation of three four-membered rings (and hence the mean ring size remains, as it must, as six). Nodes can be removed in any number of ways. The most flexible method utilises a graphical user interface (GUI) to allow the user to visualise the network to be modified. The user can then "click" on nodes to remove from the network with the newly-under-coordinated nodes on the created internal surface highlighted. Once the required number of nodes have been evapourated, the user end ends the pore creation process and potential connections between uncoordinated nodes are evaluated. The removal of nodes potentially introduces strain into the network which is removed by scaling the coordinates along both cartesian axes to locate the energy minima. Once the fully relaxed configuration is obtained the Monte Carlo bond-switching method (as described in section II A) is employed. The pore introduced via the node evaporation is treated as fixed, and so is not involved in any Stone-Wales bond switches. As a result, the bond switching will act to reduce the distortion created by the presence of the large ring; without the constraint of fixing the large ring, the simplest way to reduce strain would simply be to minimise the size of the largest ring.

C. Bilayer Generation and Harmonic Potentials.

Bilayer configurations can be generated from the two dimensional networks using the following scheme. Each node becomes a metal cation tetrahedron centre with locations halfway between each of the three neighbours becoming the three O atoms in the basal plane of that tetrahedron. This layer of O atoms is different from the M atom nodes along a direction perpendicular to the plane containing the atoms (hence forming a set of linked triangular biprisms). A mirror image of these biprisms is then constructued and joined to the original layer via a central plane which is occupied by the bridging O atoms which initially map onto the original node coordinates. In the simplest bilayer representation the tetrahedral geometry is maintained by joining the four M-O and six O-O atoms by harmonic springs, such that the harmonic energy between a given pair of atoms ij in a given tetrahedron is given by, $U^{ij}_{harm} = k(r_{ij} - r_{\alpha\beta})^2$, where $r_{\alpha\beta}$ is the MO or OO separation in an ideal tetrahedron, and k is the spring force constant. The repulsion between neighbouring tetrahedra is modelled using a shifted 12-6 potential which acts between pairs of M atoms only (*i.e.* it acts between the tetrahedral centres),

$$U = \begin{cases} 4\epsilon \left[\left(\frac{\sigma}{r}\right)^{12} - 2\left(\frac{\sigma}{r}\right)^{6} \right] + \epsilon, & r_{cut} \leq 2^{1/6}\sigma \\ 0, & \text{otherwise} \end{cases} \tag{3}$$

where ϵ is a constant and r is the Si–Si separation between atoms in adjacent tetrahedra, and σ characterises the length-scale of the short-range interaction.

Our primary aim here is to generate topologies suitable for further investigation using more accurate (and hence more computationally-demanding) potential models. The harmonic springs act to control the local (tetrahedral) geometries whilst the 12-6 potential imposes a repulsive interaction between nearest-neighbour tetrahedra. These functions are chosen as deliberately simple to improve computational efficiency and achieve high throughput of idealised networks. Furthermore, the parameters k and ϵ need have no direct physical meaning, simply controlling the meaning of the system "temperature". Our only requirement is that the respective terms generate energies of the same magnitude to allow for efficient structural evolution. The energies are minimised using a steepest descent algorithm in which the kinetic energy is quenched when it reaches a (local) maximum.

D. Inclusion of Electrostatic Interactions.

In the next stage the relaxed bilayer configurations which emerge from the harmonic energy minimisations are relaxed further usung a more accurate potential which includes a more detailed description of the underlying interatomic interactions. Here we employ the model developed by Tangney and Scandolo[52] for SiO_2 (termed the TS potential). The TS potemtial utilises an ionic description in which the interaction energy is dominated by the electrostatic interactions. The Si and O ions carry charges of $+2.4e$ and $-1.2e$ respectively (*i.e.* smaller than the full charges suggested

by their formal valences) with the relative magnitudes of the Si-O and O-O short-range interactions favouring the formation of SiO_4 tetrahedra (under ambient pressure conditions). At the simplest level (a rigid-ion model - RIM) the potential model is a pair-wise additive combination of short-range and (long-range) charge-charge electrostatic terms. In addition the model may include a description of ion polarization (a polarizable-ion model - PIM[53]) which incorporates and many-body character into the model. In network systems such as SiO_2 the anion polarizability effectively controls the angles between neighbouring connected tetrahedra (*i.e.* the Si-O-Si bond angle - see ref.[53] and references therein). The computational effort required to relax a configuration with a RIM or PIM is significantly greater compared with using a harmonic potential as the former requires double sums over all ions and a method (such as an Ewald summation) for handling the long-range electrostatic interactions whilst the latter requires only a sum over all bonded pairs and no long-range interactions. Furthermore, relaxing a configuration using a PIM requires around an order of magnitude more computational power compared with the rim owing to both the greater number of interactions which must be considered to calculate the energy (and forces) and the requirement to use a smaller integration time-step to control the changes in the induced moments[53].

III. RESULTS.

The results are presented in three sub-sections. In the first, ideal hexagonal crystalline networks are considered as probably the most useful reference state. In addition, the role of three different coherent distortions are also considered. In the second a range of potential zeolitic bilayer structures are considered, and in the third fully disordered (amorphous) networks are considered.

A. Crystalline networks.

Figure 2(a) shows the energy $v.$ area curves for the ideal hexagonal bilayer network obtained using the harmonic potential for a range of values of the parameter r_{cut} (which, recall, controls the interactions between neighbouring tetrahedra). For $r_{cut} = 0$ (corresponding to no short-range interactions between tetrahedra) the total energy can be driven to zero for $A^* \leq 1$. For the ideal hexagonal bilayer the inter-layer Si-O-Si bond angles are 180^o and, as a result, all three oxygen atoms in the basal plane of each tetrahedra lie in a single plane. In this case the problem maps onto a network of corner-sharing triangles, the centres of which join to make up the ring network. The energy $v.$ area curves in figure 2 can be used to define an effective flexibility window. For the harmonic model the upper and lower bounds on the area (labelled A^*_u and A^*_l respectively) are defined by the range over which the energy can be driven to zero, that is, all of the Si-O and O-O bonds are able to achieve their ideal length. The inset to figure 2(a) highlights how this results in the formation of the flexibility window, with "width" given by $\Delta A^* = A^*_u - A^*_l$, and which increases as r_{cut} decreases.

Figure 2 highlights how the bilayer can occupy different areas even whilst constraining the basal triangle of O atoms to sit in a single plane and whilst the harmonic energy can be driven to zero. Figure 3 shows two such examples (labelled A and B respectively) of coherent distortions which differ in the long-range order associated with the short-range displacements. The concerted distortion labelled A is the higher symmetry system, with p31m plane group symmetry. the distortion of each ring is identical, and in the basal plane there is no variation in bond angles. By contrast, the distortion labelled B is more disordered, with a lower symmetry p2gg plane group; there is visually more variation in ring shape and bond angles present. The structures are recognisable collapses of a kagome net[54], as examined alongside zeolites in previous work on flexibility windows of periodic trusses. An area of $A^* = 1$ corresponds to the Si-O-Si bond angle, projected onto the plane containing the basal O atoms, of 180^o. Alternate rotation of the projected triangles (the basal planes of the respective tetrahedra) as shown in figure 3 results in a reduction of the overall system area whilst retaining the ideal tetrahedral geometries (and hence having zero energy within the harmonic model). For example, for the highly concerted distortion (A), the area of the hexagon is given by $A_{hex} = 6\sqrt{3}r_t^2\sin^2(\alpha/2)$, where r_t is the distance from a triangle vertex to the centre of mass and α is the angle between to neighbouring vectors $\mathbf{r}_t$. At a projected angle of 180^o all of the available bending modes have been exhausted and so any further increase in system area is facilitated via stretches (with a concomitant energetic penalty). As a result, $A^* = 1$ represents the upper bound on the system area for which the energy can be quenched to zero, or its minimum density state. The inclusion of a repulsive term between tetrahedra introduces a lower bound on the area. Considering the examples shown in figure 3, as the oxide basal plane triangles rotate, the nearest-neighbour Si-Si separation is reduced. As a result, increasing the value of the parameter r_{cut} will increase the range of the Si-Si repulsion and raise the value of the lower area limit, A^*_l. For the ideal hexagonal lattice the upper area limit is controlled entirely by the geometry and is fixed, whilst the lower limit depends only on r_{cut}, as this parameter controls the repulsion between

neighbouring tetrahedra. The window "closes" ($\Delta A^* = 0$) when the short-range interaction length-scale becomes equal to r_{SiSi} for a projected angle of 180^o (*i.e.* panel (a) in figure 2). This corresponds to $r_{cut} \simeq 3.0$Å.

Figure 2 (b) shows the energies $v.$ area for the harmonic model for the type B distortion for a range of $r_{cut} = 2.63$Å$values.2.83$Å and 3.15Å respectively. In all cases the energy cannot be driven to zero for $A^* \geq 1$ as this exhausts the bending modes and requires activation of (non-zero energy) stretching modes. At the lower value of r_{cut} the flexibility window extends to the lowest areas studied whilst the window for the higher value of r_{cut} shows a lower bound. Interestingly, the width of the flexibility window (inset to figure 2(b)) is greater for the type B distortion than for type A with $\Delta A \sim 0.10$Å for A and ~ 0.12Å for B. The change in the width of the flexibility window can be rationalised by considering the different structural changes. The lower symmetry type B distortion can accommodate *both* twising of the tetrahedra perpendicular to the bilayer major plane *and* tilting of the tetrahedra in which the three atoms in the basal plane of the tetrahedra shift). The type A coherent distortion does not allow a tilt without distortion of the local tetrahedral coordination polyhedra (which, in the harmonic model, has an energetic cost). However, the type B distortion *can* accommodate such tilts and so offer an additional mechanism to relieve strain. We will develop this in section III D. The implication of the concerted distortions shown in figure 3 is that the twisting of the tetrahedra, defined in terms of rotations of the three O atoms in the basal plane, is an excellent metric to identify the upper area bound of the flexibility window. This is a metric which has been established for understanding the flexibility window in three dimensional aluminosilicate zeolites.

Moving on to the more complex models (section II D) which incorporate descriptions of the underlying electrostatic interactions, figure 4 shows the energy $v.$ area curves for both the RIM and PIM. For the RIM the starting configurations at each area is that extracted from the fully relaxed harmonic model (section II C) whilst for the PIM configurations are taken which have been fully relaxed using both the harmonic model and the RIM. The PIM shows a minimum at lower area ($A^* \sim 0.988$) and more negative energy ($U^* \sim -6609.3$kJmol^{-1}) when compared to the RIM ($A^* \sim 1.032$, $U^* \sim -6574.9$kJmol^{-1}). The more negative energy achieved using the PIM highlights the (relatively small) role or polarization (many-body effects) in determining the static structure. The inclusion of polarisation effects in this manner is essentially variational in nature and so $U^{pim} < U^{rim}$. The reduction in area at the energy minimum for the PIM reflects the role of anion polarizability in stablising more acute Si-O-Si bond angles with respect to the corresponding RIM. The energies extracted from the PIM starting from either the harmonic potential- or RIM-relaxed configurations appear near-identical, suggesting that the "intermediate" RIM relaxation may be omitted For both the RIM and PIM the type B distortion shows significantly more favourable energies at lower areas for same reasons as observed for the harmonic potential (see above). The figure also shows the predicted flexibility windows. For the RIM and PIM the energy can no longer be driven to zero (as for a harmonic model) to give a "clean" definition of the flexibility window. Here we take the area range over which the relaxed potential energy is $\Delta U = U - U^* \leq RT$, where U^* is the most favourable energy and T corresponds to room temperature, however alternative limits are proposed in section **??**. The flexibility window is approximately the same width for the RIM for all three distortions whilst it is significantly wider for the PIM for the type B distortion, reflecting the lower curvature of the U $v.$ A curves around the energy minimum for the PIM as the inclusion of the anion polarizability significantly softens the key repulsive cation-cation electrostatic interactions. Inclusion of polarization effects is also key for future work in order to reproduce dynamic (vibrational) properties (see, for example, ref.[55]). The concomitant structural changes will be considered in section III D.

B. Zeolitic networks.

The ideal hexagonal lattice can be used as a starting point for generating a wider range of crystalline bilayer structures using the *pore evaporation* method discussed in section II. A subset of zeolitic structures have been identified which can be mapped directly to bilayer structures. These are structures which are periodic when viewed along the (001) direction. As a result, these projections can be approximated to a three-coordinate (two dimensional) network. Physically, these structures were generated by removing nodes from a hexagonal net, and reconnecting the remaining nodes to give the required connectivity dictated by the zeolite. The structures selected are based on the symmetries of their underlying composite building units (CBUs) and natural tiling. For our purposes, the configuration should be composed of building units which can be split into two distinct layers, shows a plane of symmetry between these two layers, and has no nodes lying on this plane of symmetry. These are quite broad descriptions of theoretically allowed structures, but not all are equally feasible. In the absence of a rigorous symmetry-based argument, we search for CBUs which stack in the (001) direction in a layered manner (AA', where A' is a mirror image of A). By sorting known zeolite structures we generated a list of potential near-two-dimensional zeolites, from which we have selected six structures that follow these rules, and one (MOR), which does not. MOR shows AA'B stacking, with the AA' section obeying our broad symmetry requirements, but the necessity of a B layer in three dimensions meaning it does not obey our requirement of AA' stacking. MOR was included to understand whether similar structures would be

stable. These structures are listed in table I. Once the network connectivity properties are established the energy minimum is located for each network by relaxing both the atom coordinates and the simulation cell lengths. A bilayer is then constructed by adding a second layer which mirrors the original layer (as highlighted for disordered structures in ref.[31]).

Zeolite	Rings	μ_2	r
ATV	4,6,8	2.67	-0.26
AHT	4,10	8.0	-0.35
AEL	4,6,10	4.8	-0.48
AFI	4,6,12	8.0	-0.5
AET	4,6,14	8.9	-0.36
GIS	4,8	4.0	-0.5
MOR	4,5,8	6.5	-0.36

TABLE I. Near-two-dimensional bilayer zeolitic structures considered in the present work. Each zeolite is labelled using the nomenclature from ref. Column two lists the ring sizes for the given network whilst columns three and four give the resultant second moment of the ring size distribution and assortativity respectively.

Figure 5(a) shows the energy v. area curves and associated flexibility windows for the seven zeolitic bilayer structures along with the ideal hexagonal net curve for comparison. All of the energies are calculated using the PIM. All of the zeolite structures studied form (meta-)stable crystals with $\Delta U \lesssim 12\text{kJmol}^{-1}$ with respect to the hexagonal net minimum energy. As expected, the 2d zeolite structures very much reflect their 3d analogues in having inherent lattice energies close to that of the ideal hexagonal crystal. In addition, panel (c) of the figure shows the energy/area data with the former shown on a log scale in order to highlight the location of the energy minima. Figure 5(b) also shows the widths of the respective flexibility windows determined as described above. The values observed for the zeolites are lower than those for the hexagonal net (the mean average $\overline{\Delta A} \sim 0.8$ compared with that for the ideal hexagonal net of $\Delta A \sim 0.12$), again reflecting the balance of introducing smaller (more highly strained) rings to accommodate the larger rings. In these calculations the area of each structure is expressed relative to that of the equivalent hexagonal system (*i.e.* the areas for each zeolitic structure are not easily directly comparible). To allow for a clear direct comparison figure 5(d) shows the energies as a function of the number density, n_0, the number of SiO_2 molecules per unit area. The zeolitic networks all show *lower* densities than the hexagonal net (as would be expected). In ref.[36] DFT calculations are performed on a range of bilayer networks, two or which (labelled '8-4' and '8-6-4' in ref.[36]) correspond to the GIS and ATV zeolites respectively. The present results for the PIM compare well with those in reference[36]. The number densities are $n_0 = 15.5\text{nm}^{-2}$ and 16.3nm^{-2} for GIS and ATV respectively, compared with $n_0 = 15.1\text{nm}^{-2}$ and 15.8nm^{-2} from ref.[36]. The corresponding energy differences (expressed with respect to the ideal hexagonal net) are $\Delta E = 3.35\text{kJmol}^{-1}$ and 3.20kJmol^{-1} for GIS and ATV respectively, compared with $\Delta E = 3.79\text{kJmol}^{-1}$ and 3.12kJmol^{-1} from ref.[36].

The chosen zeolite bilayers can be broadly divided into two classes. In the first, six-membered rings are replaced by a larger ring ($k = 8, 10, 12$ or 14) with the concomitant formation of four-membered rings (retaining the required mean ring size of six). These are ATV, AEL, AFI and AET respectively. In the second, no six-membered rings are present (AHT, GIS and MOR respectively). Figure 6(a) shows the energy differences, ΔU, for all of the zeolite bilayers studied shown as a function of their respective second moments, μ_2. There is, as expected, a broad correlation between ΔU and μ_2. The networks containing the largest rings (and associated larger values of μ_2) appear least energetically favourable. This observation is consistent with the larger rings being more strained and accommodating more four-membered rings, both of which are energetically unfavourable, the former as they require stabilisation of more obtuse bond angles and the latter more acute angles. However, the consideration of the largest ring in a given network is not sufficient to predict its relative energetic stability. For AHT (4- and 10- membered rings) and AFI (4-, 6- and 12-membered rings), for example, $\mu_2 = 8$ in both cases and yet AFI appears significantly more stable than AHT as it retains a significant fraction of hexagons ($p_6 = 1/3$) whereas AFI retains no such rungs. Considering alternative potential correlations, figure 6(b) shows the energy differences as a function of the fraction of four-membered rings, p_4. Again, there is a clear correlation between the network energy and the number of these rings, with the greater the fraction of these rings the higher the energy, simply reflecting the relatively high strain associated with the formation of the four-membered rings. Figure 6(c) shows the energy differences of the zeolites formed by creating a single large ring plus associated four-membered rings as a function of the size of the largest ring. The energy differences become more significant as the size of the largest ring in the network increases, again linked to the greater strain associated both with adopting a large ring plus the required number of four-membered rings. Finally when considering the zeolite energies, figure 6(d) shows the relative energies as a function of the network assortativity. There appears little

correlation between the network connectivity and the relative energy, indicating that the energies are dominated by the sizes (and numbers) of rings formed rather then their relative spatial location. Figure 6(e) shows the areas of the respective energy minima as a function of the second moment of the ring size distribution. The area shows a strong correlation with μ_2, with the area scaling with the width of the ring size distribution.

C. Disordered networks.

In the previous sections the presence of a "flexibility window" was established for an ideal hexagonal net and shown to be present for a range of two-dimensional zeolites, the latter characterised by the presence of an ordered array of non-six-membered rings. In this section the effect of the presence of structural disorder, in the form of introducing non-6-membered rings, will be analysed. The level of disorder is controlled by the weighted cost function controlling the key target metrics (here $p_6 and \alpha$), and the Monte Carlo temperature (see section II A) with two constrained networks considered in which rings are limited to $k = 5 - 7$ and $k = 4 - 10$ only (see section II).

The introduction of structural disorder results in changes in both A_u^* and A_l^* linked purely to the network topology. For example, figure 7 shows energy/area curves for the $n = 5 - 7$ ring systems generated under different conditions, here the fraction of hexagons (which, for this highly constrained ring system also defines exactly the number of pentagons and heptagons), and the Aboav-Weaire parameter, α, which is a measure of the nearest-neighbour ring ordering. The energies are determined using the harmonic model. A number of key trends are common to the whole parameter space. The mean high area limit, $\langle A_u^* \rangle$, is approximately constant for each parameter set and shows a dispersion of values. The mean lower area limit, $\langle A_l^* \rangle$, shows a similar dispersion of values for each parameter set and shifts to higher area as r_{cut} increases. As for the crystalline case, the flexibility window effectively "closes" as the magnitude of the repulsive interaction, characterised by the parameter r_{cut}, increases. However, the effect of the disorder is clear. In the crystalline examples the flexibility window limits are well-defined. With topological disorder both bounds show a dispersion, indicating that the atomistic details of the disorder may be significant.

Figure 8(a) shows the evolution of the upper limiting area, A_u^*, as a function of p_6 extracted from all configurations generated, for both the 5-7 and 4-10 constrained networks. As more disorder is introduced the critical upper area falls and the dispersion in the observed values shows a concomitant increase. The 5-7 and 4-10 constrained systems follow similar behaviour with the latter able to support greater disorder (smaller p_6) as expected. As expected, as $p_6 \longrightarrow 1$ then $A_u^* \longrightarrow 1$ (*i.e.* corresponding to an ideal hexagonal net). The figure also hints at the existence of two regimes above and below $p_6 \sim 0.75$. For $p_6 \lesssim 0.75$ the networks show a significantly greater dispersion of areas. Figures 8(b) and (c) show the dependence of A_u^* and p_6 on the Aboav-Weaire parameter, α, again for both the 5-7 and 4-10 constrained systems. The Aboav-Weaire parameter shows a very weak dependence on p_6, reflecting the fact that the value of α is a subtle combination of effects. For example, a large ring may preferentially sit next to a small ring but that will necessarily lead to an increase in small rings neighbouring other small rings[40]. The dependence of A_u^* on α appears somewhat stronger, although still relatively weak highlighting that the absolute compositions of the ring sizes appears more significant then their spatial arrangement, at least on the nearest-neighbour length-scale. The effect of relaxing the ring distribution constraint from the 5-7 to 4-10 networks is subtle but clear. The use of the broader ring size distribution allows a smaller p_6 to be supported and the resulting dependence of A_u^* on p_6 is slightly weaker than for the 5-7 networks. The parameter α shows a weaker dependence on p_6 for the 4-10 networks reflecting the fact that the balance of the nearest-neighbour "interactions" noted above are necessarily more complex for a broader ring size distribution.

Figure 9 shows both the upper and lower area limits as a function of p_6 for an example repulsive potential corresponding to $r_{cut} = 2.63$Å. The flexibility window is clearly present at low levels of disorder (high p_6) and gradually decreases in width as the level of disorder increases, closing for this value of r_{cut} at $p_6 \sim 0.75$. The lower panel of the figure shows the width of the flexibility window, $\Delta A^* = A_u^* - A_l^*$, for three values of r_{cut} again highlighting how the window closes at higher p_6 as r_{cut} increases.

The use of a harmonic model allows the stress in the system to be effectively mapped by simply identifying bond lengths which deviate from the ideal (zero energy) values. Figure 10 shows specific examples of how stress is partitioned for $A > A_u^*$ (*i.e.* just outside the flexibility window). All of the snapshots shown correspond to the same short-range repulsion parameter ($\sigma = 1.7$Å) and Aboav-Weaire parameter ($\alpha = 0.2$) but with varying levels of disorder. Panels (a) and (b) show snapshots for $p_6 = 0.9$ and 0.3 respectively. In both cases the extended and compressed Si-O and Si-Si length-scales are highlighted. For $p_6 = 0.9$ the strained bonds appear to percolate across the cell in a chain and hence cannot be relaxed further (and hence $U > 0$). The most concentrated strain is observed in the region containing the most non-six-membered rings. In this case the majority of Si-O bonds not at their ideal values appear stretched. The behaviour of the nearest-neighbour Si-Si lengthscale (which, recall, is not controlled by a *direct* harmonic spring) appears more complex, with the Si-Si length-scale stretched along the direction of the percolating chain but are compressed perpendicular to this direction. For $p_6 = 0.3$ multiple percolating strain pathways are accommodated,

including the formation of a closed loop which encompasses a region with no strain.

The configurations relaxed using the (computationally-efficient) harmonic potential can now be used as the starting coordinates for the higher level PIM. Figure 11 shows the energy $v.$ area curves calculated using the full PIM across a range of levels of disorder. The results for the ideal hexagonal lattice (section III A) indicate that an "intermediate" relaxation using a RIM may not be required, and so is omitted here. The upper and lower panels show the energies for the 5-7 and 4-10-constrained systems respectively. In both cases the energies are displayed on a log scale relatived to their respective energy minima in order to highlight the dispersion in the areas attained for different configurations. The spread of areas corresponding to the energy minima is greater for the less constrained system (as would be expected). Figure 12 shows the areas (panel (a)) and corresponding energies (panel (b)) extracted from the respective energy minima as a function of p_6. The reduced areas shown in panel (a) are compared to the upper limits of the flexibility window identified using the harmonic model with repulsive parameters given by $r_{cut} = 2.63$Å, 2.85Å and 3.15Å (seen for the lowest value of r_{cut} in figure 9). As the harmonic model repulsive term is increased, the limit becomes more correlated with that extracted from the full PIM, albeit with a somewhat different dependence on p_6. This indicates that a simplifed (harmonic) model, including a highly simplified representation of the inter-tetrahedral repulsions, is able to broadly reproduce results from much higher level models. The two different constrained systems show similar behaviour at low levels of disorder (high p_6). For lower levels of disorder (high p_6) both constrained systems show similar behaviour, with the area associated with the energy minima showing a near-linear dependence on p_6, becoming smaller as p_6 is reduced, and showing a relatively low dispersion of values. For higher levels of disorder (corresponding $p_6 \lesssim 0.5$) the dispersion in both the areas and energies of the respective minima becomes significantly higher, in particular for the 4-10-constrained system which can accommodate higher levels of disorder. Note that even the spread of energies is still only $\sim$30kJmol^{-1} less favourable than the ideal crystal energy.

D. Structural Evolution.

The underlying structural behaviour can usefully be divided into distortions of the tetrahedral network (*i.e.* in which the tetrahedal coodination polyhedra retain their ideal geometry) and distortions of these local CP. The former may be further divided into "twists" and "tilts", describing the nature of the distortion in terms of the plane containing the bilayer. These distortions are clearer for the ideal crystal as they can be more easily separated. For example, figure 13(a) shows the twist angle as a function of area for the coherent type A distortion (figure 3) for the harmonic, rigid-ion and polarizable-ion models. All three models show zero twist above a critical area ($A^* = 1$ for the harmonic model) indicating the area above which the bending modes associated with the twiting motion are exhausted. For the RIM and PIM the area at which twisting appears are lower reflecting the distortions of the local tetrahedral coordination polyhedra (see below). For the type A distortion the twisting of the tetrahedra can "absorb" the change in area on compression. For the type B distortion, however, additional distortions are required. Figure 13(b) shows the tilt angle for the type B distortion (figure 3) as a function of area. In all cases the tilt angle becomes zero above a critical area, again corresponding to the tetrahedra basal planes lying in a single plane. Below this critical area the tetrahedra show a small tilt for all models investigated. The tilt angles are significantly smaller for both the RIM and PIM as, in both models, the total tetrahedral CP can distort whilst, in the harmonic model, the retention of the local tetrahedra is the dominant driving force. These changes can be rationalised in terms of changes in the respective Si-O-Si and O-Si-O bond angles. Figures 13(c) and (d) show the Si-O-Si and O-Si-O bond angles, again as a function of the reduced area, determined using the equatorial O atoms only (*i.e.* excluding the O atoms which "join" the two mirror image layers comprising the bilayers). The harmonic model shows an ideal tetrahedral O-Si-O angle for $A^* \leq 1$ (indicating that the system energy has, indeed, been driven to zero). The corresponding angles for the RIM and PIM are approximately constant below the areas at which the twisting becomes significant (figure 13(a)) with the former showing a small but significant distortion away from an ideal tetrahedron). The inclusion of many-body (polarization) effects allows the tetrahedra to relax to their near-ideal geometry for $A^* \leq 1$. The Si-O-Si angles obtained for the PIM are systematically more acute than the corresponding RIM values (again, a consequence of the screening effect of the dipoles induced on the anions[53]). Typical bulk condensed phase (crystalline and glassy) Si-O-Si bond angles are in the range $\theta_{SiOSi} \sim 145 - 150^o$[56]. In all cases the Si-O-Si angles decrease as the area is reduced, although the change is more gradual for the type B distortion as the reduction in area is accompanied by an additional tilt. Notably, the harmonic and polarizable models show similar Si-O-Si bond angles as a function of area, again validating the initial use of the computationally-less-complex model.

For the distorted (amorphous) structures, all of the distortions noted above contribute as summarised in figure 14. Figure 14 shows key metrics as a function of the level of disorder, here characterised by the variance in the ring size distribution, μ_2 and shown for both the 5-7 and 4-10 constrained networks. As the level of disorder approaches zero (corresponding to the ideal hexagonal lattice) the metrics reach their respective ideal values. In all cases the 5-7 and 4-10 constrained systems show the same trends with the latter showing a broader range of variances. Figure

14(a) shows the twist angle, which reaches a "limiting" value at high disorder of $\sim 11^o$. This limit is significantly smaller than observed in the ideal hexagonal net (figure 13(a)) reflecting the fact that the inherent distortions in the amorphous network are a combination of all the possible deviations from ideality. Figure 14(b) shows the O-Si-O bond angle (again determining using the equatorial O atoms only). The mean angle remains at around the ideal tetrahedral value with a spread which increases with the amount of disorder. The Si-O-Si angle (figure 14(c)) shows a small decrease as disorder is increased, which is correlated with the concomitant increase in the tilt angles (figure 14(d)).

Overall, therefore, specific changes in structure can be identified and quantified for specific distortions of the crystalline network. Furthermore, correlations between these changes, for example between the twist and tilt angles, can also be identified. The introduction of topological disorder is accompanied by the full spectrum of the identified distortions.

IV. DISCUSSION.

A. Hierarchy of Potential Models.

The results presented in this paper highlight how methodologies which invoke hierarchical potential models may be used to effectively *sort* network structures, allowing the more physically-realisable structures to be examined in more detail by more complex models. In the present work, for example, the harmonic model, at the simplest level, requires only (spring) connections between nearest-neighbour Si-O and O-O pairs (meaning 10 springs per tetrahedron). The rigid- and polarizable-ion models are necessarily more complex, requiring sums over all pairs of atoms as well as methods for handling the long-range electrostatic terms and, for the latter, iterative methods for calculating the many-body terms.

The ability to stablise relatively acute Si-O-Si angles indicates that such an approach should work for other tetrahedron-based systems, such as GeO_2 or more complex aluminosilicates. Critically, the ability to consider a wide range of network topologies avoids the potential problem os assuming that, for example, SiO_2-like configurations transfer "trivially' to systems such as GeO_2.

B. Relative Densities.

The results presented above allow us to consider the *relative* densities of both the zeolitic and amorphous networks when compared with the of an ideal hexagonal net. Figures 5, 6 and 12 show the range of densities observed for these two types of network. For the zeolitic structures the number densities sit in the range $14.2\text{nm}^{-2} \lesssim n_0 \lesssim 16.3\text{nm}^{-2}$, whilsts for the amorphous networks the corresponding (mean value) range is $16.9\text{nm}^{-2} \lesssim n_0 \lesssim 17.7\text{nm}^{-2}$. It is clear, therefore, that the introduction of a highly ordered arrangement of rings appears to favour networks which are *less* dense than the ideal hexagonal net, whilst the introduction of a distribution of ring sizes in an entropically-driven disordered manner, results in networks which are *more* dense. The density of each specific disordered network is highly dependent on both the distribution of ring sizes and their arrangement in space, with the range of possible densities related to the flexibility window as identified with the harmonic potential.

C. Stress Distribution.

The connectivity between the stressed bonds (as seen graphically in figure 10) highlights the potential existence of structural correlations which may persist over a range of longer length-scales. These structures may be approximately linear (and hence percolate across the periodically-repeating simulation cell) or form closed, near-circular, paths. It is clear that the geometry of these structures will have implications for the mechanical properties of the networks and will, therefore, require careful future modelling using very large simulation cells.

V. CONCLUSIONS.

In this paper two methods have been developed for generating network configurations. The networks are characterised in terms of the distribution of ring sizes and their spatial relationships. In one case a bond switching algorithm is used to generate disordered (amorphous) networks which are characterised in terms of their level of disorder (for

example, using the fraction of hexagons or the variance of the ring size distribution). In the second, a pore evaporation algorithm is used to generate zeolitic networks which are crystalline in nature, but characterised by significant numbers of non-hexagonal rings. For the disordered configurations a hierarchy of potential models has been used to show how a relatively simple (and hence computationally inexpensive) potential can be used to sort the configurations, allowing more accurate (and hence more computationally demanding) models to be applied.

VI. ACKNOWLEDGEMENTS.

We are grateful for support from the EPSRC Centre for Doctoral training, Theory and Modelling in Chemical Sciences, under grant EP/L015722/1. This paper conforms to the RCUK data management requirements.

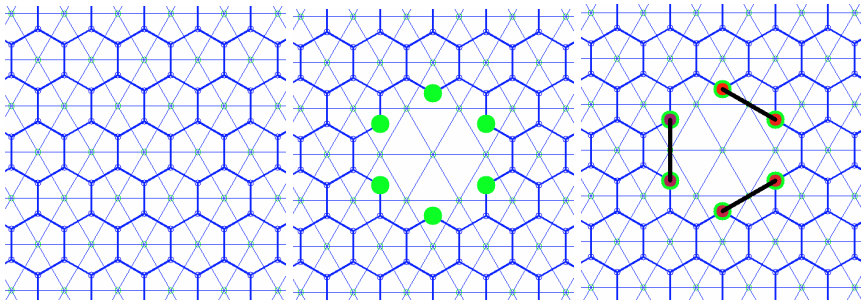

FIG. 1. Schematic diagram to show the pore evaporation process described in the text. In this example six atoms are removed from the ideal hexagonal net (left hand panel) to give the central panel (which now contains six under-coordinated nodes as shown by the green dots). These under-coordinated nodes are combined as shown in the right-hand panel to give a fully-coordinated network containing a large (12-membered) central ring as well as three four-membered rings.

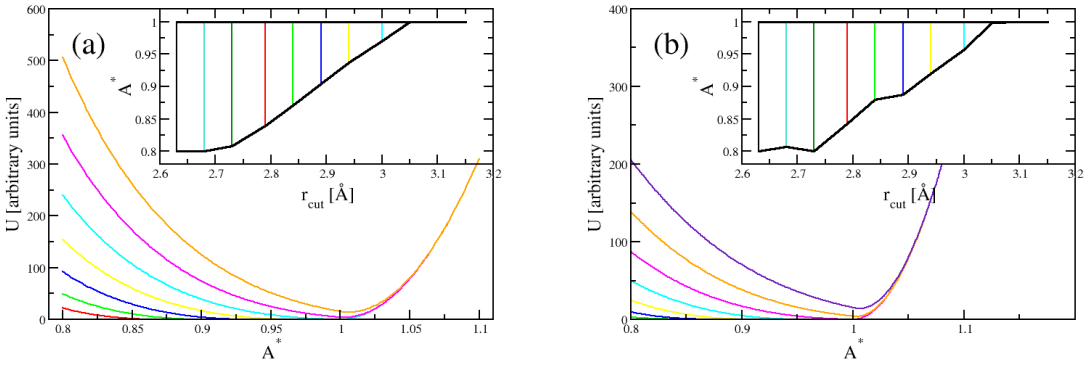

FIG. 2. Energy v. area curves starting from an ideal hexagonal lattice using the two coherent distortions shown in figure 3 (panel (a) - type "A", panel (b) - type "B"). For both distortions the curves are shown for 12 values of the repulsion parameter, r_{cut}. The insets to both panels show how the flexibility window width changes with r_{cut}. The window is defined as the range of areas over which the total system energy can be driven to zero.

[1] J.Weissenrieder, S.Kaya, J-L.Lu, H-J.Gao, S.Shaikhutdinov, H-J.Freund, M.Sierka, T.K.Todorova, and J.Sauer, Phys. Rev. Lett. **95**, 076103 (2005).
[2] J. Boscoboinik, X.Yu, B.Yang, F.D.Fisher, R.Wlodarczyk, M.Sierka, S.Shaikhutdinov, J.Sauer, and H.-J. Freund, Ange. Chem **51**, 6005 (2012).
[3] L.Lichtenstein, M.Heyde, , and H.-J. Freund, Phys. Rev. Lett. **109**, 106101 (2012).
[4] C. Buechner and M.Heyde, Prog. Surf. Sci. **92**, 341 (2017).
[5] D.A.Aboav, Metallography **3**, 383 (1970).
[6] D.Weaire, Metallography **7**, 157 (1974).
[7] S.K.Kurtz and F.M.A.Carpay, J. Appl. Phys. **51**, 5745 (1980).
[8] P.Feltham, Acta. Met. **5**, 97 (1957).
[9] H. Honda, J. theor. Biol. **72**, 523 (1978).
[10] J.C.M.Mombach, R. de Almeida, and J. Iglesias, Phys. Rev. E **47**, 3712 (1993).
[11] N.Rivier, G.Schliecker, and B.Dubertret, Acta. Biotheo. **43**, 403 (1995).
[12] F.T.Lewis, Anat. Rec. **50**, 235 (1931).
[13] V. Parfait-Pignol, G. L. Caer, and R.Delannay, Eur. Phys. J. B **4**, 499 (1998).
[14] C.Quilliet, S. Talebi, D.Rabaud, J.Kaefer, S.J.Cox, and F.Graner, Phil. Mag. Lett. **88**, 651 (2008).
[15] H.J.Ruskin and Y. Feng, Physica A **230**, 455 (1996).
[16] K.Y.Szeto, T.Aste, and W.Y.Tam, Phys. Rev. E **58**, 2656 (1998).
[17] M.A.Fortes and P.I.C.Teixeira, J. Phys. A: Math. Gen. **36**, 5161 (2003).
[18] A. Steyer, P. Guenoun, D. Beysens, and C. Knobler, Phys. Rev. B **42**, 1086 (1990).

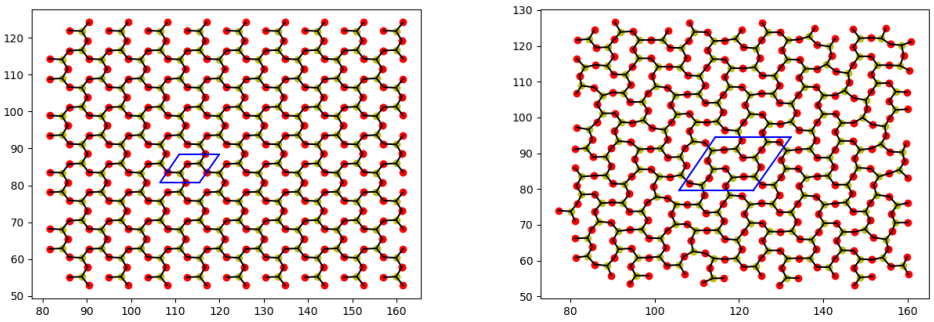

FIG. 3. The two coherent distortions used in the present work. Left - type “A”, right - type “B”.

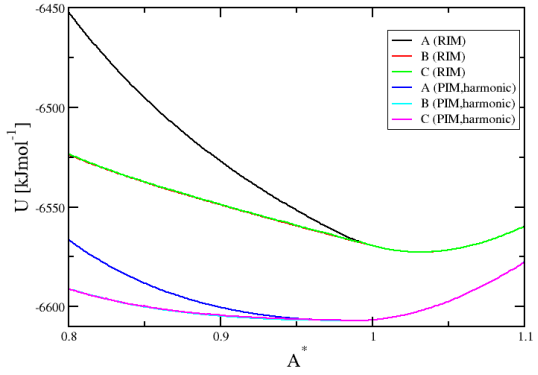

FIG. 4. Energy v. area curves for the ideal hexagonal lattice relaxed using the coherent distortions shown in figure 3 determined using both rigid- and polarizable-ion models (RIM and PIM respectively). The legend shows the model and the distortion applied. In all cases the starting configurations were generated by relaxing using a harmonic model as described in the text.

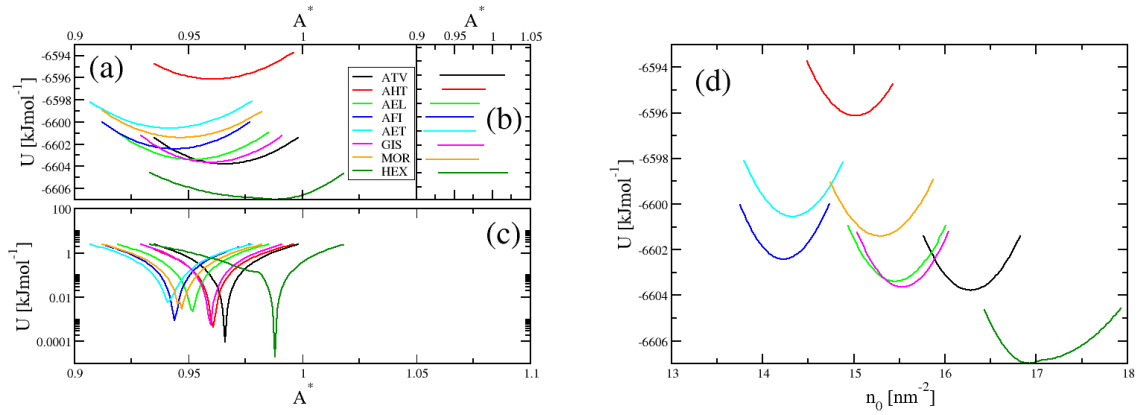

FIG. 5. Panels (a) and (c) shows the energies of the investigated zeolite networks (coloured as given in the legend) compared to the ideal hexagonal net. Panel (a) shows the absolute energies v. area whilst panel (c) shows the energies relative to the ideal hexagonal net on a logarithmic scale. Panel (b) shows the width of the respective flexibility windows determined to $T = 300$K. Panel (d) shows the zeolite network energies as a function of number density.

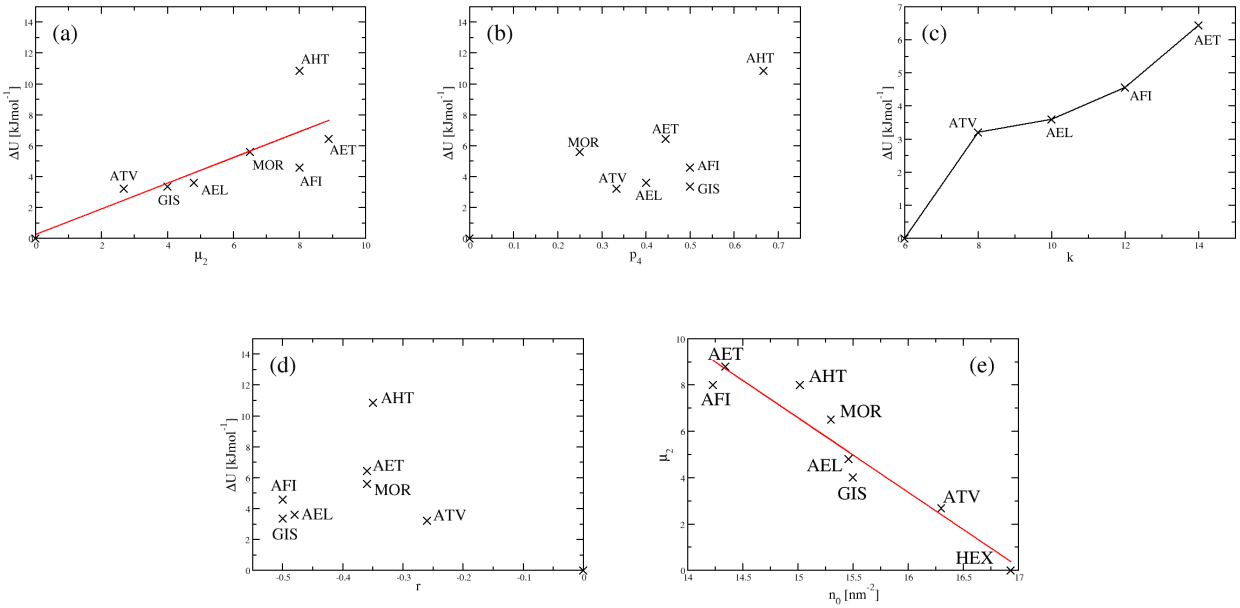

FIG. 6. Exploring potential correlations in the energies and areas extracted from figure 5. Panels (a)-(d) show the energy difference (with respect to the ideal hexagonal net) as a function of (a) the ring size distribution second moment, μ_2, (b) the fraction of four-membered rings, p_4, (c) the size of the largest ring (shown for a subset of the zeolites as described in the text) and (d) the assortativity, r. Panel (e) shows the dependence of the number density of the respective energy minima as a function of μ_2.

[19] F. Elias, C. Flament, J.-C. Bacri, O. Cardoso, and F. Graner, Phys. Rev. E **56**, 3310 (1997).
[20] P.Cerisier, S.Rahal, and N.Rivier, Phys. Rev. E **54**, 5086 (1996).
[21] D.L.Weaire and N.Rivier, Contemp.Phys. **25**, 59 (1984).
[22] L.Lichtenstein, C. Buechner, B.Yang, S.Shaikhutdinov, M.Heyde, M.Sierka, R.Wlodarczyk, J.Sauer, and H.-J. Freund, Angew. Chem. Int. Ed. **51**, 404 (2012).
[23] M.Heyde, S.Shaikhutdinov, and J.-J. Freund, Chem. Phys. Lett. **550**, 1 (2012).
[24] D.Loeffler, J.J.Uhliruch, M.Baron, B.Yang, X.Yu, L.Lichtenstein, L.Heinke, C.Buechner, M.Heyde, S.Shaikhutdinov, *et al.*, Phys. Rev. Lett. **105**, 146104 (2010).
[25] E.I.Altman, J.Gotzen, N.Samudrala, and U.D.Schwarz, J. Phys. Chem. C **117**, 26144 (2013).
[26] E.I.Altman and U.D.Schwarz, Adv. Mat. Int. **1**, 1400108 (2014).
[27] C. Buechner, Z-J.Wang, K.M.Burson, M.-G. Willinger, , M.Heyde, R.Schloegl, and H.-J. Freund, ACS Nano. **10**, 7982 (2016).
[28] C. Buechner, L.Liu, S.Stuckenholz, K.M.Burson, L. Lichtenstein, M.Heyde, H-J.Gao, and H.-J. Freund, J. Non-Crys. Solids **435**, 40 (2016).
[29] K.M.Burson, P.Schlexer, C. Buechner, L. Lichtenstein, M.Heyde, and H.-J. Freund, J. Chem. Educ. **92**, 1896 (2015).
[30] P.Y.Huang, S.Kurasch, A.Srivastava, V.Skakalova, J.Kotakoski, A.V.Krasheninnikov, R.Hovden, Q.Mao, J.C.Meyer, J.Smet, *et al.*, Nano. Lett. **12**, 1081 (2012).
[31] M.Wilson, A.Kumar, D.Sherrington, and M.F.Thorpe, Phys. Rev. B **9**, 214108 (2013).
[32] M. Sadjadi, B. Bhattarai, D. Drabold, M. Thorpe, and M. Wilson, Phys. Rev. B **96**, 201405(R) (2017).
[33] A.Kumar, D.Sherrington, M.Wilson, and M.F.Thorpe, J. Phys.: Condens. Mat. **26**, 395401 (2014).
[34] M. Sadjadi and M. Thorpe, Phys. Rev. E **94**, 062304 (2016).
[35] T. Björkman, S. Kurasch, O. Lehtinen, J. Kotakoski, O. V. Yazyev, A. Srivastava, V. Skakalova, J. H. Smet, U. Kaiser, and A. V. Krasheninnikov, Sci. Rep. **3**, 1 (2013).
[36] A. Malashevich, S. Ismail-Beigi, and E. I. Altman, J. Phys. Chem. C **120**(47), 26770 (2016).
[37] P. K. Roy, M. Heyde, and A. Heuer, Phys. Chem. Chem. Phys. **20**(21), 14725 (2018).
[38] L. Theran, A. Nixon, E. Ross, M. Sadjadi, B. Servatius, and M. Thorpe, Physical Review E **92**(5), 053306 (2015).
[39] D. Ormrod Morley and M. Wilson, J. Phys. Condens. Matter **30**(50), 50LT02 (2018).
[40] D. Ormrod Morley, A. Thorneywork, R. Dullens, and M. Wilson, Phys. Rev. E pp. 1–13 (2020).
[41] D. Ormrod Morley and M. Wilson, Mol. Phys. **117**(21), 3148 (2019), `https://doi.org/00268976.2019.1605099`.
[42] I. Zsoldos and A. Szasz, Comput. Mater. Sci. **15**, 441 (1999).
[43] R. Delannay and G. Le Caër, Phys. Rev. Lett. **73**(11), 1553 (1994).

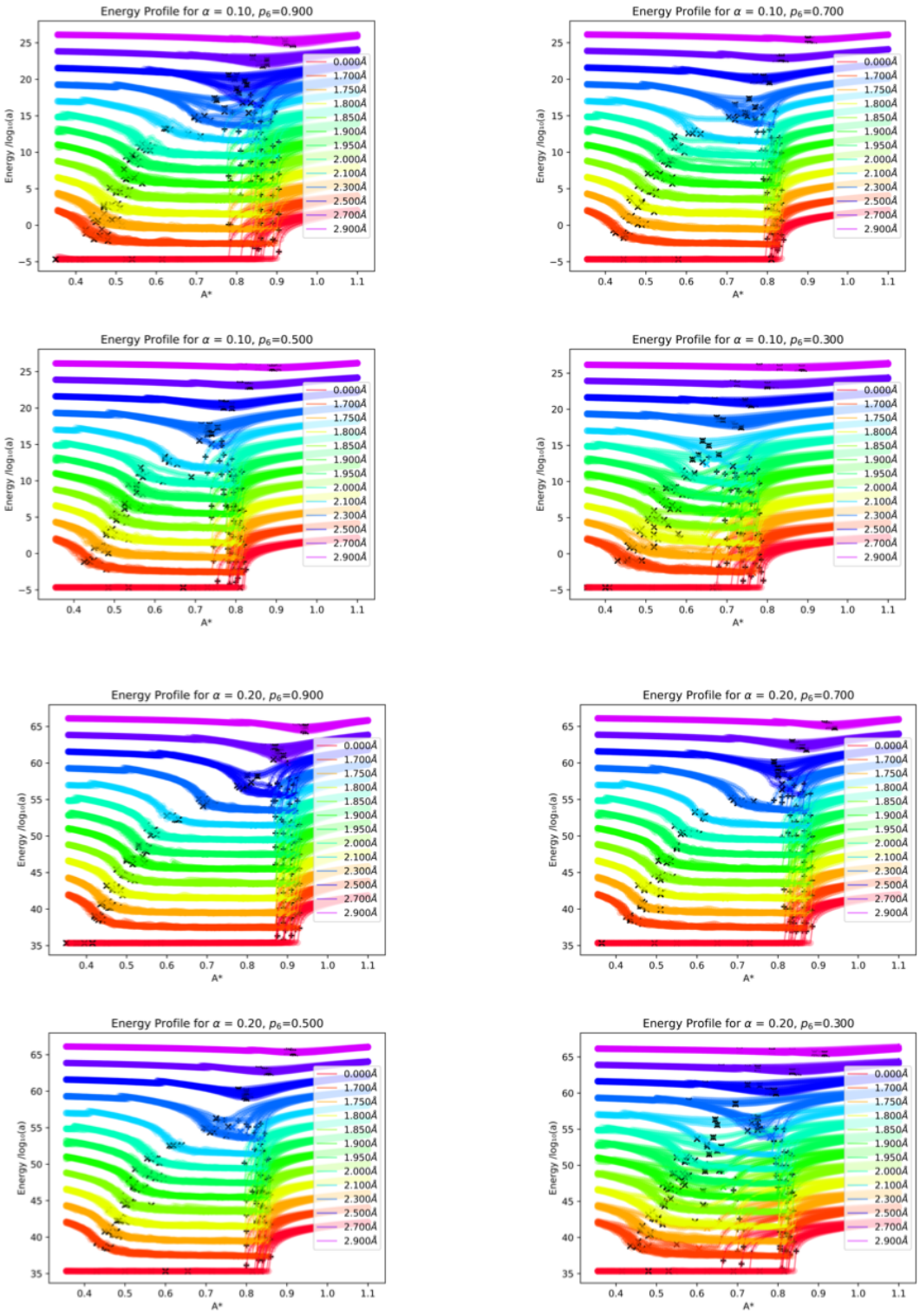

FIG. 7. Energy v. area plots for the amorphous networks constrained to contain 5-7-membered rings only and relaxed using a harmonic potential. In each panel the curves are shwon over a range of values of the short-range repulsion parameter, r_{cut} (with values as shown in the legend). Successive values of r_{cut} are offset along the abscissa for clarity. The panels are divided by the fraction of six-membered rings, p_6, and the Aboav-Weaire parameter, α, as shown at the top of each panel.

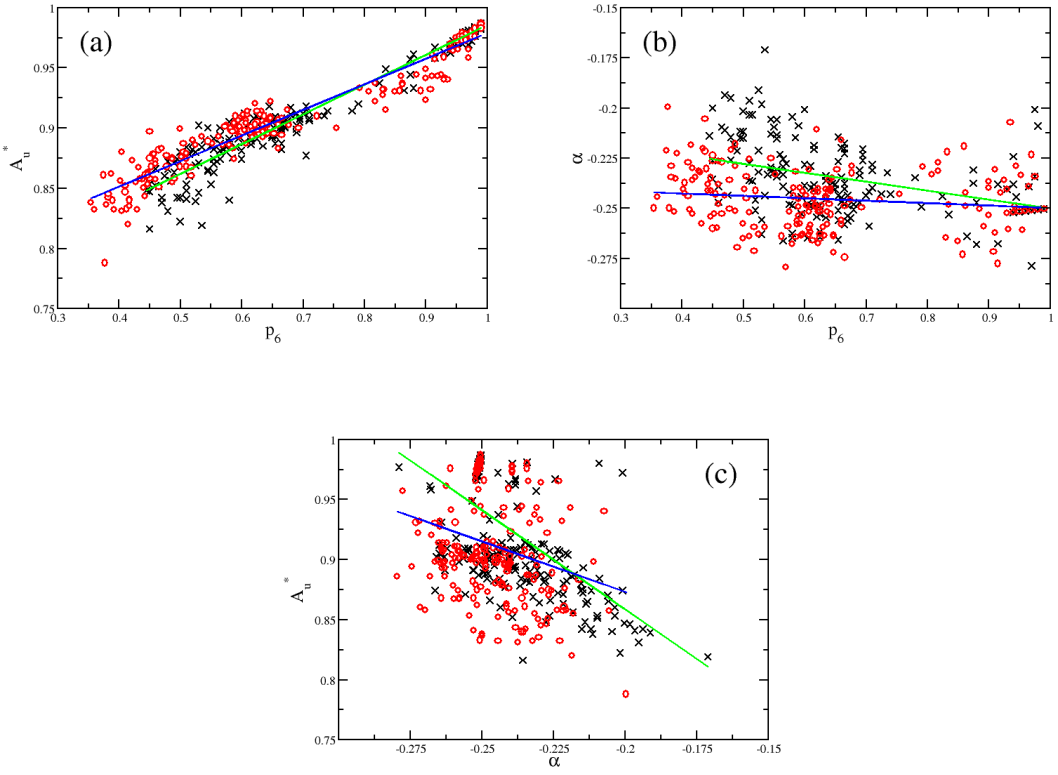

FIG. 8. Correlations between the upper critical area, A_u^*, and the fraction of six-membered rings, p_6, and the Aboav-Weaire parameter, α. Panel (a) shows A_u^* *v.* p_6, panel (b) A_u^* *v.* α, and panel (c) p_6 *v.* α. In all panels the black crosses show data for the 5-7 constrained model whilst the red circles correspond to data from the 4-10 model. The green and blue lines show the corresponding linear fits.

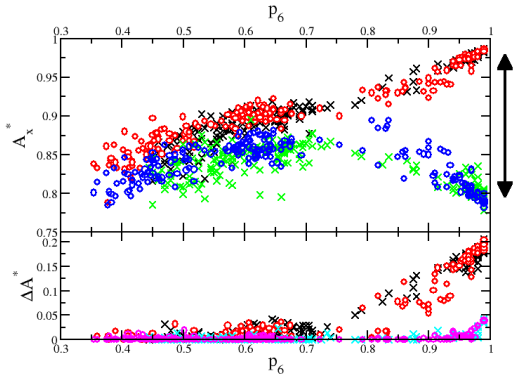

FIG. 9. (Upper panel) The behaviour of the upper and lower limits of the flexibility window as a function of the fraction of six-membered rings, p_6, with a repulsive potential controlled by the parameter $r_{cut} = 2.63$Å. The crosses and circles show the limits for the 5-7 and 4-10 constrained systems respectively with the black and red symbols corresponding to A_u^* and the green and blue to A_l^*. (Lower panel) The behaviour of the width of the flexibility window, $\Delta A = A_u^* - A_l^*$, as a function of p_6 for two values of the repulsive parameter, $r_{cut} = 2.65$Å (black and red symbols) and $r_{cut} = 3.05$Å (cyan and magenta symbols). The crosses and circles show the limits for the 5-7 and 4-10 constrained systems respectively.

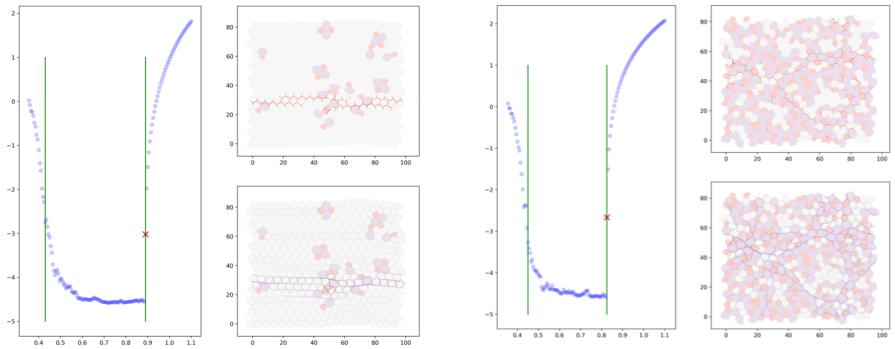

FIG. 10. Two distinct examples extracted from amorphous bilayer configurations obtained for the $5-7$ constrained networks and relaxed using a harmonic model. In each panel the left-most image shows the individual energy v. area curve wuth the area of the extracted configuration highlighted with a red cross. The corresponding configuration is displayed in the right-hand images.

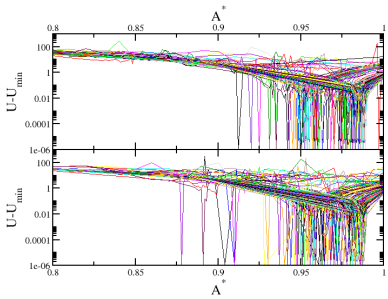

FIG. 11. Energy v. area curves for the amorphous bilayer networks obtained usng a polarizable-ion model. The energies are shown on a log scale relative to the respective energy minima. The upper and lower panels show results for the $5-7$ and $4-10$ ring constrained systems respectively. Each configuration corresponds to a given area at the energy minimum, A^*_{min}.

[44] A.Sartbaeva, S.A.Wells, M.M.J.Treacy, and M.F.Thorpe, Nature Materials **5**, 962 (2006).
[45] M.M.J.Treacy, C.J.Dawson, V.Kapko, and I.Rivin, Phil. Trans. A **372**, 20100036 (2014).
[46] F. Wooten, K. Winer, and D. Weaire, Phys. Rev. Lett. **54**, 1392 (Apr. 1985).
[47] P.N.Keating, Phys. Rev. **145**, 637 (1966).
[48] G. Barkema and N. Mousseau, Phys. Rev. B **62**(8), 4985 (2000).
[49] S. von Alfthan, A.Kuronen, and K.Kaski, Phys. Rev. B **68**, 073203 (2003).
[50] J. Lemaitre, A. Gervois, H. Peerhossaini, D. Bideau, and J. P. Troadec, J. Phys. D. Appl. Phys. **23**(11), 1396 (1990).
[51] A. Gervois, J. P. Troadec, and J. Lemaitre, J. Phys. A Gen. Phys. **25**(23), 6169 (1992).
[52] P.Tangney and S.Scandolo, J. Chem. Phys. **117**, 8898 (2002).
[53] P.A.Madden and M. Wilson, Chem. Soc. Rev. **25**, 339 (1996).
[54] V. Kapko, D. A. Drabold, and M. F. Thorpe, physica status solidi (b) **247**, 1197 (May 2010).
[55] M.Wilson, P.A.Madden, M.Hemmati, and C.A.Angell, Phys. Rev. Lett. **77**, 4023 (1996).
[56] J. Desa, J. Non-Cryst. Solids **51**, 57 (1982).

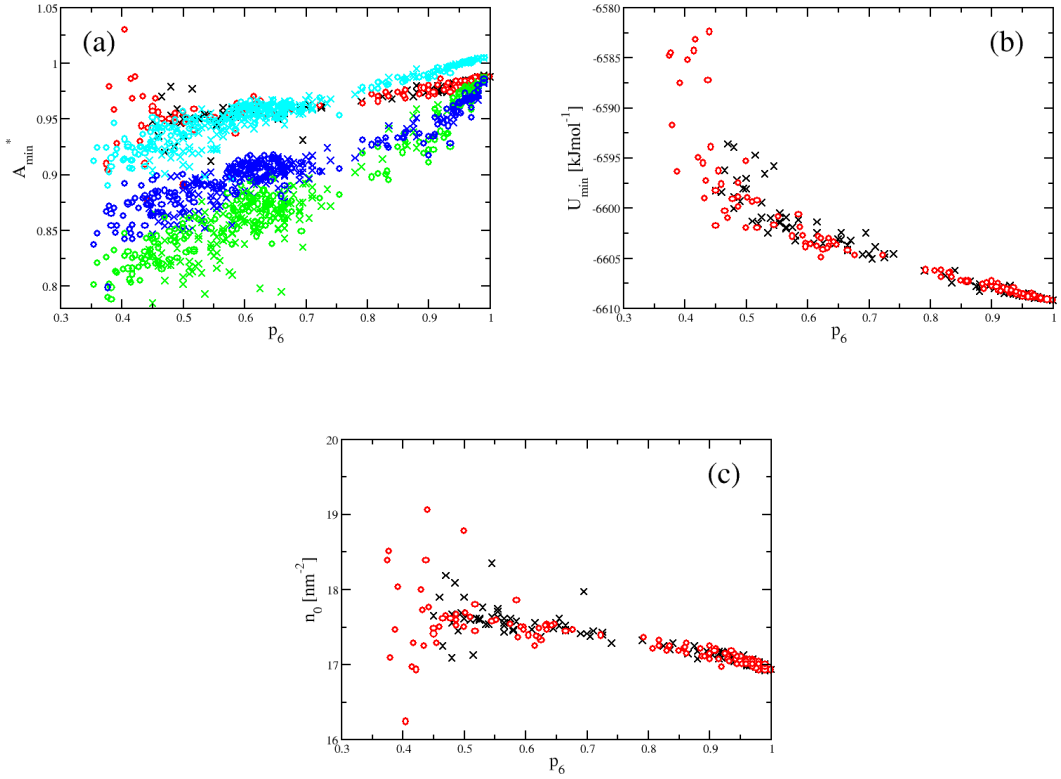

FIG. 12. Panel (a) - the dependence of the areas at the energy minima, A^*_{min}, extracted from the raw data in figure 11 for the full PIM. Panel (b) shows the corresponding energies, U_{min}, as a function of the fraction of hexagons, p_6. Panel (c) shows the data in terms of the network number density to allow for a more direct comparison with other networks. In all panels the black crosses and red circles correspond to the 5-7 and 4-10 constrained systems respectively.

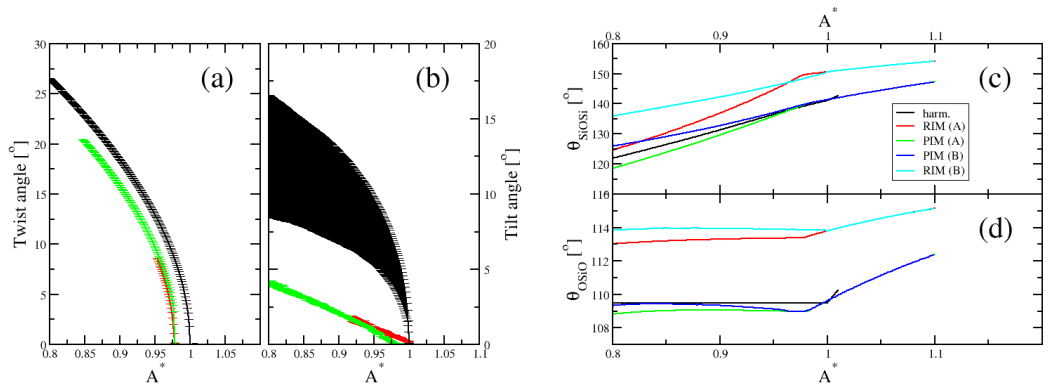

FIG. 13. Panels (a) and (b) show the twist and tilt angles for an ideal hexagonal network undergoing coherent distortions of type A and B respectively as a function of the reduced area, A^*. In both panels the black, red and green lines correspond to the harmonic, RIM and PIM models respectively. Panels (c) and (d) show the evolution of the Si-O-Si and O-Si-O bond angles determined using only the equatorial oxygen atoms (*i.e.* excluding the O atoms which link the two mirror image layers of the bilayer). The angles are determined for the harmonic model undergoing a type A distortion and the RIM and PIM undergoing both type A and B distortions as indicated in the legend.

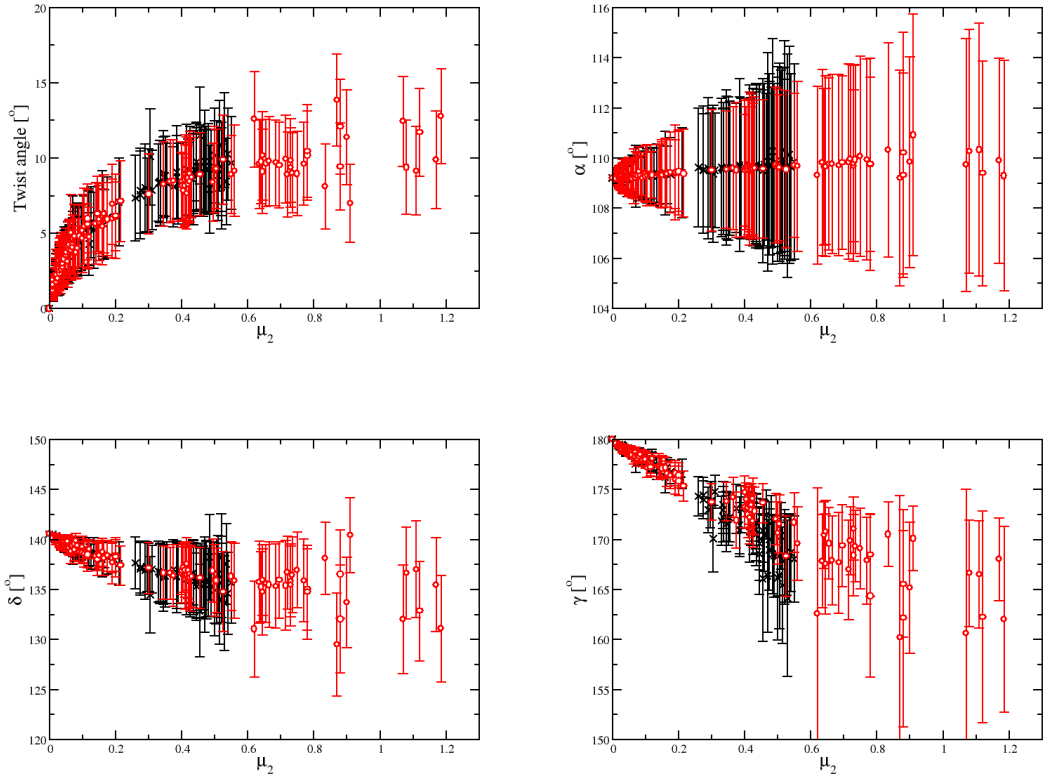

FIG. 14. The evolution of key bond angles in the amorphous networks shown as a function of the ring size distribution second moment, μ_2, indicative of the amount of topological disorder. Panels (a) and (b) show the twist and tilt angles respectively, whilst panels (c) and (d) show the Si-O-Si and O-Si-O bond angles. In all panels the black crosses and red circles correspond to the 5-7 and 4-10 constrained systems respectively.

9.3 Lower Level approximations

The highest 'level' of model applied here is to treat the system as a full atomistic bilayer. This is beyond the complexity of the level of the model presented in Chapter 5, which are all two-dimensional. It would seem simpler to use triangle raft methods as the highest level potential, however when this was attempted, networks did not reliably find a suitable energy minimum at high density. The results of the energy minimisations are shown in Figure 9.1, with three different models; harmonic bilayer, triangle raft and graphene, across area metric A*, coloured by inter-tetrahedral repulsive distances where applicable. For ordered systems (a), the triangle raft system energy replicates the bilayer system: however, introducing disorder results in regions of high energy, which did not otherwise fit the trend of data generated (b). Upon examination, these are areas where the system does not have sufficient degrees of freedom to relax, and becomes 'stuck' in high energy configurations. It is worth noting, however, that at A*$\simeq 1$, the triangle raft system reliably replicates the more detailed bilayer energetics.

9.4 Symmetry Breaking in Bilayer system simulations

Experimental observations show that bilayer structures have a plane of symmetry between layers of tetrahedra; however, this is a local minimum, stabilised experimentally by the metal surface. As our systems are compressed, it is energetically favourable for the systems to 'rumple', breaking this plane of symmetry to release some of the strain in the 'major plane'.

These structures are not experimentally realisable, and as such we look to identify these structures to remove from our data set. To do this, we must be able to quantify the symmetry breaking, whilst isolating the effect of 'tilt' modes within the structure. Figure 9.4 shows three scenarios. In the first (a), the bilayer is flat, with no tetrahedral tilt, and an intact plane of symmetry. The angle $\phi = 180°$, and the angle produced between the two Si atoms and the xy plane is $\theta = 90°$. In the second

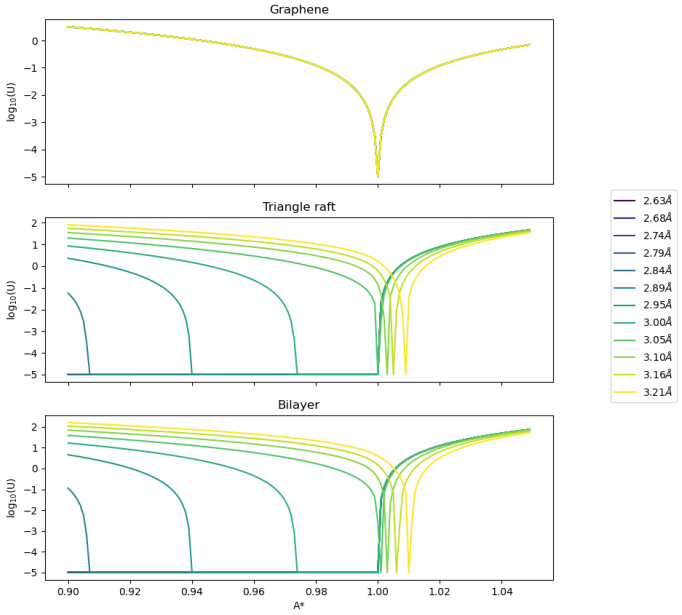

(a)

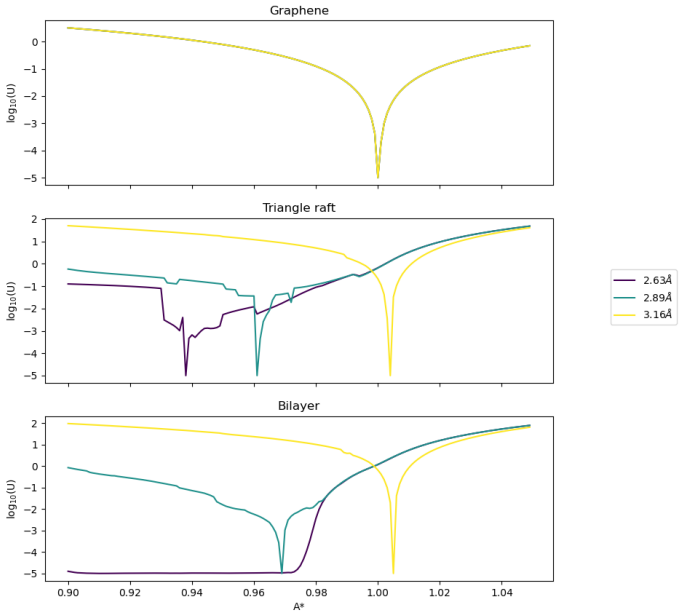

(b)

Figure 9.1: Logarithmic energy profile for different potential models for a hexagonal system (a), and a disordered system (b), across the area metric A*. Different cutoff distances for the repulsive inter-tetrahedral terms are coloured,

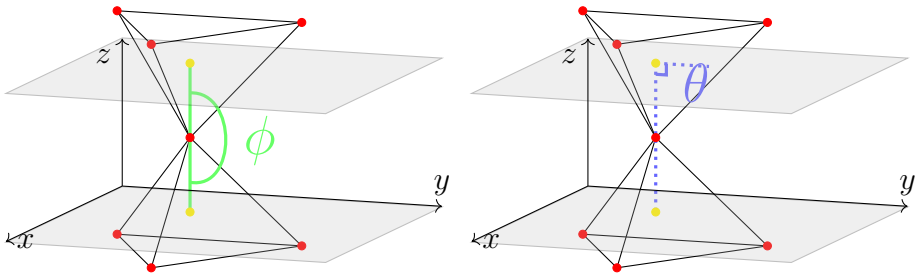

Figure 9.2: (a) Flat tetrahedra, $\phi = 180$, $\theta = 90$

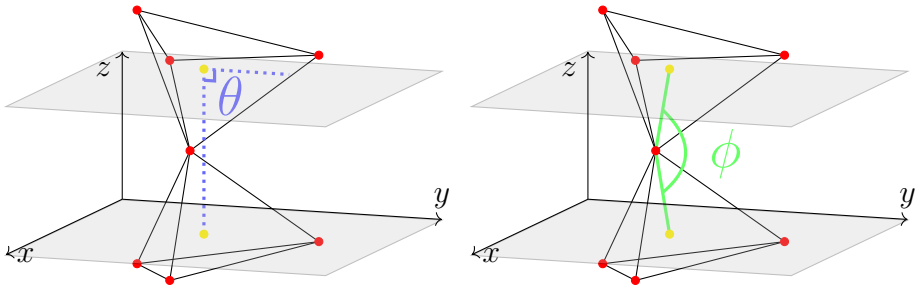

Figure 9.3: (b) Symmetric tilted tetrahedra, $\phi = 160$, $\theta = 90$

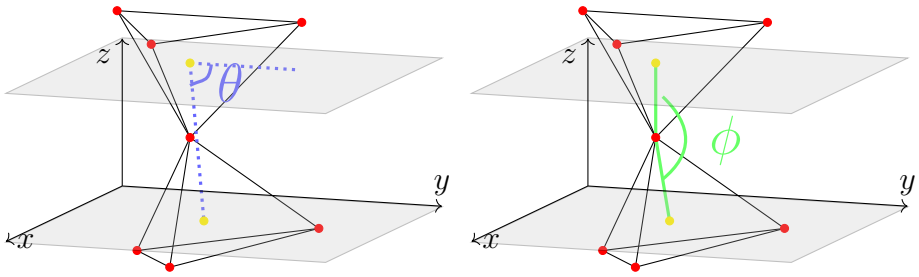

Figure 9.4: (c) Asymmetric tilted tetrahedra, $\phi = 160$, $\theta = 70$

(b), the tetrahedra are tilted, but in such a manner that maintains the symmetry of the system, meaning $\theta = 90°$. Finally, in (c), the tetrahedra are tilted such that the symmetry is broken. We can detect this as θ drops below 90°, however we note that ϕ, which might otherwise be thought of as our value of tilt, also decreases; without removing symmetry broken structures from our database in this manner, our values of ϕ can be influenced by symmetry breaking in the structures.

We set the symmetry break angle limit as 0.1°, to account for numerical inaccuracy in atom positions. Of interest is that, for all potential models, the structures show a degree of symmetry break at A*> 1.00, as shown in Figure 9.5, indicating a degree of 'slipping' of tetrahedra as the structure is stretched beyond its natural area. This is surprising, but only occurs for structures outside

of the 'flexibility window', and as such is not of concern to our understanding of the structures more generally.

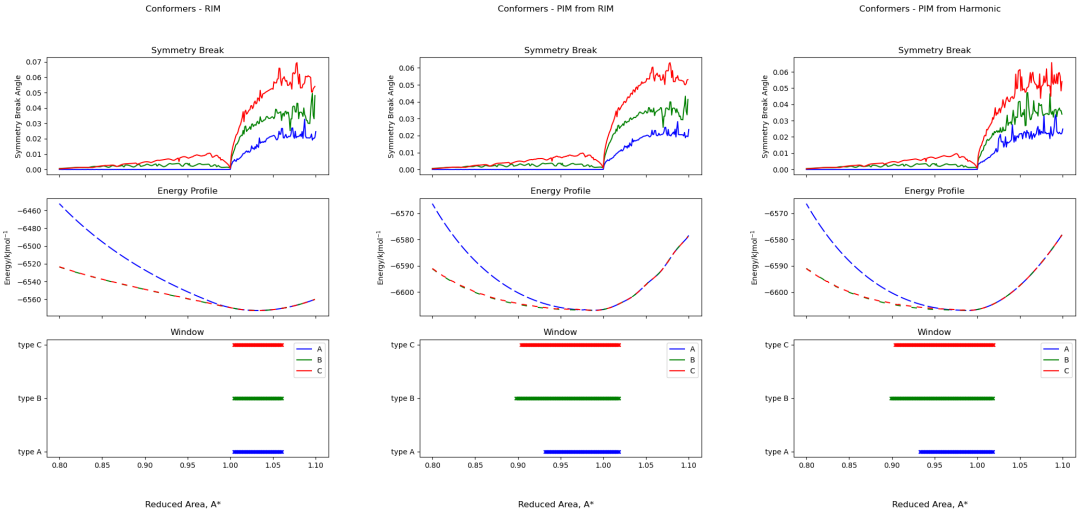

Figure 9.5: The energetics of the three conformers with higher level potentials, from the rigid ion model (RIM) on the left, to polarised ion models (PIM) with different starting points in the centre and right. Graphs are coloured by the hexagonal conformer present, with C being a symmetry equivalent form of B, with A and B as defined in Section 9.2.

9.5 Tetrahedral rotation as a zeolite metric

Zeolites have been the subject of extensive high-level modelling, as described in Section 2.4. These models are similar in complexity to our harmonic systems, with similar tetrahedral constructions; the main difference between the models is the treatment of repulsive terms, with repulsions in zeolite systems mediated by the oxygen atoms, rather than the Si atoms at the centre of the tetrahedra in our harmonic models.

As such, the metrics provided by work in this represent a helpful point of comparison, allowing an understanding of how bilayer systems fit into broader work on aluminosilicate tetrahedral systems.

Work by Wells *et. al.*[92] defined 'tetrahedral tilt' as a metric to examine the folding mechanism of three dimensional zeolite structures, also based on vertex-sharing tetrahedra of sodalite (SOD), with and without counterions. The results

of this work are shown in Figure 9.6. We can see that there is a 'takeoff' point at higher cell area, below which there is a 'predictable' degree of rotation.

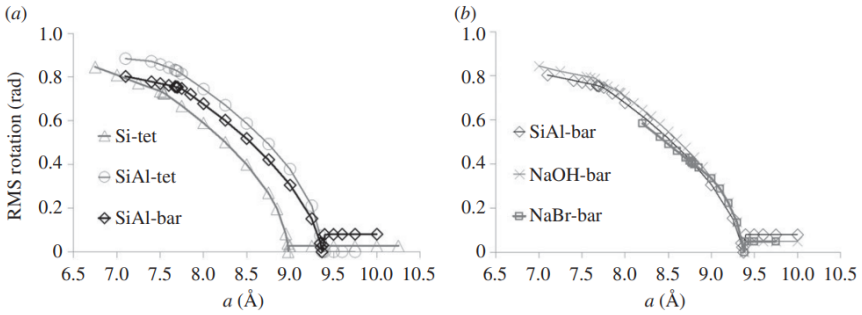

Figure 3. Tetrahedral rotation. (*a*) Degree of tetrahedral rotation of SiO_4 units as a function of cell parameter for empty SOD framework modelled with Si tetrahedra (triangles); Si and Al tetrahedra (circles); and Si tetrahedra and Al-O bar constraints (diamonds). Lines are guides to the eye. (*b*) Degree of tetrahedral rotation of SiO_4 units versus cell parameter for the SOD framework modelled with Si tetrahedra and Al-O bar constraints, with the framework empty (diamonds) as before; with spheres representing Na content (crosses); with spheres representing Na and Br content (squares).

Figure 9.6: Figure with caption describing measurements of 'tetrahedral tilt' for hard shell simulations of an aluminosilicate zeolite system, with (b) and without (a) counterions.

A similar metric was defined for our systems, namely the 'twist angle' metric in Figure 13 (a) and (b) in the draft paper above. However, as there is one fewer degree of freedom for our bilayer systems, we are able to decompose the rotations described in previous work for three dimensional systems into rotations in xy, referred to as 'twists', and z, referred to as 'tilts'. This is important for our structures as our cell parameters only change in xy, with the z cell parameter constrained. This is because the structural disorder exhibited by these pseudo-two-dimensional systems is only apparent in xy. We can see that for type A systems, all of our potential models show good agreement with the predictions from zeolite systems, indicating a similar folding mechanism. However, whilst the harmonic type B systems show a similar trend, the RIM and PIM models both show a linear trend; however, this is likely to be a result of the systems reliance on tetrahedral 'tilt', alongside 'twist' modes, to stabilise the structure. These results indicate that, although bilayers have fewer degrees of freedom, they appear to fold similarly to three dimensional zeolite structures when the cell size is reduced.

9.6 Conclusions

Escalating potential methods, as laid out in Section 4.5, have been employed to move from high level, computationally 'cheap' potentials across a wide range of configurations, with a narrower area of the phase space subjected to higher level, computationally 'expensive' potentials. Whilst triangle raft potentials have shown to be effective at lower densities, we have shown that they may lead to errors at higher densities, and so the next most detailed system, a bilayer of harmonic tetrahedra, has been employed in its place. Bilayers across a range of distortions have been generated, and analysed by their structures and energetics. For crystalline hexagonal structures, we have evaluated the energy for two conformers, and identified 'flexibility windows' in the harmonic bilayer structures, indicating densities over which the structure can be expanded and compressed with no energetic cost. Bilayer zeolite networks are proposed, and their energies are evaluated with respect to the hexagonal crystalline silica bilayer, showing minimum energy structures at lower density than the crystalline hexagonal structure. The energies of the bilayer zeolite structures are shown to be comparable to the crystalline bilayers, with the energy difference correlated to the ring size distribution variance, μ_2. A large number of systems across a range of disorder are generated, and their minimum energy structures evaluated, which show correlation between both system density and system energy with the ring size distribution variance, μ_2.

10 Procrystalline Systems

10.1 Motivations

So far, we have examined structures generated from introducing Stone-Wales defects into crystalline hexagonal networks. Alternate methods of generating structures allow the formation of configurations which occupy different areas of the phase space. Procrystals offer one such alternative. These are systems that lack translational symmetry but have an underlying high symmetry lattice. The ordered array of lattice points opens a pathway to generating layered three-dimensional structures, which we can use as a point of comparison for silica bilayer structures discussed in Chapter 9.

10.2 Nature of Procrystal Structures

Procrystals are a classification for structures constructed from an ordered array of lattice points, forming a crystalline lattice of nodes. However, the connections between nodes are disordered, resulting in a disordered dual network. Each node in real space may have the same coordination number but different orientations of the connections. As a result, procrystals appear crystalline in their atomic pair distribution functions and structure factors, whereas the difference between the atom coordination number and the natural coordination of the underlying lattice leads to disorder in the ring structure. Examples of such structures are shown in

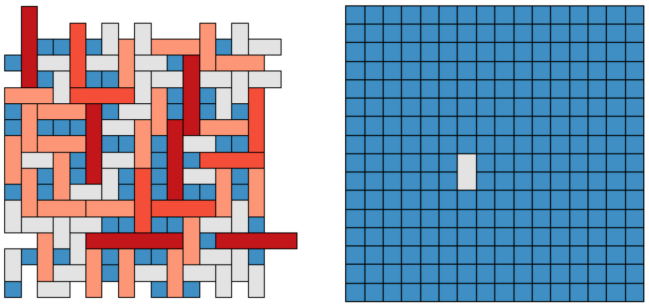

(a) (b)

Figure 10.1: Examples to show two procrystal systems, showing ordered lattice points but disordered connectivity, resulting in the ring distributions present. Two coordination environments are shown, (a) two four coordinate sites in a three coordinate lattice (b) two three coordinate sites in a four coordinate lattice.

Figure 10.1, based on a square lattice with different coordination environments. We can see that the nodes present are arranged in a crystalline lattice, but their connectivities show a level of disorder, which leads to a ring size distribution.

These networks can be considered to sit somewhere in between crystals and amorphous systems. Experimentally they are occur in self-assembled molecular monolayers[162], classical bond valence solids[163], mixed-anion perovskites[164], and order/disorder ferroelectrics[165]. The crystalline nature of the lattice offers a unique means of understanding differences within structures, focusing on connections between atoms rather than their positions. The underlying lattice may introduce constraints. For a square net, for example, the structures produced contain only even membered rings. Procrystalline structures also provide a logical step toward generating 3D systems from stacking 2D systems, with the high symmetry lattice providing a framework for inter-layer connections.

Designing and constructing three dimensional networks for molecular modelling, especially those with tuneable disorder, is a long standing challenge. Networks of this form are generally generated from thermalised structures, with connectivity inferred from inter-atomic distances.

The crystalline coordinate sites of procrystal structures allow a unique opportunity to created layered networks, either to replicate known structures in a systematic manner or to generate novel structures. Generating these structures

requires consideration for the two-dimensional structures which stack to form three dimensional structures.

The focus of the three dimensional system generation in this work is to lay the foundation for the generation of novel structures by demonstrating the capability of generating known structures of interest from a procrystalline basis.

10.3 Selection of a Procystal Model

A variety of procrystal models have been investigated in previous work[166], based on a range of underlying high symmetry lattices, onto which three coordinate nodes were introduced, allowing for a dispersion in ring sizes. Whilst these models have the desired node coordination, they have different limits on ring sizes, which narrows our options for modelling silica systems. Silica systems have been observed to form ring sizes $n \geq 4$, and as such systems that readily create three membered rings are not good candidates for modelling our systems.

With this condition, the best fit for our work is a square lattice, defined in literature as a 4,3-square lattice, shown in Figure 10.1 (a), formed by placing three coordinate tiling units on a primitive lattice of nodes.

As the direction of edge connection is tightly controlled, there is a strong limit on the size of rings which can be formed by this method, with only even membered rings allowed. This is a function of the underlying lattice, and is invariant with node coordination number. In addition, without two coordinate sites, the rings formed must be linear.

10.4 Network Generation

Generating networks using these methods is non-trivial, as with stringent atom position requirements, only four connection orientation positions are allowed per node. These connection patterns then need to be arranged in such a way that there are no under-coordinated sites. As such, a variety of methods have been evaluated for creating procrystal samples.

10.4.1 Directed Structures

The simplest way to understand how disorder is introduced into a system is by hand. As such, I have created a graphical user interface (GUI), which allows the user direct control over the coordination of tiles in the network and their orientation. An example image from the GUI is presented in Figure 10.3. Starting from a hexagonal net in (a), when the user clicks on a tiling unit, it rotates it clockwise (b-d). For tiling units where their coordination is unsaturated, the tiling unit appears red, for ease of identification. Using this method, it is easily apparent how difficult it can be to minimise a structure. Starting from a saturated system, we see that a single distortion propagates out through the entire system maintaining a consistent degree of under-coordination, before settling on a fully coordinated system (e). Introducing even the simplest disorder into the system requires defect percolation across all four periodic boundaries: Using a GUI allows a better understanding of low percolation structures, and also allows for the directed generation of structures of interest. In particular for this work, the generation of zeolite structures. For example, we can readily create an ATV structure by directed manipulation of the system, as shown in Figure 10.4, presenting a novel approach to visualising a subset of zeolite structures.

Whilst a user-directed approach is useful for understanding a small subset of more directed systems, it has less utility for understanding the range of structures avaliable and is very user intensive.

10.4.2 Exact Tiling

It has shown in previous work that exact tiling approaches are effective in evaluating unique solutions for small ($\lesssim$ 100 ring) systems[166]. However exponential scaling reduces the effectiveness of this strategy, with periodic cell sizes large enough to well approximate amorphicity (256 rings in this work) proving computationally intractable.

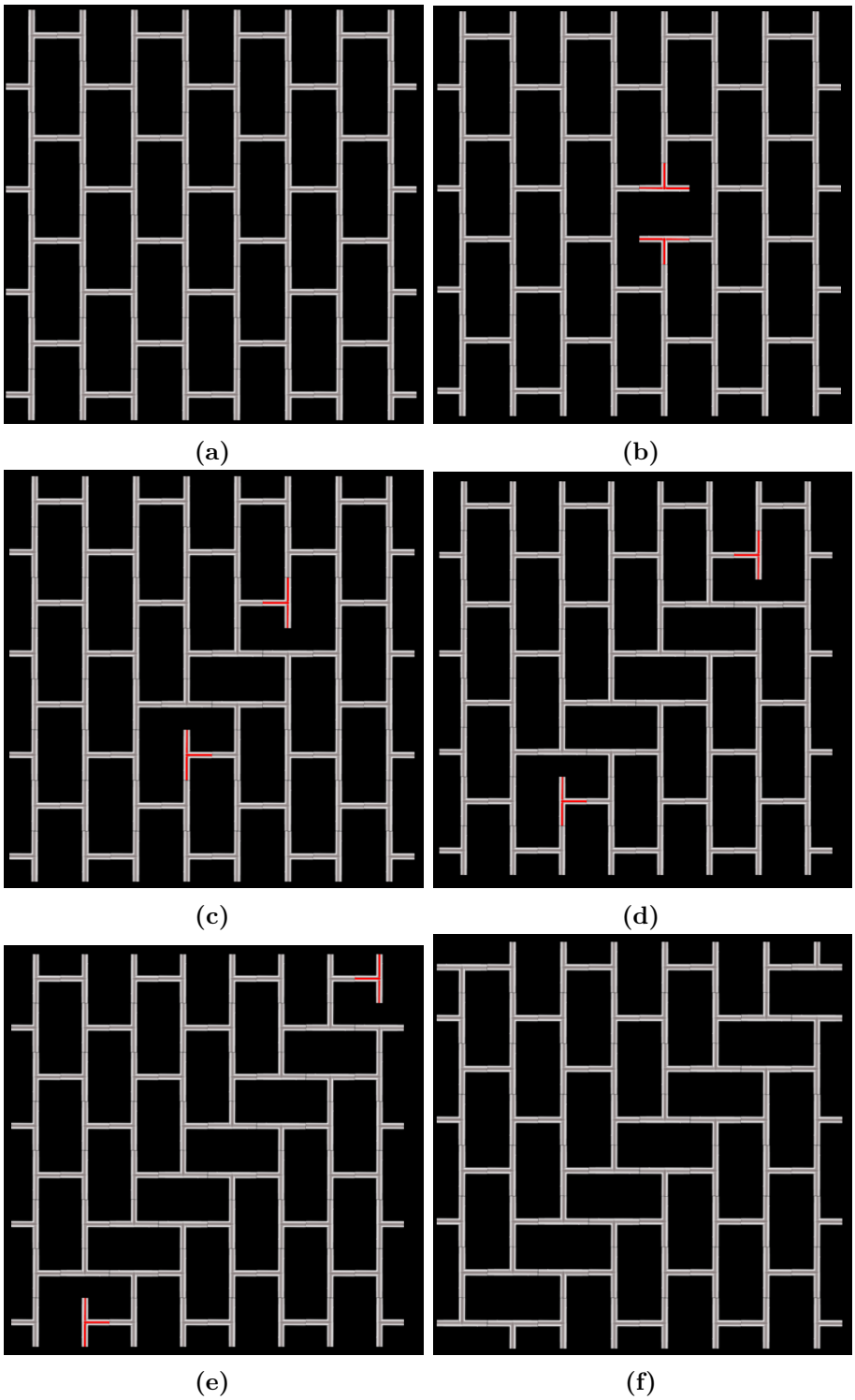

Figure 10.2: Propagation of distortion through a procrystal system.

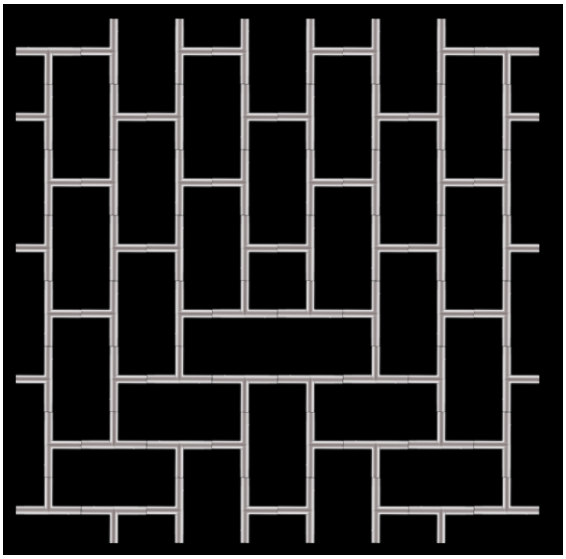

Figure 10.3: Directed distortion to create a 4-8 pair.

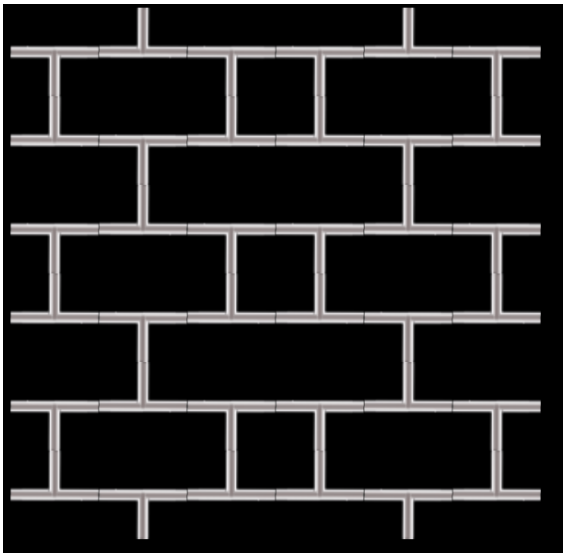

Figure 10.4: Directed distortion to create an ATV structure in a procrystal net.

10.4.3 Machine Learning

An alternative technique evaluated was a machine learning approach, which resulted in similar problems; evaluating the consequences of a given move and it's likelihood of success involves significant branching of the search algorithm. By comparison to a soluble system at the limit of our computational ability, the 'connect4' game, we can see that our system is significantly more complex. The reversibility of each step and the fact that each grid value can take one of three values are significant

complications, which put evaluating a given undercoordinated procrystal structure for possible solutions of arbitrary size beyond the analytical limit.

10.5 Monte Carlo Methods

Instead, Monte Carlo (MC) methods are used, as described in Chapter 4. This allows for the trialling of random moves, with the aim of moving towards a fully coordinated configuration. However, the enthalpies of these systems are not well defined. With identical tiling units, all saturated systems have the same local structures, and so the same enthalpies. As seen in Figure 10.3, altering the tiling units connectivity between one of the four orientations results in unsaturated coordination, with dangling bonds. The number of unsaturated connections provides a suitable target value for our Monte Carlo simulation energy, with any system with dangling bonds possessing an energy $E > 0$, and a saturated structure $E = 0$. From Equation 4.2.4.4, the probability of a transition is $P = e^{-\frac{\Delta E}{k_b T}}$. For the purposes of our work, we have assigned the energy of each 'unmatched' bond as $E = 1$. With $\Delta E = 0$, $P = 1$, allowing us to travel infinitely along energetic contours. The wide availability of energetically equivalent structures explains the widespread propagation of defects, independent of the Monte Carlo 'temperature' used.

10.5.1 Comparison to Stone-Wales Defect methods

Previous work in this thesis has centred on minimising structures amorphised from an ideal hexagonal structure. In contrast, our procrystal structures are generated from rotating three coordinate sites on a rectangular cubic lattice. There are also significant differences in the types of rings formed. As discussed above, the rectangular cubic nature of the underlying lattice means that procrystals can only form even ring sizes. This is true whether the nodes in the procrystals are three- or four-coordinate, limiting the range of structures which can be produced.

In addition, the generation of fully coordinated defects in the procrystal lattice is significantly more complicated, especially away from the entropic limit. Whereas in Stone-Wales (SW) defect generation, an MC move is guaranteed to saturate all

bonds in the network, the same is not true of simple procrystal moves. Procrystal defects are not self contained and can easily percolate long distances, proving effective for introducing disorder in a concerted manner, but providing challenges for directing the ring statistics of such systems. This is because defect propagation has unpredictable consequences. These distortions themselves are incredibly difficult to predict, and are intrinsically linked to the symmetry and dimensions of the system used. As such, there is no natural control of the level of disorder in procrystal systems when controlled by MC; instead, simulations of procrystals will form systems near the entropic limit.

10.6 Considerations for 3D modelling

Understanding the potential of procrystal systems for modeling three dimensional structures requires us to map 3-coordinate sites onto two-dimensional planes.

10.6.1 6-Coordinate Sites

The simplest system to model is sites that are 6-coordinate in three dimensions. In a cubic lattice, there is only one possible tiling unit, as shown in Figure 10.5. Decomposing this structure into its projections onto three constituent planes, we see that this system can be represented by the intersection of three planes, each of which has a four coordinate node at this point. Building a three dimensional structure from the intersection of three planes of four coordinate sites gives a rock salt structure. This is a complicated way of arriving at a rock salt structure, but it allows us to decompose the structure in a novel manner, which allows for the simple generation of a three dimensional structure. In reality, only two of these deconstructed planes are necessary to fully define the structure, with the third following inevitably.

10.6.2 5-Coordinate Sites

Reducing the coordination number introduces disorder into the structure. Although there is still only one symmetry equivalent structure that can be adopted, the orientation of this structure introduces entropy to the system. The structure can

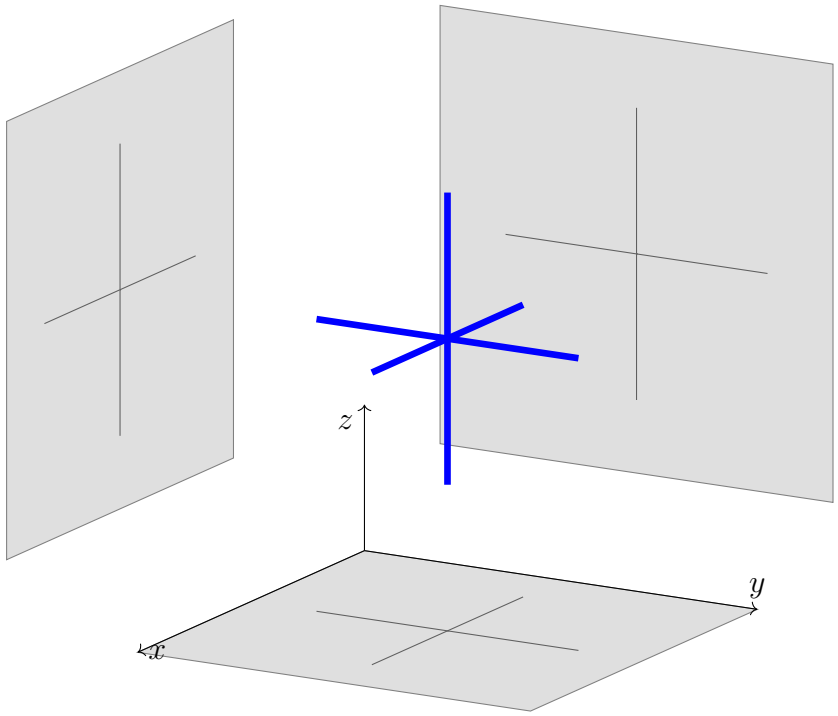

Figure 10.5: 6-Coordinate site, projected onto two-dimensional planes

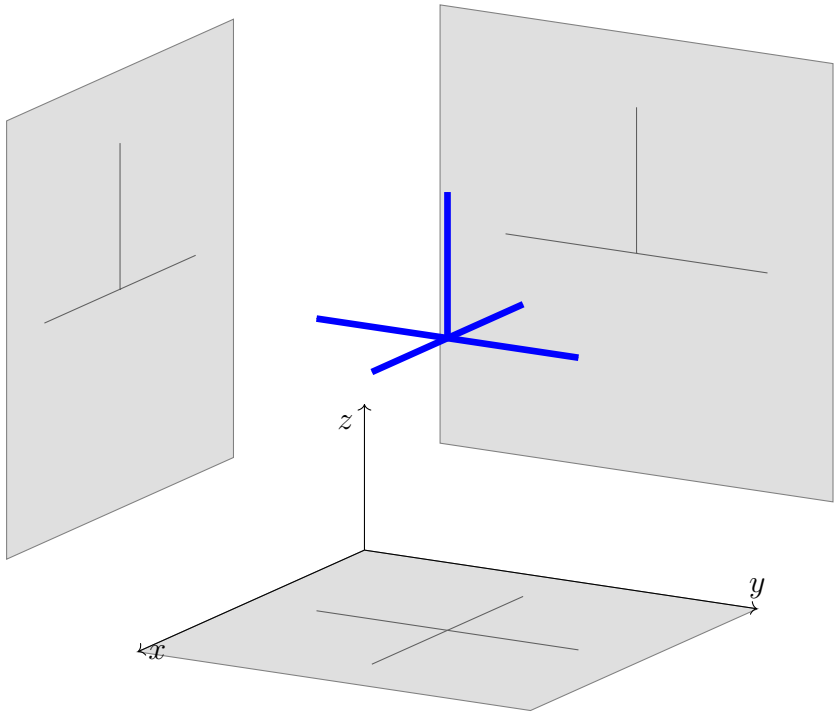

Figure 10.6: 5-Coordinate site, projected onto two-dimensional planes

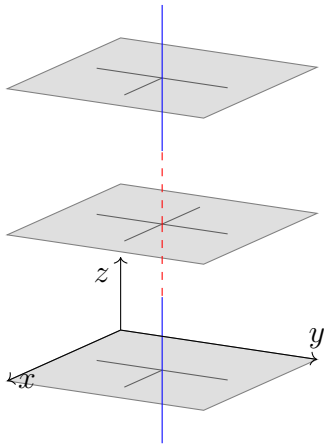

Figure 10.7: An example pathological configuration for 5 coordinate sites. There is no way to orient connections between planes (blue and red) in such a way that 5 coordination is consistently maintained

now adopt one of 6 orientations, with the location of the three coordinate sites distinguishing these conformations. As shown in the projections of the 3D node in Figure 10.6, a disordered structure of this format would have 2/3 of the sites 3-coordinate, and 1/3 4-coordinate. However, the intersection of random planes of this format will not necessarily form only 5-coordinate sites, and can lead to pathological configurations where the different planes do not predict the same tiling unit or tiling orientation. As such, from a modelling standpoint, it is best practice to form planes in two-dimensionals (say xy), and stack further xy planes on top of it, and ensure the correct coordination by controlling connections between planes. Careful consideration must be made in the alignment of different planes. For example, creating a 3-4-3 stack in z, as in Figure 10.7, results in a pathological structure, where not all nodes can be 5 coordinate. This imposes significant restrictions on the system as a whole, but can be managed well at the cost of reducing the symmetry as required. This is because stacking 4 or 3 coordinate nodes in pairs never results in a pathological configuration. As such, stacking pairs of sheets will always produce saturated coordination, so long as consideration is paid to the orientation of the initial connection. It is possible to replicate this effect with more effort, by starting at a given plane, and determining the coordination site in the plane above or below based on this approach.

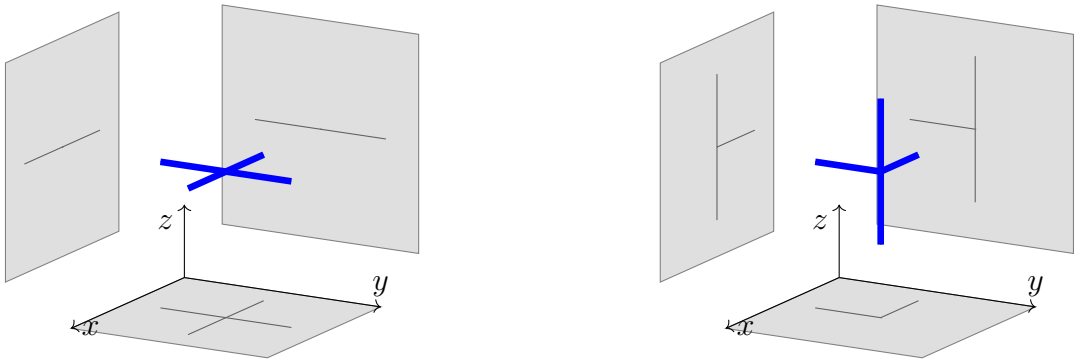

Figure 10.8: The two symmetry inequivalent forms of a 4-coordinate site in three dimensions

10.6.3 4-Coordinate Sites

Of most interest to this work are four coordinate sites, as seen in silica systems. Compared to 5 coordinate sites, we have additional degrees of freedom, with two symmetry inequivalent tiling units, each with symmetry equivalent versions, as shown in Figure 10.8 (a) and (b). One key finding of this way of viewing the system is the need to introduce 2-coordinate sites into 2D projections to properly understand stacking in three dimensions. Two coordinate sites have two symmetry equivalent structures, linear and bent.

10.7 Mixed Coordination Lattices

In order to model disordered networks with 4- and 5-coordinate sites in 3D, we will need to understand the effect of introducing mixed coordination (2,3,4-coordinate sites) in the same lattice. This presents a novel challenge, and requires a level of understanding of procrystal structures with mixed coordination, which has not so far been addressed. The mean ring size as a function of coordination number composition is presented in Figure 10.9, indicating the global effect of introducing 2- and 4- coordinate sites to a 3-coordinate system. Whilst 4-coordinate sites have a relatively small impact on mean ring size ($\langle k \rangle$), resulting in a range $4 \leq \langle k \rangle \leq 6$, 2-coordinate sites have a significant impact, allowing for the formation of very large rings, resulting in a broad range for mean ring size $3 \leq \langle k \rangle \leq 400$, which extends to the limit of our 400 node network size.

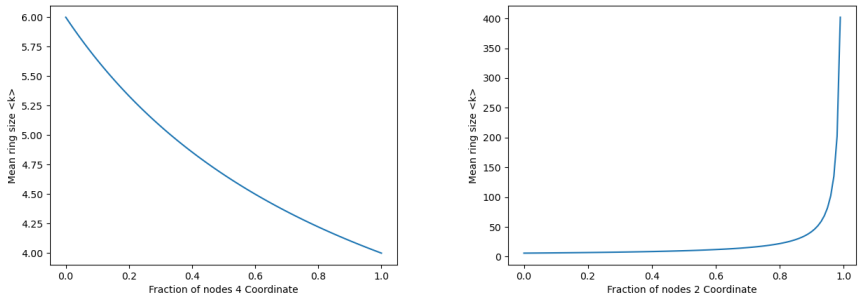

Figure 10.9: Mean Ring size as a function of 2, 4 coordinate node prevalence

10.7.1 3-Coordinate Sites

As a starting point to understanding the effect of introducing varied coordination, we need an understanding of the systems with fixed coordination number. The distribution of 1000 samples with 3-coordinate sites is shown in Figure 10.10, compared to the mean entropy expected, with the maximal value marked. We can see that the distribution sits about the maximal value, indicative of entropy-driven configurations. Visualisations of the systems at the upper and lower limits of p_6 are shown in Figures 10.11 (a) and (b) respectively. We can see that for the more

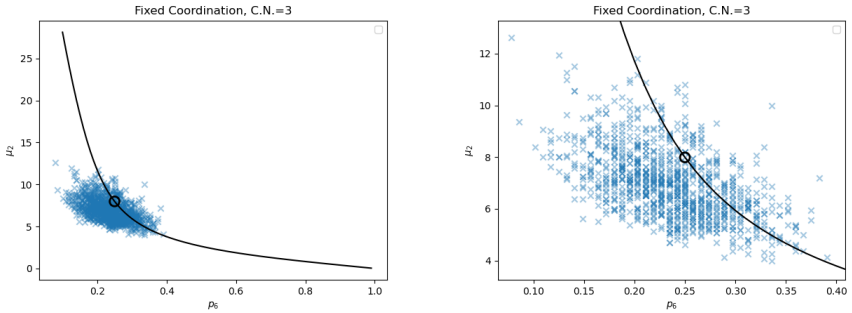

Figure 10.10: Distribution of 3-coordinate procrystal structures, as compared to the maximum entropy solution Lemaître curve

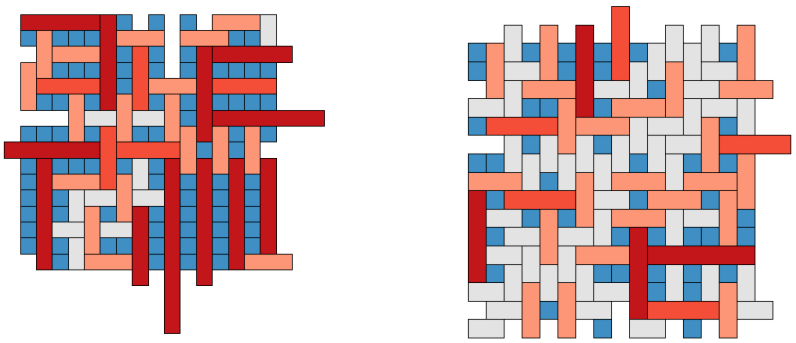

(a) **(b)**

Figure 10.11: Visualisations of samples at the lower and upper limits of p_6 for 3-coordinate systems.

disordered system (a), very large rings form, accommodated by the concomitant formation of 4-membered rings.

10.7.2 3/4-Coordinate sites

Introducing 4-coordinate sites into a 3-coordinate lattice decreases the mean ring size towards 4. This has the effect of limiting the number of unique ring distributions available to the system, and so as the percentage of four coordinate sites increases as in Figure 10.12 (a) to (d), the ring size distribution variance μ_2 decreases. We can see that increasing the proportion of four coordinate sites pushes the system towards a higher p_6; decreasing the mean ring size towards $\langle k \rangle = 4$ has the effect of shifting the ring distribution towards $k = 4$, and so with broad ring distributions

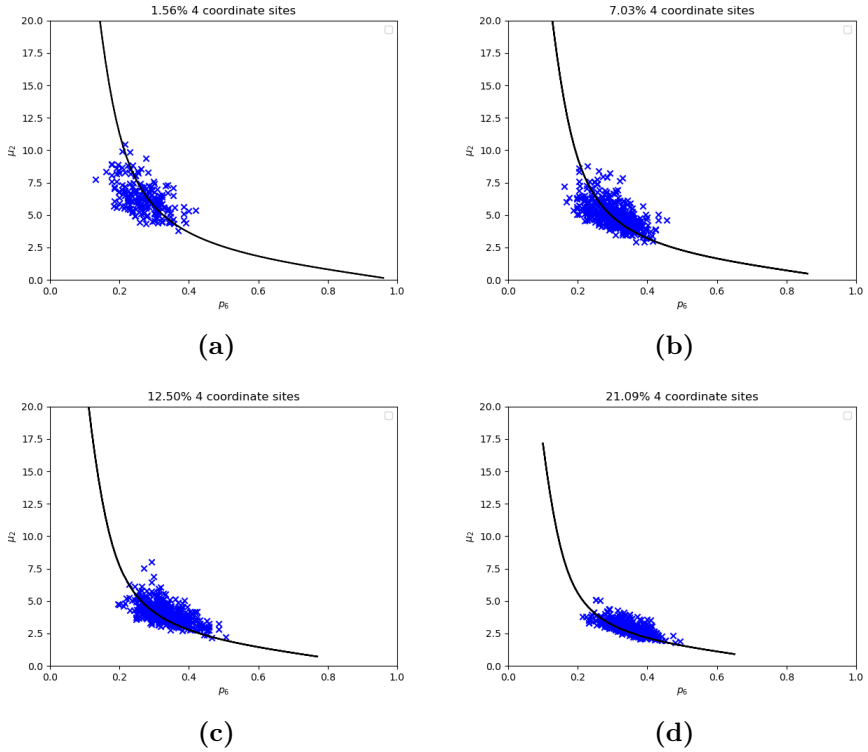

Figure 10.12: Examining the effect of introducing 4-coordinate sites on the ring distribution, with the percentage of 4-coordinate sites increasing from (a) through (d).

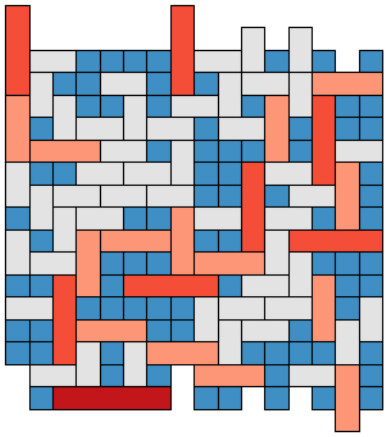

Figure 10.13: Example ring structure at 21.09% 4-coordinate sites

this also increases p_6. An example system is shown in Figure 10.13, showing a large number of four coordinate sites.

10.7.3 3/2-Coordinate sites

Figure 10.14 shows the effect of introducing 2-coordinate sites into a 3-coordinate site lattice. Whilst there is a minimal change to p_6, the variance increases significantly, as the mean ring size rises rapidly and so the distribution widens to high k.

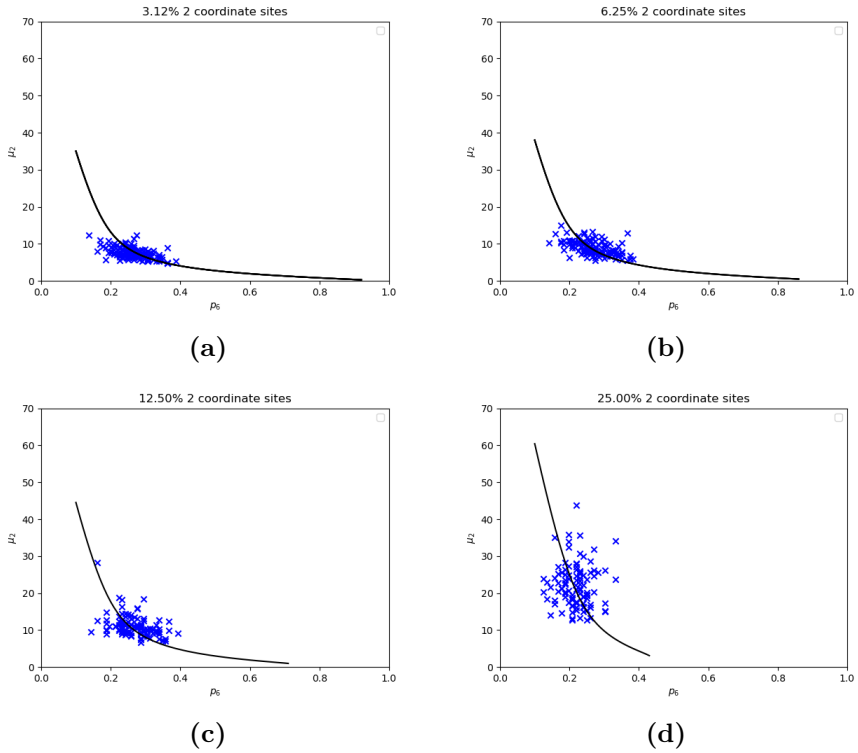

Figure 10.14: Examining the effect of introducing 2-coordinate sites on the ring distribution, with the percentage of 2-coordinate sites increasing from (a) through (d).

We can see that increasing the proportion of two coordinate sites pushes the

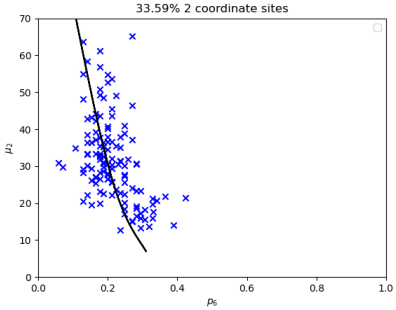

Figure 10.15: Ring distribution for high 2-coordinate site occupancy ($\simeq 1/3$), as required for 4-coordinate sites in three dimensions.

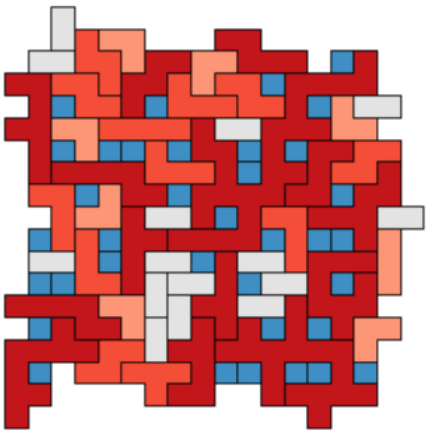

Figure 10.16: Example ring structure at 33.59% 2-coordinate sites

system towards lower p_6. As the mean ring size increases, p_6 becomes a poorer descriptor of the system, and the variance increases dramatically. However, its is of note that high proportions of two coordinate sites ($\simeq 0.33$) can be readily produced and generally understood by comparison the maximum entropy structures, as shown in in Figure 10.15. An example of such a configuration is presented in Figure 10.16, showing large rings which open up large areas of the structure. We can understand these structures in three dimensions as cavities within the structure. This finding raises the possibility of modelling three dimensional 4-coordinate sites as stacked procrystals, as the required coordination number for each layer is readily available using this method.

10.8 Three Dimensional Structures

For the purposes of this work, a limited set of relevant structures have been generated for comparison to structures we have realised as bilayers through other methods (Chapter 9). These are two crystalline silica structures and one zeolites structure, examined as silica bilayers and as 3D structures by stacking crystalline hexagonal planes in xy.

10.8.1 Identifying Interlayer Structure

The three dimensional structures we are interested in are layered structures. The simplest forms of these structures rely on stacking the same plane in xy, with alternating connections between the layers. For these structures, we have well defined coordination in xy. Where all the coordination in this plane is three coordinate, the three dimensional units created can only be those in Figure 10.8 (b). As such, we expect that the 2D projections which show 2-coordinate sites will be orthogonal to xy (*i.e.* in xz and yz). Where these two coordinate sites occur predominantly in one of these projections, we expect to find more large rings, which when they extend beyond the periodic boundaries of the system, are referred to as pores. For the examples below, the xz planes are exclusively 2-coordinate, as a result of the structures being crystalline; as such, there are pores which extend through the structure. For structures showing mixed coordination in the xy plane, this will not be the case, rather a range of coordination sites will be seen distributed across all plane projections. An example of the simplest many layer structures are given in Figure 10.17 (a), where the same xy planes are stacked on top of each other, with the only difference being the connectivity between the planes. As per the interlayer connectivities shown in black, the result of this stacking is 'boat' form interlayer hexagons, forming a lonsdaleite type structure. Figure 10.17 (b) considers an alternative situation, where the planes are shifted such that stacking forms 'chair' form interlayer hexagons, resulting in a diamond like structure. Although the lower plane here could be considered a different xy plane to the top, for this example we treat them as offset versions of each other. Bilayers make up an edge case of this approach, where only two planes are used. As such, all interlayer connections must be between the planes, as shown in Figure 10.18.

The result is two layers linked by edge sharing 4-membered rings for both pairs of planes, which reflects the reality of the situation in our bilayers.

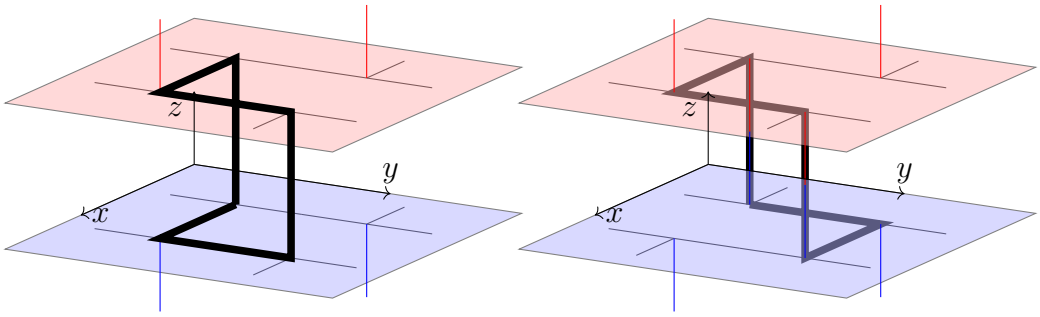

(a) (b)

Figure 10.17: Image to show two different stacking environments of the same sheet in blue and red. In (a), xy planes align exactly in z, creating 'boat' form interlayer hexagons, whereas for (b) the top xy layer is offset such that 'chair' form interlayer hexagons form.

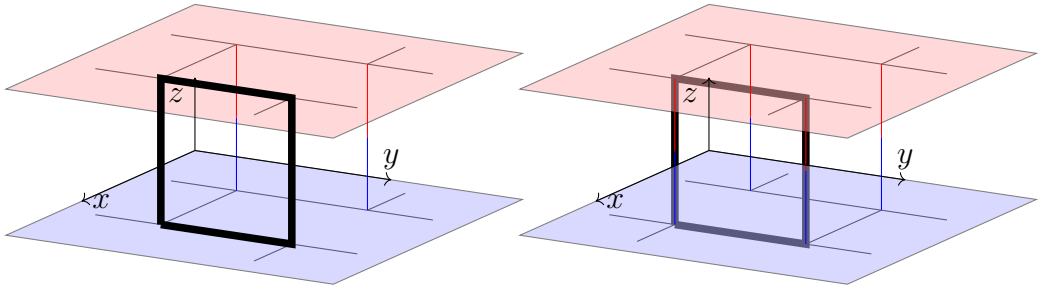

(a) (b)

Figure 10.18: Examples of bilayer stacking, using (a) planes that directly align and (b) shifted planes.

10.8.2 Minimisation Techniques

Procrystal structures do not have a useful 'natural area', and as such we cannot use the same techniques for minimisation as for Stone-Wales amorphised structures. Instead, we must find a way to sequentially find the minimum energy structure in two-dimensionals. We have accomplished this using a modified gradient descent method, as for our pores in Chapter 8, except using the triangle raft network as a reference, rather than graphene. A trial set of periodic box lengths is determined, and the structure is minimised within these constraints. Then, to build up a potential energy surface, 10 equally spaced periodic boundary limits are selected, which form a circle about our initial point radius r. The system is rescaled and constrained within each of these new periodic boundary conditions, the structure is minimised and the energy recorded. This gives an approximation to the potential energy surface at our initial point. We can then move down the potential energy

surface, with the step size linked to our approximation of the force gradient at our initial point. Using this technique, we are able to approximate the periodic cell dimensions which give the lowest energy. In three dimensions, the same technique is used, except with a sphere consisting of 100 equidistant points, rather than a circle.

10.8.3 Hexagonal Structures

Having formed network structures in three dimensions, we can adorn them with atoms and determine their energies. For this section, the process involves a harmonic minimisation, followed by a empirical potential, as in Chapter 9.

Bilayer structures

Figure 10.19 shows the systems in Figure 10.18, minimised using an empirical potential. We can see that the shifted structure, (b), appears significantly more

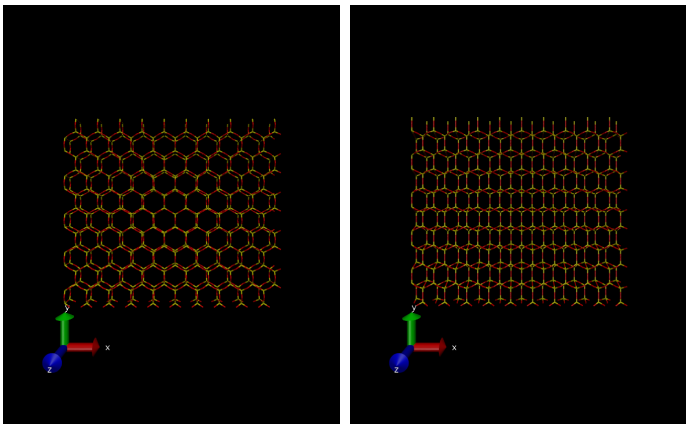

(a) **(b)**

Figure 10.19: Bilayer structures constructed from (a) aligned planes (b) shifted planes.

strained, and has no plane of symmetry, whereas (a) resembles experimental bilayer structures. The energies presented in Table 10.1 reflect this, with a significantly higher energy for the shifted system.

System	Number of Atoms	Energy (Hartree)	E ($kJmol^{-1}$)
SiO_2 Bilayer	1200	-1006.90	-6606.69
SiO_2 Bilayer shifted	1200	-1003.91	-6587.07

Table 10.1: Energy values for shifted and aligned bilayers.

Many Layer structures

Figures 10.20 and 10.21 show the structures formed from Figure 10.17. In Figure 10.20 (b) , we can see that aligned hexagonal planes produce hexagonal pores in z not present in Figure 10.21. Evaluating the energies of these two structures, Table

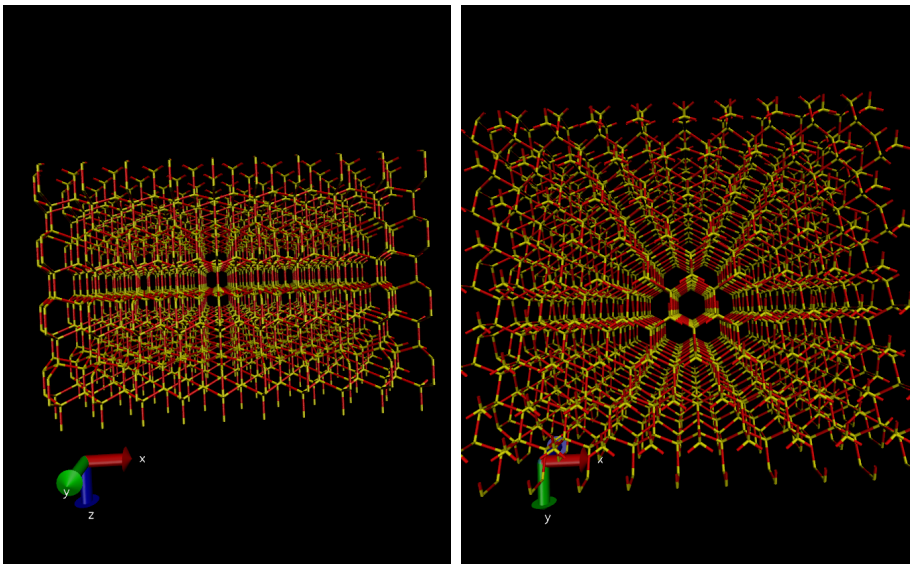

(a) **(b)**

Figure 10.20: Many layer structures for aligned hexagonal planes, shown in three different orientations. The resulting structure resembles hexagonal diamond (Lonsdalite).

10.2 shows that the energies are similar, but that our cubic structure is slightly lower in energy, as would be expected from the greater degree of staggered SiO_3-SiO_3 interactions (compare Figure 10.20 (b) to Figure 10.21 (b)), and as in keeping with our understanding of diamond structures. Of particular note, the difference in energy between conformers of SiO_2 and bilayer structures is low, providing a point of comparison for bilayer stability.

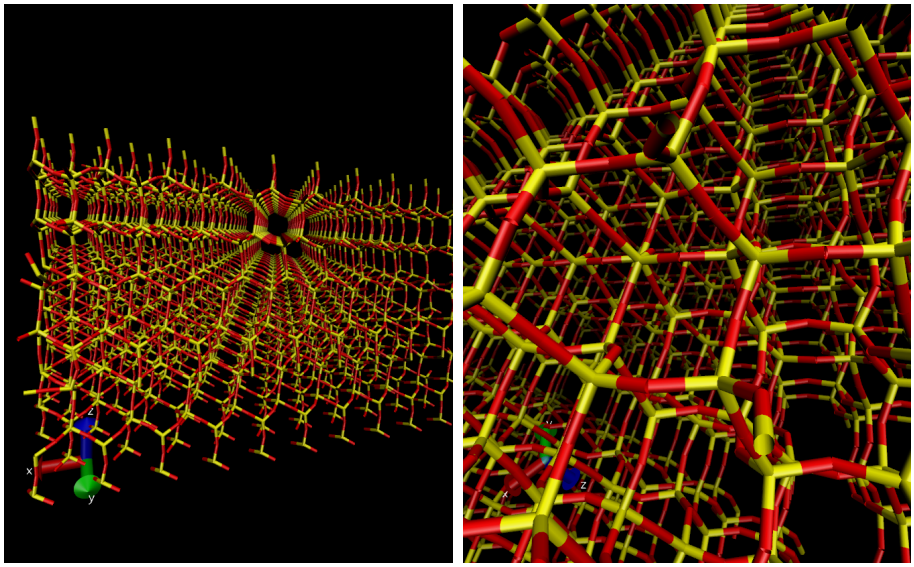

(a) (b)

Figure 10.21: Many layer structures for shifted hexagonal planes, shown in two different orientations. The resulting structure resembles cubic diamond, although slight distortion of bridging oxygens clouds this effect to a degree.

System	Number of Atoms	Energy (Hartree)	E ($kJmol^{-1}$)
SiO_2 Manylayer	4800	-4027.38	-6606.33
SiO_2 Manylayer shifted	4200	-3527.43	-6610.96

Table 10.2: Energy values for shifted and aligned many layer hexagonal structures.

10.8.4 Sample zeolite structure: ATV

In Chapter 9, we have discussed a subset of zeolites which we believe are the best candidates for silica bilayer analogues. These are zeolite structures which, using the nomenclature of this section, are composed of AB layers. The construction of three dimensional zeolites from a basis set provides a useful point of comparison for our work on zeolite bilayers, providing a better understanding of how the energy values we have calculated fit into their wider stability compared to the stability of known three dimensional structures. With zeolite structures, the IZA database has sample cell dimensions for silica equivalents, which we refer to as 'reference' dimensions. Figure 10.22 shows the structures of bilayers (a) and many layers (b) of these systems, with each showing pores in the z direction. The energies of these

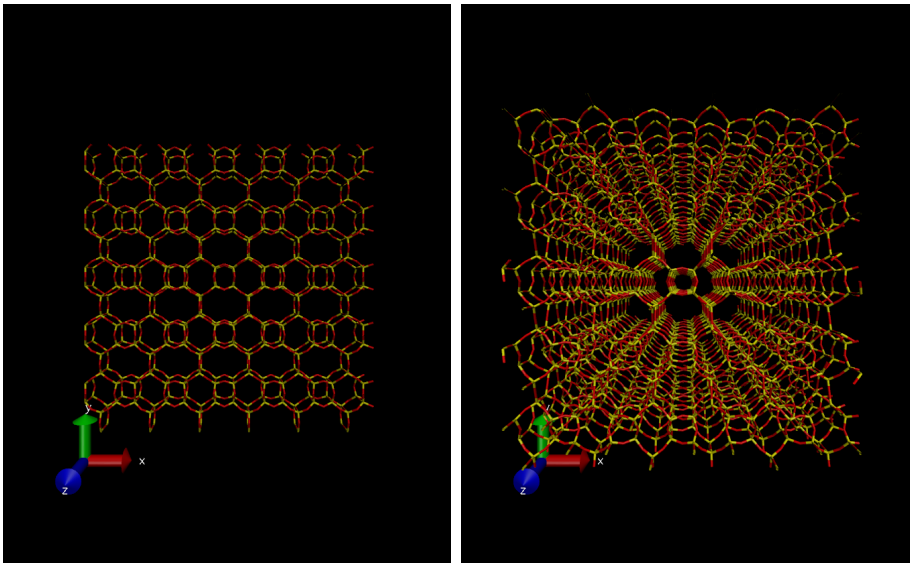

(a) **(b)**

Figure 10.22: Bilayer (a) and many layer (b) structures of ATV, a zeolite structure.

structures are given in Table 10.3, with two bilayer structures recorded, the first with cell dimensions determined by minimisation as per Section 10.8.2, and the second using reference values from the International Zeolite Association[84] for three dimensional structures. We can see that using the reference dimensions from 3D ATV for the bilayer results in a higher energy than with minimised cell dimensions. This is to be expected, as the three dimensional structure is less 'flat' in xy by virtue of the additional degree of freedom of relaxing into z; the implication of this finding is that given the density between minimised bilayer cell dimensions and the reference values, we may see different pore topologies and permeation characteristics. Evaluating the energy of the 3D ATV structure, we see that it sits slightly above that of our lowest energy SiO_2 hexagonal structure, as expected.

System	Number of Atoms	Energy (Hartrees)	Energy ($kJmol^{-1}$)
SiO_2 Bilayer	1080	-905.69	-6602.90
SiO_2 Bilayer*	1080	-905.14	-6598.89
SiO_2 Manylayer*	4320	-3627.11	-6610.83

Table 10.3: Energy values for bilayer and many layer ATV structures. Structures marked with '*' are evaluated using cell dimensions from IZA literature[84], otherwise cell dimensions are determined using local minimisation.

10.9 Conclusions

An alternative method for generating disordered systems using a procrystal basis is presented as an alternative to the Stone-Wales defect basis used elsewhere in this work. The crystalline basis of node positions lends itself to stacking layers of two-dimensional structures to form three dimensional structures. The requirements for the two-dimensional layers used to create 4-, 5- and 6-coordinate sites in three dimensions are laid out, and a range of networks to fit those criteria are generated, demonstrating sufficient flexibility in the Monte Carlo method to accommodate the required diversity in node coordination. Three sample structures were selected for further analysis, and used to create bilayer and 3D networks onto which empirical potentials could be applied for SiO_2 systems. These structures were crystalline, with two hexagonal conformers and one zeolite structure, ATV. The energies of these systems are evaluated using a polarised ion model (as in Chapter 9), allowing a point of comparison between previous work on bilayer structures. Calculations confirm low energy differences between bilayer structures and bulk crystalline silica, and between bulk crystalline silica and our zeolite, in line with literature results[6].

11 Conclusions

The overarching theme of this thesis is the development of two-dimensional methods with the explicit goal of modelling a range of experimental systems. The reasoning and methodology behind the approaches taken have varied, but at their heart each method is designed to be applicable to a given system. Two dimensional systems were selected as the focus of this work because of the breadth of their properties, with the ultimate goal being to understand and control their ring structures to facilitate the design and synthesis of technologically useful materials. Moving to very thin films, we can see an entirely different world of mechanical and electrical properties, and the ability to harness and tune these properties will come from an understanding of the connectivity that forms them. For the most part, the systems I have chosen to model are atomic systems. The particular focus of this work has been silica bilayer and graphene systems, while the learnings from these systems have led to the development of branching models of boron nitride and mammalian cell networks. In order to emulate these systems, work has first focused on low computational cost models. This has allowed for the creation of large data sets, spanning a range of disorder, in an attempt to fully encapsulate the potential configurational space for each structure. To compare and contrast between systems and across degrees of disorder, a range of classical network theory metrics, alongside novel metrics, have been utilised.

Where there is a great deal of disparate data, such as surrounding the cell structure of the corneal endothelium, classical analysis methods such as evaluation against maximum entropy distributions and area metrics provide a clear point of comparison, allowing us to condense large data sets to a limited set of useful metrics. This simplifies the process of finding a model that best fits the experimental data.

Whilst the classical network methods provided a useful point of comparison for large data sets of cell systems, metrics derived from focusing on the experimental data allow us to hone in on individual system ring properties that differentiate atomic systems from mathematical models. In particular, investigations into the even ring proportions, and specifically the predominance of 4- and 5-membered rings in silica bilayer systems, reveal a greater complexity which makes these systems unique, and which if understood could further their applicability. These new analysis routes also open up comparisons between network systems of rings, and other chemical systems. One theme through this work is the evaluation of ring structures as charged liquids, with the rings as the centres of ions whose charge is proportional to the ring size. The energies of this charge-based evaluation for systems formed by triangle raft networks show a strong correlation with disorder, even in extreme cases where very large rings are introduced. It is hoped that findings such as these will further both our modelling techniques and understanding of silica systems. Evaluating across a range of disorder allows us to bridge the gap between experimentally observed levels of disorder. Silica bilayers have been observed across a wide range of amorphicity, but with understandably limited experimental data, the relative likelihood of forming a given level of disorder is not well understood. The high throughput methods presented in this thesis have allowed for a systematic approach to disorder, employing parameterised models to probe the correlations between disorder and energy, density, and structure. In particular, the effect of disorder on the density of bilayers (which requires calculations across a range of cell areas) has not been quantified, beyond a general trend in increased density with disorder. Understanding these relationships enables us to understand the

energetic cost of a given level of distortion, which informs the design and synthesis of systems of a given level of disorder.

Modelling techniques also allow us to use our understanding of structural models to propose structures predicted to have desirable properties. For this work, these structures are systems with permeability characteristics. While both graphene and silica bilayers have been shown to be permeable to atomic and molecular species, the range of permeable species is low for the experimental structures evaluated. With finer control over the system, in particular the largest ring in the system, should come a widening of the permeability properties, critical for applications such as gas filtration, which has become ever more important in the modern world. Whilst graphene has been shown to support larger pores when irradiated, silica bilayers are more likely candidates for filtration applications, with the oxygen bridges between silicon atoms expanding the edge lengths of each ring, through which species can diffuse. However, although experimental images of poor silica bilayer coverage show the ability of the system to adopt nanometer sized holes, there is no published work on controlling pore size. There is a very high experimental cost of forming pores using templating methods, requiring finely tuned atom deposition. There is also a great deal of risk involved; if the templated rings are too large, or too close together, then the deposition will fail. By modelling both graphene and triangle raft systems with ring sizes outside of the observed range, we hope to gain an understanding of how templating or irradiation might affect the stability of the ring structure surrounding pores of a given size, to predict pore sizes of interest and their stability with density, with the ultimate goal of informing experimental processes. Whilst this work not meant as an experimental justification, our draft publication on pores is the first step towards proposing silica bilayer systems with tuneable large pores. Another area of proposed structures are zeolite analogues as bilayers, which like zeolites in three dimensions, are expected to have notable permeation characteristics. This work presents a detailed analysis of seven bilayer zeolite structures, of which five are novel, with low corresponding energy differences to the crystalline hexagonal bilayer. With over 200 experimentally confirmed zeolite

structures, we hope these findings will open up new avenues for research into the relative stabilities of and synthesis routes for zeolite bilayer systems.

Finally, procrystal structures are presented as a means to leverage our understanding of two dimensional networks in three dimensions. As a proof of concept, procrystal structures with the coordination requirements for modelling four coordinate nodes in three dimensions are generated, and six three-dimensional structures are generated by stacking two dimensional planes. These structures are then decorated as silica systems and geometry optimised using empirical potentials, showing good agreement with both values within this thesis and in literature.

I hope that this work will provide a step forward in the process of understanding two dimensional systems, in particular in understanding the impact of disorder on their design and applications, alongside a hopeful vision of paths for future development.

Appendices

A

Applying Tersoff potential to periodic Monte Carlo simulations

Applying Tersoff potentials to our network systems poses a challenge in terms of how we define connectivity. As noted in strain analysis of graphene systems[167, 168] and work to generate pores in graphene[34, 169], defects in graphene can cause a reduction of coordination. As such, our network theory approach breaks down, as both our assumptions about average ring size and our ring definitions in regions of reduced coordination break down. As such, with our defect introduction being based on connectivity, a direct Tersoff application fails here. However, by evaluating the single point energy of the coordinates of a Keating graphene system using a Tersoff potential, we can approximate the energy sufficiently for a Monte Carlo approach, which looks only at the difference in energy between the intial and final structures.

References

[1] W. H. Zachariasen. "The atomic arrangement in glass". In: *Journal of the American Chemical Society* 54 (10 1932), pp. 3841–3851.

[2] J. Kotakoski et al. "From point defects in graphene to two-dimensional amorphous carbon". In: *Physical Review Letters* 106 (10 2011), pp. 1–4.

[3] Alex W. Robertson et al. "Spatial control of defect creation in graphene at the nanoscale". In: *Nature Communications* 3 (2012), p. 1144. URL: http://www.ncbi.nlm.nih.gov/pubmed/23093181%5C%5Cnhttp://www.nature.com/doifinder/10.1038/ncomms2141.

[4] P.Y. Huang et al. "Imaging the Atoms in a Two-Dimensional Silica Glass on Graphene". In: *Microscopy and Microanalysis* 18 (S2 2012), pp. 1496–1497.

[5] Avishek Kumar, Mark Wilson, and M. F. Thorpe. "Amorphous graphene: A realization of Zachariasens glass". In: *Journal of Physics Condensed Matter* 24 (48 2012), p. 485003. URL: http://stacks.iop.org/0953-8984/24/i=48/a=485003?key=crossref.a5c6d7cb18fb40da82b9e14b3164b8d5.

[6] Leonid Lichtenstein et al. "The atomic structure of a metal-supported vitreous thin silica film". In: *Angewandte Chemie - International Edition* 51 (2 2012), pp. 404–407.

[7] Shamil Shaikhutdinov and Hans-joachim Freund. "Metal-Supported Aluminosilicate Ultrathin Films as a Versatile Tool for Studying the Surface Chemistry of Zeolites". In: *ChemPhysChem* 14 (2013), pp. 71–77.

[8] Adrián Leandro Lewandowski et al. "Atomic structure of a metal-supported two-dimensional germania film". In: *Phys. Rev. B* 97 (2018), p. 115406.

[9] Panagiotis Trogadas, Thomas F. Fuller, and Peter Strasser. "Carbon as catalyst and support for electrochemical energy conversion". In: *Carbon* 75 (2014), pp. 5–42.

[10] Litao Sun, Florian Banhart, and Jamie Warner. "Two-dimensional materials under electron irradiation". In: *MRS Bull.* 40 (01 2015), pp. 29–37. URL: http://www.journals.cambridge.org/abstract_S0883769414003030.

[11] Christin Büchner and Markus Heyde. "Two-dimensional silica opens new perspectives". In: *Progress in Surface Science* 92 (4 2017), pp. 341–374.

[12] Daniil Naberezhnyi et al. "Molecular Permeation in Freestanding Bilayer Silica". In: *Nano Letters* 22 (3 2022), pp. 1287–1293.

[13] Karn Vohra et al. "Global mortality from outdoor fine particle pollution generated by fossil fuel combustion: Results from GEOS-Chem". In: *Environmental Research* 195 (2021).

[14] J. Lelieveld et al. “The contribution of outdoor air pollution sources to premature mortality on a global scale”. In: *Nature* 525 (7569 2015), pp. 367–371.

[15] J. Lelieveld et al. “Effects of fossil fuel and total anthropogenic emission removal on public health and climate”. In: *Proceedings of the National Academy of Sciences of the United States of America* 116 (15 2019), pp. 7192–7197.

[16] A J Stone and D J Wales. “Theoretical Studies of Icosahedra C60 and Some Related Species”. In: *Chem. Phys. Lett.* 128 (5,6 1986), pp. 501–503.

[17] D A Aboav. “Arrangement of grains in a polycristal”. In: *Metallography* 3 (1970), pp. 383–390.

[18] D. Weaire. “Some remarks on the arrangement of grains in a polycrystal”. In: *Metallography* 7 (2 1974), pp. 157–160.

[19] J Lemaitre et al. “Arrangement of cells in Voronoi tesselations of monosize packing of discs”. In: *Philos. Mag. B* 67 (3 1993), pp. 347–362.

[20] Hagen W. Klemm et al. “A Silica Bilayer Supported on Ru(0001): Following the Crystalline-to Vitreous Transformation in Real Time with Spectro-microscopy”. In: *Angewandte Chemie - International Edition* 59 (26 2020), pp. 10587–10593.

[21] Mark Wilson et al. “Modeling vitreous silica bilayers”. In: *Physical Review B - Condensed Matter and Materials Physics* 87 (21 2013).

[22] L. Lichtenstein et al. “The atomic structure of a metal-supported vitreous thin silica film”. In: *Angew. Chem. Int. Ed.* 51 (2012), p. 404.

[23] Xi Zhang et al. “Structural and mechanical properties of monolayer amorphous carbon and boron nitride”. In: *Phys. Rev. B* 109 (17 2024), p. 174106. URL: https://link.aps.org/doi/10.1103/PhysRevB.109.174106.

[24] Marika Schleberger and Jani Kotakoski. “2D material science: Defect engineering by particle irradiation”. In: *Materials* 11 (10 2018).

[25] Alistair R Overy et al. “Design of crystal-like aperiodic solids with selective disorder–phonon coupling”. In: *Nat. Commun.* 7 (2016), p. 10445.

[26] K S Novoselov et al. “Electric Field Effect in Atomically Thin Carbon Films”. In: *Phys. Rev. Lett* 404 (2004), p. 3824. URL: www.arXiv.org/quant-ph/.

[27] Jermey N. A. Matthews. “The highs and lows of graphene’s strength”. In: *Physics Today* 64.1 (2011), pp. 21–21. eprint: https://pubs.aip.org/physicstoday/article-pdf/64/1/21/9880478/21_2_online.pdf. URL: https://doi.org/10.1063/1.3578252.

[28] Dimitrios G. Papageorgiou, Ian A. Kinloch, and Robert J. Young. “Mechanical properties of graphene and graphene-based nanocomposites”. In: *Progress in Materials Science* 90 (2017), pp. 75–127. URL: https://www.sciencedirect.com/science/article/pii/S0079642517300968.

[29] Mingyu Sang et al. “Electronic and Thermal Properties of Graphene and Recent Advances in Graphene Based Electronics Applications”. In: *Nanomaterials* 9 (3 2019), p. 374.

[30] Shuaiwei Wang et al. “Large-Scale Molecular Simulations on the Mechanical Response and Failure Behavior of a defective Graphene: Cases of 5–8–5 Defects”. In: *Sci. Rep.* 5 (April 2015), p. 14957. URL: http://www.nature.com/articles/srep14957.

[31] Peng Zhang et al. “Fracture toughness of graphene”. In: *Nature Communications* 5 (2014).

[32] Santosh K. Tiwari et al. *Stone–Wales Defect in Graphene*. 2023.

[33] Jannik C. Meyer et al. “Direct imaging of lattice atoms and topological defects in graphene membranes”. In: *Nano Letters* 8 (11 2008), pp. 3582–3586.

[34] Tieshan Yang et al. *Tailoring pores in graphene-based materials: From generation to applications*. 2017.

[35] Zakariya El-Machachi, Mark Wilson, and Volker L. Deringer. “Exploring the configurational space of amorphous graphene with machine-learned atomic energies”. In: *Chemical Science* 5 (2022).

[36] M. Mohr et al. “Phonon dispersion of graphite by inelastic x-ray scattering”. In: *Physical Review B - Condensed Matter and Materials Physics* 76 (3 2007).

[37] Yumeng Shi et al. “Synthesis of Few-Layer Hexagonal Boron Nitride Thin Film by Chemical Vapor Deposition”. In: *Nano Letters* 10.10 (2010). PMID: 20812716, pp. 4134–4139. eprint: https://doi.org/10.1021/nl1023707. URL: https://doi.org/10.1021/nl1023707.

[38] Seokmo Hong et al. “Ultralow-dielectric-constant amorphous boron nitride”. In: *Nature* 582 (7813 2020), pp. 511–514.

[39] Nicholas R. Glavin et al. “Amorphous Boron Nitride: A Universal, Ultrathin Dielectric for 2D Nanoelectronics”. In: *Advanced Functional Materials* 26 (16 2016), pp. 2640–2647.

[40] Cindy Y. Chen et al. “Tailoring amorphous boron nitride for high-performance two-dimensional electronics”. In: *Nature Communications* 15 (1 2024), p. 4016.

[41] Ki Kang Kim et al. “Synthesis of Monolayer Hexagonal Boron Nitride on Cu Foil Using Chemical Vapor Deposition”. In: *Nano Letters* 12.1 (2012), pp. 161–166.

[42] Willi Auwärter et al. “Synthesis of One Monolayer of Hexagonal Boron Nitride on Ni(111) from B-Trichloroborazine (ClBNH)3”. In: *Chemistry of Materials* 16.2 (2004), pp. 343–345.

[43] Y. T. Zhang et al. “Structure of amorphous two-dimensional materials: Elemental monolayer amorphous carbon versus binary monolayer amorphous boron nitride”. In: *Nano Letters* 22 (2022), p. 8018.

[44] L. C. Felix et al. “On the mechanical properties and thermal stability of a recently synthesized monolayer amorphous carbon”. In: *Journal of Physical Chemistry C* 124 (2020), p. 14855.

[45] W. Xie and Y. Wei. “Roughening for strengthening and toughening in monolayer carbon based composites”. In: *Nano Letters* 21 (2021), p. 4823.

[46] Y.-T. Zhang et al. “Thermal transport of monolayer amorphous carbon and boron nitride”. In: *Applied Physics Letters* 120 (2022), p. 222201.

[47] J. Weissenrieder et al. “Atomic structure of a thin silica film on a Mo(112) substrate: A two-dimensional network of SiO4 tetrahedra”. In: *Physical Review Letters* 95 (7 2005).

[48] D. Loeffler et al. “Growth and structure of crystalline silica sheet on ru(0 0 0 1)”. In: *Phys. Rev. Lett.* 105 (2010), p. 146104.

[49] E.I. Altman et al. “Growth and Characterization of Crystalline Silica Films on Pd(100)”. In: *J. Phys. Chem. C* 117 (2013), pp. 26144–26155.

[50] Eric I. Altman and Udo D. Schwarz. “Structural and Electronic Heterogeneity of Two Dimensional Amorphous Silica Layers”. In: *Advanced Materials Interfaces* 1.7 (2014), p. 1400108. eprint: https://onlinelibrary.wiley.com/doi/pdf/10.1002/admi.201400108. URL: https://onlinelibrary.wiley.com/doi/abs/10.1002/admi.201400108.

[51] C. Buechner et al. “A large-area transferable wide band gap 2d silicon dioxide layer”. In: *ACS Nano* 10 (2016), p. 7982.

[52] A. Kumar et al. “Ring statistics of silica bilayers”. In: *J. Phys.: Condens. Matter* 26 (2014), p. 395401.

[53] P. Tangney and S. Scandolo. “Polarization effects in pairwise interactions of silica bilayers”. In: *J. Chem. Phys.* 117 (2002), p. 8898.

[54] Bing Yang et al. “Thin silica films on Ru(0001): Monolayer, bilayer and three-dimensional networks of [SiO 4] tetrahedra”. In: *Physical Chemistry Chemical Physics* 14 (32 2012), pp. 11344–11351.

[55] Mahdi Sadjadi et al. “Refining glass structure in two dimensions”. In: *Phys. Rev. B* 96 (2017), 201405(R).

[56] J.-H. Jhang et al. “Growth of two dimensional silica and aluminosilicate bilayers on Pd (111): from incommensurate to commensurate crystalline”. In: *Phys. Chem. Chem. Phys.* (2017).

[57] Avishek Kumar et al. “Ring statistics of silica bilayers”. In: *Journal of Physics Condensed Matter* 26 (39 2014).

[58] Mahdi Sadjadi and M. F. Thorpe. “Ring correlations in random networks”. In: *Physical Review E* 94 (6 2016), pp. 1–7.

[59] T. Schroeder et al. “Epitaxial growth of SiO2 on Mo(112)”. In: *Surf. Rev. Lett.* 7 (2000), pp. 7–14.

[60] X. Yu et al. “Support effects on the atomic structure of ultrathin silica films on metals”. In: *Appl. Phys. Lett.* 100 (2012), p. 151608.

[61] Kristen M. Burson et al. “Characterizing Crystalline-Vitreous Structures: From Atomically Resolved Silica to Macroscopic Bubble Rafts”. In: *Journal of Chemical Education* 92 (11 2015), pp. 1896–1902.

[62] Torbjörn Björkman et al. “Defects in bilayer silica and graphene: Common trends in diverse hexagonal two-dimensional systems”. In: *Scientific Reports* 3 (2013).

[63] Pinshane Y. Huang et al. “Imaging Atomic Rearrangements in Two-Dimensional Silica Glass: Watching Silica’s Dance”. In: *Science* 342.6155 (2013), pp. 224–227. eprint: https://www.science.org/doi/pdf/10.1126/science.1242248. URL: https://www.science.org/doi/abs/10.1126/science.1242248.

[64] Enlai Gao, Bo Xie, and Zhiping Xu. "Two-dimensional silica: Structural, mechanical properties, and strain-induced band gap tuning". In: *J. Appl. Phys.* 119 (1 2016).

[65] Andrei Malashevich, Sohrab Ismail-Beigi, and Eric I Altman. "Directing the structure of two-dimensional silica and silicates". In: *J. Phys. Chem. C* 120 (2016), pp. 26770–26781.

[66] Edmar A. Soares et al. "Structure and registry of the silica bilayer film on Ru(0001) as viewed by LEED and DFT". In: *Physical Chemistry Chemical Physics* 24 (48 2022), pp. 29721–29730.

[67] Mark Wilson and Harry Jenkins. "Crystalline thin films of silica: Modelling, structure and energetics". In: *Journal of Physics Condensed Matter* 30 (47 2018).

[68] Yi Li and Jihong Yu. "New Stories of Zeolite Structures: Their Descriptions, Determinations, Predictions, and Evaluations". In: *Chemical Reviews* 114 (14 2014). PMID: 24844459, pp. 7268–7316. URL: https://doi.org/10.1021/cr500010r.

[69] Scott M. Auerbach, Kathleen A. Carrado, and Prabir K. Dutta. *Handbook of Zeolite Science and Technology*. CRC Press, 2003.

[70] Ruren Xu et al. *Chemistry of Zeolites and Related Porous Materials*. Wiley, 2007.

[71] Jiři Čejka, Avelino Corma, and Stacey Zones, eds. *Zeolites and Catalysis*. Wiley, 2010.

[72] R. A. van Santen and G. J. Kramer. "Reactivity Theory of Zeolitic Broensted Acidic Sites". In: *Chemical Reviews* 95 (3 1995), pp. 637–660.

[73] Avelino Corma. "From Microporous to Mesoporous Molecular Sieve Materials and Their Use in Catalysis". In: *Chemical Reviews* 97 (6 1997), pp. 2373–2420.

[74] Pierfranco Demontis and Giuseppe B. Suffritti. "Structure and Dynamics of Zeolites Investigated by Molecular Dynamics". In: *Chemical Reviews* 97 (8 1997), pp. 2845–2878.

[75] Martin Hartmann and Larry Kevan. "Transition-Metal Ions in Aluminophosphate and Silicoaluminophosphate Molecular Sieves: Location, Interaction with Adsorbates and Catalytic Properties". In: *Chemical Reviews* 99 (3 1999), pp. 635–664.

[76] Imre Kiricsi et al. "Generation, Characterization, and Transformations of Unsaturated Carbenium Ions in Zeolites". In: *Chemical Reviews* 99 (8 1999), pp. 2085–2114.

[77] Rolf Fricke et al. "Incorporation of Gallium into Zeolites: Syntheses, Properties and Catalytic Application". In: *Chemical Reviews* 100 (6 2000), pp. 2303–2406.

[78] Alenka Ristić et al. "The Performance of Small-Pore Microporous Aluminophosphates in Low-Temperature Solar Energy Storage: The Structure–Property Relationship". In: *Advanced Functional Materials* 22 (9 2012), pp. 1952–1957.

[79] Hermenegildo García and Heinz D. Roth. "Generation and Reactions of Organic Radical Cations in Zeolites". In: *Chemical Reviews* 102 (11 2002), pp. 3947–4008.

[80] Colin S. Cundy and Paul A. Cox. “The Hydrothermal Synthesis of Zeolites: History and Development from the Earliest Days to the Present Time”. In: *Chemical Reviews* 103 (3 2003), pp. 663–702.

[81] Berend Smit and Theo L. M. Maesen. “Molecular Simulations of Zeolites: Adsorption, Diffusion, and Shape Selectivity”. In: *Chemical Reviews* 108 (10 2008), pp. 4125–4184.

[82] Alexandra Navrotsky, Olga Trofymluk, and Andrey A. Levchenko. “Thermochemistry of Microporous and Mesoporous Materials”. In: *Chemical Reviews* 109 (9 2009), pp. 3885–3902.

[83] Rajamani Krishna, Berend Smit, and Sofia Calero. “Entropy effects during sorption of alkanes in zeolites”. In: *Chemical Society Reviews* 31 (3 2002), pp. 185–194.

[84] IZA. *Database of Zeolite Structures, Zeolite Framework Types*. Accessed: 2024. 2024. URL: `https://asia.iza-structure.org/IZA-SC/ftc_table.php` (visited on 09/27/2024).

[85] Michael W. Deem et al. “Computational Discovery of New Zeolite-Like Materials”. In: *The Journal of Physical Chemistry C* 113.51 (2009), pp. 21353–21360. URL: `https://doi.org/10.1021/jp906984z`.

[86] M. E. Davis. “Design for sieving”. In: *Nature* 417 (2002), p. 813.

[87] V. Kapko et al. “On the collapse of locally isostatic networks”. In: *Proceedings of the Royal Society A: Mathematical, Physical and Engineering Sciences* 465 (2111 2009), pp. 3517–3530.

[88] S. Pellegrino. “Structural computations with the singular value decomposition of the equilibrium matrix”. In: *International Journal of Solids and Structures* 30.21 (1993), pp. 3025–3035. URL: `https://www.sciencedirect.com/science/article/pii/002076839390210X`.

[89] S.D Guest and J.W Hutchinson. “On the determinacy of repetitive structures”. In: *Journal of the Mechanics and Physics of Solids* 51.3 (2003), pp. 383–391. URL: `https://www.sciencedirect.com/science/article/pii/S0022509602001072`.

[90] Asel Sartbaeva et al. “The flexibility window in zeolites”. In: *Nature Materials* 5 (12 2006), pp. 962–965.

[91] M M J Treacy and K B Borisenko. “The Local Structure of Amorphous Silicon”. In: *Science (80-.).* 335 (2012), pp. 950–953.

[92] Stephen A. Wells et al. “Defining the flexibility window in ordered aluminosilicate zeolites”. In: *Royal Society Open Science* 4 (9 2017).

[93] Yi Li and Jihong Yu. “Emerging applications of zeolites in catalysis, separation and host–guest assembly”. In: *Nature Reviews Materials* 6 (12 2021), pp. 1156–1174.

[94] H. Koningsveld. *Compendium of Zeolite Framework Types*. 1st ed. Vol. 1. Elsevier Science, 2007, pp. 1–418.

[95] Vladislav A. Blatov et al. “Three-periodic nets and tilings: natural tilings for nets”. In: *Acta Crystallographica Section A Foundations of Crystallography* 63 (5 2007), pp. 418–425.

[96] IZA. *Composite Building Units*. https://europe.iza-structure.org/IZA-SC/CBUList.html. Accessed: 2024. 2024. URL: https://europe.iza-structure.org/IZA-SC/CBUList.html (visited on 09/27/2024).

[97] C Allain and L Limat. "Regular Patterns of Cracks Formed by Directional Drying of a Collodial Suspension". In: *Phys. Rev. Lett.* 74 (15 1995), p. 2981.

[98] J. C. Earnshaw and D. J. Robinson. "Topological correlations in colloidal aggregation". In: *Physical Review Letters* 72 (23 1994), pp. 3682–3685.

[99] Mingming Tong et al. "Geometry and Topology of Two-Dimensional Dry Foams : Computer Simulation and Experimental Characterization". In: *Langmuir* 33 (2017), pp. 3839–3846.

[100] Marc Durand et al. "Statistical mechanics of two-dimensional shuffled foams: Prediction of the correlation between geometry and topology". In: *Phys. Rev. Lett.* 107 (2011), p. 168304.

[101] Lucas Goehring and Stephen W Morris. "Cracking mud, freezing dirt, and breaking rocks". In: *Phys. Today* 67 (11 2014), p. 39.

[102] C.A. Rogers. "Lagerungen in der ebene auf der Kugel und im Raum. By L. Fejes Toth Pp. x, 197. DM 24; geb. DM 27. 1953 Grundlehren der Mathematischen Wissenschaften 65 (Springer, Berlin)". In: *The Mathematical Gazette* 39.327 (1955), pp. 73–74.

[103] C P Nieuwendaal et al. "Morphology and function of the corneal endothelium after long-term contact lens wear." In: *Investigative Ophthalmology and Visual Science* 35.7 (1994), pp. 3071–3077. eprint: https://arvojournals.org/arvo/content_public/journal/iovs/933405/3071.pdf.

[104] Michael J. Doughty and Desmond Fonn. "Pleomorphism and endothelial cell size in normal and polymegethous human corneal endothelium". In: *International Contact Lens Clinic* 20 (5-6 1993), pp. 116–123.

[105] J P Schoessler. "Contact lens wear and the corneal endothelium." In: *Journal of the American Optometric Association* 58 (10 1987), pp. 804–10.

[106] T Suda. "Mosaic pattern changes in human corneal endothelium with age". In: *Japanese journal of ophthalmology* 28.4 (1984), pp. 331–338. URL: http://europepmc.org/abstract/MED/6530835.

[107] Y. Kim and T. Kim. "Scientific Reports". In: *Scientific Reports* 11 (2021).

[108] B. Chowdhury et al. "Indian Journal of Ophthalmology". In: *Indian Journal of Ophthalmology* 69 (2021), pp. 1718–1724.

[109] K. Inoue et al. "Jpn J Ophthalmol". In: *Jpn J Ophthalmol* 46 (2002), pp. 65–69.

[110] J. Lee et al. "Eye". In: *Eye* 20 (2006), pp. 315–318.

[111] N. Taşlı, E. Icel, and Y. Karakurt et al. "BMC Ophthalmology". In: *BMC Ophthalmology* 20 (2020).

[112] K. Carlson, W. Bourne, and R. Brubaker. "Investigative Ophthalmology and Visual Science". In: *Investigative Ophthalmology and Visual Science* 29 (1988), pp. 185–193.

[113] C. Nieuwendaal, M. Odenthal, and J. Kok et al. “Investigative Ophthalmology and Visual Science”. In: *Investigative Ophthalmology and Visual Science* 35 (1994), pp. 3071–3077.

[114] J. Lee et al. “Graefe’s Archive for Clinical and Experimental Ophthalmology”. In: *Graefe’s Archive for Clinical and Experimental Ophthalmology* 239 (2001), pp. 1–4.

[115] S.-W. Chang, F.-R. Hu, and L.-K. Lin. “Ophthalmologica”. In: *Ophthalmologica* 215 (2001), pp. 197–203.

[116] Leonhard Euler. “Solutio problematis ad geometriam situs pertinentis”. In: *Commentarii academiae scientiarum Petropolitanae* (8 1741), pp. 128–140. URL: https://scholarlycommons.pacific.edu/euler-works/53.

[117] Markus Gamper. “Social Network Theories: An Overview”. In: *Social Networks and Health Inequalities: A New Perspective for Research*. Ed. by Andreas Klärner et al. Cham: Springer International Publishing, 2022, pp. 35–48. URL: https://doi.org/10.1007/978-3-030-97722-1_3.

[118] Wenlin Liu et al. “Social Network Theory”. In: *The International Encyclopedia of Media Effects*. John Wiley and Sons, Ltd, 2017, pp. 1–12. eprint: https://onlinelibrary.wiley.com/doi/pdf/10.1002/9781118783764.wbieme0092. URL: https://onlinelibrary.wiley.com/doi/abs/10.1002/9781118783764.wbieme0092.

[119] Jun Wang et al. “Research on Artificial Spider Web Model for Farmland Wireless Sensor Network”. In: *Wireless Communications and Mobile Computing* 2018 (2018).

[120] S Boccaletti et al. “Complex networks : Structure and dynamics”. In: *Phys. Rep.* 424 (2006), pp. 175–308.

[121] Steven H Strogatz. “Exploring complex networks”. In: *Nature* 410 (2001), p. 268.

[122] Matthew C Gibson et al. “The emergence of geometric order in proliferating metazoan epithelia”. In: *Nature* 442 (2006), pp. 1038–1041.

[123] Ross Carter et al. “Pavement cells and the topology puzzle”. In: *Development* 144 (23 2017), pp. 4386–4397. URL: http://dev.biologists.org/lookup/doi/10.1242/dev.157073.

[124] David Ormrod Morley et al. “Generalized network theory of physical two-dimensional systems”. In: *Physical Review E* 101 (4 2020).

[125] David P Landau and Kurt Binder. *A Guide to Monte Carlo Simulations in Statistical Physics*. 4th ed. Cambridge University Press, 2014.

[126] David J Wales and Harold A Scheraga. “Global Optimization of Clusters, Crystals, and Biomolecules”. In: *Science (80-.).* 285 (1999), pp. 1368–1372.

[127] Andrea C Levi and Miroslav Kotrla. “Theory and simulation of crystal growth”. In: *J. Phys. Condens. Matter* 9 (1997), p. 299.

[128] C Ratsch and J A Venables. “Nucleation Theory and the Early Stages of Thin Film Growth”. In: *J. Vac. Sci. Technol. A* 21 (2003), S96.

[129] Wlater Kob. “Computer simulations of supercooled liquids and glasses”. In: *J. Phys. Condens. Matter* 11 (1999), R85.

[130] Pablo Jensen. "Growth of nanostructures by cluster deposition: Experiments and simple models". In: *Rev. Mod. Phys.* 71 (5 1999), pp. 1695–1735.

[131] Jakša Cvitanić, Levon Goukasian, and Fernando Zapatero. "Monte Carlo computation of optimal portfolios in complete markets". In: *Journal of Economic Dynamics and Control* 27.6 (2003). High-Performance Computing for Financial Planning, pp. 971–986. URL: https://www.sciencedirect.com/science/article/pii/S0165188902000519.

[132] Paul A Madden and Mark Wilson. "'Covalent' effects in 'ionic' liquids". In: *Journal of Physics: Condensed Matter* 12.8A (2000), A95.

[133] David Ormrod Morley and Mark Wilson. "Controlling disorder in two-dimensional networks". In: *Journal of Physics Condensed Matter* 30 (50 2018).

[134] David Ormrod Morley and Mark Wilson. "Constructing bilayers with tuneable ring statistics and topologies". In: *Mol. Phys.* 117 (21 2019), pp. 3148–3157. URL: https://doi.org/00268976.2019.1605099.

[135] Franz Bamer, Firaz Ebrahem, and Bernd Markert. "Elementary plastic events in a Zachariasen glass under shear and pressure". In: *Materialia* 9 (2020), p. 100556.

[136] F Wooten, K Winer, and D Weaire. "Computer Generation of Structural Models of Amorphous Si and Ge". In: *Phys. Rev. Lett.* 54 (13 1985), pp. 1392–1395.

[137] S. Von Alfthan, A. Kuronen, and K. Kaski. "Realistic models of amorphous silica: A comparative study of different potentials". In: *Physical Review B - Condensed Matter and Materials Physics* 68 (7 2003), pp. 1–4.

[138] Richard L.C. Vink. "A finite-temperature Monte Carlo algorithm for network forming materials". In: *Journal of Chemical Physics* 140 (10 2014).

[139] Yuhai Tu et al. "Properties of a Continuous-Random-Network Model for Amorphous Systems". In: *Phys. Rev. Lett.* 81 (22 1998), pp. 4899–4902.

[140] B R Djordjevic, M F Thorpe, and F Wooten. "Computer model of tetrahedral amorphous diamond". In: *Phys. Rev. B* 52 (8 1995), pp. 5685–5690.

[141] Normand Mousseau and G T Barkema. "Binary continuous random networks". In: *J. Phys. Condens. Matter* 16 (2004), S5183–S5190. URL: http://stacks.iop.org/0953-8984/16/i=44/a=015?key=crossref.01b11c9db95552f4d994b3e3f816264c.

[142] E M Huisman, C Storm, and G T Barkema. "Monte Carlo study of multiply crosslinked semiflexible polymer networks". In: *Phys. Rev. E* 78 (2008), p. 51801.

[143] C P Broedersz and F C Mackintosh. "Modeling semiflexible polymer networks". In: *Rev. Mod. Phys.* 86 (2014), pp. 995–1036.

[144] Sandeep K Jain and Gerard T Barkema. "Rupture of amorphous graphene via void formation". In: *PCCP* 20 (2018), pp. 16966–16972.

[145] Avishek Kumar, Mark Wilson, and M. F. Thorpe. "Amorphous graphene: A realization of Zachariasens glass". In: *Journal of Physics Condensed Matter* 24 (48 2012).

[146] A. P. Thompson et al. "LAMMPS - a flexible simulation tool for particle-based materials modeling at the atomic, meso, and continuum scales". In: *Comp. Phys. Comm.* 271 (2022), p. 108171.

[147] Avishek Kumar et al. “Ring statistics of silica bilayers”. In: *Journal of Physics Condensed Matter* 26 (39 2014).

[148] Avishek Kumar et al. “Structural Modelling of Two Dimensional Amorphous Materials”. PhD thesis. Arizona State University, 2014.

[149] Yu Tian Zhang et al. “Structure of Amorphous Two-Dimensional Materials: Elemental Monolayer Amorphous Carbon versus Binary Monolayer Amorphous Boron Nitride”. In: *Nano Letters* 22 (19 2022), pp. 8018–8024.

[150] J. H. Los et al. “Extended Tersoff potential for boron nitride: Energetics and elastic properties of pristine and defective h -BN”. In: *Physical Review B* 96 (18 2017).

[151] J. Anibal Boscoboinik et al. “Building blocks of zeolites on an aluminosilicate ultra-thin film”. In: *Microporous and Mesoporous Materials* 165 (2013), pp. 158–162.

[152] Jorge Anibal Boscoboinik et al. “Modeling zeolites with metal-supported two-dimensional aluminosilicate films”. In: *Angewandte Chemie - International Edition* 51 (24 2012), pp. 6005–6008.

[153] James F Shackelford. *TRIANGLE RAFTS-EXTENDED ZACHARIASEN SCHEMATICS FOR STRUCTURE MODELING*. 1982.

[154] Projesh Kumar Roy, Markus Heyde, and Andreas Heuer. “Modelling the atomic arrangement of amorphous 2D silica: A network analysis”. In: *Physical Chemistry Chemical Physics* 20 (21 2018), pp. 14725–14739.

[155] David Ormrod Morley and Mark Wilson. “Controlling disorder in two-dimensional networks”. In: *Journal of Physics Condensed Matter* 30 (50 2018).

[156] Tomaso Aste and David Sherrington. “Glass transition in self-organizing cellular patterns”. In: *J. Phys. A. Math. Gen.* 32 (41 1999), pp. 7049–7056.

[157] Alejandro M. Boscoboinik et al. “Structural evolution of two-dimensional silicates using a “bond-switching” algorithm”. In: *Nanoscale* 13 (4 2021), pp. 2408–2419. URL: http://dx.doi.org/10.1039/D0NR07623F.

[158] Franz Bamer, Firaz Ebrahem, and Bernd Markert. “Athermal mechanical analysis of Stone-Wales defects in two-dimensional silica”. In: *Comput. Mater. Sci.* 163 (2019), pp. 301–307. URL: https://doi.org/10.1016/j.commatsci.2019.03.050.

[159] Christin Büchner. “Adding a Novel Material to the 2D Toolbox: Properties and Transfer of a Silica Bilayer”. In: (2016), pp. 1–127.

[160] P. Z. Sun et al. “Exponentially selective molecular sieving through angstrom pores”. In: *Nature Communications* 12 (1 2021).

[161] Tuan T. Tran et al. “A contactless single-step process for simultaneous nanoscale patterning and cleaning of large-area graphene”. In: *2D Materials* 10 (2 2023).

[162] Matthew O Blunt et al. “Random Tiling and Topological Defects in a Two-Dimensional Molecular Network”. In: *Science (80-.).* 322 (2008), pp. 1077–1081.

[163] P W Anderson. “RESONATING VALENCE BONDS" A NEW KIND OF INSULATOR?” In: *Mat. Res. Bull.* 8 (1973), pp. 153–160.

[164] Philip J Camp, Amparo Fuertes, and J P Attfield. "Subextensive Entropies and Open Order in Perovskite Oxynitrides". In: *J Am Chem Soc* 134 (2012), pp. 6762–6766.

[165] R Comes, M Lambert, and A Guinier. "THE CHAIN STHUCTURE OF BaT1O3 AND KNbO3". In: *Solid State Commun.* 6 (1968), pp. 715–719.

[166] D Ormrod Morley, A L Goodwin, and M Wilson. "Ring structure of selected two-dimensional procrystalline lattices". In: *Physical Review E* 102 (6-1 2020).

[167] Teng Zhang and Huajian Gao. "Toughening Graphene With Topological Defects: A Perspective". In: *Journal of Applied Mechanics* 82 (5 2015), p. 051001. URL: http://appliedmechanics.asmedigitalcollection.asme.org/article.aspx?doi=10.1115/1.4030052.

[168] Teng Zhang, Xiaoyan Li, and Huajian Gao. "Fracture of graphene: a review". In: *International Journal of Fracture* 196 (1-2 2015), pp. 1–31.

[169] Kangning Zhao et al. "Tuning Pore Size in Graphene in the Angstrom Regime for Highly Selective Ion-Ion Separation". In: *ACS Nano* (2023).